



BIOLOGICAL MATERIALS

MECHANICAL PROPERTIES
OF BULK BIOLOGICAL MATERIALS



© Manuel Elices and Gustavo V. Guinea

Translated by John Morton.

The authors wish to express their appreciation to Dr. John Morton for his helpful collaboration on the translation.

ISBN: ?????

Legal deposit: M-?????-2021

Design and layout: Albatros Comunicación, S.L.

It is strictly forbidden, without the written authorization of the copyright holder, under the sanctions established in the laws, the total or partial reproduction of this work by any means or procedure, known or unknown, including reprography, computer processing and distribution. of copies of it by rent or public loan.

Index

CHAPTER 1. GENERAL CONCEPTS	5
1.1. Introduction	5
1.2. Composite and cellular materials	6
1.3. Biomineralisation	8
CHAPTER 2. MECHANICAL PROPERTIES	9
2.1. Introduction and objectives	9
2.2. Test and characterisation techniques	10
2.2.1. Tensile, compression, torsion and flexure tests	10
2.2.2. Rupture tests	26
2.2.3. Indentation tests	33
2.3. Mechanical behaviour	45
2.3.1. Introduction	45
2.3.2. Homogeneous materials	46
2.3.3. Heterogeneous materials	60
2.3.4. Cellular materials	67
CHAPTER 3. EXAMPLES	83
3.1. Mollusc shells	83
3.1.1. Introduction	83
3.1.2. Structure	86
3.1.3. Mechanical properties	89
3.1.4. Final remarks	99
3.2. Wood	102
3.2.1. Introduction	102
3.2.2. Structure	103
3.2.3. Mechanical properties	107
3.4.4. Final remarks	115
3.3. Bone	119
3.3.1. Introduction	119
3.3.2. Structure	121
3.3.3. Mechanical properties	123
3.4.4. Final remarks	137
3.4. Cartilage	139
3.4.1 Introduction	139
3.4.2. Structure	141
3.4.3. Mechanical properties	143
3.4.4. Final remarks	153
REFERENCES	157
SUBJECT INDEX	165

1

CHAPTER

General concepts

1.1. Introduction

1.2. Composite and cellular materials

1.3. Biomineralisation

1.1. INTRODUCTION

The focus of this section is the class of biological materials in which it is necessary to consider the three spatial dimensions (3D) for an adequate description and study. Previous volumes reviewed materials in which only one or two dimensions were relevant –fibres and membranes–. However, in the case of bulk materials different techniques and approaches must be used to test and model their mechanical behaviour.

The structure of these materials is complex and, almost always, extremely hierarchical. Biological materials are usually soft and when they must perform structurally, the required stiffness and strength are achieved by introducing minerals, producing composite materials and sophisticated cellular structures. Cancellous (spongy) bone is a classic example of this strategy; showing great strength combined with low density thanks to a cellular structure and, in turn, to the cell walls which are true composite materials in which the reinforcements are particulate minerals, in this case hydroxiapatite.

Mechanical tests on 3D biological materials are, to some degree, a generalisation of the simple experiments mentioned in the previous volumes; tensile, compression and torsion tests. To these is added the flexure test, almost exclusive to 3D materials, since very thin fibres and membranes are usually very flexible and do not lend themselves to this type of characterisation.

Modelling the mechanical behavior of three-dimensional biological materials is also, to some extent, a generalisation of the methods introduced earlier, but with some caveats.

Even though the basic concepts are essentially the same, the mathematical tools are more complicated, but they can be greatly simplified when the materials are rigid –which occurs in many cases– since the deformations are usually small and, often, can be performed in an analysis in a linear elastic regime. Powerful computers are commonly used in numerical calculations in which complex geometries are modelled; for example, for cellular materials it is not necessary to use regular models in which a unit cell is repeated periodically, it is possible to construct Voroni cells, which have different geometries and positions at random. Defects and other imperfections can also be modelled with finite element methods. The difficulty in this approach lies not in the modelling but in the material constitutive equations; in practice, for small deformations, equations which provide acceptable results are available, but when the materials response depends upon time and the load history the problem becomes very complicated.

At the end of this volume some three-dimensional biological materials of great interest are described in some detail: Mollusc shell, an example of a composite material; wood, an example of a bidimensional cellular material; spongy bone, an example of a three-dimensional cellular material, and cartilage, an example of a multiphase material.

1.2. 1.2. COMPOSITE AND CELLULAR MATERIALS

In the majority of man-made materials, and particularly in metals and ceramics, strength and toughness are conflicting properties: the greater the strength, the more brittle (less tough). The design of very strong and simultaneously tough materials is a challenging objective for the materials engineer. Nature has achieved this in both the plant and animal kingdoms, fabricating composite materials with polymers and minerals. In some materials the matrix is a polymer –such as bone in which the matrix is collagen– and in others the polymer is the reinforcement –as in wood, in which the reinforcement consists of cellulose fibres–.

When the increase in stiffness implies an increase in weight, a drawback for the living organism –such as in the case of birds, for example– Nature overcomes the problem by achieving maximum stiffness for a minimum weight by means of cellular structures.

Strength and toughness are optimised in many biological materials through hierarchical structures, with a skillful combination of composite materials and cellular structures which provide stiffness and energy dissipation mechanisms during crack propagation. We can find examples –in both animal and plant tissue– of how Nature has engineered them by combining composite materials and cellular structures to achieve both strength and toughness.

Plant tissues have a cellular structure. The cell walls are composite materials in which the *reinforcement* consists of cellulose fibres –a glucose polymer which forms very strong and tough fibres– and the *matrix* is an amorphous polymer (lignin) and a semi-crystalline glucose polymer (hemicellulose). The cellulose content in the walls can reach 50%. The walls are not homogeneous, but formed of various layers in which the orientation of the fibres varies from one to another, conferring stiffness and toughness. Details of the cellular structure and cell arrangement in tree trunks are discussed below in section 3.2, but it is worth mentioning that evolution has endowed trees with sufficient strength and toughness to withstand storms; when a tree falls during a gale generally this is because it has been uprooted, rarely because the trunk has broken; some branches may break but the tree will survive.

In some plants the flexural strength of the stem is optimised using all of the above strategies; composite material in the cells and cellular hierarchical structure.

The stem of the horsetail –genus *Equisetum* provides a simple example of the side of the pteridophytes; ferns and allies–. Figure 1a shows, in a simplified form, the stem section in which a compact cellular structure in the outer and inner edges of the ring can be observed, together with a more open cellular structure with large pores on the inside. The sandwich construction strategy is repeated in many biological materials and the accumulation of material in a ring rather than distributing it homogeneously optimises the bending resistance of the stem.

Animal tissue can be classified into two large families; *organic tissue*, such as skin, composed almost entirely of organic materials and *bioceramic tissue*, such as bone, with a polymeric base and a high mineral content. The latter tissues have a structural role and in order to increase the stiffness they need to include large amounts of mineral which is a brittle component. Nature has solved the problem by creating bioceramic materials which are stiff, strong and tough. This time a different process from that in plants is followed; the reinforcements are now crystals (rather than cellulose fibres) and the matrix is a polymer. The toughness is achieved thanks to the hierarchical structure of the composite which provides diverse energy dissipation mechanisms when a crack is propagates, as will be discussed later.

The mineral component of mollusc shells is calcium carbonate, a brittle but abundant material in the sea. From this, apparently brittle, material molluscs fabricate very strong and tough shells capable of inspiring armour for military vehicles (Yao et al., 2010). The calcium carbonate, almost always in the form of aragonite, occupies about 95% of the volume of the composite material. In some cases the matrix which represents only 1% of the volume, is a complex biopolymer with chitin and a protein similar to the fibroin present in silk fibres. The shells are formed of densely packed microscopic ceramic bricks bonded by a fine glue which constitutes the matrix. To create some patterns, in pearlescent shells such as mother-of-pearl, the aragonite bricks have a thickness of some tenths of a micron and an average length of several microns, while the thickness of the cement which binds them is a few tens of nanometres. The value of the rupture stress in a flexural test can reach 200 MPa and the specific fracture energy about 500 J/m². Other shells with a crossed lamellar structure are tougher, achieving fracture energies of an order of magnitude greater. The structure and mechanical properties of shells are discussed in detail in section 3.1.

The skeleton of a living fossil, the *armoured crab* (also known as the pan or bayonet crab), provides an example of the combination of a composite material with a hierarchical cellular structure, similar to that of the stem of the horsetail. Figure 1b shows the cross section of the shell in which the sandwich structure can be observed, together with its stiff walls and the interior with a progressive cellular structure, including large holes. Once again, this structural arrangement optimises the mechanical behaviour of the shell.

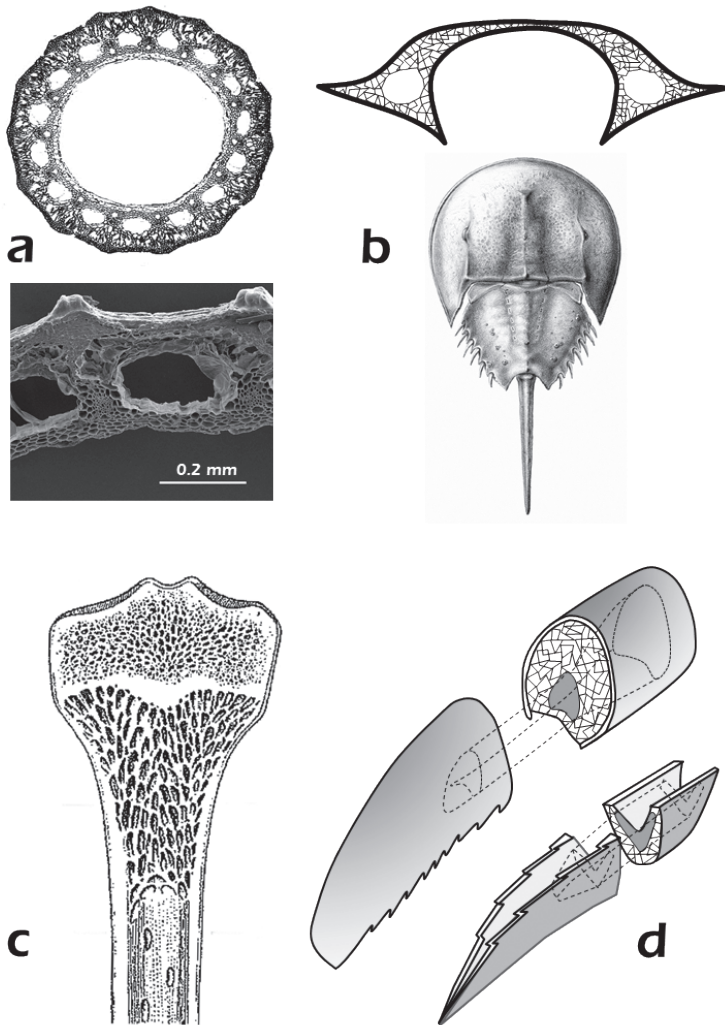


Fig. 1.2.1. Hierarchical cellular structures
 a. Stem of the horsetail.
 b. Section of the shell of the armoured crab.
 c. Section of a long bone.
 d. Toucan beak.

The mineral component of bones is calcium phosphate (hydroxyapatite) and the matrix consists of collagen fibres. Both components have similar proportion by volume. There is a certain parallel between the cellular structure and hierarchy of bone and that of wood, despite the great differences in the chemistry of the constituents. In bone the collagen fibres are the matrix, while in wood cellulose fibres are the reinforcement. Young bones, with abundant collagen, are enriched by the disposition of hydroxyapatite nanoplates. With the passage of time the mineral content increases and osteons are formed –cylindrical laminas concentrated around a neurovascular canal– which have the strength and stiffness to withstand the loads that will act upon the mature organism. At the macroscopic scale it is possible to identify a dense type of bone, called compact (or cortical), which covers the bone and a form of bone with a cellular structure, called **cancellous** (or trabecular) bone, that usually fills the vertebrae, the extremities of long bones (figure 1c) and the interior of some bony plates such as in the skull. This combination of dense structures and pores serve to increase the stiffness for a given amount of material, or in other words, to optimise the specific stiffness. Bones can be very tough, the specific resistance values ranging from 500 to 5000 J/m², considerable values compared to some advanced ceramics (about 500 J/m²). Bones have properties that are very attractive to engineers, they are materials which are strong, tough, multifunctional and capable of self-repair and also to adapt themselves in response to mechanical loads. The structure and mechanical properties of bones are considered in detail in section 3.3.

The beaks of some birds offer another example of the combination of composite materials and cellular structures. Bird beaks are often short and thick or long and thin. The beak of the toucan (a climbing american bird) is an exception; the beak is long –a third of the length of the body– and very thick. It probably needs a long beak to get fruit, but not too heavy because its habitat is in very tall trees. For this, evolution has furnished it with a light stiff beak which has a structure formed of a hard keratin cover and an interior with a cellular structure (figure 1d). Keratin can be considered as a composite material reinforced with keratin fibres embedded in a protein matrix. Mineralisation with calcium and other elements contributes to give the keratin rigidity. The cellular structure is not open, such as in cancellous bone, but closed by fine membranes. Most of the loads borne by a toucan's beak make it work in flexure and the structure is especially adapted for that; the flexural strength is much greater than that which would be achieved if all the mass of the beak were concentrated in an outer layer –as if it were a cylindrical bone–, thanks to the interior cellular structure, as demonstrated by Meyers and co-workers (Seki et al. 2005).

1.3. BIOMINERALISATION

The previous section described how some biological materials acquire the required stiffness by incorporating minerals into their structure, a process known as *biomineralisation*, and which is worth comment in its relation to Materials Science.

Organic molecules in solution can influence the shape and orientation of inorganic crystals if there is some affinity between them. An understanding of the processes in which living organisms control the growth and structure of inorganic materials can aid important advances in Materials Science and Engineering and open the door to many novel techniques for synthesising components from the nanometric scale.

Biomineralisation implies the selective extraction and incorporation of elements that are in the environment and their integration into functional structures, all of which under biological control. Unlike other biological transformations that leave no trace in the environment, the formation of hard minerals by biomineralisation –such as the shells of molluscs or bones– leave a fossil footprint that provides valuable information for paleoentology, sedimentology, geochemistry, marine science and many other fields related to chemistry, biology and geology.

Furthermore, biomineralisation, as well as providing strength and stiffness to organisms, can fulfill other biological functions, such as; protection, locomotive systems, defensive mechanisms, and gravity, optical or magnetic sensors.

Among the minerals associated with the biomineralisation process **calcium** plays an essential role, not just because it is very abundant but because it is the component in very familiar structures such as bones and mollusc shells. Note, as has already been mentioned, that the calcium in bones is in the form of calcium phosphate while in shells it is calcium carbonate; the reason for these differences is, as yet, unknown. Both calcium carbonate and calcium phosphate have a high bond energy and have low solubilities and, in consequence, are thermodynamically stable in biological environments. This is not the case with the hydrates, such as calcium oxalate or calcium sulphate, which are more soluble and therefore less common.

Silicon is another element which takes part in biomineralisation but with a lesser role than that of calcium. It seems that the use of the salts of calcium is metabolically more economical, which justifies its abundance. The motive as to why some organisms prefer to use amorphous silica over calcium carbonate is also unclear. According to some authors it could be because there are advantages when it comes to making very fine but strong spicules because amorphous silica contains no defects that would initiate cracks, like the steps in calcite crystals. In some plants the presence of silica spicules in cell walls serves to make them unappetising to predators. Equisetales, such as horstail mentioned above, have high silica content, up to 25% by weight when dry, and due to their abrasive qualities have been used for brushes. Similar quantities of silica are found in rice husks which have come to be used as a raw material for the production of silicon nitride. More delicate silica structures are found in many unicell organisms, such as diatoms and radiolaria capable of displaying beautiful filigree.

The mineralized silica skeletal system of the hexactinellid sponge, *Euplectella aspergillum*, commonly known as the Venus' flower basket, has received considerable attention from the engineering and materials science communities for its remarkable hierarchical architecture and mechanical robustness across multiple length scales. The sponge's diagonal reinforcement strategy achieves the highest buckling resistance for a given amount of material. (M C Fernandes et al. 2020)

2

CHAPTER

Mechanical Properties

2.1. Introduction and objectives

2.2. Test and characterisation techniques

2.2.1. Tensile, compression and flexural tests

2.2.2. Rupture tests

2.2.3. Indentation tests

2.3. Comportamiento mecánico

2.3.1. Introduction

2.3.2. Homogeneous materials

2.3.3. Heterogeneous materials

2.3.4. Cellular materials

2.1. INTRODUCTION AND OBJECTIVES

The three-dimensionality of the the material adds further complexity to the study and interpretation of experiments on biological materials in which none of the three dimensions can be ignored.

This chapter first addresses the peculiarities of the most common mechanical tests (tensile, compression and torsion) which require consideration of the three dimensions of the material, in particular the associated extensometry (measurements of the movements of the specimen) and the possible anisotropy. The flexural test frquently used to measure the **modulus of rupture** is also presented. Special attention is paid to fracture tests due to an increasing interest in determining the toughness of biological materials.

Previously, in the study of membranes and laminas, tear and peel tests were mentioned, which strictly speaking are also three-dimensional tests but ones in which the transverse dimension could, to a first approximation, be ignored. Indentation tests are also used when standard specimens cannot be fabricated or when it is not possible to obtain a sample of the material and the whole element must be tested. It is also used to obtain local properties of the material. The information provided by these tests is not very precise, but they are cited in scientific articles so their scope and limitations should be recognised.

Secondly, the previously discussed concepts of stress, strain and the relationships between them for one and two dimensions will be amplified. The commentry is practically limited to materials that behave elastically and experience small deformations. Even so, the results obtained are very useful in the study of anisotropic materials, composite materials, such as mollusc shells, or cellular materials, such as wood or bone.

2.2. TEST AND CHARACTERISATION TECHNIQUES

2.2.1. Tensile, compression, torsion and flexure tests

Tensile tests

Tensile tests (simple or uniaxial tension, and biaxial tension) were analysed in detail in the volumes corresponding to fibres (“Biological Fibres”, section 2.2.1) and membranes (“Biological Membranes”, section 2.3.1). The tests are preferably used on homogeneous isotropic materials. They are also applied to anisotropic materials where it is possible to find the traction directions which coincide with the axes of symmetry of the material, since in this way the stress and strain tensors are diagonal in the test directions, and do not produce shear (angular) deformations.

Tensile tests are useful for determining the properties of fibres and membranes since they are easy to interpret because these materials are, in general, very flexible, and it is easy to obtain a relatively large zone in which the stress and strain are uniform, that is to say, independent of position (figure 2.1a). Measuring the extension between two points within this zone allows simple determinations of the strain throughout the zone, in order to relate it to the applied stress, which is also easy to calculate merely by averaging the force applied through the grips, as shown in the corresponding sections.

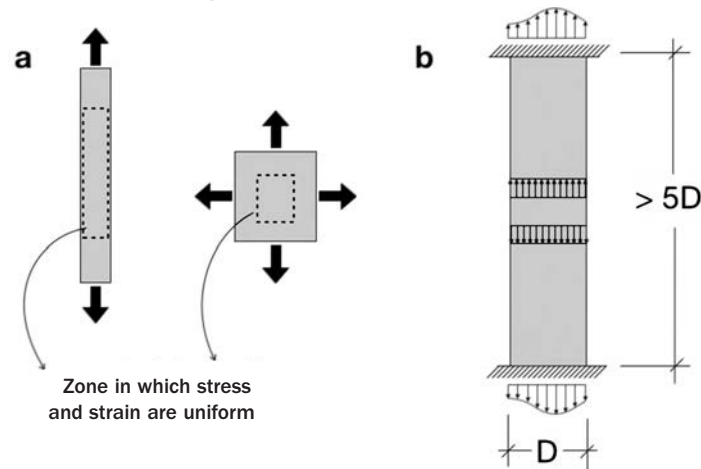


Fig. 2.1. Tensile test
a. Uniform deformation zone
b. Specimen dimensions

The tensile test on three-dimensional geometries which, due to their proportions cannot be treated as linear bodies

is particularly complicated since it is very difficult, if not impossible, to obtain a zone of uniform deformation. This is due the difficulty of gripping the specimen in a way that the load is transmitted uniformly. A practical rule for establishing the specimen dimensions is usually to take the free length between to grips to be greater than five times the mean diameter. In this way, the inhomogeneity produced by the grips is attenuated sufficiently³ so that in the central section the stress-strain state can be considered uniform (figure 2.1b).

As we saw in the analysis of the tensile test (section in the “Biological Fibres” volume), the values of the stress and strain which can be achieved during the test are limited by the appearance of a necking instability, originating from a local deformation. The heterogeneity of the material and the use of specimens which are too short generated stress concentrations which accelerated the appearance of necking.

The above issues restrict the tensile test to situations in which sufficiently slender specimens can be obtained. This is the case with Evans’ tests on specimens taken from the proximal third of the human femur, shown in figure 2.2. The specimens are cut in the longitudinal direction in the compact (cortical) area of the bone, using the dimensions recommended in the ASTM E8 standard.

The results show that the human compact (cortical) bone is quite strong and stiff. The fracture stresses lie at about 80MPa and the bone has a marked initially linear behaviour, with an elastic modulus of about 18GPa (dry) and 14GPa (wet). The values of the rupture strains are small; being about 0.4% (dry) and 1.2% (wet).

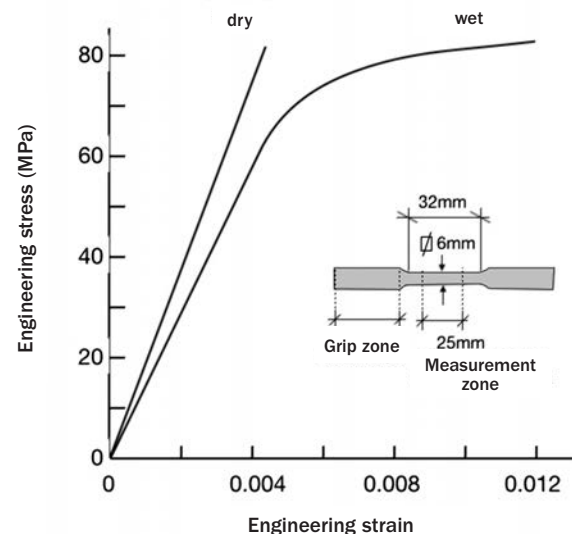


Fig. 2.2. Tensile tests on the human femur. Adapted from Evans 1969.

³ According to the Saint-Venant principle the difference between the effects of two statically equivalent loading systems becomes arbitrarily small at sufficiently large distances for the points of application of the loads.

EXERCISE 1

Calculate the relative error in estimating the strains in the femoral bone when true and engineering stresses are taken to be equivalent. What will the relative error in stresses and the initial elastic modulus be? Use the data from figure 2.2.

SOLUTION:

In EXERCISE 1 in section 2.2.1 of the “Biological Fibres” volume, the relative error considering engineering strain is calculated. Its value depends upon the level of strain reached and is given by

$$\text{relative error} = \frac{e - \varepsilon}{\varepsilon} = \frac{1}{\varepsilon} (\exp(\varepsilon) - 1 - \varepsilon) = \frac{e}{\ln(1+e)} - 1$$

where the engineering strain $e = (L - L_0) / L_0$ and the true strain $\varepsilon = \ln(L / L_0)$. L is the deformed length of the gauge section, whose initial length is L_0 .

If the maximum possible strain is e_{\max} we obtain

$$\begin{aligned} \text{maximum relative error} &= \frac{e_{\max}}{\ln(1+e_{\max})} - 1 = \frac{0.004}{\ln(1.004)} - 1 = 0.002 \text{ (dry)} \\ &\quad \frac{0.012}{\ln(1.012)} - 1 = 0.006 \text{ (wet)} \end{aligned}$$

We see that the maximum error is very small and lies between 0.2 and 0.6%, so that $e \approx \varepsilon$ and it will be fully justified to use the theory of small deformations with this material.

In section 2.2.1 of “Biological Fibres” we saw that, assuming conservation of volume, the relationship between the engineering stress (s) and the true stress (σ) was (equation 7)

$$\sigma = s(1+e)$$

the maximum relative error will, therefore, be

$$\text{relative error} = \frac{s - \sigma}{\sigma} = \frac{1}{1+e} - 1 = \frac{-e}{1+e}$$

which yields values of -0.4% (dry) and -1.2% (wet). The actual value will lie between these values and zero, since because bone is not strictly incompressible its volume increases with deformation and true stresses will be less than those given by equation 7. In any case, just as with the strain, we see that the values are very small and that we can consider that $s \approx \sigma$.

The initial elastic modulus is calculated by

$$E = \left. \frac{d\sigma}{d\varepsilon} \right|_{\varepsilon=0} = \left. \frac{ds}{de} \right|_{e=0}$$

since $\varepsilon = \ln(1+e)$ and $d\varepsilon = de / (1+e)$, and at the origin ($e = \varepsilon = 0$), then $de = d\varepsilon$.

On the other hand, from the definition of stress, $\sigma A = s A_0$ so that

$$d\sigma = \frac{A_0}{A} ds - \frac{A_0}{A^2} s dA$$

at the origin, when $A = A_0$ and $s = 0$, then $d\sigma = ds$. Using this result we see that

$$E = \left. \frac{d\sigma}{d\varepsilon} \right|_{\varepsilon=0} = \left. \frac{ds}{de} \right|_{e=0}$$

and the initial elastic modulus will be independent of which stress or strain is used for its calculation –true or engineering– since both representations coincide at the origin. We conclude then that the error will always be zero.

For practical purposes, when handling stress-strain curves determined by points, there will always be a small error due to the impossibility of calculating the the tangent at the origin with precision.

Compression test

A compression test consists of applying a compressive load through two opposing faces of a specimen while measuring its shortening (figure 2.3a). This test is suitable for characterising tissues which, during their physiological function, are usually subjected to compressive stresses, such as bone and cartilage. Furthermore, the compression test has certain advantages over the tensile test since it needs smaller specimens, and easier to obtain, generally cubic or cylindrical, and do not need complex gripping systems to transmit the loads. Also, as noted above, the compression test does not introduce intrinsic instabilities, as can happen in the tensile test when necking occurs.

Compressive tests, like those in tension, are preferably performed on homogeneous isotropic materials, or on anisotropic materials whose axes of symmetry are parallel or perpendicular to the axis of compression. In this way complex states of stress, which make the analysis of the results difficult, are avoided. The interpretation of the results is easier and more direct if there is a region of the specimen in which the stress state can be taken as uniform (figure 2.3b).

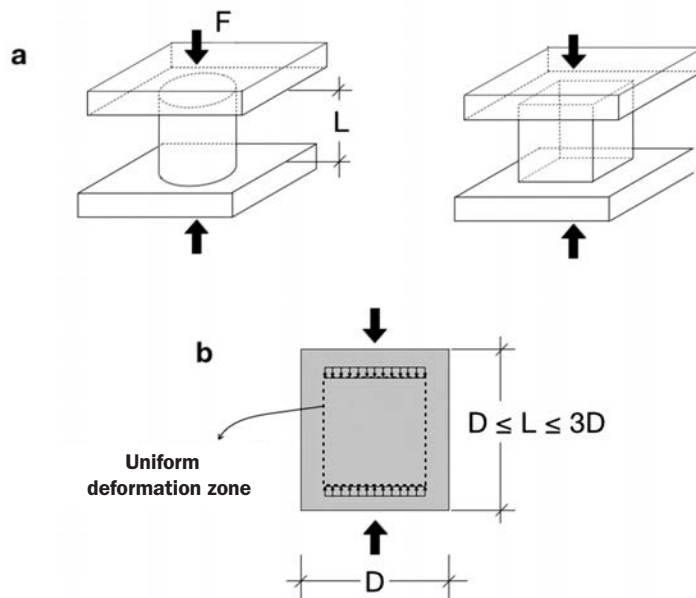


Fig. 2.3. Compression test
a. Cylindrical and prismatic specimens
b. Uniform deformation zone

Despite its apparent simplicity, performing and interpreting a compression test is not without its difficulties which have to be taken into account. In the first place, although the test –as has been said – is intrinsically stable, an instability can be caused by buckling if the specimen is too slender. In order to avoid this it is recommended that the height of the specimen be between one and three times the width ($D \leq L \leq 3D$).

Regarding these difficulties of an experimental nature, first it is necessary to ensure sufficient parallelism of the surfaces on which the compressive load is applied, in order to avoid stress concentrations which produce local damage and a non-uniform stress-strain state (figure 2.4a). A practical criterion is to establish a maximum difference between the strains produced on the load surface which is less than 1/10 of the strain corresponding to the elastic limit. Since this requirement is especially demanding in rigid materials (such as cortical bone) it is common to recourse to placing a ball joint on one of the load plates with the aim of achieving a uniform contact (figure 2.4b). In order to avoid instabilities during the test it is important that the ball joint is adjusted at the start of the experiment, with the specimen unloaded or with a very small value of load, and preventing its movement during the rest of the test.

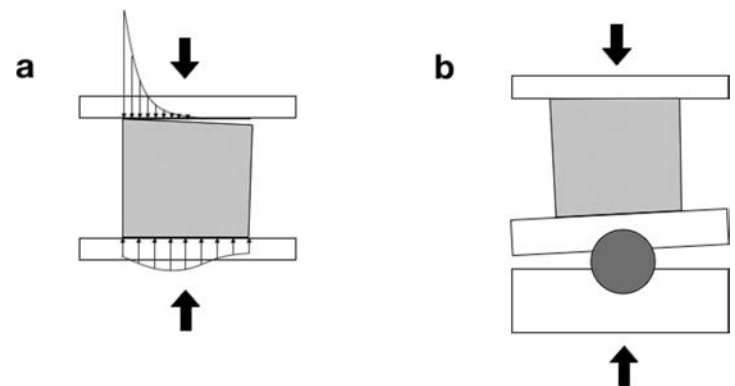


Fig. 2.4. Lack of parallelism in the specimen
a. Local stress concentration
b. Pivoting support

Another relevant experimental problem is the occurrence of friction between the loading surfaces and the faces of the specimen due to the differential lateral expansion. The friction increases with the test load and can become very important. There is no effective solution and it is usual to try to reduce the coefficient of friction as much as possible by using very flat surfaces (such as glass when testing cartilage) and lubricants such as low viscosity oils (Linde et al., 1989).

The edge effect, generated by the abrupt interruption of the microstructure caused by machining the surface of the specimen (figure 2.5) produces a local deformation increase in the zones near the surfaces which leads to an overestimate of the ductility and flexibility of the specimen. Its effect is greater as the size of the microstructure approaches that of the specimen. The zone affected by the machining can be estimated at about five times the size of the microstructure⁴ so the solution to the problem is to measure the deformation of the specimen in regions sufficiently remote from the surfaces, in which there is a uniform state of stress and strain. In materials with large scale microstructure (such as cancellous or trabecular bone, with millimetric microstructure), the edge effect can greatly influence the minimum size of specimen required for testing.

Compression tests on biological materials are usually performed using, as a guide, the existing standards for artificial materials (ASTM C39, ASTM E-9, ASTM D-695), adapted for the conditions of the tissue, especially the amount of available material. Like the other mechanical tests, the compression test is very sensitive to the heterogeneity and anisotropy of the material, and to the boundary conditions, especially the load rate and the moisture content of the sample, as well as the movement of tissue fluid into and out of it. Compression tests are usually carried out on saturated samples, submerged in physiological serum or in PBS.⁵

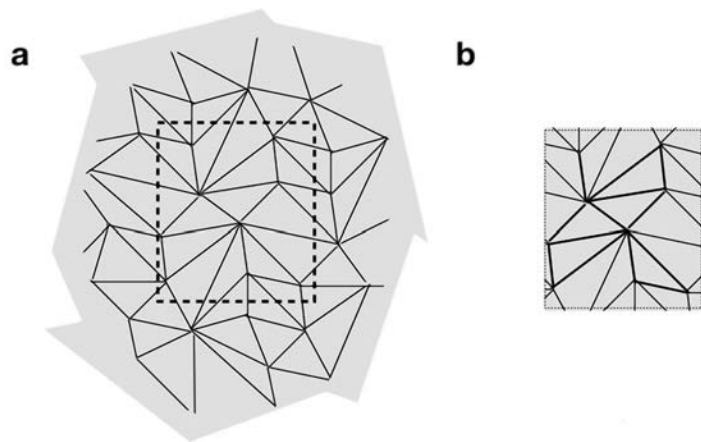


Fig. 2.5. Edge effect in a trabecular material
a. Unmachined material. The dotted lines represent the surfaces of the cut.
b. Machined specimen. Only the darkest trabeculae retain their bonds.

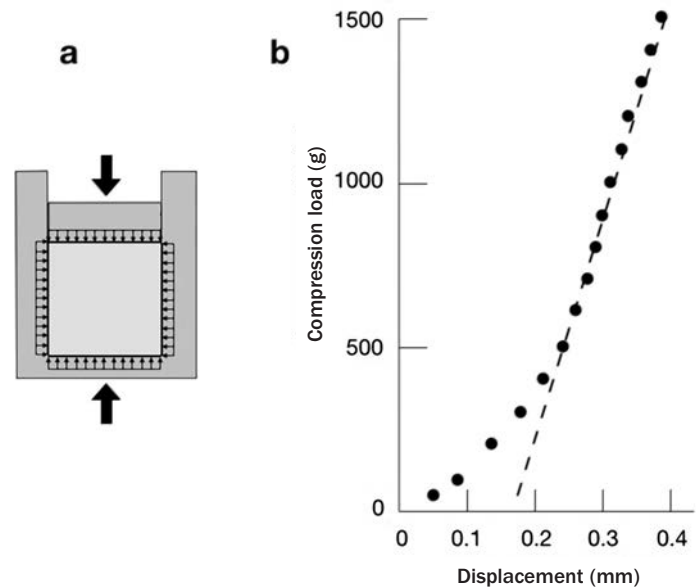


Fig. 2.6. a. Constrained compression test
b. Load-displacement curves for a constrained compression test with cylindrical specimens of bovine cartilage, short term (1s). Specimen diameter 6.4 mm, thickness 1.8 mm. (Adapted from Mow et al. 1980)

The **constrained compression** test (figure 2.6a) is a special case of the compression test which is useful for soft tissue (including cartilage) in which it is difficult to maintain the sample geometry during the test, and where there may be interstitial fluid movement. In the test the sample is constrained laterally adjusting its size with the greatest possible precision to the more rigid side walls. Generally the walls are impermeable while the upper plate through which the load is applied is usually porous to allow drainage of the sample.

By way of example, figure 2.6b contains the load-displacement curve for a constrained compression test on cartilage from the bovine femoral condyle, obtained by Mow and co-workers (Mow et al. 1980). In this case drainage of the specimen was allowed although the data were obtained in the short term, applying each load for one second. The results indicate an initial nonlinear region while the sample adjusts to the diameter of chamber which was a little wider. From ~500 g, true specimen constraint is produced. From the figure we can obtain the value for the aggregate modulus H_A of the material (defined as the ratio of the compressive stress to the strain in the sample) which comes out at 3.6 MPa, five times greater (~0.7 MPa) than that obtained were each load step allowed to stabilise until it reached equilibrium.

⁴ Using a criterion similar to that set forth for tensile tests, based on St Venant's principle.

⁵ Phosphate buffered saline, (tampón fosfato salino) is an aqueous solution of sodium chloride, sodium phosphate, potassium chloride and potassium phosphate whose osmolarity and ion concentration are very similar to mammal tissue extracellular liquid.

EXERCISE 2

Analyse the uniaxial compression test and determine the relationship between the engineering stress and strain (s, e) and the true stress and strain (σ, ϵ). Apply the results to the case of a material whose true stress-strain relationship is linear $\sigma = E \epsilon$.

Could an instability could be produced during the test?

HINT: To solve the problem assume that there is no friction at the load surfaces and use the principle of conservation of volume.

SOLUTION:

In section 2.2.1 of the “Biological Fibres” volume the uniaxial tensile test was analysed. Everything stated there is valid for the uniaxial compression test with no more than taking into account that now $F < 0$ and therefore:

$$\lambda = \frac{L}{L_0} < 1 \quad ; \quad e = \frac{L - L_0}{L_0} = \lambda - 1 < 0 \quad ; \quad \epsilon = \ln \lambda = \ln(1 + e) < 0 \quad ;$$

$$s = \frac{F}{A_0} < 0 \quad ; \quad \sigma = \frac{F}{A} < 0 \quad \text{and} \quad \sigma = s\lambda = s(1 + e) \quad \text{due to volume conservation} \quad AL = A_0L_0$$

Applying the previous expressions we obtain the s - e relationship:

$$s = \frac{\sigma}{1 + e} = \frac{\ln(1 + e)}{1 + e} E$$

which is shown in the Figure along with $\sigma = E \epsilon$

As stated in section 2.2.1 of “Biological Fibres”, equation (8), a loading instability occurs when $dF = 0$, which –using conservation of volume– leads to the condition $\sigma = d\sigma/d\epsilon$.

In a compression test it is impossible to fulfill the previous relationship since the true stress-strain curve of a real material is always monotonically increasing and $d\sigma/d\epsilon > 0$, while in the compression test we have $\sigma < 0$.

This is illustrated by the curve $\sigma = E \epsilon$ in the figure, in which we observe that the engineering stress-strain curve s - e (or s/E - e) has a maximum (instability) in tension but there is no similar point in compression.

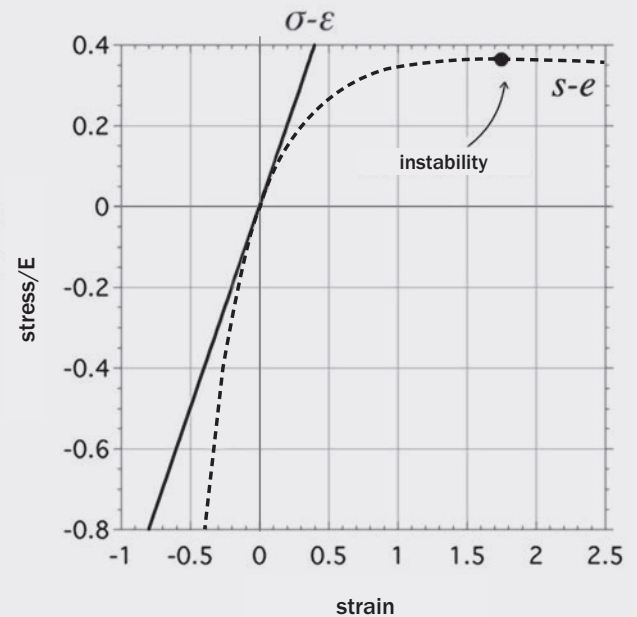
The instability point in a tensile test will occur when $\sigma = \frac{d\sigma}{d\epsilon}$

In this example

$$\sigma = \frac{d\sigma}{d\epsilon} = E \quad ; \quad \epsilon = \frac{\sigma}{E} = 1$$

and, therefore, on the s - e diagram the instability values will be

$$e = e^{\epsilon} - 1 = e - 1 = 1.72 \quad ; \quad s = \frac{\sigma}{1 + e} = \frac{E}{e} = 0.37E$$



EXERCISE 3

Analyse the constrained compression test for a linear elastic, homogeneous, isotropic material (small deformations) with modulus of Elasticity E and Poisson's ratio ν . Calculate the aggregate modulus, H_A , defined as the ratio of the compressive stress and strain in the sample. Assume that there is no friction at the loading surfaces.

SOLUTION:

Given the linear relationship between stress and strain, we will solve the problem using the principle of superposition. Later in this chapter (section 2.3.2) we will draw up the equations that relate the stresses and strains for a linear-elastic, homogeneous, isotropic body. With these it is possible to obtain a much more direct and rapid solution to the problem, which we leave, as an exercise, to the reader.

The load state in which we find the specimen is the sum of three uniaxial compressions, one along the axis of compression (σ_{11}) and two along the perpendicular axes (σ_{22} , σ_{33}).

The compressive stress-strain state along the 1 axis will be (see figure 8a of the "Biological Fibres" volume)

$$\sigma_{11} \quad \sigma_{22} = 0 \quad \sigma_{33} = 0 \quad \varepsilon_{11} = \frac{\sigma_{11}}{E} \quad \varepsilon_{22} = -\nu \frac{\sigma_{11}}{E} \quad \varepsilon_{33} = -\nu \frac{\sigma_{11}}{E}$$

where σ_{11} is the applied compressive stress. A compressive stress will appear along the 2 and 3 axes due to the constraint effect. For the 2 axis we have

$$\sigma_{11} = 0 \quad \sigma_{22} \quad \sigma_{33} = 0 \quad \varepsilon_{11} = -\nu \frac{\sigma_{22}}{E} \quad \varepsilon_{22} = \frac{\sigma_{22}}{E} \quad \varepsilon_{33} = -\nu \frac{\sigma_{22}}{E}$$

and for the 3 axis

$$\sigma_{11} = 0 \quad \sigma_{22} = 0 \quad \sigma_{33} \quad \varepsilon_{11} = -\nu \frac{\sigma_{33}}{E} \quad \varepsilon_{22} = -\nu \frac{\sigma_{33}}{E} \quad \varepsilon_{33} = \frac{\sigma_{33}}{E}$$

The resulting state, the sum of the three previous, will be equal to

$$\sigma_{11} ; \sigma_{22} ; \sigma_{33} ; \varepsilon_{11} = \frac{\sigma_{11}}{E} - \frac{\nu}{E}(\sigma_{22} + \sigma_{33}) ; \varepsilon_{22} = \frac{\sigma_{22}}{E} - \frac{\nu}{E}(\sigma_{11} + \sigma_{33}) ; \varepsilon_{33} = \frac{\sigma_{33}}{E} - \frac{\nu}{E}(\sigma_{11} + \sigma_{22})$$

The resultant state must be such that the strain in the 2 and 3 axes is zero, which leads to

$$\varepsilon_{22} = \frac{\sigma_{22}}{E} - \frac{\nu}{E}(\sigma_{11} + \sigma_{33}) = 0 \rightarrow \sigma_{22} = \nu(\sigma_{11} + \sigma_{33})$$

$$\varepsilon_{33} = \frac{\sigma_{33}}{E} - \frac{\nu}{E}(\sigma_{11} + \sigma_{22}) = 0 \rightarrow \sigma_{33} = \nu(\sigma_{11} + \sigma_{22})$$

which we solve to obtain

$$\sigma_{22} = \sigma_{33} = \frac{\nu}{1-\nu} \sigma_{11}$$

Substituting the values of σ_{22} and σ_{33} in the strain expression ε_{11} along the 1 axis

$$\varepsilon_{11} = \frac{\sigma_{11}}{E} - \frac{\nu}{E}(\sigma_{22} + \sigma_{33}) = \frac{\sigma_{11}}{E} \frac{(1+\nu)(1-2\nu)}{(1-\nu)}$$

with which we obtain

$$H_A = \frac{\sigma_{11}}{\varepsilon_{11}} = \frac{(1-\nu)E}{(1+\nu)(1-2\nu)}$$

Torsion test

The torsion test was introduced in section 2.2.2 of the “Biological Fibres” volume. In it, a circular cylinder was subjected to two opposing torsional moments (torques) T at its ends, while measuring the rotation ϕ with respect to the axis (figure 2.7).

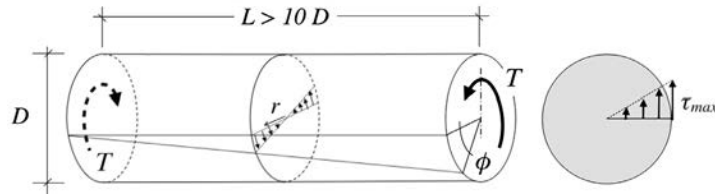


Fig. 2.7. Torsion test on a circular section bar

As in the tensile test, the objective of the torsion test is to produce a state of pure shear, easy to characterise from the external actions, in this case the torsional moment T applied at the ends, and the rotation ϕ of one end of the test piece with respect to the other. The principal advantage of the torsion test is that it does not cause necking and larger values of strain can be attained.

In order to avoid the occurrence of complex stress states in the torsion test it is only performed on homogeneous and isotropic materials or transversely isotropic materials whose axis of symmetry is the axis of the cylinder (the torsional axis). Furthermore, the specimens must be sufficiently slender, it being normal to take as a practical rule a separation between the load points of at least ten times the diameter of the cylinder. In the following we shall assume that both conditions are satisfied.

The torsion test produces, as explained in section 2.2.2 (“Biological Fibres”), a state of pure shear whose shear strain is the same in every section of the cylinder, and only varies linearly with the distance r from the torsional axis (equation 11, section 2.2.2 “Biological Fibres”).

$$\gamma(r) = r \phi / L \quad (2.2.1-1)$$

If the material behaviour is **linear elastic**, the shear stress and strain are proportional through the shear modulus ($\tau = G \gamma$). In this situation it is easy to calculate the maximum shear stress (see section 2.2.2, “Biological Fibres”).

For a **circular** section of diameter D (figure 2.7) the maximum shear stress is reached at the periphery and its value is (ex. 14, sec. 2.2.2, “Biological Fibres”):

$$\tau_{\max} = \frac{16T}{\pi D^3} \quad (2.2.1-2)$$

When the section is **elliptical** with semi-axes a and b (figure 2.8a) the calculation is much more complex. At any point in the elliptical section the shear stress is proportional to the distance from the centre of the ellipse and its direction is parallel to the tangent at the point of intersection of the radius with the surface, as shown in the figure. The shear stress at point (x, y) is equal to (Timoshenko, 1975):

$$\tau_{xz} = -\frac{2T}{\pi ab^3} y \quad \tau_{yz} = \frac{2T}{\pi a^3 b} x \quad (2.2.1-3)$$

The maximum value of the shear stress occurs at the ends of the minor sem-axes, and its value is (Timoshenko, 1975):

$$\tau_{\max} = \frac{2T}{\pi ab^2} \quad (2.2.1-4)$$

The rotation per unit length ϕ / L for this problem is:

$$\phi / L = \frac{T}{G} \frac{a^2 + b^2}{\pi a^3 b^3} \quad (2.2.1-5)$$

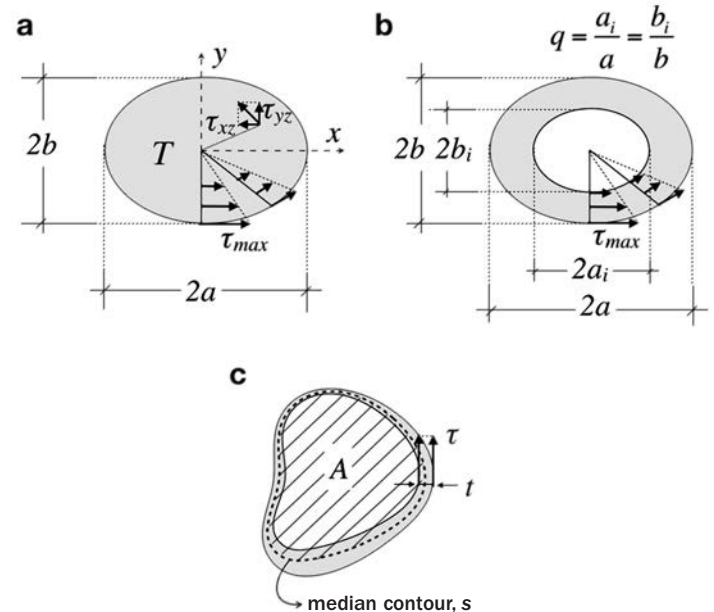


Fig. 2.8. Cross sections in torsion tests

- a. Elliptical
- b. Hollow elliptical
- c. Thin-walled tube

A frequent use of the the torsion test is the characterisation of long bones whose geometry resembles that of a tube. Using the solution for an elliptical section it is easy to obtain the solution for a tube with elliptical walls whose semi-axes are proportional, as shown in figure 2.8b. In this case the stresses at (x, y) are:

$$\tau_{xz} = -\frac{2T}{\pi ab^3} \frac{y}{1-q^4} \quad \tau_{yz} = \frac{2T}{\pi a^3 b} \frac{x}{1-q^4} \quad (2.2.1-6)$$

where $q = a_i/a = b_i/b$ the ratios of the semi-axes. The maximum shear stress occurs, as before, at the ends of the minor semi-axes:

$$\tau_{\max} = \frac{2T}{\pi ab^2(1-q^4)} \quad (2.2.1-7)$$

and the rotation per unit length ϕ/L is:

$$\phi/L = \frac{T}{G} \frac{a^2 + b^2}{\pi a^3 b^3 (1-q^4)} \quad (2.2.1-8)$$

A very practical solution for thin-walled tubes of linear elastic material, variable thickness and arbitrary geometry (figure 2.8c) is (Timoshenko, 1975):

$$\tau = \frac{T}{2At} \quad , \quad \frac{\phi}{L} = \frac{T}{4A^2 G} \oint \frac{ds}{t} \quad (2.2.1-9)$$

which provide the shear stress at a point in the section and the value of the rotation per unit length. The wall thickness t (always small) can vary. In the expressions above A is the values of the area enclosed by the median contour of the section and s is the arc measured on the median contour (figure 2.8c). When the section thickness is constant:

$$\tau = \text{constant} = \frac{T}{2At} \quad , \quad \frac{\phi}{L} = \frac{Ts}{4A^2 Gt} \quad (2.2.1-10)$$

where s is the length of the median contour of the tube.

For a thin-walled circular tube, the stress and strain are determined directly from the boundary conditions:

$$\tau = \frac{2T}{\pi t D^2} \quad , \quad \gamma = \frac{\phi D}{2L} \quad (2.2.1-11)$$

it not being necessary to assume any relationship between them (linear elastic or otherwise), since the value is fixed by the equations of equilibrium and compatibility (2.2.1-11)

EXERCISE 4

From the solution for an elliptical cross section, derive expressions 2.2.1-6, 2.2.1-7 y 2.2.1-8 for tubes with an elliptical boundary.

SOLUTION:

Consider an elliptical cylinder subjected to a torsional moment T as represented in the figure. If we imagine a cylinder inside this with proportionate semi-axes we can see that the stresses on the lateral surface of this inner cylinder must be zero, as indicated by the expressions 2.2.1-3, since the shear stress is tangent to the elliptical boundary.

We can then consider that the internal cylinder functions as it were decoupled from the outermost part—it alone—supporting a torque T^* . The stresses on the boundary will be (equation 2.2.1-3)

$$\tau_{xz} = -\frac{2T^*}{\pi a_i b_i^3} y \quad \tau_{yz} = \frac{2T^*}{\pi a_i^3 b_i} x$$

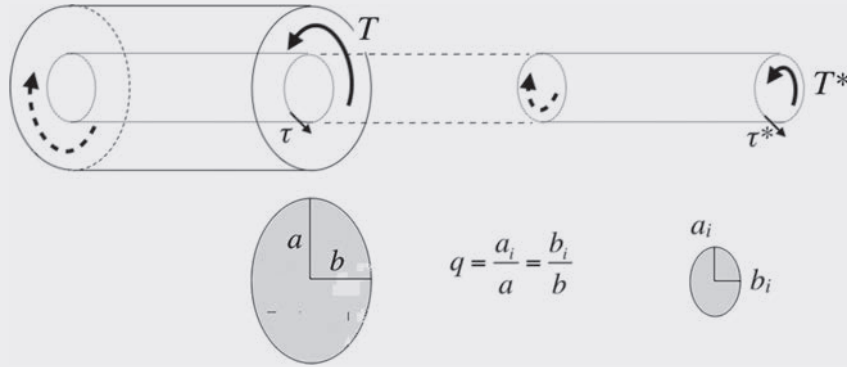
where

$$\frac{x^2}{a_i^2} + \frac{y^2}{b_i^2} = 1$$

The stresses on the boundary of the inner cylinder, now calculated from the stress state of the solid cylinder, will be

$$\tau_{xz} = -\frac{2T}{\pi ab^3} y \quad \tau_{yz} = \frac{2T}{\pi a^3 b} x$$

since these must be coincident, then $T^* = Tq^4$, where $q = a_i/a = b_i/b$ the ratio of the semi-axes.



From the above analysis we see that the inner cylinder supports the torque T^* while the external zone, which is an elliptical tube with external semi-axes (a, b) and interior (a_i, b_i) carries the remaining torsional moment $T - T^* = T(1 - q^4)$.

If we now consider an elliptical tube on its own, we see that stresses induced are caused only by the torque which acts upon it: $T_{tube} = T - T^* = T(1 - q^4)$ so that the stress solution for the tube problem will be the same equations 2.2.1-3 but with the substitution $T = T_{tube} / (1 - q^4)$, that is:

$$\tau_{xz} = -\frac{2T_{tube}}{\pi ab^3} \frac{y}{1 - q^4} \quad \tau_{yz} = \frac{2T_{tube}}{\pi a^3 b} \frac{x}{1 - q^4}$$

which are equations 2.2.1-6. In a similar manner we arrive at equations 2.2.1-7 and 2.2.1-8.

EXERCISE 5

The figure provides the results of a torsion test (torquer T – twist angle ϕ) in a rat femur, performed by Ekeland and co-workers (Ekeland et al. 1981, 1982). The figure also shows the central cross section and length of the femur.

From these data, calculate the shear stress at rupture, and estimate the shear modulus G of the bone.

SOLUTION:

The initially concave part of the torsion curve is due –as in many other tests– to the initial articulation of the experimental apparatus, and provides no information on the material. To correct for this, a straight line is fitted to the rectilinear part of the response which follows it, representative of the linear elastic behaviour of the material, and its intersection with $T = 0$ is taken as zero on the abscissa.

From the corrected $T - \phi$ curve, we measure the rupture data which are $T_u = 0.55 \text{ Nm}$; $\phi_u = 17^\circ = 0.297 \text{ rad}$ and the elastic slope: $K = 0.0387 \text{ Nm}/^\circ = 2.215 \text{ Nm/rad}$

To obtain the stresses and strains we approximate the bone section to an elliptical tube, as shown in the figure, obtaining the parameters:

$$2a = 4.5 \text{ mm}; 2b = 2.8 \text{ mm}$$

$$2a_i = 3.2 \text{ mm}; 2b_i = 2.0 \text{ mm}$$

$$\text{where } q = a_i/a = b_i/b = 0.71.$$

$$\text{From equation 2.2.1-7 we obtain: } \tau_u = \frac{2T_u}{\pi a b^2 (1 - q^4)} = 53 \text{ MPa}$$

From equation 2.2.1-8 we can determine the shear modulus in which we have substituted $T/\phi = K$, obtained from the fitted line.

$$G = \frac{T}{\phi} \frac{L(a^2 + b^2)}{\pi a^3 b^3 (1 - q^4)} = 487 \text{ MPa}$$

If we use the *thin-walled* assumption, we can calculate the maximum stress with the aid of equation 2.2.1-9, which yields

$$\tau_u = \frac{T_u}{2At} = 84 \text{ MPa}$$

In this case we have taken the area $A = 6.8 \text{ mm}^2$ enclosed by the median boundary (see the figure) and the minimum wall thickness $t = 0.48 \text{ mm}$.

If we calculate G from equation 2.2.1-10, taking a mean thickness calculated from the median contour and the area of the cross section

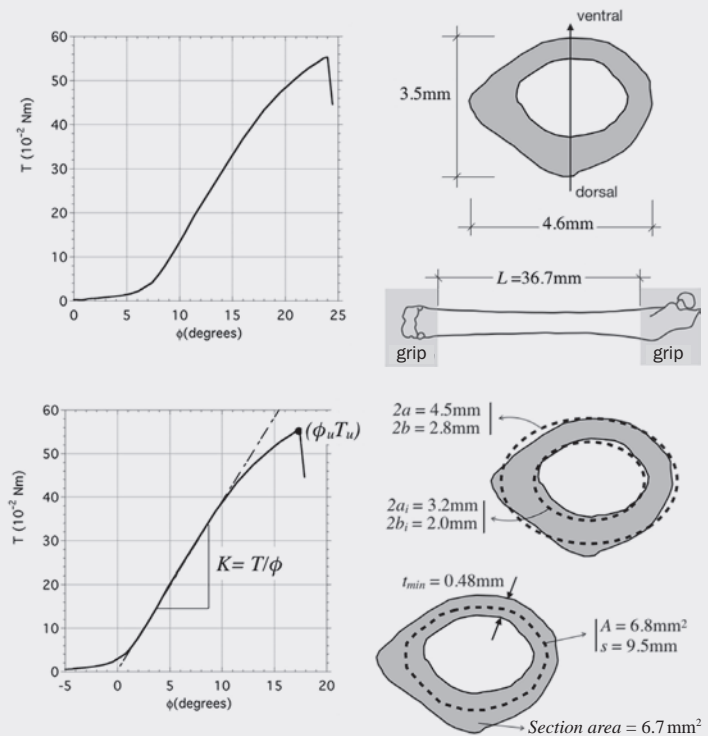
$$\langle t \rangle = \frac{\text{Área sección}}{s} = \frac{6.7}{9.5} = 0.7 \text{ mm}$$

we obtain

$$G = \frac{T}{\phi} \frac{sL}{4A^2 \langle t \rangle} = 5960 \text{ MPa}$$

We see that these values are very different from those assuming an elliptical tube.

In any case, the poor of uniformity of the section generates large discrepancies between the values obtained so most of the time these tests are used to make comparisons between bones with different treatments rather than to obtain the intrinsic properties of materials.



Flexure test

Introduction

The flexure test is a simple method of characterising a material and consists of measuring the load and deflection produced in a bar of constant and symmetric cross section, usually rectangular, subjected to loads which are perpendicular to its axis (figure 2.9). Generally the bar is supported at its ends and loaded in its central region by one (three point bending, figure 2.9a) or two forces (four point bending method, figure 2.9b).

The flexure tests provides a relatively straight forward method of measuring the strength and stiffness of materials. It is also useful as a technological test for evaluating and comparing the suitability of elements that must work in flexure. For example, for long bones where it is very common to use the test to study the strength after fracture and repair of the bone.

The flexure test is used preferentially on homogeneous and isotropic materials, and also on orthotropic materials whose axis of symmetry is perpendicular to the axis of the bar and contained in the plane of the load. In all of these cases, the resulting stress state can be simplified by assimilating it to a combination of uniaxial tensile and compressive states which act parallel to the axis of the specimen (figure 2.9c). If the bar were ideally divided into layers parallel to its axis, the upper parts would be compressed while the lower portions would carry tensile stresses, and would be stretched. The line (in projection) parallel to the axis which separates the compressed and stretched regions is called the *neutral axis*. All points on the neutral axis maintain their original length, suffering neither stretching nor shortening.

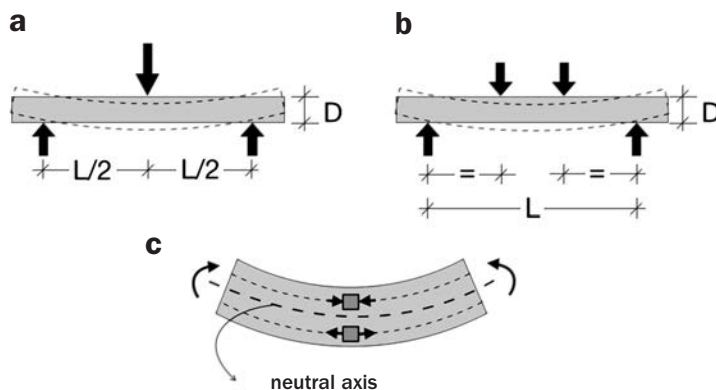


Fig. 2.9. Flexure test
a. Three-point bending
b. Four-point bending
c. Stress state

In contrast to tensile and compression tests, the flexure test generates a stress state which is not homogeneous, making it difficult, if not impossible, to obtain the stress-strain curve for the material directly⁶. Thus, in almost all cases it is usual to assume a particular constitutive equation –generally linear-elastic– whose parameters are determined from the results of the test.

Experimental configuration

With regard to its experimental configuration –as in all tests on biological materials– it is necessary to take into account the effect of load rate and the environmental variables (humidity and temperature). The flexure test is mechanically robust and relatively insensitive to specimen surface imperfections or the load arrangement. Even so, it is advisable to use rollers to even out possible geometric defects as shown in figure 2.10a. The rollers must be coupled together and locked before the start of the test to avoid instabilities during test execution.

Loads in the test are applied through rigid cylindrical, usually steel, fixtures whose radius of curvature must be large enough to avoid indentation and contact damage, and possible local compression fracture (figure 2.10b). For stiff, strong, biological materials such as bone it is customary to take as a guide the ASTM standards for testing plastics (ASTM D790 and ASTM D6272) which recommend a minimum radius of curvature of 5 mm.

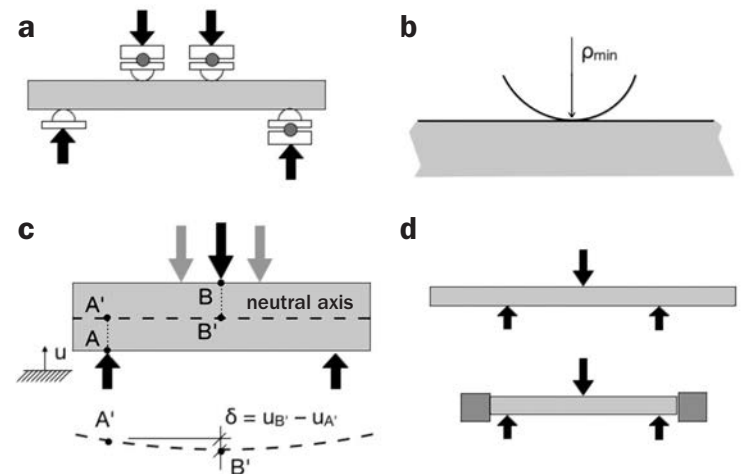


Fig. 2.10. Experimental configuration in flexure tests
a. pivoting supports
b. curvature in the loading zone
c. measurement of the vertical displacement δ of the central section
d. compensation for self-weight

⁶ Deriving the constitutive relationship from the results of a flexure test (finding the best fit to the experimental data by means of a numerical model which simulates the test) turns out to be a mathematically ill-conditioned problem which lacks a unique solution even in the ideal case of having accurate experimental results.

The curvature of the supports also has an important effect on the measurement of the *displacement in the central section of the specimen*, δ , which is often used—as will be seen later—to determine the elastic modulus of the material. If the displacement were evaluated by taking as a reference the displacement of the load points (points A and B in figure 2.10c) it must be borne in mind that these value depend critically upon the size of the contact zone, which is, in turn, a function of the radius of the cylindrical load surface (Planas et al. 1994). In the absence of a customised analysis that accounts for the extent of the true support region, it is advisable to determine the displacement of the central section of the specimen from the displacements measured on the neutral axis of the specimen, ($\delta = u_{B'} - u_{A'}$), as illustrated in figure 2.10c.

With regard to the slenderness of the specimen, it may be taken that, in both three-point and four-point tests above a length/depth ratio (L/D) of 4 a state of flexure is fully developed. Nonetheless, the ASTM D790 and ASTM 6272 standards usually recommend that the tests are performed on specimens which are much more slender ($L/D=16$) in order to reduce the effect of the shear deformation produced by the vertical forces. Some authors, for tests on bone, increase the recommended value to as much as 20 or even 25 (Spatz et al. 1996). With high slenderness ratios, it is essential, on the other hand, to take care not to induce nonlinear effects due to excessive changes in the position of the loads during the test.

Even though the self-weight of the specimen is generally very small, its effect can be easily eliminated using double length specimens, although this will depend upon the availability of the material. An alternative is to add counterweights to balance the test piece (figure 2.10d).

Analysis of the mechanics

The analysis of the mechanics of the flexure test on a homogeneous isotropic material is shown in figure 2.11. It is assumed that the strains in the fibres of the bar are very small (infinitesimal strain theory) and also Navier's hypothesis⁷ that plane cross sections of the bar remain plane after deformation. This hypothesis is satisfied reasonably well provided that the specimen is sufficiently slender and the effects of the shear stresses can be ignored.

Consider the coordinate system shown in figure 2.11a, whose axes (y, z) are perpendicular to the axis of the bar while the x -axis runs along the length of the bar. The x - y plane lies in the plane of symmetry of the bar, in which the flexure is produced. The location of the neutral axis $y = y_0$, is also shown in the figure, which lies in the plane⁸.

The deformation of a small section of the bar $\Delta x = \Delta l_0$ is illustrated in figure 2.11b. Its extremities rotate through an angle $\Delta\theta$ remaining plane (according to Navier's hypothesis) and the fibres of the section are curved. If ρ_0 is the radius of curvature of the neutral axis, located in y_0 , then:

$$\Delta l_0 = \rho_0 \Delta\theta \quad (2.2.1-12)$$

The radius of curvature $\rho(y)$ of the section of fibre located at position y will be:

$$\rho(y) = \rho_0 - (y - y_0) \quad (2.2.1-13)$$

and the change in length of this section will be equal to:

$$\rho(y) \Delta\theta - \Delta l_0 = [\rho_0 - (y - y_0)] \Delta\theta - \Delta l_0 \quad (2.2.1-14)$$

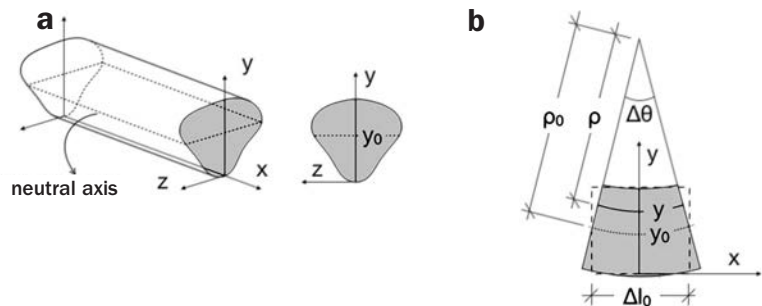


Fig. 2.11. Analysis of the flexure test
a. coordinate system
b. deformation between two adjacent cross sections

⁷ As a result of this hypothesis and his contribution to the study of beam bending, the French engineer, Claude-Louis Marie Henri Navier (1785- 1836), is considered the father of the theory of Strength of Materials and structural analysis.

⁸ Note that the term "neutral axis" refers to the projection on the x - y plane.

The **strain** in the fibre can be calculated from this value, by simply dividing by Δl_0 and using equation (2.2.1-12) for $\Delta\theta$:

$$\varepsilon(y) = -\frac{1}{\rho_0}(y - y_0) \quad (2.2.1-15)$$

Every point in the cross section of the bar will be subjected to a normal tensile or compressive stress whose value will be determined by the strain (equation 2.2.1-15) and the constitutive equation $\sigma = \sigma(\varepsilon)$ of the material. Points where $y > y_0$, above the neutral axis (neutral plane), will be under a state of compression producing a shortening of the fibres. The opposite happens for points where $y < y_0$, located below the neutral axis (figure 2.11c).

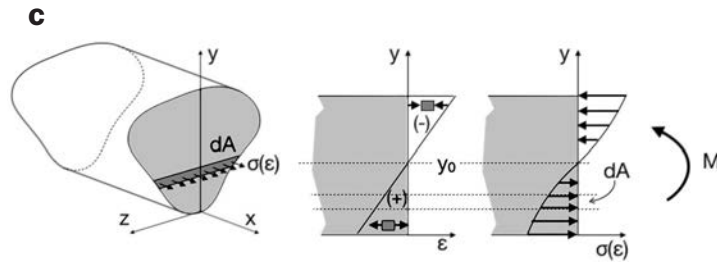


Fig. 2.11. c. Stress-strain state

In order to evaluate the strains at a given point in the cross section of the bar it will be necessary to know the value of the radius of curvature ρ_0 and the position of the neutral axis y_0 , as deduced from equation (2.2.1-15). Both values are obtained by setting up the equations of equilibrium of forces and moments on the cross section.

Figure 2.12 shows the forces acting on a cross section of the bar, caused by the external loads. The axial force on any cross section is zero while the moment of the external forces varies with position along the bar. For a three-point bending test (see figure 2.12a) the bending moment is smallest at the supports and reaches its maximum at the central section ($M_{max,3P} = FL/4$). In the case of the four-point bending specimen (see figure 2.12b), we see that the region between the two central loads is subjected to a maximum, constant, value of $M_{max,4P} = Fs/2$, where L and s are shown in the figure 2.12.

The first equation of equilibrium relates to the forces normal to the cross section of the bar. Since there are no forces in the direction of the axis of the bar (x -axis), the resultant of the stresses on the cross section of the bar (of area A) must be zero:

$$\int_A \sigma(\varepsilon(y)) dA = 0 = \int_A \sigma(-(y - y_0)/\rho_0) dA \quad (2.2.1-16)$$

The second equation, establishes that the moment M on the cross section produced by the external loads (whose value depends upon the section analysed, as can be seen in figure 2.12), must be equal to the internal moment produced by the stresses (figure 2.11c). Taking moments about the neutral axis⁹ we obtain:

$$M = -\int_A (y - y_0) \sigma dA \quad (2.2.1-17)$$

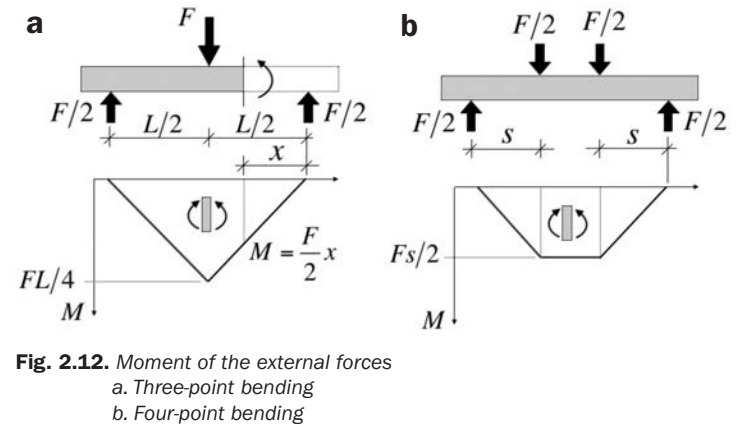


Fig. 2.12. Moment of the external forces
a. Three-point bending
b. Four-point bending

Equations (2.2.1-16) and (2.2.1-17), together with the function $\sigma(\varepsilon)$ which relates the stresses and strains in the material, allow calculation of the values of (ρ_0, y_0) at any cross section along the bar. From these, the **strain** and **stress** at any point are immediately obtained by means of equation (2.2.1-15) and the constitutive equation $\sigma(\varepsilon)$.

When the function $\sigma(\varepsilon)$ is odd (that is to say $\sigma(-\varepsilon) = -\sigma(\varepsilon)$) and the cross section of the bar has a centre of symmetry CS, then the position of the neutral axis coincides with the centre of symmetry. (See exercise 6).

$$y_0 = y_{CS} \quad (2.2.1-18)$$

In the most common case of assuming a linear-elastic relationship between stresses and strains ($\sigma = \varepsilon E$), the position of the fibre coincides with the centroid C of the cross section, (see EXERCISE 6).

$$y_0 = y_C = \frac{1}{A} \int_A y dA \quad (2.2.1-19)$$

In this case, and taking into account equation (2.2.1-15), equation (2.2.1-17) becomes:

$$M = -\int_A (y - y_0) E \varepsilon dA = \frac{E}{\rho_0} \int_A (y - y_C)^2 dA = \frac{EI}{\rho_0} \quad (2.2.1-20)$$

in which I is the second moment of area of the section about an axis parallel to the z -axis and which passes through the centroid of the section.

⁹ Since the sum of the stresses is zero, the moment is always the same and the point about which moments are taken is irrelevant.

The stresses on the cross section of the bar follow a linear law given by:

$$\sigma(y) = -\frac{E}{\rho_0}(y - y_C) = -\frac{M}{I}(y - y_C) \quad (2.2.1-21)$$

and the maximum tensile stress (positive) occurs in the lowest fibre (figure 2.11c), when $(y - y_C)$ is minimum (negative):

$$\sigma_{\max} = \sigma_f = -\frac{M}{I}(y_{\min} - y_C) \quad (2.2.1-22)$$

The value of the maximum tensile stress produced in the bar at the instant of rupture is called the *rupture modulus* (σ_f) or *flexural strength* of the material. Even though theoretically its value should coincide with the *tensile strength*, in reality it is always greater¹⁰.

The calculation of the central displacement of the bar is somewhat more laborious. The interested reader may refer to Timoshenko (1980). The result, for the case of a linear elastic material ($\sigma = \varepsilon E$) is

$$\delta_{3P} = \frac{FL^3}{48EI} \quad (2.2.1-23)$$

for three-point bending, and

$$\delta_{4P} = \frac{Fs}{48EI}(3L^2 - 4s^2) \quad (2.2.1-24)$$

for a specimen in four-point bending.

EXERCISE 6

Derive equations (2.2.1-18) and (2.2.1-19).

SOLUTION:

Proof of equation (2.2.1-18) follows directly, since if we take $y_0 = y_{CS}$ equation (2.2.1-16) is satisfied. To see this it is sufficient to consider the coordinate $v = y - y_{CS}$, with origin at the centre of symmetry of the cross section, and separate the integral (2.2.1-16) into two parts depending upon whether v is greater than or less than zero:

$$\int_A \sigma \left(-\frac{y - y_0}{\rho_0} \right) dA = \int_A \sigma(-v/\rho_0) dA = \int_{v>0} \sigma(-v/\rho_0) dA + \int_{v<0} \sigma(-v/\rho_0) dA$$

By symmetry, for each one of the elemental surfaces dA located in $v < 0$ there is an identical corresponding one in $v > 0$. Therefore, the integral over the region $v < 0$ will be identical to the integral over $v > 0$ with only the sign of v changed

$$\int_{v>0} \sigma(-v/\rho_0) dA + \int_{v<0} \sigma(-v/\rho_0) dA = \int_{v>0} \{ \sigma(-v/\rho_0) + \sigma(+v/\rho_0) \} dA$$

and given that σ changes sign with its argument we see that the integral is zero.

When $\sigma = \varepsilon E$ in equation (2.2.1-16) the result is: $\int_A \sigma \left(-\frac{y - y_0}{\rho_0} \right) dA = 0 = \int_A -\frac{E}{\rho_0}(y - y_0) dA = -\frac{E}{\rho_0} \int_A (y - y_0) dA$

and recalling the definition of the centroid of a plane section: $y_C = \frac{1}{A} \int_A y dA$

we see that we can write equation (2.2.1-16) as: $-\frac{E}{\rho_0} \int_A (y - y_0) dA = -\frac{E}{\rho_0}(y_C - y_0) A = 0$

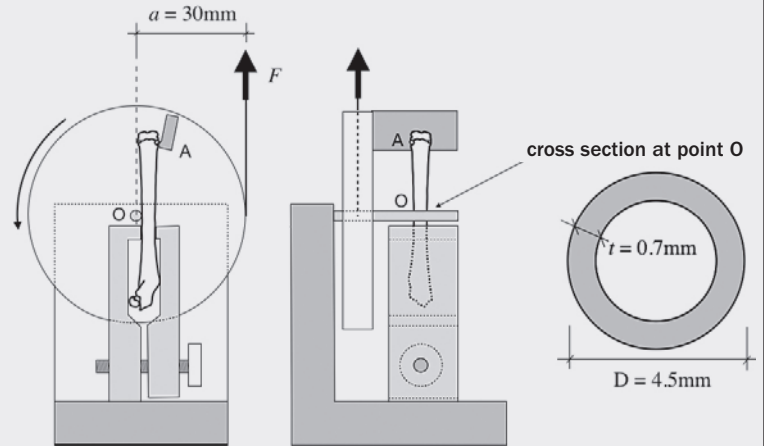
from which equation (2.2.1-19) flows immediately.

¹⁰ In ceramic materials it is about 30% greater. A much simplified explanation is that in the flexure test the volume of material subjected to the elevated stresses is much smaller than in a conventional tensile test and, therefore, it is more difficult to find a large crack which causes rupture in the volume (of elevated stress).

EXERCISE 7

Ekeland and co-workers (Ekeland et al. 1981) used a cantilever flexure test to measure the rupture strength of rat femurs. The figure gives a sketch of the experimental set-up. In the test a force is applied to the end of a disc which rotates about a shaft O and induces a bending moment $M = Fa$ on the cross section of the bone located in O. If rupture occurs when $F = 24\text{N}$ calculate the flexural strength (rupture modulus) of the bone.

Assume that the material is linear-elastic and that the cross section of the bone in the area of contact with the shaft O can be approximated to a circular tube of 4 mm external diameter and thickness 0.7 mm.

**SOLUTION:**

The experimental rig is called a “cantilever” since the test piece is rigidly clamped at one end while the free end is loaded, as shown schematically in the adjoining figure.

In these circumstances, the maximum bending moment is reached at the end of the embedded region (grip), which corresponds to the point O. The cross section of the bone at this point is subjected to a bending moment

$$M = Fa = 24 \cdot 0.03 = 0.72 \text{ Nm}$$

The bending moment will produce a linear distribution of stresses, given by equation (2.2.1-21). The maximum value of the stress is reached at the surface of the bone opposite the contact with the shaft O, and its value will be given by equation (2.2.1-22)

$$\sigma_{\max} = -\frac{M}{I}(y_{\min} - y_c) = +\frac{Fa}{I} \frac{D}{2}$$

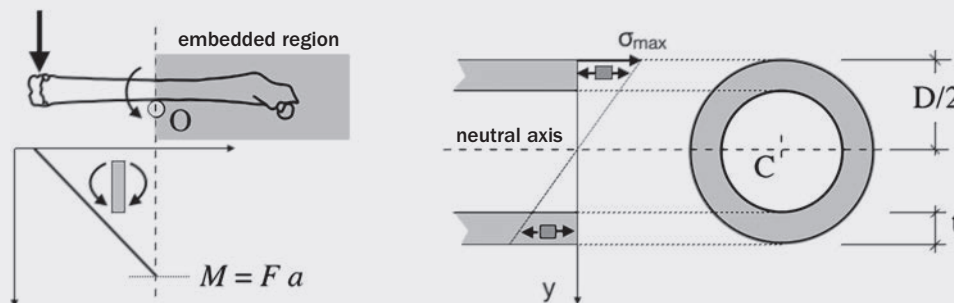
The second moment of area I of the tube cross section about its centroidal axis (neutral axis) will be:

$$I = \frac{\pi}{4} \left[\left(\frac{D}{2} \right)^4 - \left(\frac{D}{2} - t \right)^4 \right] = 9.8935 \cdot 10^{-12} \text{ m}^4$$

with which the resulting value of the maximum stress is:

$$\sigma_{\max} = \sigma_f = \frac{Fa}{I} \frac{D}{2} = 163.7 \text{ MPa}$$

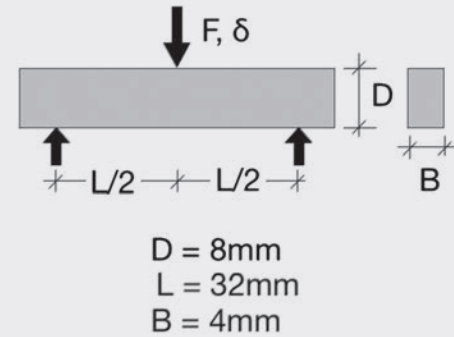
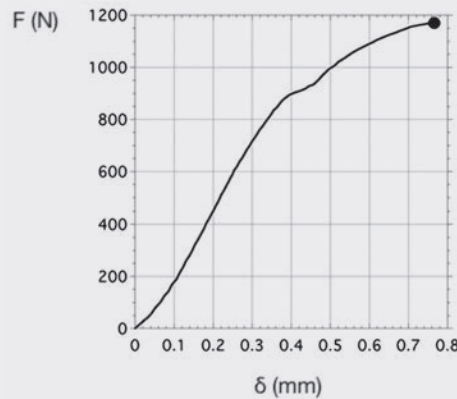
which will be the value of the rupture modulus of the bone.



EXERCISE 8

The figure shows the force-displacement curve for a three-point bending test carried out by Libonati and Vergani (2016) on a bovine cortical bone specimen whose length was aligned with the direction of the osteons. The specimen directions are shown in the figure.

Calculate the rupture modulus of the bone and its elastic modulus assuming linear-elastic behaviour.

**SOLUTION:**

In order to calculate the modulus of rupture, σ_f , we turn to equation (2.2.1-22) taking into account that the second moment of area of the rectangular cross section about its centroidal axis is:

$$I = \frac{1}{12}BD^3$$

with which the expression for the rupture modulus becomes: $\sigma_{\max} = \sigma_f = \frac{M}{I} \frac{D}{2} = \frac{3FL}{2BD^2}$

Examining the F - δ curve we see that rupture occurs when $F=1170\text{N}$, which substituted in the above equation yields:

$$\sigma_f = 219.4\text{MPa}$$

In order to obtain the elastic modulus, E , we need to determine the slope of the initial linear-elastic section of the curve.

From the F - δ curve we observe that, for very low loads at the start of the test, the curve is concave which is usually due to the adjustment (settling in) of the loading system. For that reason we make the fit to the subsequent linear zone, with gives:

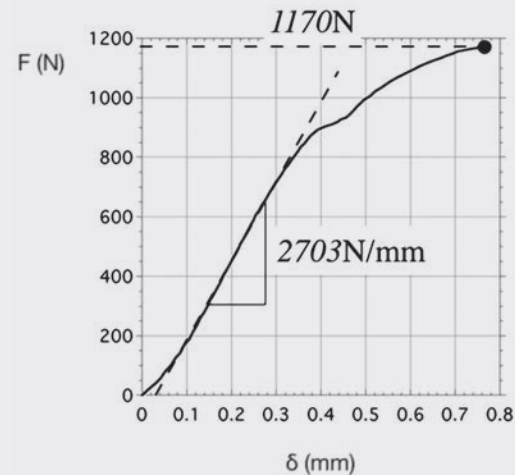
$$\left(\frac{F}{\delta}\right)_{\text{linear}} = 2703\text{N/mm}$$

and with the aid of equation (2.2.1-22) we calculate the value of the elastic modulus:

$$E = \frac{FL^3}{48I\delta} = \left(\frac{F}{\delta}\right) \frac{L^3}{4BD^3} = 10.8\text{GPa}$$

In their series of experiment the authors obtained an average value of the flexural strength (modulus of rupture) of $\sigma_f = 220 \pm 10\text{ MPa}$, and an elastic modulus $E = 12 \pm 1\text{ GPa}$, values that fit in well with our measurements.

In their series of experiment the authors obtained an average value of the flexural strength (modulus of rupture) of $\sigma_u = 111 \pm 30\text{ MPa}$ and $E = 20 \pm 5\text{ GPa}$, rather different from the flexure test results which gave, approximately, double the strength and half the stiffness. In this case, in addition to the differences between the two types of test (observed on isotropic material), there is also the fact that the cortical bone is orthotropic.



2.2.2. Rupture tests

General Fracture Mechanics concepts

Rupture of a material begins with the propagation of a pre-existing defect –nearly always, a crack– or one which is formed during the loading process. *Fracture Mechanics* aims to determine the load which a cracked material can support, or up to what size a crack might grow without producing catastrophic failure. This branch of mechanics was developed and consolidated in the second half of the 20th century.

Rupture criteria are well-established for elastic materials –linear or otherwise–, but this is not the case when there is plasticity or visco-plasticity (behaviour commonly found in biological materials). For the moment, our observations on fracture analysis will focus on elastic materials because almost all of the standard fracture tests are based on this type of behaviour and they are the most frequently used to characterise biological materials.

The treatment of failure criteria is based on two approaches, **global** and **local**.

The *global* approach is based on an energy balance between energy available (that supplied from the outside and the elastic stored energy) and the energy expended in fracture. The energy approach has several advantages; it is simple (being based on the principle of conservation of energy) and it is general (allowing application to any elastic material, even if non-linear).

The *local* approach is based on the fact that for elastic materials it is possible to describe the fracture criterion locally, as a function of the stress and displacement near the crack tip. These (stress and displacement) fields –in linear elastic materials– are fully characterised if the stress intensity factor (K) is known and failure is produced when K reaches a critical value.

It is, then, is equally possible to express the failure criterion (for a linear elastic material) as a function of the available energy or the stress intensity factor: a crack becomes unstable when either the strain energy, or the stress intensity factor, reaches a critical value.

The advantage of the local criterion over the global is that it is usually much easier to calculate the stress intensity factor than the available energy (because for most problems these factors are tabulated in handbooks and because, when dealing with linear elastic materials, the principle of superposition can be applied). The drawback is that its application is restricted to linear elastic materials.

Later, brief comment will be made on some issues and definitions that are needed in order to apply the procedures, described above, in the fracture tests. The concepts and the theory behind *Fracture Mechanics* have no place here but the interested reader can refer to a book written by the present authors (Elices and Guinea, 2021), and the references contained in it.

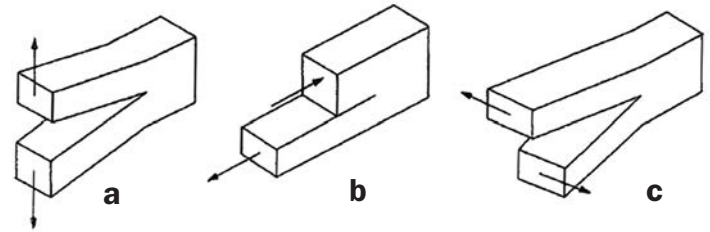


Fig. 2.13. Basic modes of fracture.
a. Mode I: Opening (tensile) mode.
b. Mode II: (In-plane) Shearing mode.
c. Mode III: (Out-of plane shear) Tearing mode.

The analysis of the propagation of a crack in a solid subjected to any distribution of forces and displacements is complex. In order to facilitate its study, the general propagation of a crack is decomposed into three basic modes, represented in figure 2.13; simple tensile opening, or Mode I (figure 2.13a), sliding, by in-plane shear, or Mode II (figure 2.13b), and tearing (out-of-plane shear), or Mode III (figure 2.13c). Most fractures occur in Mode I which, furthermore, is the most studied and that on which the tests discussed below are based. Mode III is characteristic of tearing fractures which originate in laminas and membranes, a subject discussed previously in section 2.3.3 of the “Biological Membranes” book.

The **local approach** is written as:

$$K = K_C \quad (2.2.2-1a)$$

The first term, K , called the *stress intensity factor*, is a function which must be **calculated** in every case and which characterises the state of stress near the tip of a crack tip. This function, K , is defined for, and only makes sense in, *linear elastic materials*.

The second term, K_C , called the *fracture toughness* (or critical stress intensity factor), is a material property and its **measurement** is governed by standards (for example, in the ASTM E399, ASTM E1304 and ASTM E1820 standards). Strictly speaking K_C is not a material property, it varies with thickness until a state of plane strain is achieved.

The **global approach** can be written as:

$$G = G_C \quad (2.2.2-1b)$$

The first term is the *strain energy*, per unit area, (or strain energy release rate) to break the material –which is represented by G – and the second is the specific fracture energy, which is assumed to be a characteristic of the material.

G is a quantity that is **calculated** and is a function of the applied load, crack length and the geometry of the body. G_C is a property which is **measured** and depends upon the temperature and the loading rate, in a state of plane strain.

The values of K and G , are not independent. For a crack propagating in Mode I

$$K_I^2 = E' G \quad (2.2.2-2)$$

where E' is the generalised elastic modulus of the material, which is equal to the elastic modulus E in a state of plane stress (thin specimens) and to $E/(1-\nu^2)$ in plane strain (thick specimens). ν is the Poisson's ratio of the material. When the crack propagates the relationship above leads to:

$$K_{IC}^2 = E' G_C$$

Measurement of G_C can be performed directly, measuring the area enclosed in a process of loading and unloading after a small amount of stable crack propagation, or by indirect measurements from a force-displacement record in a cracked specimen of a given geometry. The latter process is specified in the ASTM Standard E1820.

Standard tests

Measurement of the fracture toughness, K_{IC}

When measuring the value of the toughness which initiates the propagation of a crack, in pre-cracked specimens, it is found that this value usually decreases as the specimen thickness increases, until it reaches a practically constant value beyond a certain thickness. This limiting value is a material property called the fracture toughness (or more properly the plane strain fracture toughness) and which is denoted K_{IC} . The fracture toughness does not always depend upon the thickness provided the dimensions of the specimen are large enough compared to the size of the plastic zone, and it can be assumed that around the crack tip there is a state of plane strain.

It has also been established that the fracture toughness (K_{IC}), varies with temperature and the loading rate, as happens with other material parameters; such as the yield stress or the modulus of elasticity.

Measurement of the plane strain fracture toughness, K_{IC} , is standardised –like the measurement of G_{IC} – in the ASTM Standards (E399, E1304 y E1820). All of these contain details of the specimens, test fixtures and the mechanical testing machines.

The test consists of loading a cracked specimen in Mode I and measuring the critical load which initiates crack growth, taking care to ensure that the plastic zone at the crack tip is small and that the test takes place under plane strain conditions. For the measurement of K_{IC} ASTM Standard E399 proposes the specimens shown in figures 2.14a and 2.14b.

The first step towards the determination of K_{IC} , once the type of specimen has been chosen, consists of specifying the specimen thickness. The limitations regarding the specimen thickness and the crack length, which are practically the same, are determined by the conditions set out above in order to ensure that the value of the fracture toughness obtained from the test is a characteristic of the material. These conditions are:

- That the stress state is plane strain.
- That the size of the plastic zone at the tip of the crack is small compared to the specimen dimensions.

Once the specimen thickness has been selected the specimen can be fabricated. It is recommended that the cracks are large, with $0.5 \leq a/W \leq 0.70$. Machining of the notch and the generation of the starter crack at the end of the notch are delicate processes. These starter cracks are produced by notching the specimen and inducing a fatigue crack at the tip of the notch, so that the resulting crack is close to the ideal crack (zero crack-tip radius). The test standard provides details as to how the specimen should be fatigued in order to avoid creating an excessively large plastic zone at the tip of the crack because the residual stresses resulting from excessive plasticity would invalidate the test results.

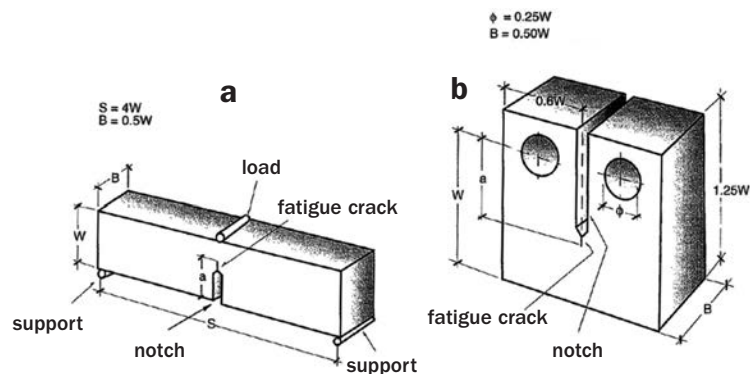


Fig. 2.14. ASTM Standard E399 for fracture tests
a. Recommended geometry for a beam type specimen
b. Recommended geometry for a compact tension specimen

Once the specimen has been fabricated the K_{IC} test is performed, subjecting the specimen to an increasing load until rupture, while recording the applied force F and the relative displacement w of the lips of the crack.

After rupture, the length of the crack is determined from the average of its length at the centre of the specimen and those at two points midway between the centre and the two lateral faces of the specimen.

Later, with the length of the crack, a , calculated in this way, the critical stress intensity factor, K_Q , is determined (see figure 2.14c). For this, in the graph (F , w), the secant line which passes through the origin of coordinates and which has a slope of 95% of the gradient of the tangent at the origin of the curve is drawn. The point at which the secant cuts the curve defines a load P_5 . If the load at all points in the data record before P_5 is less than this value, then $P_Q = P_5$ is taken. If, on the other hand, there is a maximum in the load prior to P_5 greater than this value, P_Q is taken to be that maximum value.

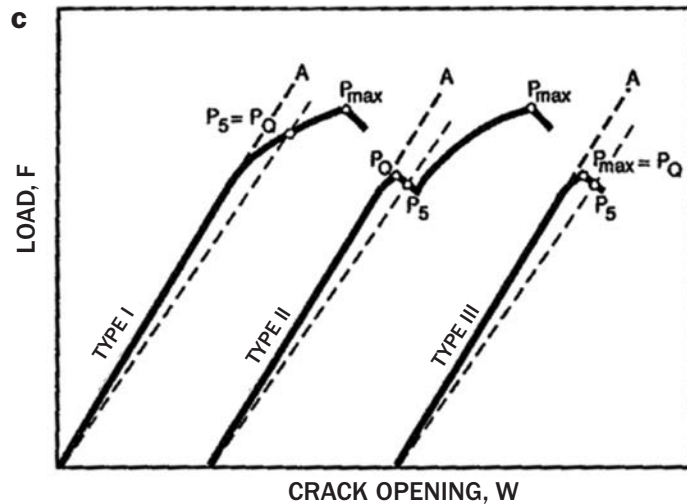


Fig. 2.14. c. Recommendations for calculating the value of K_{IC}

Subsequently, P_{max}/P_Q is calculated, where P_{max} is the maximum load borne by the specimen during the test. If that ratio is less than 1.10, P_Q can be used to calculate K_Q ; if that is not the case, then this indicates that there is too much plasticity in the test to allow definition of a K_{IC} and the test is invalid.

When there is a valid value of P_Q it is possible to calculate K_Q with the following expressions, depending upon the type of chosen specimen:

– for the beam specimen

$$K_Q = \frac{6P_Q}{BW^{1/2}} \sqrt{\alpha} \frac{1.99 - \alpha(1-\alpha)(2.15 - 3.93\alpha + 2.7\alpha^2)}{(1+2\alpha)(1-\alpha)^{3/2}} \quad (2.2.2-3)$$

– for the compact tension specimen

$$K_Q = \frac{P_Q}{BW^{1/2}} \frac{(2+\alpha)(0.886 + 4.64\alpha - 13.32\alpha^2 + 14.72\alpha^3 - 5.6\alpha^4)}{(1-\alpha)^{3/2}} \quad (2.2.2-4)$$

where $\alpha = a/W$, and a, W, B, S , are defined in figures 2.14a and 2.14b.

The final step, before declaring the test as valid, is to check that the condition

$$B, b > 2.5 \left(\frac{K_Q}{\sigma_c} \right)^2 \quad (2.2.2-5)$$

is satisfied where σ_c is yield stress of the material (or 0.2% off-set stress). The value K_Q is introduced into this expression in order to determine if the thickness of the specimen tested is sufficient to satisfy the inequality. In the affirmative case, it can be taken that the fracture toughness K_{IC} is equal to the determined value K_Q . In the opposite case, it is necessary to repeat the test with a thicker specimen. For ductile materials the thickness can be so large that it is impossible to measure K_{IC} from the available thicknesses.

Another specimen, which has also been proposed for measuring K_{IC} , is that shown in figure 2.15, which is commonly called the short cylinder or short bar specimen. One advantage, together with its compact dimensions, is that this specimen does not have to be pre-fatigue-cracked, which is a major benefit when testing very brittle materials, such as ceramics. A detailed description of the characteristics of the specimen and the interpretation of the test results can be found in the ASTM Standard E1304.

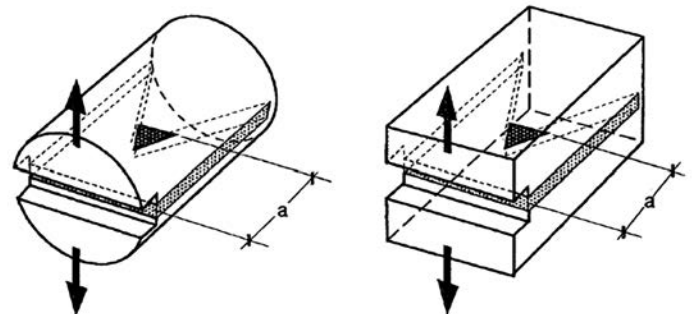
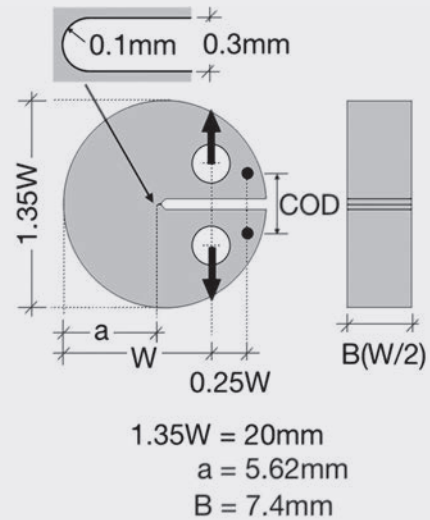
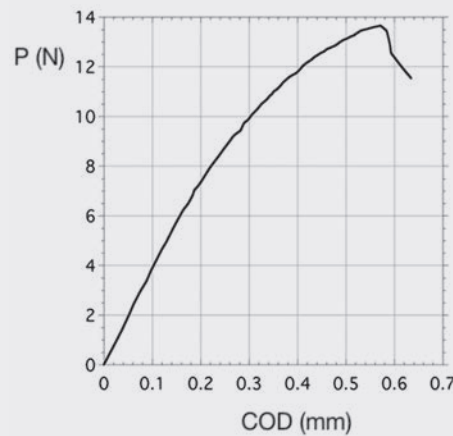


Fig. 2.15. Specimen geometries for measurement of fracture toughness using the ASTM Standard E130.

EXERCISE 9

Cook and Zioupos studied the fracture toughness of trabecular bone under pathological conditions (2009). The figure shows the force-crack opening displacement (COD) curve from an experiment performed on a standard specimen in the form of a disc of trabecular bone taken from the head of the femur of a person with osteoporosis. The specimen dimensions are also shown. The plane of the crack lies perpendicular to the predominant direction of the trabeculae.



Calculate the value of K_{IC} according to the ASTM Standard E1820.

SOLUTION:

The compact disc-shaped specimen is one of the standard geometries proposed in the ASTM Standard E1820. The following formula is used for the calculation of K_I :

$$K_Q = \frac{P_Q}{BW^{1/2}} \frac{(2 + \alpha)(0.76 + 4.8\alpha - 11.58\alpha^2 + 11.43\alpha^3 - 4.08\alpha^4)}{(1 - \alpha)^{3/2}}$$

which is very similar to equation (2.2.2-4).

To determine the crack initiation load P_Q a straight line must be drawn from the origin at 95% of the initial slope and the point of intersection with the experimental curve found. This process is better performed numerically, with a digitised curve, since the errors in a hand construction can be quite high.

In our case we obtained the initial tangent by fitting it to the section (0, 7N) which is reasonably linear. The resulting line is: $P_{100}(N) = 37.9 \text{ COD}(\text{mm})$ and the corresponding 95% line $P_{95}(N) = 36.0 \text{ COD}(\text{mm})$, which gives a load $P_Q = 8.1 \text{ N}$.

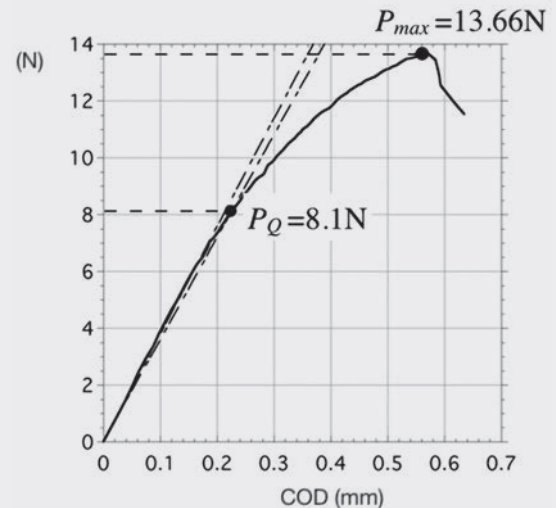
Since it turns out that $P_{max}/P_Q = 1.7 > 1.1$ the specimen has undergone too much plastic deformation so it is not possible to obtain a valid value of K_{IC} and here the test would end.

However, and for the sole purpose of illustrating the procedure, if we suppose that the valid value of P_Q were $P_Q = P_{max}$, from the formula for K_I we would obtain $K_Q = 0.1074 \text{ MPam}^{1/2}$. To perform a final validation of K_Q we should check equation (2.2.2-5). Taking a conservative value of 10 MPa for the yield stress of the trabecular bone used (with an apparent density of 0.33 g/cm^3) we obtain:

$$B = 7.4 \text{ mm}, b = W - a = 9.19 \text{ mm} > 2.5 \left(\frac{K_Q}{\sigma_c} \right)^2 = 0.29 \text{ mm}$$

so the validity conditions are met, and $K_{IC} = K_Q$.

An interesting aspect of the test is the materialisation of the crack. We see in the figure in the exercise that the specimen had a machined notch (rather than a crack) with a tip radius of curvature of $100 \mu\text{m}$. Bearing in mind that the scale of the microstructure (the size of the trabecula) is greater than 1 mm it seems reasonable to regard this notch as a crack, the notch tip radius being an order of magnitude less than the material microstructure.



Measurement of the specific fracture energy; G_C

In this test it is assumed that the work done by the external forces is converted, solely, into cracking the specimen. Therefore, the specific fracture energy is obtained by dividing the work done by the area of the crack.

ASTM Standard E1820 provides a method of measuring G_C for materials which are not very brittle and which, once cracked, are capable of supporting some degree of stable crack propagation before sudden failure. This Standard combines the processes of measuring G_C and K_{IC} , and allows the determination of the values of the specific fracture energy under conditions for which ASTM Standard E399 is not applicable, as happens when there are small amounts of plastic deformation which cannot be ignored.

The major difficulty lies in determining the precise instant of crack initiation. The Standard allows an estimation of this value by extrapolation, from specimens in which the crack has propagated a certain distance and, in addition, allows verification that the experiment was performed under elastic conditions. The ideas upon which the test procedure is based are outlined below.

Since one of the options in the ASTM Standard E1820 is to measure the fracture toughness K_{IC} the specimen fabrication processes and the testing are the same as those already described for the E399 Standard. After completing the test, K_Q is calculated and it is checked to see if this value is valid for K_{IC} .

If it is valid, G_C is determined from the expression:

$$G = \frac{K_{IC}^2 (1 - \nu^2)}{E} \quad (2.2.2-6)$$

where, E and ν are the modulus of elasticity and Poisson's ratio of the material, respectively.

If it is not valid, the specific fracture energy G_C can be estimated from

$$G = \frac{K_Q^2 (1 - \nu^2)}{E} + J_{pl} \quad (2.2.2-7)$$

The specimens must be tested under controlled displacement while recording the force F as a function of the displacement u of the load point. The values of J_{pl} , are calculated from this record, applying the following expressions

$$J_{pl} = \frac{1.9 A_{pl}}{Bb} \quad \text{for beam specimens} \quad (2.2.2-8)$$

$$J_{pl} = \frac{\eta A_{pl}}{Bb} ; \quad \eta = 2 + 0.522(1 - a/W) \quad \text{for compact tension specimens} \quad (2.2.2-9)$$

The area enclosed by the $F-u$ curve, represented by A_{pl} , $b = W - a$, and B is the specimen thickness, indicated in figure 2.16. a includes the length of the notch and fatigue crack, but not the stable crack propagation produced during the test.

In the first version of the ASTM Standard a single equation that integrated the elastic and plastic components was used:

$$G = \frac{2A}{Bb} \quad \text{for beam specimens} \quad (2.2.2-10)$$

$$G = \frac{\eta A}{Bb} ; \quad \eta = 2 + 0.522(1 - a/W) \quad \text{for compact tension specimens} \quad (2.2.2-11)$$

where A is the total area enclosed by the $F-u$ curve, without elastic unloading. This procedure has the advantage that it does not depend upon the values of the elastic parameters E and ν in equation 2.2.2-7.

In principle, according to the above, a single test should be enough to obtain the critical value of G , but in reality this is not done since it is difficult to detect the on-set of propagation. In practice, a series of tests are performed in which the crack is allowed to grow different amounts Δa . In each case a value of G is calculated, G is represented as a function of Δa and extrapolated to that when Δa tends to zero. Experience has shown that this extrapolation can be improved if, instead of considering the intersection with the vertical axis ($\Delta a = 0$), the intersection with a line parallel to the line drawn through $\Delta a = 0.2$ mm is used.

$$G = 2\sigma_0 \Delta a \quad (2.2.2-12)$$

The line represents, in a conventional sense, the line of blunting of the crack. The stress σ_0 can be any value between the yield stress $\sigma_{0.2}$ and the fracture stress, σ_R . The Standard recommends that the value $(\sigma_{0.2} + \sigma_R)/2$ is taken..

Essentially, and according to the above Standard, the process for measuring G_C consists of performing a series of tests, representing the corresponding values of G as a function of Δa and performing a least squares fit of the potential curve, $G = C \Delta a^m$ to these values after discarding the extreme values (which are those which fall outside the zone indicated in figure 2.16a, where $G_{max} = b \sigma_0 / 7.5$) and as long as there are four or more remaining. The value of G_Q is obtained from the intersection of this curve with the parallel to the line of blunting plotted by $\Delta a = 0.2$ mm, as shown in the figure.

Once G_Q is calculated, it is necessary to verify that the experiment has been performed within the hypotheses used for deducing equations (2.2.2-10) and (2.2.2-11) and that this value corresponds to G_C . Following an in-depth experimental study (see the references cited in the Standard), it has been established that G_Q can be taken as a reliable measure of G_C if the following conditions are satisfied:

$$B > \frac{25G_Q}{\sigma_0} \quad b > \frac{25G_Q}{\sigma_0} \quad \left. \frac{dG}{da} \right|_Q < \sigma_0 \quad (2.2.2-13)$$

where $(dG/da)_Q$ is the slope of the regression curve at the ordinate point G_Q . As has already been indicated, this summary is only intended to give an idea of how the process works, the quoted Standard contains many more details about how to perform the test and validate the results.

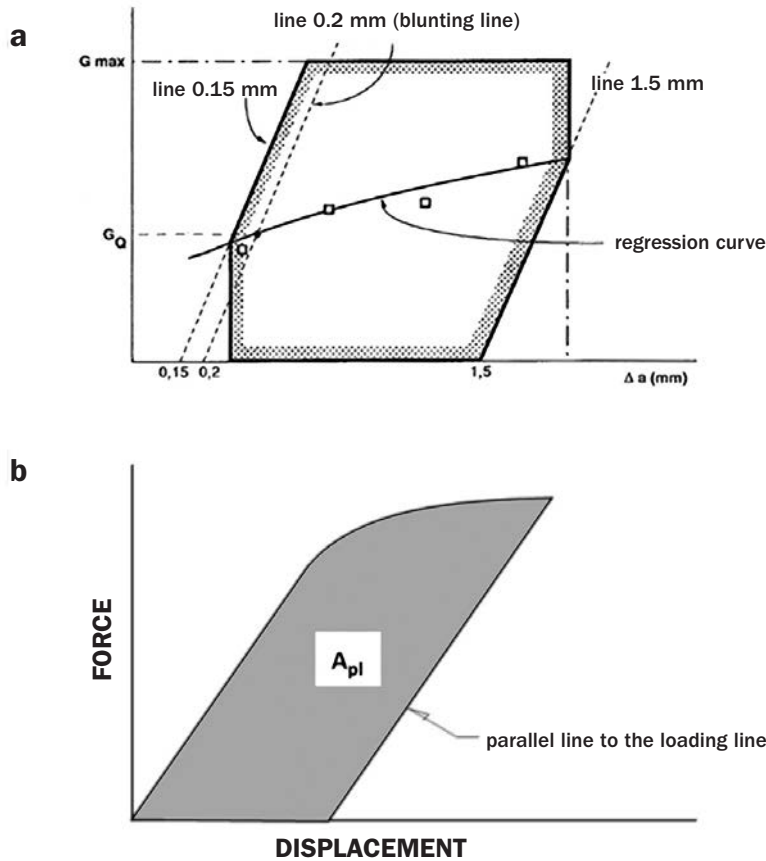


Fig. 2.16. ASTM Standard E1820 for fracture tests
a. Recommendations for calculating G_C and valid zone tests.
b. Recommendations for calculating A_{pl}

EXERCISE 10

Determine if it is possible to obtain an estimation of the value G_C from the data in Exercise 9.

SOLUTION:

For specimens in which it is not possible to measure K_{IC} , ASTM Standard E1820 prescribes the taking of several measurements with different amounts of stable crack propagation with the aim of estimating the value G_C at the initiation of fracture. In our case, Cook and Zioupos show in their work (2009) that the nonlinearity of the test is due to the collapse of the trabecula (plastic deformation) near the crack tip but not to its propagation, which starts when P_{max} is reached. For this reason we will estimate G_C from the maximum load data assuming that at this instant $\Delta a = 0$.

Since there is no direct record of the load line displacement, we are going to estimate its value from the force-COD curve, which takes, as a reference, points very close to the load, as shown in the figure. On the other hand, in order to avoid having to estimate the elastic parameters, E and ν in equation 2.2.2-7, we use equation 2.2.2-11 valid for both elastic and plastic situations.

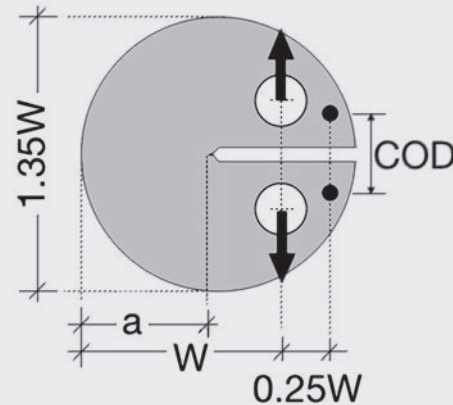
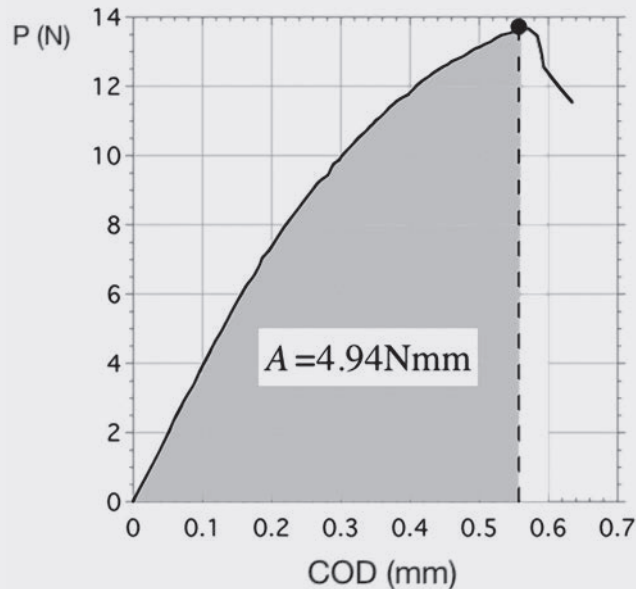
In this way we arrive at:

$$G_C = \left\{ 2 + 0.522(1 - a/W) \right\} \frac{A}{Bb} = 159.7 \text{ J/m}^2$$

a value which is in agreement with those of other authors.

Taking –as in Exercise 9– a value of the yield stress $\sigma_0 = 10 \text{ MPa}$, we can verify that the estimated value of G_C , satisfies equations 2.2.2-13:

$$B = 7.4 \text{ mm}, \quad b = W - a = 9.19 \text{ mm} > \frac{25G_C}{\sigma_0} = 0.4 \text{ mm}$$



2.2.3. Indentation tests

Introduction

In order to perform conventional tensile, flexure or fracture tests it is necessary to start with a specimen of a particular geometry (cylinders, plates, beams, etc.) as has been discussed in the corresponding sections. Sometimes it is not possible to prepare the specimens with the desired dimensions because the precursor material does not allow it, because there is not enough material or because the stiffness of the material makes it impracticable; all of these circumstances may arise with biological materials. In these cases, tests based on *indenting* (pressing with a suitable punch) a small region of the material can, sometimes, give information on the elastic modulus or yield stress of the material.

Mollusc shells, when large, allow specimens to be cut to carry out traditional mechanical tests, as mentioned in section 3.3.1. But when the shell thickness is small, less than 1 mm, then it is necessary to resort to nanoindentation techniques in order to estimate the mechanical properties of its various components (see, for example, Yao et al., 2010).

Thickening of the arterial walls and loss of elasticity are the principal characteristics of a group of illnesses called *arteriosclerosis*. One form of this illness is the *arteriosclerosis*, characterised by the formation of lesions called *atherosclerotic plaques* in the walls of the small and medium arteries. The rupture of these plaques can provoke damage to the heart and infarcts, therefore it is interesting to know the mechanical behaviour of these plaques; in particular their stiffness and fragility. Again, it is not possible to fabricate conventional specimens from these plaques so indentation tests may be used in order to extract some mechanical parameters (see, for example, Ebenstein et al., 2009).

Another situation, in which it is not possible to machine conventional specimens, is when soft materials need to be characterised; a very interesting case, in particular, occurs in the study of the mechanical properties of cells. The atomic force microscope (AFM) is a powerful tool which permits not only a study of the shape of the cells but also to interact with them under physiological conditions through the tip of a cantilever, if used as an indenter (see, for example, Ikai, 2009).

The idea of indenting a material and extracting information of the imprint is old, dating at least from the experiments proposed by Brinell¹¹ in 1900. The procedure consists of using as an indenter, in the first instance, a hard steel ball and, later, a tungsten carbide ball, and pressing it with 3000 kgf force (approximately 30 kN) onto the material. The load is held in place for 30 seconds and the diameter of the (projection of) the imprint left in the surface is measured. The Brinell hardness (HB), measured in kg/mm², is the ratio of the applied, F , and the contact area.

The next step was to correlate the hardness with some mechanical property. For steels there is an empirical correlation between the hardness and the yield stress, σ_c , given by

$$HB = 3.2\sigma_c \quad (2.2.2-14)$$

In the middle of the last century, with the development of electronics, equipment became available to measure simultaneously the force F and the imprint h , which facilitated the test. If, moreover, the device was attached to a microscope it was possible to extend the range of indentations to micron-sized regions of the material.

At the beginning of this century, with the appearance of atomic force microscopes, these techniques have now entered the nanometre domain.

Hardness test are standardised, for example, in ISO 14577. This Standard defines three areas in which hardness is measured:

- Macroscopic domain: for values of F between 2 N and 30000 N
- Microscopic domain: for values of F less than 2 N and h greater than 0,02 μm
- Nanoscopic domain: for values of h , less than 0,02 μm

Below, a brief introduction to each domain is presented, although for biological materials the domains of interest are the microscopic and nanoscopic.

¹¹ Johan August Brinell (1849- 925) was a Swedish metallurgical engineer. He proposed his method at the 1900 Paris Exposition.

Indentation in the macroscopic domain

The advantage of macroscopic tests is that they are relatively simple and non-destructive. However, it is not easy to obtain reliable absolute values of the mechanical properties so the tests are, almost always, used to compare materials or different batches of the same material.

The hardness of a material is not a well-defined property, moreover, there are several different modes of indentation for measuring it (Brinell, Rockwell or Vickers). For a detailed description of the different methods see, for example, ASM Handbook Vol. 8. What these tests measure, in reality, is a combination of the elastic, plastic and, sometimes, fracture responses of the material. Deducing the modulus of elasticity or the yield stress of a material from these test data is not always a rigorous exercise.

The Brinell hardness (HB) is defined in the Standard BS EN ISO 6506. The indenter is a tungsten carbide ball, between 5 and 10 mm in diameter, through which a force of between 500 and 3000 kgf is applied for a certain time, between 10 and 30 seconds. After removing the load the diameter, d , of the imprint projection on the initial surface is measured and the value of the hardness calculated from:

$$HB \approx \frac{2F}{\pi D \left(D - \sqrt{D^2 - d^2} \right)} \quad (2.2.2-15)$$

where F is the applied force and D the diameter of the ball (see Fig. 2.17). Details of this test, its limitations and the necessary precautions can be found in ASM Handbook Vol. 8.

The Rockwell hardness (HR) is defined in the Standard, ISO 3738. This test is used for hard materials. The Rockwell hardness is different from the Brinell hardness (HB) because the indentation is applied in two successive stages; one with a small force and the other with a greater force, and the difference in the depths is used to better estimate the size of the imprint, in this way initial errors are eliminated and the measurement is more precise. The duration of the test is from 5 to 10 seconds. The indenters are tungsten carbide spheres or diamond in the shape of a cone with a rounded tip, see figure 2.17 (ASM Handbook Vol. 8, contains more details).

The Vickers hardness (HV) is defined in the Standard EN 23878. The indenter is a diamond pyramid (see figure 2.17) and the method is similar to that used for measuring the Brinell hardness, because the indenter is pressed into the material and then withdrawn. The diagonals of the imprint are measured, the projected area calculated and the hardness obtained by dividing the load by the area. This test is also used in the micro-indentation domain when the applied forces are less than 1 kgf (ASM Handbook Vol. 8, provides more details). For materials in which the values of E or σ_c depend on time that they bear the load—a common feature of biological materials—it can be expected that the size of the imprint will also vary with time and, consequently, so will the value of (HV).

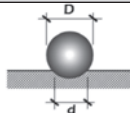
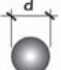
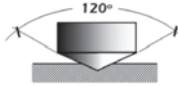
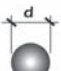
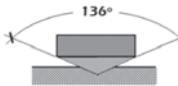

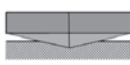
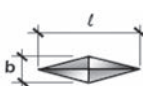


HARDNESS TEST				
Test	Indenter	Indentation shape		Hardness
		Side view	Plan view	
Brinell	WC ball			$HB = \frac{2P}{\pi D \left[D - \sqrt{D^2 - d^2} \right]}$
Rockwell	Diamond cone			HR
Vickers (Microhardness)	Diamond Pyramid			$HV = 1.854 P / d_1^2$
Knoop (Microhardness)	Diamond Pyramid			$HK = 14.2 P / l^2$
Berkovich (Microhardness)	Pyramid			HBk

Fig. 2.17. Hardness tests: Geometry of the indenters and the notation used.

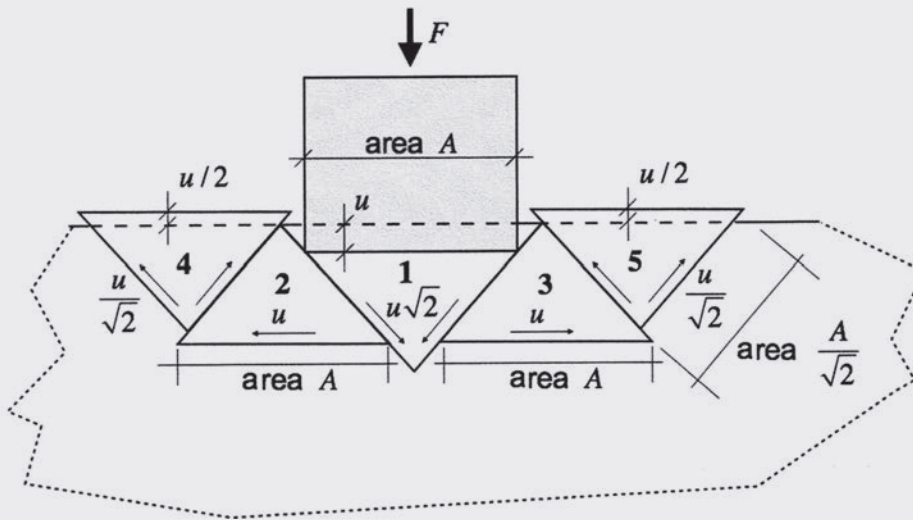
Another aspect to bear in mind is that it is always assumed that any material *support* does not affect the results, or in other words, the support material is considered to be a semi-infinite medium. This assumption is used in the

following sections. However, at the end of this chapter some comments will be made on how to tackle the indentation of laminas, where it is essential to take account of their thickness in indentation measurements.

EXERCISE 11

Derive the empirical correlation between the hardness and the yield stress for steel (2.2.2-14).

Consider a two-dimensional case (a three-dimensional calculation would produce the same results, approximately) in which the material does not strain-harden and yields along the planes of maximum shear stress (at 45°) as shown in the figure, where the value of the maximum shear stress is k . Assume, also, that the force applied to the indenter is F , the contact area A and the vertical displacement u .



SOLUTION:

Equating the work done by the indenter, Fu , to the work of the shear stress on the sliding planes we obtain:

$$Fu = 2 \cdot \frac{Ak}{\sqrt{2}} u\sqrt{2} + 2 \cdot Ak \cdot u + 4 \cdot \frac{Ak}{\sqrt{2}} \frac{u}{\sqrt{2}} = 6Ak$$

The work done by k on block 1 is the first term, the work on blocks 2 and 3 is the second term and the work on blocks 4 and 5 is the third.

If the relationship between the yield stress σ_c and maximum value of the shear stress k , is $\sigma_c = 2k$ and the hardness H , is expressed as $H = F/A$, resulting in:

$$H = 3\sigma_c$$

In reality, sliding is not confined to the planes drawn in the figure, but along many 45° planes near the indenter. Even if the real geometry were different, the result obtained is an upper bound (this is a consequence of a theorem in the *theory of plasticity*).

Indentation in the microscopic domain

To measure the hardness in microscopic domains –for example, in polycrystalline materials to examine the interior of grains or grain boundaries– very small forces are employed; the ASTM Standard E384 suggests forces between 1 gf and 1000 gf, and to achieve this special indenters have been developed. The hardness is measured in the conventional way by dividing the force, F , by the area of contact, A .

The values obtained from microhardness tests cannot be extrapolated, in general, to those obtained from macroscopic tests because the areas investigated may not be analogous; the data obtained for a nanocrystalline grain does not have to coincide with that measured on a polycrystal, for example.

The most used micro-indentation tests are the Vickers and Knoop tests.

The Vickers hardness (HV) is measured as described in the previous section. The force is applied gradually and contact held for 10 or 15 seconds. After unloading, the diagonals of the imprint are measured and their average value d calculated and the hardness evaluated using the following expression:

$$HV = \frac{2 \sin 68^\circ F}{d^2} \approx \frac{1.8544 F}{d^2} \quad (2.2.2-16)$$

where F is measured in kgf and d in mm. (For details see, for example the ASTM Standard E384).

The Knoop harness (HK) is measured with a diamond indenter in the form of a stretched pyramid (see figure 2.17) which has a width-to-height ratio of 7:1 and face angles of 172 degrees for the long edge and 130 degrees for the short edge. The hardness is given by the formula:

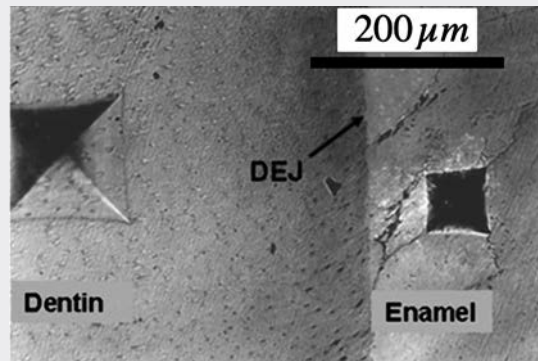
$$HK = \frac{14229 F}{L^2} \quad (2.2.2-17)$$

where F is measured in gf and L (the length of the major diagonal) in microns. The depth of the imprint is small in these tests, so they are suitable for thin materials, in which the effect of the support could influence the measurements.

For soft materials, such as elastomers or many biological materials, other means of indentation are needed, such as the Shore durometers, in which the indenter is steel stylus which terminates in a truncated cone (Shore A or C) or in a rounded shape (Shore D). Hardness is measured on a scale which goes from 0 to 100 (ASTM D2240). One variant of these durometers is the indenter proposed by the International Rubber Association, in which the hardness scale used, the IRHD (International Rubber Hardness Degrees), is very similar to Shore A.

EXERCISE 12

The figure shows Vickers indentation tests performed by Deliormandi and Guden (2006) on human dentin and enamel. If the indentation load was 1 kgf determine the value of the Vickers hardness for both materials.

**SOLUTION:**

We shall use equation 2.2.2-16, which has as its parameters the applied force F and the diagonal d of the imprint.

Measuring from the micrograph, we obtain:

$$d_{\text{dentin}} = \frac{1}{2}(172.6 + 182.7) = 177.7 \mu\text{m}$$

$$d_{\text{enamel}} = \frac{1}{2}(90.8 + 88.2) = 89.5 \mu\text{m}$$

which are the average values of the two diagonals. With these values and noting that $F = 1 \text{ kgf}$ we obtain

$$HV_{\text{dentin}} = \frac{1.8544 \cdot 1}{0.1777^2} = 58.7 \text{ Kgf/mm}^2 = 575.8 \text{ MPa}$$

$$HV_{\text{enamel}} = \frac{1.8544 \cdot 1}{0.0895^2} = 231.5 \text{ Kgf/mm}^2 = 2.271 \text{ GPa}$$

Note that the hardness has dimensions of stress, therefore it is more appropriate to write it in S.I. units.

However, it is customary to write the hardness without units, as it comes from the formulas that define it, without decimals but referring to the load used in kgf. For example, in our case the results are written in the form:

$$HV_{\text{dentin}} \rightarrow 59 \text{ HV1}$$

$$HV_{\text{enamel}} \rightarrow 232 \text{ HV1}$$

Generally, the duration of the load application is understood to be between 10 and 15 seconds. If a value outside this range were used, it would also be included with the resulting measurement, for example:

$$HV_{\text{dentin}} \rightarrow 59 \text{ HV1} / 20$$

$$HV_{\text{enamel}} \rightarrow 232 \text{ HV1} / 20$$

if the load were applied for 20 seconds.

From the result obtained we demonstrate that enamel is almost four times harder than dentin, which is the substrate supporting it. The hardness of enamel is superior to mild steel (which is about 150 HV) but below ceramics (HV greater than 1000).

Indentation in the nanoscopic domain

The nanometric domain is investigated with more sophisticated indenters which began to evolve in the final quarter of the last century with the development of electronics and the start of this century with the appearance of the atomic force microscope.

First generation nano-indenters were, essentially, computer controlled indenters which simultaneously measured the force and the depth of the imprint. A schematic representation of these devices is shown in figure 2.18a. The indenter is, almost always, a Berkovich pyramid (figure. 2.17), which produces imprints such as that of figure 2.18b. The resolution of the applied loads can be less than 50 nN and the displacement less than 0.02 nm.

During the test, loading-unloading curves, such as those shown in figure 2.18c, are obtained and the hardness measured following the usual process by $H = F_{max}/A$, where F_{max} is maximum load and A is the projection on the plane of the contact area corresponding to the maximum load.

The area A , as a function of the contact depth h_c (see figure 2.18d), is obtained by assuming that the indenter is rigid and hardly deforms, and it is only a function of h_c . The following expression is recommended.

$$A = a + bh_c^{1/2} + ch_c + dh_c^{3/2} + 24.56h_c^2 \quad (2.2.2-18)$$

where a , b , c and d are coefficients to be adjusted (see, for example, Oliver and Pharr, 1992). For an ideal Berkovich indenter the coefficients a , b , c and d are zero. In practice, however, they are not zero because the tip of the indenter becomes blunt.

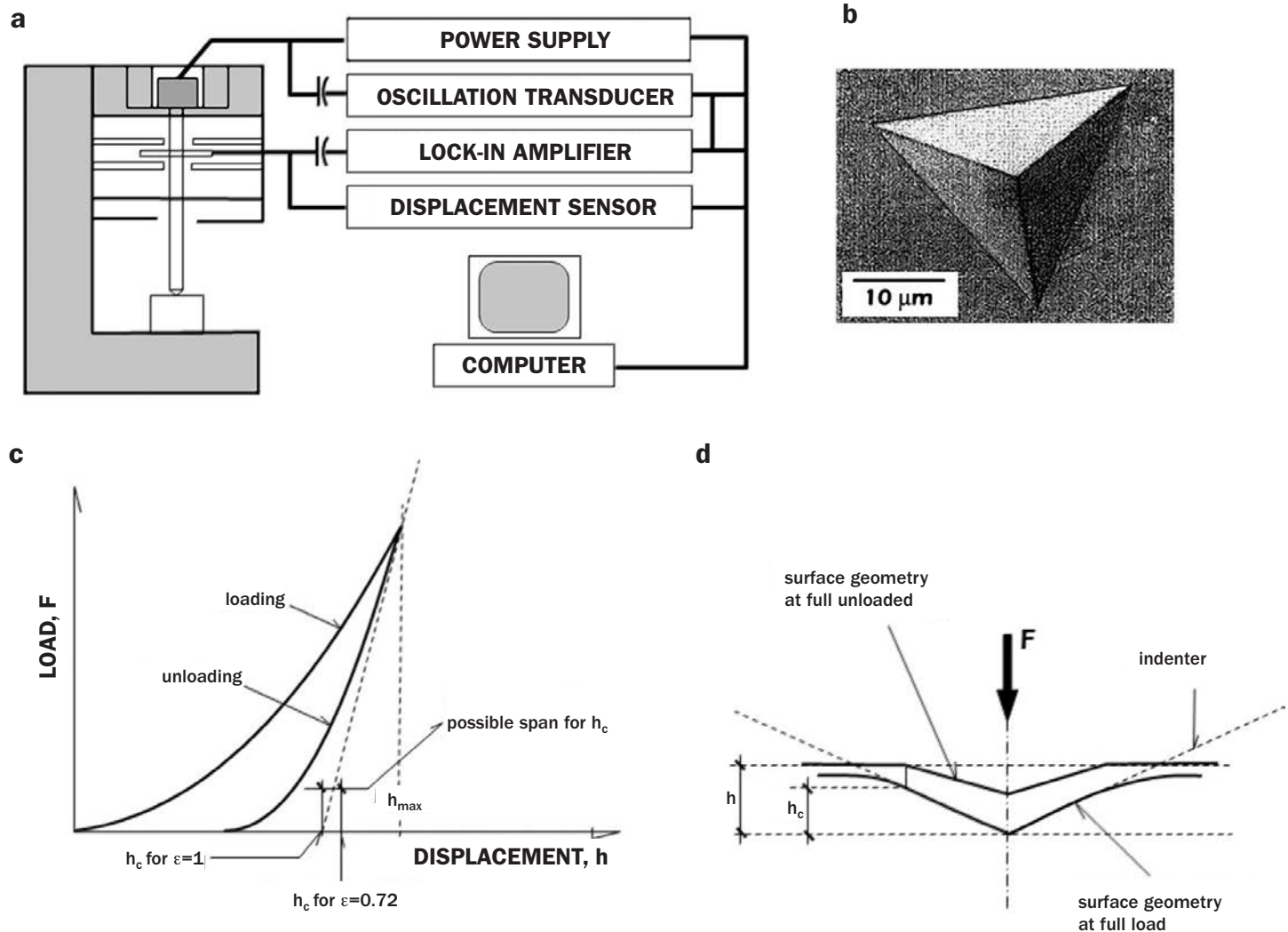


Fig. 2.18. Nanoindentation tests.

a. Sketch of a nano-indentation device.

b. Nano-indentation imprint.

c. Load-displacement curve during loading and unloading.

d. Indentation profiles under load and after load removal.

The stiffness S , (see figure 2.18c), can be calculated from the following expression (Oliver and Pharr, 1992):

$$S = \frac{dF}{dh} = \frac{2}{\sqrt{\pi}} E_r A^{1/2} \quad (2.2.2-19)$$

where E_r is the reduced modulus of the specimen-indenter combination, which can be approximated by (Dorener and Nix, 1986):

$$\frac{1}{E_r} = \frac{1-\nu_i^2}{E_i} + \frac{1-\nu_m^2}{E_m} \quad (2.2.2-20)$$

where ν and E are the Poisson's ratio and the elastic modulus and the subindices i and m correspond to the indenter and specimen, respectively.

More accurate results can be obtained by means of dynamic indentation tests in which a small harmonically oscillating force is superimposed and the displacement of the indenter and the phase angle between the force and displacement are recorded continuously (see, for example, Oliver and Pharr, 1992).

The mechanical properties of biological materials are investigated, more and more, using nano-indentation techniques due to the difficulty in producing conventional test pieces. However, biological materials are far removed from exhibiting the elasto-plastic characteristics of the materials that underpinned the development of first generation indentation tests, so it is not possible to extrapolate those procedures to these new materials whose responses to indentation depend upon time and other variables; temperature, load rate, humidity, or load and deformation history. The article by Oyen and Cook (2009) contains a critical review of the use of nano-indenters on biological materials.

The next stage in the development of nano-indenters was the use of the tip of the cantilever in the atomic force microscope. The device was developed to obtain representations of the topological surface of samples but, if operated in the axial mode (perpendicular to the surface) instead of the tangential mode (or sweep, as initially), it could be used to nano-indent the surface of the specimen and to investigate the mechanical performance at the nanometric scale (Tang and Ngan, 2011). In these tests the arrow on the cantilever tip and the displacement of the support (as indicated in figure 2.19) are recorded, which allows the force F exerted by the point to be determined and a relationship between it and the penetration, d , into the sample to be calculated. In order to interpret these results

the Hertzian elastic contact model which relates F and d to the (plane strain) elastic modulus of the sample is usually employed, that is:

$$F = a \cdot E d^2 \quad (2.2.2-20)$$

where a is a constant which depends upon the geometry of the indenter (Daza et al. 2015). Since the majority of biological materials exhibit visco-elasto-plastic behaviour, the values of E are only indicative but can be used to compare diverse materials or for the control of the same material.

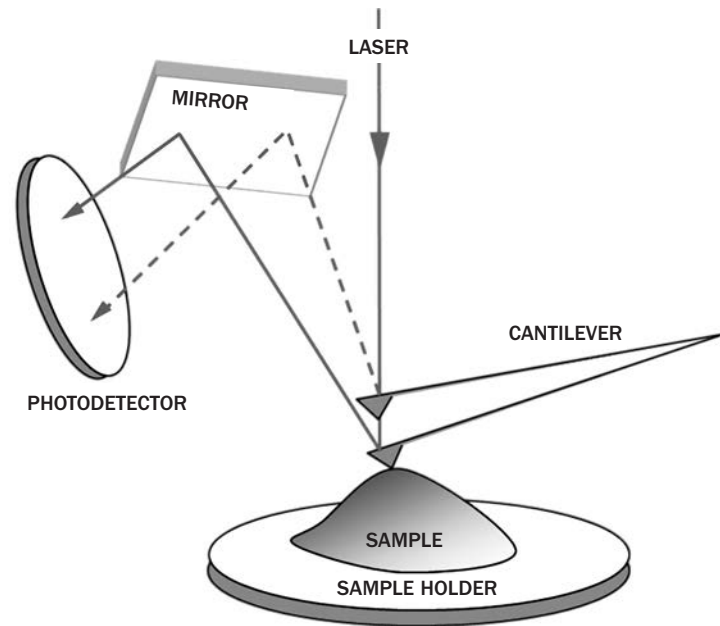


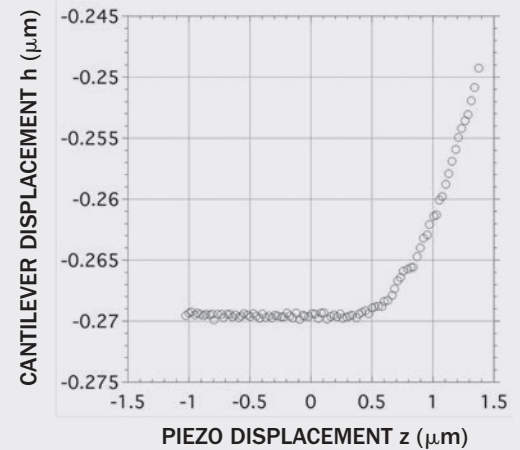
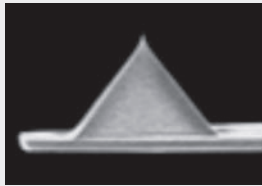
Fig. 2.19. Schematic representation of a nano-indentation device based on the atomic force microscope (AFM).

Some of the difficulties which emerge when trying to measure the stiffness of visco-elasto-plastic materials, such as the variation of the modulus with load-rate, can be overcome by measuring the instantaneous modulus during the application of a sudden load (ideally, a step load). This is the rate-jump procedure proposed by Tang and Ngan (2011). Essentially, instead of loading the specimen under a constant rate of displacement, it is applied rapidly so that the load increases rapidly as well. The aforementioned authors claim that by adopting this procedure stiffness values of the material are obtained which are more representative of the material according to Chan and Ngan (2010) (see, for example, a study performed on cells. Zhou et al. 2012).

EXERCISE 13

The figure shows the indentation curve for a murine leukocyte, using an AFM (Daza et al., 2015). The recorded data correspond to the displacement of the cantilever tip as a function of the sample movement produced by a piezoelectric actuator.

Calculate the stiffness (or the elastic modulus) of the leukocyte assuming the simplified linear-elastic Hertzian contact model.

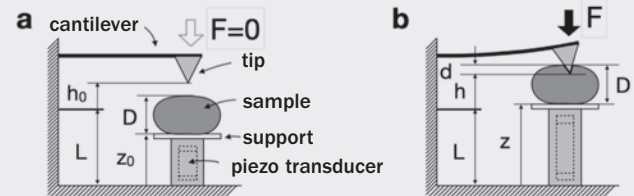
**DATA:**

Four-sided silicon nitride pyramid indenter; semi-angle $\theta = 39^\circ$

Cantilever $200 \mu\text{m}$ (long) $\times 20 \mu\text{m}$ (wide) $\times 0.4 \mu\text{m}$ (thick); elastic constant $k_C = 0.05 \text{ N/m}$

SOLUTION:

Sketches of the operation of the atomic force microscope are shown in figures a) and b). The sample support is displaced by means of a piezoelectric actuator, by an amount z in the vertical direction. The interaction between the sample and the indenter flexes the cantilever, producing a tip deflection h . Observe that the reference points for the measurements of h and z are different.



Since the sample is deformable, the following relationship between the displacements of the sample (z), cantilever tip (h) and the resulting indentation (d) is obtained:

$$d = z + D - h - L$$

where D is the sample size and L the difference between the references for z and h .

The relationship between the force F exerted by the point and its displacement h is linear and governed by the flexure of the cantilever, which can be written as:

$$F = \begin{cases} k_C(h - h_0) & \text{si } h \geq h_0 \\ 0 & \text{si } h < h_0 \end{cases}$$

where k_C is the elastic constant of the cantilever.

If the pyramidal indenter is much more rigid than the sample –which is almost always the case with biological specimens– the penetration d is small and the sample can be modelled as a linear elastic half-space, the relationship between the applied force F and the penetration d can be approximated by the expression (Rico et al., 2005):

$$F = \frac{1}{\sqrt{2}} \frac{E \tan \theta}{(1 - \nu^2)} d^2 = k_s d^2$$

where θ is the semi-angle of the indenter, and E and ν are the elastic modulus and Poisson's ration of the sample, respectively.

Combining the three previous equations to eliminate F and d we obtain a quadratic equation in h :

$$k_C(h - h_0) = k_S[z + D - h - L]^2$$

which can be solved to yield:

$$h = z + D - L + \frac{k_C}{2k_S} - \sqrt{\left(z + D - L - h_0\right) \frac{k_C}{k_S} + \frac{1}{4} \left(\frac{k_C}{k_S}\right)^2}$$

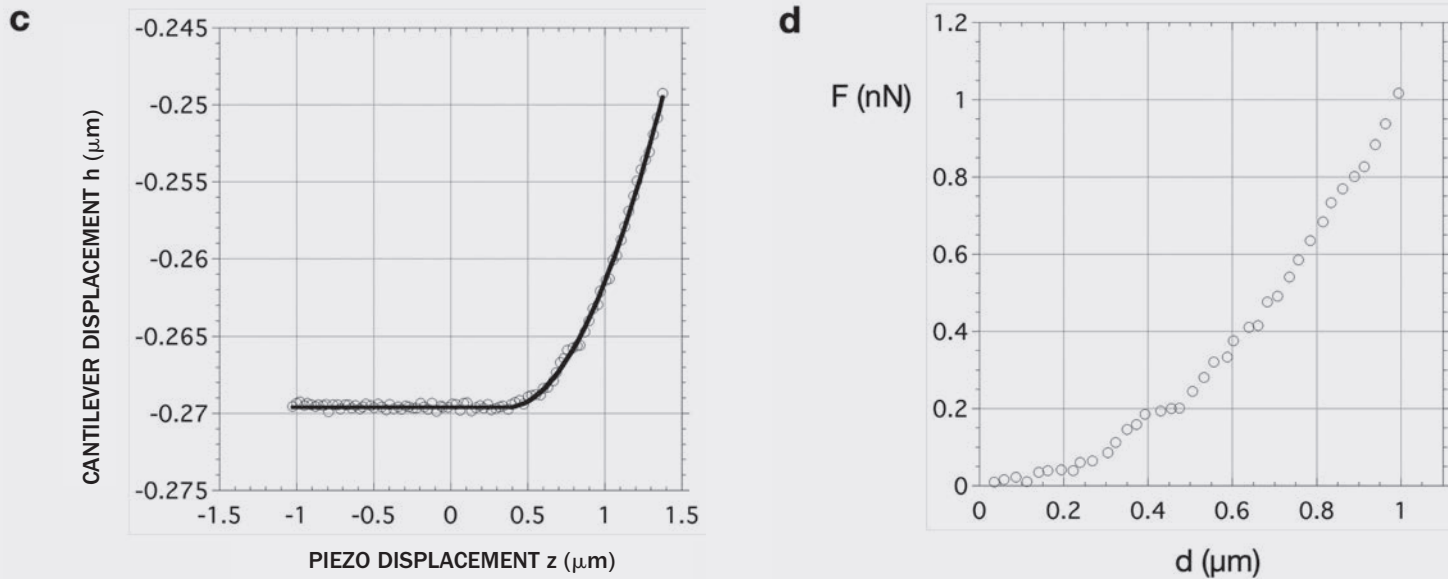
The sign (of the square root) in the above equation has been determined by taking into account that when $z + D - L = h_0$ then $h = h_0$. In this equation $k_C = 0.05 \text{ N/m}$, and the term h_0 is deduced from the constant horizontal section of the experimental graph, when the cantilever has not yet come into contact with the sample ($h_0 = -0.2696 \mu\text{m}$) (see figure c).

The values $D - L$ and k_S are unknown, but can be obtained by fitting with the experimental data (note that it is not possible the determine D and L separately).

Figure c) shows the curve fit, which yields the parameters $D - L = -0.6297 \mu\text{m}$ and $k_S = 1015 \text{ N/m}^2$. With this last value, and assuming that the Poisson's ratio $\nu = 0.5$ for lymphocytes, (since they contain high concentrations of water, it may be assumed that deformation occurs under constant volume) we finally arrive at the Rico et al. expression for the elastic modulus:

$$E = \frac{\sqrt{2}(1 - \nu^2)}{\tan \theta} k_S = 1329 \text{ Pa}$$

Figure d) shows the force-penetration curve obtained with the above values



Indentation techniques for measuring fracture toughness

Techniques for measuring fracture toughness based on indentation were developed possibly because of the difficulties encountered with brittle materials, such as ceramics. Measurement of the fracture toughness of these materials, following the traditional procedures, is not easy because, in many cases, it is difficult to introduce the starter crack without breaking the specimen, and if notched specimens (no crack) are used they are not reliable. For these reasons, techniques based on measuring cracks induced by a diamond-tipped indenter are attractive because they are easy and do not need elaborate equipment. The success achieved with ceramic materials has led to its application with hard biological materials but its reliability, for the moment, is limited for reasons which will be set out below.

Indentation techniques for measuring the fracture toughness of ceramic materials are described in depth in Chapter 8 of Lawn's book (B. Lawn, 1993). In essence, it is assumed that the material behaviour is ideal brittle-elastic and that cracks are created due the stresses produced during unloading of the indenter. The expression obtained for the fracture toughness, K_C , is:

$$K_C = \alpha \sqrt{\frac{E}{H}} \frac{F}{c^{3/2}} \quad (2.2.2-21)$$

where F is the applied force, E the elastic modulus, H the hardness (Vickers, is the most common), and c the trace of the semi-circular crack (see figure 2.20). α is an empirical constant which lies between 0.016 ± 0.004 (B. Lawn, 1993).

Ritchie and co-workers (Kruzic et al. 2009) have published a critical review of indentation techniques for measuring fracture toughness, in particular when applied to hard biological materials, and conclude that they are not reliable for obtaining absolute values but can be useful for comparative purposes. Their arguments are based on the fact that biological materials are composites with soft organic components which can undermine the hypothesis upon which the techniques that were developed for ceramic materials were based. The also drew attention to the possible formation of spurious cracks which could originate during the drying of samples, particularly if they are examined in an electron microscope. Another issue to bear in mind is that some biological materials exhibit an increase in fracture toughness during crack growth (an R -curve), again, this effect is not detectable in an indentation test.

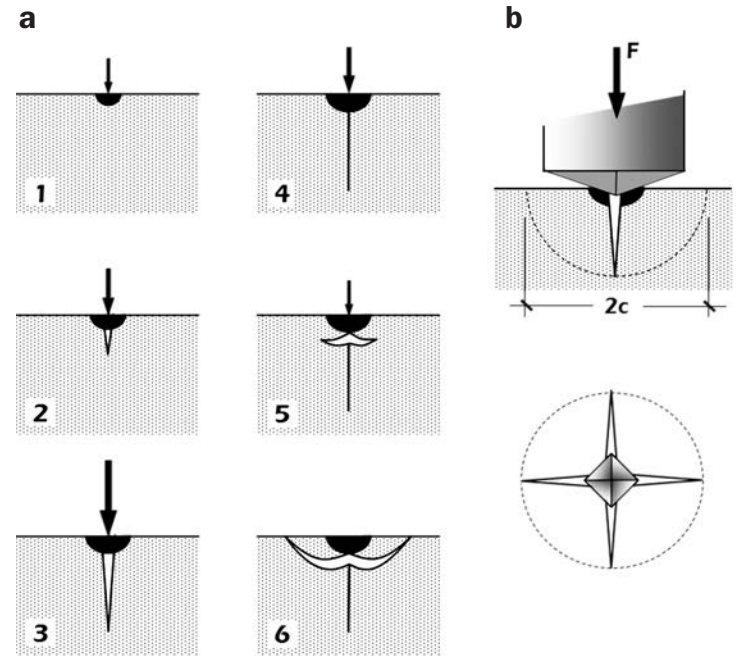


Fig. 2.20. Cracks created by indentation.

a. Evolution during a cycle of loading (+) and unloading (-). The dark zones denote regions in which the deformation is irreversible.
b. Trace of the semi-circular crack.

Indentation of laminas and thin films; stiffness and hardness

The main difficulty with the indentation of thin laminas is to avoid contamination of the results, due to the properties of the substrate. The most common approach to addressing this problem is to restrict the depth of the indentation to less than one tenth of the lamina thickness, though this treatment has no firm physical basis (Hay et al. 1998).

For laminas of a certain stiffness it is possible to justify an analogous expression to the cited above by considering the stiffness S in the nanoscopic domain, that is:

$$\frac{dF}{dh} = \frac{2}{\sqrt{\pi}} E_{ef} A^{1/2} \quad (2.2.2-22)$$

where F , h and A have the same meaning as before and E_{ef} is an effective modulus.

King, 1987 has proposed the following expression for the effective modulus:

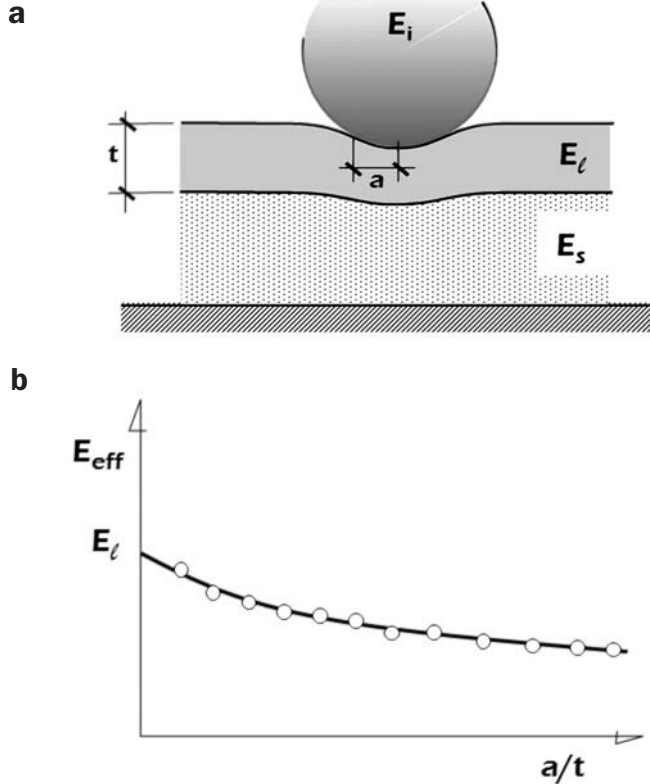
$$\frac{1}{E_{ef}} = \frac{1 - \exp(-\alpha t A^{-1/2})}{E_l^*} + \frac{\exp(-\alpha t A^{-1/2})}{E_s^*} + \frac{1}{E_i^*} \quad (2.2.2-23)$$

where t , is the thickness of the lamina, α an empirical constant, and E_l^* , E_s^* and E_i^* are the plane strain elastic moduli, for the lamina, the substrate and the indenter (see figure 2.21a).

Another expression for the effective modulus is that proposed by Gao et al. (1992),

$$E_{ef} = E_s + (E_l - E_s) I(a/t, \nu) \quad (2.2.2-24)$$

where I is a function of the lamina thickness, t , the radius of contact a and the Poisson's ratio ν of the lamina. This function tends to zero as t becomes vanishingly small and tends to 1 as t tends to infinity.



A practical means of obtaining the elastic modulus of the lamina E_l , consists of carrying out several measurements for different values of penetration (h or a) and extrapolating the results back to the origin, as indicated in figure 2.21b.

Measurement of the hardness of a lamina presents the same difficulties and uncertainties as mentioned above. The most commonly used expression is analogous to that of the effective modulus, that is to say, an effective hardness, H_{ef} is defined by means of the following expression.

$$H_{ef} = H_s + (H_l - H_s) B(h/t, E_s/E_l, \sigma_{c,s}/\sigma_{c,l}, \nu) \quad (2.2.2-25)$$

where B is now a function of h/t , the relative depth of the indentation, and $\sigma_{c,s}/\sigma_{c,l}$ is the ratio of the yield stresses of the substrate and the lamina, respectively.

For soft laminas on a rigid substrate, Bhattacharga and Nix (1988) have proposed the following expression for B :

$$B = \exp \left[- \frac{\sigma_{c,l}}{\sigma_{c,s}} \frac{E_s}{E_l} \left(\frac{h}{t} \right)^2 \right] \quad (2.2.2-26)$$

As yet there are no sufficiently general expressions for soft or hard laminas on hard or soft substrates. The rule of one tenth of the thickness is the most used, although finite element modelling suggests that for soft laminas on hard substrates the maximum value of h/t can be relaxed to about 0.3.

Fig. 2.21. a. Schematic representation of the indentation of a lamina on a substrate.

b. Obtaining the elastic modulus of a lamina by extrapolation (for geometrically similar indenters)

EXERCISE 14

Estimate the fracture toughness of human enamel for the data in Exercise 12.

SOLUTION:

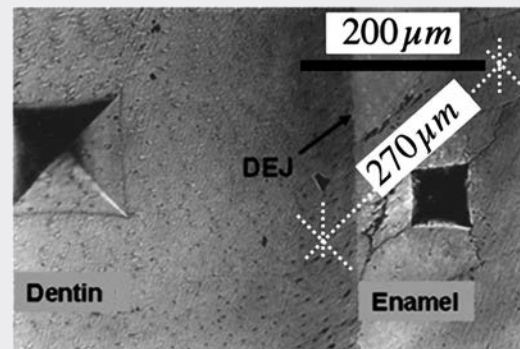
We see that in the micrograph indentation of the enamel has produced a diagonal crack. Even though its size cannot be determined with sufficient precision, we can try to bound the length of the crack $2c$ (see figure 2.19) as

$$2c \geq 270 \mu\text{m}$$

Using equation 2.2.2-21 we obtain

$$K_C = \alpha \sqrt{\frac{E}{H}} \frac{F}{c^{3/2}} \leq 0.016 \sqrt{\frac{50}{2.27}} \frac{9.81 \text{ N}}{(135 \mu\text{m})^{3/2}} = 0.47 \text{ MPa}\sqrt{\text{m}}$$

This value is slightly below the range quoted by other authors who tested this material (0.7 to 1.5 MPa $\sqrt{\text{m}}$).



2.3. MECHANICAL BEHAVIOUR

2.3.1. Introduction

The information obtained from tensile, compression, torsion, flexure, fracture or indentation tests is valuable for characterising the mechanical behaviour of bulk biological materials (those in which all three dimensions are significant). In practice, the number of such materials that are amenable to modelling today is quite small and restricted to biological materials that deform little and behave essentially elastically; mollusc shells, bones or wood, for example. However, this does not prevent a small incursion being made, in this text, into the visco-elasto-plastic regime when, later, cartilage is considered.

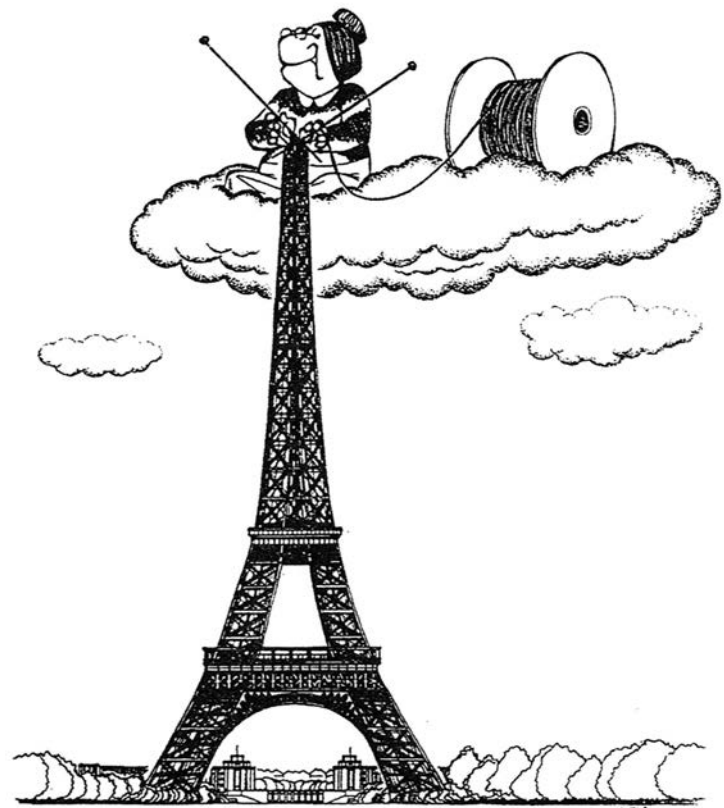
Even though it is possible to formulate the constitutive equations for materials undergoing large deformations with inelastic behaviour and which, also, depend upon the load history, the reasons that the study is limited to the cited materials is because the associated mathematical complexity and the large number of parameters necessary to fit the models make them impractical and, often, of dubious predictive capacity.

Another issue to consider in the modelling of these materials is the hierarchical structure. Predicting the mechanical behaviour of biological materials is like predicting the behaviour of a large structure –a bridge or a skyscraper– from the properties of their structural components –steel and concrete– and their structural geometry. For this reason emphasis has been placed, in this book, on the behaviour of basic biological materials, since predictions of the mechanical behaviour of hierarchical biological materials is increasingly a structural analysis problem, which is beyond the scope of this book.

For the reasons mentioned above, only the essential basic three-dimensional elasticity concepts are summarised in this section, as a complement to the ideas introduced in the earlier studies of fibres (one-dimensional situations) and membranes and laminas (two-dimensional treatments).

Within the field of homogeneous materials it is worth dwelling on those which have a cellular structure due to their appearance in several biological materials.

In order to account for the heterogeneity of some materials, a brief incursion is also made into the field of composite materials.



¿Material or structure? (With permission of G. Jeronimidis in Structural Biological Materials, M. Elices Ed.)

2.3.2. Homogeneous materials¹²

The aim of this section is to summarise the most common expressions that relate the stresses and strains in a three-dimensional homogenous material which experiences small strains and displacements¹³ and which behaves elastically. The detailed development of these concepts is beyond the scope of this book, for this the interested reader may find it helpful to consult, for example, the Landau and Lifshitz (1986) book on elasticity.

The infinitesimal strain tensor in three-dimensions is a generalisation of the two-dimensional concept introduced in the “Biological Membranes” book (Equation 23), where, now $i = 1, 2, 3$. That is

$$\boldsymbol{\varepsilon} = \frac{1}{2} \left[\frac{\partial \mathbf{u}}{\partial \mathbf{X}} + \left(\frac{\partial \mathbf{u}}{\partial \mathbf{X}} \right)^T \right] \quad \text{or} \quad \varepsilon_{ij} = \frac{1}{2} \left[\frac{\partial u_i}{\partial X_j} + \frac{\partial u_j}{\partial X_i} \right] \quad (2.3.2-1)$$

where \mathbf{u} is the displacement of a material point initially located at reference position \mathbf{X} (see section 2.2.2 of the “Biological Membranes” book and Figure 18).

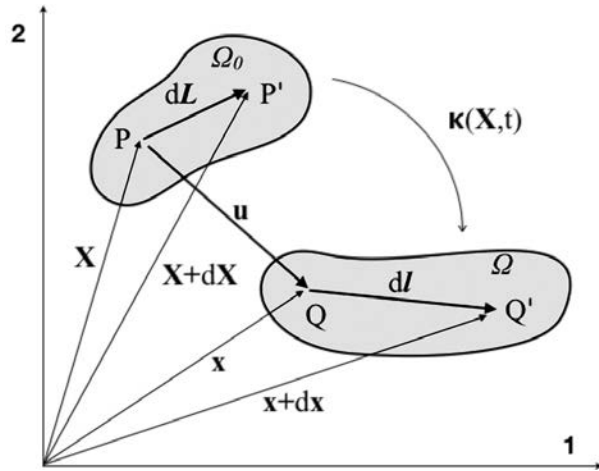


Fig. 18. Notation used in the reference Ω_0 and deformed Ω configurations.

In order to simplify the notation in what follows we shall use Einstein's summation convention in which a repeated index indicates the sum of the terms over all possible values of the index¹⁴.

Note that the **strain tensor** is symmetrical and, therefore, has six independent components. Note also that since the

displacements and strains are very small (ideally infinitesimal) the previous equation can be equally written using the values of the deformed position \mathbf{x} , or the reference position \mathbf{X} .

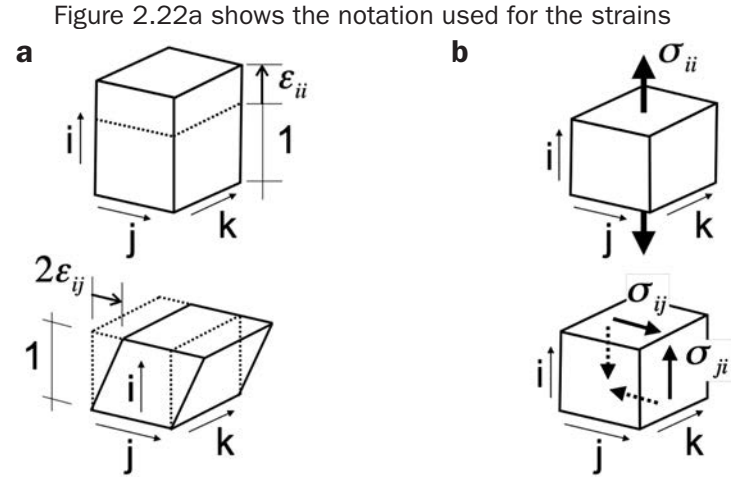


Fig. 2.22 a. Notation employed for strains.
b. Notation employed for stresses.

The **stress tensor** σ_{ij} is also a generalisation of that which was defined in the “Biological Membranes” book (section 2.2.2, Equation 25). The tensor is symmetrical and, therefore, has only six independent components. Figure 2.22b shows the notation used.

Equilibrium of an elemental cube now obeys the following equations

$$\begin{aligned} \frac{\partial \sigma_{11}}{\partial x_1} + \frac{\partial \sigma_{21}}{\partial x_2} + \frac{\partial \sigma_{31}}{\partial x_3} + \rho g_1 &= 0 \\ \frac{\partial \sigma_{12}}{\partial x_1} + \frac{\partial \sigma_{22}}{\partial x_2} + \frac{\partial \sigma_{32}}{\partial x_3} + \rho g_2 &= 0 \\ \frac{\partial \sigma_{13}}{\partial x_1} + \frac{\partial \sigma_{23}}{\partial x_2} + \frac{\partial \sigma_{33}}{\partial x_3} + \rho g_3 &= 0 \end{aligned} \quad (2.3.2-2)$$

which –using the Einstein convention– can be written in the compact form

$$\frac{\partial \sigma_{ij}}{\partial x_i} + \rho g_j = 0 \quad (2.3.2-3)$$

with $i = 1, 2, 3$. g_i are the components of the gravitational acceleration and ρ is the density.

¹² A material is homogeneous if the material properties are the same at every point.

¹³ Even if a body undergoes small strains the displacements may not always be small. An example is the bending of a very long cantilever beam. Although the strains in each section of the beam are small, the accumulated movement at the end of the beam can be so large that the change in shape of the beam must be incorporated into the analysis. This case is known as geometrically nonlinear and leads to nonlinear behaviour of the structure even when the material is perfectly linear-elastic.

¹⁴ e.g. $e_{ii} = e_{11} + e_{22} + e_{33}$ if $i = 1, 2, 3$.

The constitutive equations for the situation under consideration –small strains and elastic behaviour– are relatively simple. Using the first law of thermodynamics we can establish that the variation of the internal energy per unit volume will be equal to the heat gained less the work done by the internal stresses. For a reversible process the amount of heat is TdS , where T is the absolute temperature and S is the entropy per unit volume. The work per unit volume is given by $-\sigma_{ij}d\epsilon_{ij}$. Therefore:

$$dU = TdS + \sigma_{ij}d\epsilon_{ij} \quad (2.3.2-4)$$

If a material is subjected only to a uniform pressure p and the effects of gravity can be ignored, the equilibrium forces on the boundary leads to internal hydrostatic stresses $\sigma = -p \mathbf{1}$ (or $\sigma_{ij} = -p\delta_{ij}$). Under these conditions the work per unit volume is $-\sigma_{ij}d\epsilon_{ij} = -p d\epsilon_{ii} = -p d(tr\epsilon)$. Observing that $d(tr\epsilon) = dV/V$ is the elemental change suffered by a unit volume (see exercise 17), Equation (2.3.2-4) takes on the more familiar form of the first law of thermodynamics for hydrostatic systems (p, T, V):

$$dU = TdS - pdV \quad (2.3.2-5)$$

Taking as independent variables the entropy and the strains (S, ϵ_{ij}), we can write dU as

$$dU = \left(\frac{\partial U}{\partial S} \right)_{\epsilon_{ij}} dS + \left(\frac{\partial U}{\partial \epsilon_{ij}} \right)_S d\epsilon_{ij} \quad (2.3.2-6)$$

which, comparing to Equation (2.3.2-4), leads to

$$\sigma_{ij} = \left(\frac{\partial U}{\partial \epsilon_{ij}} \right)_S \quad (2.3.2-7)$$

an equation which allows calculation of the stress tensor from the internal energy per unit volume of the material, expressed as a function of the entropy and the strains $U(S, \epsilon_{ij})$.

If, instead of using the internal energy U , the free energy per unit volume, $F = U - TS$, is introduced into Equation (2.3.2-4), the following is obtained

$$dF = -SdT + \sigma_{ij}d\epsilon_{ij} \quad (2.3.2-8)$$

and now taking F as a function of the temperature and the strains $F(T, \epsilon_{ij})$, we arrive at

$$\sigma_{ij} = \left(\frac{\partial F}{\partial \epsilon_{ij}} \right)_T \quad (2.3.2-9)$$

which allows calculation of the stresses if $F(T, \epsilon_{ij})$ is known.

EXERCISE 15

Calculate the infinitesimal strains in a homogeneous bar which undergoes a uniform extension along its axis and a narrowing, also uniform, of its diameter, preserving its volume.

SOLUTION:

The situation described is shown in the Figure. The bar, with initial dimensions (L, R) , is deformed homogeneously until it has dimensions $(L+\Delta L, R+\Delta R)$, complying with $L R^2 = (L+\Delta L) (R+\Delta R)^2$.

The movement of a point \mathbf{X} is given by

$$\mathbf{x} = X_1 \frac{R+\Delta R}{R} \hat{\mathbf{e}}_1 + X_2 \frac{R+\Delta R}{R} \hat{\mathbf{e}}_2 + X_3 \frac{L+\Delta L}{L} \hat{\mathbf{e}}_3$$

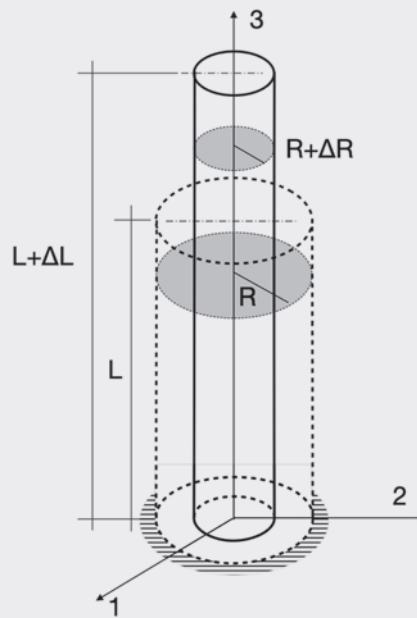
and its displacement \mathbf{u} will be

$$\mathbf{u} = \mathbf{x} - \mathbf{X} = X_1 \frac{\Delta R}{R} \hat{\mathbf{e}}_1 + X_2 \frac{\Delta R}{R} \hat{\mathbf{e}}_2 + X_3 \frac{\Delta L}{L} \hat{\mathbf{e}}_3$$

Applying Equation (2.3.2-1) we obtain

$$\begin{aligned} \varepsilon_{11} = \varepsilon_{22} &= \frac{\Delta R}{R}, \quad \varepsilon_{33} = \frac{\Delta L}{L} \\ \varepsilon_{12} = \varepsilon_{21} = \varepsilon_{13} = \varepsilon_{31} = \varepsilon_{23} = \varepsilon_{32} &= 0 \end{aligned}$$

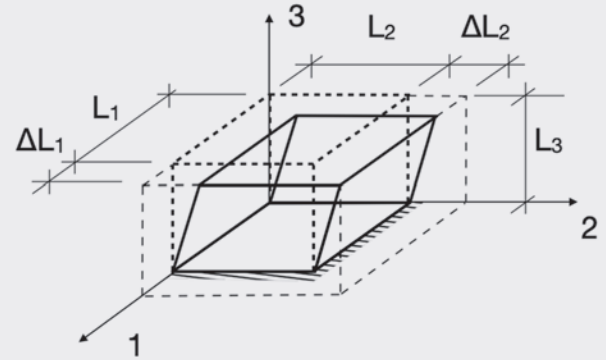
We see that the only strains are the normal strains ε_{11} , ε_{22} , and ε_{33} , which have the simple physical interpretation of being the ratio increase in length to the initial length, as illustrated in Figure 2.22.



EXERCISE 16

Calculate the infinitesimal strains in a homogenous prism subjected to a displacement of its upper face, which is parallel to the (12) plane, as indicated in the Figure.

Assume that all points are displaced only horizontally and uniformly.

**SOLUTION:**

The movement of the points in the body can be represented by

$$\mathbf{x} = \left(X_1 + \Delta L_1 \frac{X_3}{L_3} \right) \hat{\mathbf{e}}_1 + \left(X_2 + \Delta L_2 \frac{X_3}{L_3} \right) \hat{\mathbf{e}}_2 + X_3 \hat{\mathbf{e}}_3$$

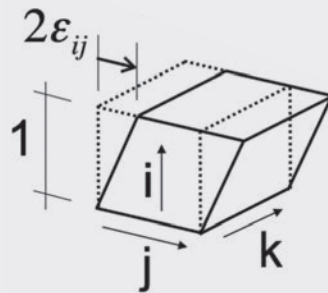
The displacement \mathbf{u} is

$$\mathbf{u} = \mathbf{x} - \mathbf{X} = \Delta L_1 \frac{X_3}{L_3} \hat{\mathbf{e}}_1 + \Delta L_2 \frac{X_3}{L_3} \hat{\mathbf{e}}_2$$

Applying Equation (2.3.2-1) we obtain

$$\begin{aligned} \varepsilon_{11} = \varepsilon_{22} = \varepsilon_{33} &= 0 \\ \varepsilon_{12} = \varepsilon_{21} &= 0, \quad \varepsilon_{13} = \varepsilon_{31} = \frac{\Delta L_1}{2L_3}, \quad \varepsilon_{23} = \varepsilon_{32} = \frac{\Delta L_2}{2L_3} \end{aligned}$$

in which we show that the shear strains ε_{13} and ε_{23} correspond to half the angle of distortion of the dihedral of the faces, as shown in Figure 2.22.



EXERCISE 17

Show that the unit change in volume at a point during the deformation can be calculated by the trace of the strain tensor. Apply the result to Exercises 15 and 16.

SOLUTION:

Given a point in the material, consider, without loss of generality, the special directions in which the strain tensor ε at this point is diagonal (every symmetric tensor such as the strain tensor can always be diagonalised). This means that we take the principal axes (1, 2, 3) as coordinate directions of the strain tensor at that point. Therefore $\varepsilon_{ij} = 0$, $i \neq j$ and also

$$\varepsilon = \frac{1}{2} \left[\frac{\partial \mathbf{u}}{\partial \mathbf{X}} + \left(\frac{\partial \mathbf{u}}{\partial \mathbf{X}} \right)^T \right] = \frac{\partial \mathbf{u}}{\partial \mathbf{X}} \quad \text{or} \quad \varepsilon_{ij} = \frac{1}{2} \left[\frac{\partial u_i}{\partial X_j} + \frac{\partial u_j}{\partial X_i} \right] = \frac{\partial u_i}{\partial X_j}$$

as deduced from Equation (2.3.2-1).

The displacement of a material point \mathbf{u} is given by $\mathbf{u} = \mathbf{x} - \mathbf{X}$ where \mathbf{x} is the deformed position and \mathbf{X} that of the reference. An elemental vector, $d\mathbf{X}$ is transformed into another, $d\mathbf{x}$ given by $d\mathbf{x} = d\mathbf{u} + d\mathbf{X}$ or $dx_i = du_i + dX_i$ which, making use of the strain tensor, we can write as

$$d\mathbf{x} = \frac{\partial \mathbf{u}}{\partial \mathbf{X}} d\mathbf{X} + d\mathbf{X} = (\mathbf{1} + \varepsilon) d\mathbf{X} \quad \text{or} \quad dx_i = \frac{\partial u_i}{\partial X_j} dX_j + dX_i = (\delta_{ij} + \varepsilon_{ij}) dX_j$$

where $\mathbf{1}$ is the three-dimensional unit tensor and δ_{ij} is the Kronecker delta ($\delta_{ij} = 0$, $i \neq j$; $\delta_{ij} = 1$, $i=j$).

We now consider three vectors $d\mathbf{A}$, $d\mathbf{B}$ and $d\mathbf{C}$ parallel, respectively, to the three coordinate axes, which define a cuboid of volume $dV = dA dB dC$. These vectors are transformed into vectors $d\mathbf{a}$, $d\mathbf{b}$ and $d\mathbf{c}$ according to the above expression:

$$d\mathbf{a} = (1 + \varepsilon_{11}) d\mathbf{A} \quad , \quad d\mathbf{b} = (1 + \varepsilon_{22}) d\mathbf{B} \quad , \quad d\mathbf{c} = (1 + \varepsilon_{33}) d\mathbf{C}$$

We see that since ε is a diagonal tensor, each transformed vector will be parallel to the initial vector and, therefore, the deformed figure will also be a cuboid of volume dv

$$dv = da db dc = (1 + \varepsilon_{11}) dA (1 + \varepsilon_{22}) dB (1 + \varepsilon_{33}) dC = dV (1 + \varepsilon_{11} + \varepsilon_{22} + \varepsilon_{33} + \varepsilon_{11}\varepsilon_{22} + \varepsilon_{11}\varepsilon_{33} + \varepsilon_{22}\varepsilon_{33} + \varepsilon_{11}\varepsilon_{22}\varepsilon_{33})$$

Neglecting second and higher order terms, (by considering small strains) we calculate the unit volumetric strain as:

$$\frac{dv - dV}{dV} = \varepsilon_{11} + \varepsilon_{22} + \varepsilon_{33} = \text{tr} \varepsilon$$

which is independent of the axes we take for ε , the trace being a tensor invariant.

In the case of **Exercise 15** we see that the trace of the strain tensor is

$$\varepsilon_{11} + \varepsilon_{22} + \varepsilon_{33} = \frac{2\Delta R}{R} + \frac{\Delta L}{L}$$

For the conditions set out we know that $LR^2 = (L + \Delta L)(R + \Delta R)^2$, an expression that we can expand

$$LR^2 = LR^2 + L(\Delta R)^2 + 2LR\Delta R + \Delta L R^2 + \Delta L(\Delta R)^2 + 2\Delta L R \Delta R \approx LR^2 + 2LR\Delta R + \Delta L R^2$$

since ΔL and ΔR are small. From this equation we deduce that $2\Delta R/R = -\Delta L/L$ with which we show that $\text{tr}(\varepsilon) = 0$.

The strains calculated in **Exercise 16** yield $\text{tr}(\varepsilon) = 0$, which indicates that the volume remains constant. The same result is obtained by observing that the deformed figure is an oblique prism of volume $L_1 L_2 L_3$. Note that, whatever the material, a movement without normal stresses such as that described does not produce a change in volume.

Isotropic materials¹⁵

If it is assumed that the *temperature remains constant* and that *initially there are no residual stresses*, the free energy per unit volume, for an isotropic and homogeneous material, can be expressed up to second order terms in ε_{ij} by (Landau, 1986)

$$F = F_0 + \frac{1}{2} \lambda (\varepsilon_{kk})^2 + G \varepsilon_{ij} \varepsilon_{ij} \quad (2.3.2-10)$$

since F cannot depend upon the orientation of the axes in which we express ε_{ij} and, therefore, must be function only of the invariants of ε . The symbols λ and G are the Lamé coefficients.

In Exercise 17 it was shown that during deformation the unit variation of volume is given by $tr \varepsilon = \varepsilon_{ii}$. When $tr \varepsilon = 0$ there is no change in volume and the shape of the material is only a distortion during deformation. This state is denoted *pure shear*. Equation (2.3.2-10) shows that, in this case, the constant term F_0 corresponds to the strain-free state, furthermore, there is a term due to the distortion. The corresponding coefficient G , is given the name *modulus of rigidity or shear modulus*.

In the contrary case, when there are no shear stresses ($\varepsilon_{ij} = 0, i \neq j$) the material maintains its shape but changes size. The state is called *hydrostatic tension (or compression)*.

It should be observed that the states refer to particular points in the material, and can change from one point to another. When the strain is the same at every point in the material it is said that the body is subjected to a *homogeneous* deformation.

Taking into account these concepts, any deformation can be written as the sum of hydrostatic and a pure shear strain components. For this, it is sufficient to consider the identity:

$$\varepsilon_{ij} = \left(\varepsilon_{ij} - \frac{1}{3} \varepsilon_{kk} \delta_{ij} \right) + \frac{1}{3} \varepsilon_{kk} \delta_{ij}$$

or

$$\varepsilon = \left[\varepsilon - \frac{1}{3} (tr \varepsilon) \mathbf{1} \right] + \frac{1}{3} (tr \varepsilon) \mathbf{1} \quad (2.3.2-11)$$

The first of the two addends corresponds to a pure shear strain, or deviator ε'_{ij}

$$\varepsilon'_{ij} = \varepsilon_{ij} - \frac{1}{3} \varepsilon_{kk} \delta_{ij} \quad \text{or} \quad \varepsilon' = \varepsilon - \frac{1}{3} (tr \varepsilon) \mathbf{1} \quad (2.3.2-12)$$

since the sum of their diagonal terms (ii) is zero. The second tensor $\varepsilon_{kk} \delta_{ij}/3$ is purely hydrostatic, with no off-diagonal components and proportional to the unity tensor.

Form these expressions, the free energy (Equation 2.3.2-10) can be written separating both types of strain into different terms

$$F = \frac{1}{2} \lambda (\varepsilon_{kk})^2 + G \varepsilon_{ij} \varepsilon_{ij} = \frac{1}{2} K (\varepsilon_{kk})^2 + G \varepsilon'_{ij} \varepsilon'_{ij} \quad (2.3.2-13)$$

We have eliminated, for simplicity, the constant term F_0 which, as will be seen later, does not affect the relationship between stress and strain. The constant K is called the *bulk, compressibility or hydrostatic modulus* and G is, as before, the shear or modulus of rigidity. It can be shown that $K = \lambda + 2G/3$.

The **relationship between stress and strain** is obtained from Equation (2.3.2-9) by differentiating F :

$$\sigma_{ij} = K \varepsilon_{kk} \delta_{ij} + 2G \varepsilon'_{ij} = K \varepsilon_{kk} \delta_{ij} + 2G \left(\varepsilon_{ij} - \frac{1}{3} \varepsilon_{kk} \delta_{ij} \right) \quad (2.3.2-14)$$

or, in vector form

$$\sigma = K (tr \varepsilon) \mathbf{1} + 2G \varepsilon' = K (tr \varepsilon) \mathbf{1} + 2G \left(\varepsilon - \frac{1}{3} (tr \varepsilon) \mathbf{1} \right) \quad (2.3.2-15)$$

We see that the stress tensor is also decomposed into a hydrostatic stress tensor σ_h , responsible for the volumetric strain (relative change in volume), which can be characterised by a pressure $p = -K \varepsilon_{kk}$

$$\sigma_{h,ij} = K \varepsilon_{kk} \delta_{ij} = -p \delta_{ij} \quad \text{or} \quad \sigma_h = K (tr \varepsilon) \mathbf{1} = -p \mathbf{1} \quad (2.3.2-16)$$

to which is added a pure shear tensor, called the deviatoric stress tensor σ' , which does not give rise to a change in volume

$$\sigma'_{ij} = 2G \varepsilon'_{ij} = 2G \left(\varepsilon_{ij} - \frac{1}{3} \varepsilon_{kk} \delta_{ij} \right)$$

or

$$\sigma' = 2G \varepsilon' = 2G \left(\varepsilon - \frac{1}{3} (tr \varepsilon) \mathbf{1} \right) \quad (2.3.2-17)$$

Equation (2.3.2-16) shows that K , the bulk modulus, measures the relationship between the applied pressure relative change in volume of the material when it is compressed, therefore

$$K = -\frac{p}{\varepsilon_{kk}} = -\frac{p}{(\Delta V / V_0)} \quad (2.3.2-18)$$

since ε_{kk} is the unitary change in volume, as was shown in Exercise 17. An incompressible material will have an infinite value of K .

¹⁵ A material is isotropic when its properties do not depend upon the direction in which it is examined.

The **inverse relationship between the strain and stresses** is

$$\varepsilon_{ij} = \frac{\sigma_{kk}\delta_{ij}}{9K} + \frac{\sigma'_{ij}}{2G} = \frac{\sigma_{kk}\delta_{ij}}{9K} + \frac{1}{2G} \left(\sigma_{ij} - \frac{1}{3}\sigma_{kk}\delta_{ij} \right) \quad (2.3.2-19)$$

These results show that there is a linear relationship between the strain tensors ε_{ij} and the stress tensors σ_{ij} . Or, in other words, that the strain is proportional to the applied forces. This conclusion, valid only for small strains, is given the name *Hooke's Law*.

Another, more common, form of writing Equations (2.3.2-14) and (2.3.2-19) is:

$$\sigma_{ij} = \frac{E}{1+\nu} \left(\varepsilon_{ij} + \frac{\nu}{1-2\nu} \varepsilon_{kk}\delta_{ij} \right) \quad (2.3.2-20)$$

and

$$\varepsilon_{ij} = \frac{1}{E} \left[(1+\nu)\sigma_{ij} - \nu\sigma_{kk}\delta_{ij} \right] \quad (2.3.2-21)$$

where E is the *elastic modulus* and ν is the *Poisson's ratio*, parameters related to K and G by means of the expressions

$$E = \frac{9KG}{3K+G} \quad (2.3.2-22)$$

and

$$\nu = \frac{1}{2} \frac{3K-2G}{3K+G} \quad (2.3.2-23)$$

The reader is invited to revise section 2.3.2 of the “Biological Fibres” book for a better interpretation of the physical meaning of the parameters E , G and ν .

EXERCISE 18

From Equations (2.3.2-20 and 2.3.2-21) write expressions for σ_{ij} and ε_{ij} ($i, j = 1, 2, 3$). Apply the result to the constrained compression test and the uniaxial tensile test.

SOLUTION:

The stresses are obtained from Equation (2.3.2-20) when the volumetric strain $\varepsilon_{kk} = \varepsilon_{11} + \varepsilon_{22} + \varepsilon_{33}$ and taking into account the properties of the Kronecker delta function δ_{ij}

$$\sigma_{11} = \frac{E}{1+\nu} \left[\varepsilon_{11} + \frac{\nu}{1-2\nu} (\varepsilon_{11} + \varepsilon_{22} + \varepsilon_{33}) \right] = \frac{E}{(1+\nu)(1-2\nu)} [\varepsilon_{11}(1-\nu) + \nu(\varepsilon_{22} + \varepsilon_{33})]$$

$$\sigma_{22} = \frac{E}{(1+\nu)(1-2\nu)} [\varepsilon_{22}(1-\nu) + \nu(\varepsilon_{11} + \varepsilon_{33})]$$

$$\sigma_{33} = \frac{E}{(1+\nu)(1-2\nu)} [\varepsilon_{33}(1-\nu) + \nu(\varepsilon_{11} + \varepsilon_{22})]$$

$$\sigma_{12} = \sigma_{21} = \frac{E}{1+\nu} \varepsilon_{12} \quad , \quad \sigma_{13} = \sigma_{31} = \frac{E}{1+\nu} \varepsilon_{13} \quad , \quad \sigma_{23} = \sigma_{32} = \frac{E}{1+\nu} \varepsilon_{23}$$

expressions in which we have made use of the symmetry of the stress and strain tensors.

In order to obtain the strains we proceed in a similar manner using Equation (2.3.2-21)

$$\varepsilon_{11} = \frac{1}{E} [\sigma_{11} - \nu(\sigma_{22} + \sigma_{33})]$$

$$\varepsilon_{22} = \frac{1}{E} [\sigma_{22} - \nu(\sigma_{11} + \sigma_{33})]$$

$$\varepsilon_{33} = \frac{1}{E} [\sigma_{33} - \nu(\sigma_{11} + \sigma_{22})]$$

$$\varepsilon_{12} = \varepsilon_{21} = \frac{(1+\nu)}{E} \sigma_{12} \quad , \quad \varepsilon_{13} = \varepsilon_{31} = \frac{(1+\nu)}{E} \sigma_{13} \quad , \quad \varepsilon_{23} = \varepsilon_{32} = \frac{(1+\nu)}{E} \sigma_{23}$$

In a **constrained compression** test all of the strains are zero except for that in the direction of the loading axis. If the compression is applied in the 1-direction, the stress state is obtained from the previous expressions for the stresses by making all of the strains zero except ε_{11} , that is:

$$\sigma_{11} = \frac{E(1-\nu)}{(1+\nu)(1-2\nu)} \varepsilon_{11}$$

$$\sigma_{22} = \sigma_{33} = \frac{\nu E}{(1+\nu)(1-2\nu)} \varepsilon_{11} = \frac{\nu}{1+\nu} \sigma_{11}$$

$$\sigma_{12} = \sigma_{21} = \sigma_{13} = \sigma_{31} = \sigma_{23} = \sigma_{32} = 0$$

From these expressions it is easy to obtain the aggregate modulus H_A for the constrained compression test, already calculated in Exercise 3. The ratio of the stress and strain becomes: $\sigma_{11}/\varepsilon_{11} = H_A = E(1-\nu)/[(1+\nu)(1-2\nu)]$.

In the case of a **uniaxial tensile test** in the 1-direction, the only stress acting is σ_{11} and we can calculate the strains as:

$$\varepsilon_{11} = \frac{\sigma_{11}}{E}$$

$$\varepsilon_{22} = \varepsilon_{33} = \frac{-\nu}{E} \sigma_{11} = -\nu \varepsilon_{11}$$

$$\varepsilon_{12} = \varepsilon_{21} = \varepsilon_{13} = \varepsilon_{31} = \varepsilon_{23} = \varepsilon_{32} = 0$$

We see that the ratio of the applied stress and the strain in the loading direction is $\sigma_{11}/\varepsilon_{11} = E$, the elastic modulus of the material. We also note that the ratio of the strain in the direction perpendicular to the loading direction and that in the loading direction is $-\nu$, the value of the Poisson's ratio with the sign changed.

EXERCISE 19

Derive the expressions (2.3.2-22) and (2.3.2-23) and discuss the conditions under which it is possible to consider that the deformation of the material occurs without change in volume (an incompressible material).

SOLUTION:

From Equation (2.3.2-20) we obtain

$$\sigma_{ij} = \frac{E}{1+\nu} \varepsilon_{ij} + \frac{E\nu}{(1+\nu)(1-2\nu)} \varepsilon_{kk} \delta_{ij}$$

which compared to Equation (2.3.2-14) yields the identities

$$2G = \frac{E}{1+\nu} \quad \text{and} \quad K - \frac{2G}{3} = \frac{E\nu}{(1+\nu)(1-2\nu)}$$

from which expressions (2.3.2-22) and (2.3.2-23) may be readily deduced

$$E = \frac{9KG}{3K+G} \quad \text{and} \quad \nu = \frac{1}{2} \frac{3K-2G}{3K+G}$$

and with which we can also write the inverse relationships

$$G = \frac{E}{2(1+\nu)} \quad \text{and} \quad K = \frac{E}{3(1-2\nu)}$$

Looking at the above equations it is interesting to reflect upon the concept of incompressibility of a material, and the criteria which allow us to assume that a particular material maintains its volume (that is to say, it is incompressible) during any deformation process. All of this uses a very simple approximation, the hypothesis of linear-elastic behaviour.

Strictly speaking, taking the value of the bulk modulus K as the criterion, no real material is incompressible (K would have to be infinite, according to Equation (2.3.2-18)) and, even less so, biological materials with elevated water content. The bulk modulus of water $K_{agua} \approx 2 \text{ GPa}$ is much less than that of steel (160 GPa) or cortical bone (15 GPa), and similar to that of polymers (2 to 4 GPa).

However, the assumption of incompressibility is common, and often taken as a given for many biological materials, including tissues with moderate amounts of water such as bone.

By measuring the Poisson's ratio ν –s– if it is known– we can estimate accurately the degree of incompressibility of a material, since from Equations (2.3.2-21) we see that when $\nu = 1/2$

$$\varepsilon_{kk} = \varepsilon_{11} + \varepsilon_{22} + \varepsilon_{33} = \frac{1}{E} \left[\left(1 + \frac{1}{2} \right) \sigma_{kk} - \frac{1}{2} 3\sigma_{kk} \right] = 0$$

always and the volumetric strain is zero, no matter what the state of stress. This, as we have seen, is a state of pure shear in which only the deviatoric strains ε' exist.

Given that the experimental determination of ν is not easy in biological materials, it is more practical to measure parameters like E and G (see chapters 2.3.2 of the “Biological Fibres” book and 2.2.1 in this volume). From the equations developed in the Exercise above we can see that $E/G = 2(1 + \nu)$.

For $\nu = 1/2$ the previous expression leads to $E = 3G$. This is the maximum possible value of the elastic modulus which satisfies the relationship

$$0 < E < 3G$$

since $-1 < \nu < 1/2$, as was shown in section 2.3.2 of the “Biological Fibres” book.

The closer the value of E gets to $3G$ the more incompressible the material and the volume is conserved to a greater degree during deformation.

In the case of soft biological materials –constituted to a large part by water, between 70 and 90%– then G is much reduced. (Ideal fluids –inviscid– offer no resistance to shear stress and in these $G = 0$. Soft materials, as a function of their degree of hydration, have a behaviour similar to viscous fluids, in which G may also be small if the speed of the application of the shear stress is reduced). The average values of different biological materials, even in the case of tissue such as cortical bone (~20% water), it has been shown that this hypothesis is reasonably correct (Cowin and Dotv. 2007).

Alternatively, it is possible to assess the incompressibility of a material by means of the ratio G/K , which is directly related to the ratio of the shear and the volumetric strains. In this case Equation (2.3.2-23) provides the relationship between the Poisson’s ratio ν and G/K

$$\nu = \frac{1}{2} \frac{3K - 2G}{3K + G} = \frac{1}{2} \frac{3 - 2G/K}{3 + G/K}$$

In this we see that when $G/K = 0$ then $\nu = 1/2$. From Equation (2.3.2-22) we also see that, in this case, $E = 3G$. For a ratio $G/K = 1/30$ then $\nu \approx 0.48$ and $E \approx 2.97G$.

Note that in order to establish the degree of incompressibility of a material in no case is it possible to consider the value of E (or of K) in isolation, since the shear stresses –which do not produce a change in volume, unlike the normal strains– are determined by the shear modulus G of the material, as was shown in Equation (2.3.2-19).

Anisotropic materials

When the material is no longer isotropic, but still linear elastic, the problem is complicated. If the process is isothermal and there are no residual stresses initially the free energy per unit volume F for small strains can be approximated by a quadratic function of the strain tensor, but instead of having two coefficients there are many more. In general, the free energy will be of the form

$$F = \frac{1}{2} \lambda_{ijkl} \varepsilon_{ij} \varepsilon_{kl} \quad (2.3.2-24)$$

According to Equation (2.3.2-9), the stress tensor σ_{ij} will be given by,

$$\sigma_{ij} = \frac{\partial F}{\partial \varepsilon_{ij}} = \frac{1}{2} \lambda_{ijkl} \varepsilon_{kl} + \frac{1}{2} \lambda_{klij} \varepsilon_{kl} = C_{ijkl} \varepsilon_{kl} \quad (2.3.2-25)$$

where $C_{ijkl} = (\lambda_{ijkl} + \lambda_{klij})/2$ is a second order symmetric tensor, called the **elastic modulus tensor**.

In principle, the tensor C_{ijkl} , which relates the nine components of stress to the nine components of strain, will have 81 constants. The symmetry condition which we have noted reduces the number of independent constants to 45. On the other hand, the symmetry of the stress tensor ($\sigma_{ij} = \sigma_{ji}$) leads to $C_{ijkl} = C_{jikl}$ and that of the strain tensor ($\varepsilon_{ij} = \varepsilon_{ji}$) to $C_{ijkl} = C_{jilk}$, leaving only 21 truly independent constants.

It is often more convenient to represent the six independent tensor components σ_{ij} and ε_{ik} as vectors (Voigt notation). In this form, the elastic modulus tensor is represented as a second order 6×6 tensor C_{ij} which relates the vectors $[\sigma_{11}, \sigma_{22}, \sigma_{33}, \sigma_{23}, \sigma_{31}, \sigma_{12}]$ and $[\varepsilon_{11}, \varepsilon_{22}, \varepsilon_{33}, \varepsilon_{23}, \varepsilon_{31}, \varepsilon_{12}]$. Since it is symmetric, the maximum number of independent components is 21.

These relationships are set out in Figure 2.23 for the case of general anisotropy (21 independent constants), for an orthotropic material (9 independent constants), for a transversely isotropic material (5 independent constants), and for an isotropic material (2 independent constants).

An **orthotropic** material is one which has three orthogonal planes of symmetry; the expression in Figure 2.23 refers to the three axes formed by the intersection of said planes.

Symmetry with respect to the plane $x_1 = 0$ implies that states of symmetric loading with respect to this plane such as σ_{11} , σ_{22} , σ_{33} or σ_{23} cannot provoke unsymmetric strains with respect to the same, like the strains ε_{31} or ε_{12} . Therefore, $C_{15} = C_{16} = C_{25} = C_{26} = C_{35} = C_{36} = C_{45} = C_{46} = 0$. Proceeding in a similar manner with planes of symmetry $x_2 = 0$ and $x_3 = 0$ we see that also $C_{14} = C_{24} = C_{34} = C_{56} = 0$, resulting in the 9-coefficient matrix of Figure 2.23.

A **transversely isotropic** material is one in which every point has a plane in which the behaviour is isotropic, that is to say, one in which the properties are the same in any direction in the plane. In Figure 2.23, the plane $x_3 = 0$ is taken as the plane of isotropy. Every direction contained within this plane will have identical properties, so that the axes 1 and 2, and consequently the indices 1 and 2 are interchangeable. With that we see that $C_{11} = C_{22}$, $C_{13} = C_{23}$ and $C_{44} = C_{55}$. Furthermore, any state of pure shear strain $\varepsilon_{12} = \gamma/2$ in the plane of isotropy must be equivalent to the sum of a state of traction $\varepsilon_{11} = \gamma/2$ together with another perpendicular compression $\varepsilon_{22} = \gamma/2$ (see the first exercise in section 2.3.2 of the book "Biological Fibres") so that $C_{66} = (C_{11} - C_{12})/2$ and only 5 independent constants remain.

The case of extreme symmetry occurs when the material is **isotropic** and every plane is a plane of symmetry. In this case all of the directional indices are interchangeable so that $C_{13} = C_{12}$, $C_{33} = C_{11}$ and $C_{44} = (C_{11} - C_{12})/2$ resulting in only 2 independent constants.

The inverse relationship between the stresses and strains is $\varepsilon_{ij} = S_{ijkl} \sigma_{kl}$ where $[S_{ijkl}]$ is known as the **elastic flexibility tensor** and which can be obtained by inverting Equation (2.3.2-25). Using the Voigt notation, we can also write $\varepsilon_i = S_{ij} \sigma_j$ ($i = 1, 6$), and the tensor $\mathbf{S} = [S_{ij}]$ is obtained by inverting the tensor $\mathbf{C} = [C_{ij}]$ shown in Figure 2.23. Except in cases of isotropy and transverse isotropy, this operation is not simple. In any case, the symmetry conditions are still valid for \mathbf{S} , whose structure will be identical to that shown in Figure 2.23 for \mathbf{C} , with the exception that now the diagonal term $S_{66} = S_{11} - S_{12}$, and similarly the terms S_{44} , S_{55} and S_{66} of the isotropic material are equal to $S_{11} - S_{12}$.

GENERAL ANISOTROPY (21 constants)									
σ_{11}	=	C_{11}	C_{12}	C_{13}	C_{14}	C_{15}	C_{16}		ϵ_{11}
σ_{22}		C_{12}	C_{22}	C_{23}	C_{24}	C_{25}	C_{26}		ϵ_{22}
σ_{33}		C_{13}	C_{23}	C_{33}	C_{34}	C_{35}	C_{36}		ϵ_{33}
σ_{23}		C_{14}	C_{24}	C_{34}	C_{44}	C_{45}	C_{46}		ϵ_{23}
σ_{31}		C_{15}	C_{25}	C_{35}	C_{45}	C_{55}	C_{56}		ϵ_{31}
σ_{12}		C_{16}	C_{26}	C_{36}	C_{46}	C_{56}	C_{66}		ϵ_{12}
ORTHOTROPIC (9 constants)									
σ_{11}	=	C_{11}	C_{12}	C_{13}	0	0	0		ϵ_{11}
σ_{22}		C_{12}	C_{22}	C_{23}	0	0	0		ϵ_{22}
σ_{33}		C_{13}	C_{23}	C_{33}	0	0	0		ϵ_{33}
σ_{23}		0	0	0	C_{44}	0	0		ϵ_{23}
σ_{31}		0	0	0	0	C_{55}	0		ϵ_{31}
σ_{12}		0	0	0	0	0	C_{66}		ϵ_{12}
TRANSVERSELY ISOTROPIC (5 constants)									
σ_{11}	=	C_{11}	C_{12}	C_{13}	0	0	0		ϵ_{11}
σ_{22}		C_{12}	C_{22}	C_{23}	0	0	0		ϵ_{22}
σ_{33}		C_{13}	C_{23}	C_{33}	0	0	0		ϵ_{33}
σ_{23}		0	0	0	C_{44}	0	0		ϵ_{23}
σ_{31}		0	0	0	0	C_{44}	0		ϵ_{31}
σ_{12}		0	0	0	0	0	$(C_{11} - C_{12})/2$		ϵ_{12}
ISOTROPIC (2 constants)									
σ_{11}	=	C_{11}	C_{12}	C_{12}	0	0	0		ϵ_{11}
σ_{22}		C_{12}	C_{11}	C_{12}	0	0	0		ϵ_{22}
σ_{33}		C_{13}	C_{12}	C_{11}	0	0	0		ϵ_{33}
σ_{23}		0	0	0	$(C_{11} - C_{12})/2$	0	0		ϵ_{23}
σ_{31}		0	0	0	0	$(C_{11} - C_{12})/2$	0		ϵ_{31}
σ_{12}		0	0	0	0	0	$(C_{11} - C_{12})/2$		ϵ_{12}

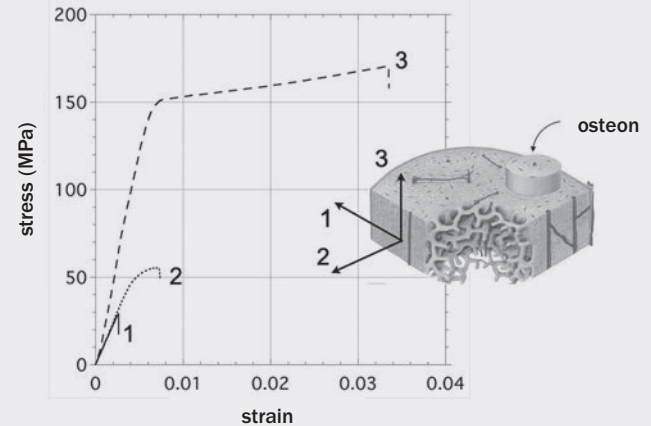
Fig. 2.23 Second order (6 x6) elastic modulus tensors C_{ij} for various classes of material..

EXERCISE 20

a) Cortical bone is a material which responds very differently depending upon the direction of the applied loading, as will be discussed in detail later in section 3.3. The Figure, taken from that section, contains three curves from uniaxial tensile tests performed on bovine cortical bone specimens, orientated in the radial (1), circumferential (2) and axial (3) directions. Discuss the applicability of the linear elastic model to this material.

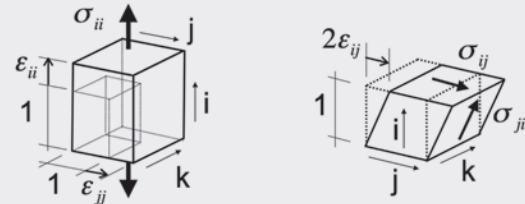
b) Measurements of the elastic modulus and Poisson's ratio performed by Knets and Malmeister (1977) on human cortical bone (tibia) are shown in the Table.

Assuming that the linear elastic model is applicable discuss which type of material (orthotropic, transversely isotropic or isotropic) best fits the experimental data.



E_1	E_2	E_3	G_{12}	G_{31}	G_{23}	ν_{12}	ν_{13}	ν_{23}
6.91	8.51	18.4	2.41	3.56	4.91	0.49	0.12	0.14
E, G (GPa)			directions: (1) radial, (2) circumferential, (3) axial					

$$E_i = \frac{\sigma_{ii}}{\varepsilon_{ii}} \quad \nu_{ij} = -\frac{\varepsilon_{ij}}{\varepsilon_{ii}} \quad G_{ij} = \frac{\sigma_{ij}}{2\varepsilon_{ij}}$$

**SOLUTION:**

a) We observe from the curves in the Figure that cortical bone exhibits an initially very linear stress-strain response, practically up to the value of the yield stress in all of them. In this linear zone it is possible to establish a proportionality between the stresses and strains.

On the other hand, the strains at which the yield stress is reached are very low, between 0.0026 and 0.006 depending upon the measurement direction, which implies that mechanical functioning of the bone will always be within the zone of very small strains, as is required by the theory of linear elasticity. In the “Biological Fibres” book we show that the relative error introduced by using the engineering rather than the true stress (first Exercise in section 2.2.1) is of the order of half of the maximum strain achieved which, in the worst case, becomes $0.006/2 = 0.3\%$. Another way of arriving at the same result is to estimate the values of the second order terms (proportional to the square of the strain), which can be neglected in the linear elastic approximation. In our case we see that $0.006^2 = 0.000036$ which is almost three orders of magnitude less than 0.006, and justifies the approximation of infinitesimal strains.

The characteristics that we have discussed (linearity and small strains) are appropriate for hard biological materials. The linear-elastic model may be adequate for characterising their behaviour, provided the effects of temperature are excluded. For this to occur, generally only those situations in which the mechanical load is either very rapid or very slow are considered.

b) Using the moduli E and G and ν values defined in the problem statement, we can write an equation which links the flexibility tensor, the stresses and strains for an **orthotropic** material. When a stress σ_{ij} produces the strains

$$\varepsilon_{ii} = \sigma_{ii}/E_i \quad \text{and} \quad \varepsilon_{jj} = -\nu_{ij}\varepsilon_{ii} = (-\nu_{ij}/E_i)\sigma_{ii}$$

If the applied stress is σ_{ij} then the strains produced are

$$\varepsilon_{ij} = \sigma_{ij}/(2G_{ij})$$

Therefore, bearing in mind that for a linear strain model, when the several stresses act, it is possible to sum the individual strains from each state, we write the complete relationship by means of the flexibility tensor

$$\begin{bmatrix} \varepsilon_{11} \\ \varepsilon_{22} \\ \varepsilon_{33} \\ \varepsilon_{23} \\ \varepsilon_{31} \\ \varepsilon_{12} \end{bmatrix} = \begin{bmatrix} 1/E_1 & -\nu_{21}/E_2 & -\nu_{31}/E_3 & & & \\ -\nu_{12}/E_1 & 1/E_2 & -\nu_{32}/E_3 & & & \\ -\nu_{13}/E_1 & -\nu_{23}/E_2 & 1/E_3 & & & \\ & & & 1/(2G_{23}) & & \\ & & & & 1/(2G_{31}) & \\ & & & & & 1/(2G_{12}) \end{bmatrix} \begin{bmatrix} \sigma_{11} \\ \sigma_{22} \\ \sigma_{33} \\ \sigma_{23} \\ \sigma_{31} \\ \sigma_{12} \end{bmatrix}$$

With the data from the problem statement, all the parameters except ν_{21} , ν_{31} and ν_{32} , can be calculated, noting that the tensor **S** is symmetric, and therefore

$$-\frac{\nu_{21}}{E_2} = -\frac{\nu_{12}}{E_1} \quad -\frac{\nu_{31}}{E_3} = -\frac{\nu_{13}}{E_1} \quad -\frac{\nu_{32}}{E_3} = -\frac{\nu_{23}}{E_2}$$

expressions which lead to values $\nu_{21} = 0.603$, $\nu_{31} = 0.320$ and $\nu_{32} = 0.303$. With these data the orthotropic material model is complete

$$\begin{bmatrix} \varepsilon_{11} \\ \varepsilon_{22} \\ \varepsilon_{33} \\ \varepsilon_{23} \\ \varepsilon_{31} \\ \varepsilon_{12} \end{bmatrix} = \begin{bmatrix} 0.144 & -0.0709^* & -0.0174^* & & & \\ -0.0709 & 0.118 & -0.0165^* & & & \\ -0.0174 & -0.0165 & 0.0543 & & & \\ & & & 0.102 & & \\ & & & & 0.140 & \\ & & & & & 0.207 \end{bmatrix} \begin{bmatrix} \sigma_{11} \\ \sigma_{22} \\ \sigma_{33} \\ \sigma_{23} \\ \sigma_{31} \\ \sigma_{12} \end{bmatrix}$$

with all these coefficients in GPa. The values with (*) correspond to those calculated from the experimental data.

As was seen above, for a material to behave in a **transversely isotropic** manner, it must be the case that

$$\begin{aligned} S_{11} &= S_{22} \quad (0.144 \text{ vs } 0.118) \\ S_{13} &= S_{23} \quad (-0.0174 \text{ vs } -0.0165) \\ S_{44} &= S_{44} \quad (0.102 \text{ vs } 0.140) \\ S_{66} &= S_{11} - S_{12} \quad (0.207 \text{ vs } 0.214) \end{aligned}$$

conditions which, even if not completely satisfied, indicate that the behaviour of bone is close to being that of a transversely isotropic material.

However, it is more difficult to fit the **S** matrix to that of **purely isotropic** behaviour since the requirements are

$$\begin{aligned} S_{11} &= S_{22} = S_{33} \quad (0.144 \text{ vs } 0.118 \text{ vs } 0.0543) \\ S_{13} &= S_{23} = S_{12} \quad (-0.0174 \text{ vs } -0.0165 \text{ vs } -0.0709) \\ S_{44} &= S_{44} = S_{66} = S_{11} - S_{22} \quad (0.102 \text{ vs } 0.140 \text{ vs } 0.207 \text{ vs } 0.214) \end{aligned}$$

conditions that are not satisfied, even approximately.

2.3.3. Heterogeneous materials¹⁶

All biological materials are heterogeneous if observed with sufficiently close detail but, in practice, many of them are treated as if they were homogeneous when making calculations, by considering an **elemental volume** which is sufficiently large for the average value of properties to be representative of the material as a whole. In other words: the heterogeneous material is replaced with a homogenous one whose average properties on the boundaries are identical when considering volume elements of equal or larger size than the elemental volume. Consequently, in the analysis, the stresses and strains which are obtained by this method at any point only make sense when they are understood to be average values for these volumes, losing all physical meaning if they are ascribed to regions smaller than the elemental volume. Note that this simplification does not prevent the homogenised material from being anisotropic, as happens in the case of wood or bone, for example.

The study of heterogeneous materials, or composite materials, is interesting because it permits an understanding of the behaviour of both from a knowledge of the components and, even more, the design of new materials with superior properties to each of the separate material components. Nature, through biological materials, demonstrates these aspects continuously; for example, the shells of molluscs –a composite material of aragonite and a polymeric cement– has a strength and toughness far greater than that of its components.

The simplest composite materials consist of two phases; the *matrix*, which may be polymeric, metallic or ceramic, and the *reinforcement*, in the form of particles or fibres, (which, in turn, may also be polymeric, metallic or ceramic). In some cases, one of the phases may be a gas, as occurs in foams and sponges, very interesting materials to which the following chapter is dedicated. The next step in material complexity of composite materials is in their hierarchical structures which, as has been mentioned on many occasions, appear to a greater or lesser extent in all biological materials.

In this chapter the aim is only to summarise some of the useful basic concepts for modelling the mechanical behaviour of the simplest composite materials and which occur in the analysis of biological materials. The purpose of these models is to predict the behaviour of the composites in terms of the constituent properties, the proportion of each of them and, in the more sophisticated models, their geometry. There are numerous books on composite materials, with various levels of sophistication and complexity, for example; Chawla (2012), Christensen (1979) or Capaldi (2012).

An accurate prediction of the mechanical behaviour of composite materials is only possible in very few cases. One of these is the prediction of the elastic modulus for a perfectly aligned continuous fibre reinforced material, from the values of the moduli of the matrix and fibre, provided that both have the same Poisson's ratio. The problem is more complicated when the fibres are not continuous and have distributions of length and orientation. This is also the case for particle reinforced materials where exact solutions are only found for ordered and special particles. Even so, it is often possible to find very simple models –as will be seen later– which permit estimates of the elastic modulus, strength or other parameters of interest.

¹⁶ A material is heterogeneous if its composition, and therefore its properties, vary from point to point

There are two very simple models for predicting the elastic modulus of a material composed of two alternating phases of linear-elastic material which extend throughout the volume. Both models are shown in Figure 2.24 and, to a certain degree, can be considered as two aspects of the same homogenisation model, according to the type of loading (parallel or perpendicular to the laminas).

In the model, the composite material is represented as two joined families of perfectly parallel laminas, and made equivalent to a homogeneous linear-elastic material, analysing their combined response in one direction or another. In this case, the elemental volume must be large enough to contain sufficient laminas to allow averaging the forces.

If the loading is **parallel to the laminas**, as shown in Figure 2.24a, the *strain* will be the same in all of them and it is easy to show that the elastic modulus of the composite material E_c , as a function of the modulus of the matrix E_m , and that of the reinforcement E_f is given by,

$$E_c = E_m v_m + E_f v_f \quad (2.3.3-1)$$

where v_m and v_f are the respective volume fractions of the matrix (one of the lamina families) and the reinforcement (the other family). This result is known as the *Voigt model*, *rule of mixtures*, *two phase parallel model* or the *homogeneous strain model*.

If the loading is **perpendicular to the laminas**, as shown in Figure 2.24b, the stress in them will be the same and it can be shown that the elastic modulus of the composite material will now be given by:

$$\frac{1}{E_c} = \frac{v_m}{E_m} + \frac{v_f}{E_f} \quad (2.3.3-2)$$

This result is known as the Reuss model, the two phases in series model or the homogeneous stress model.

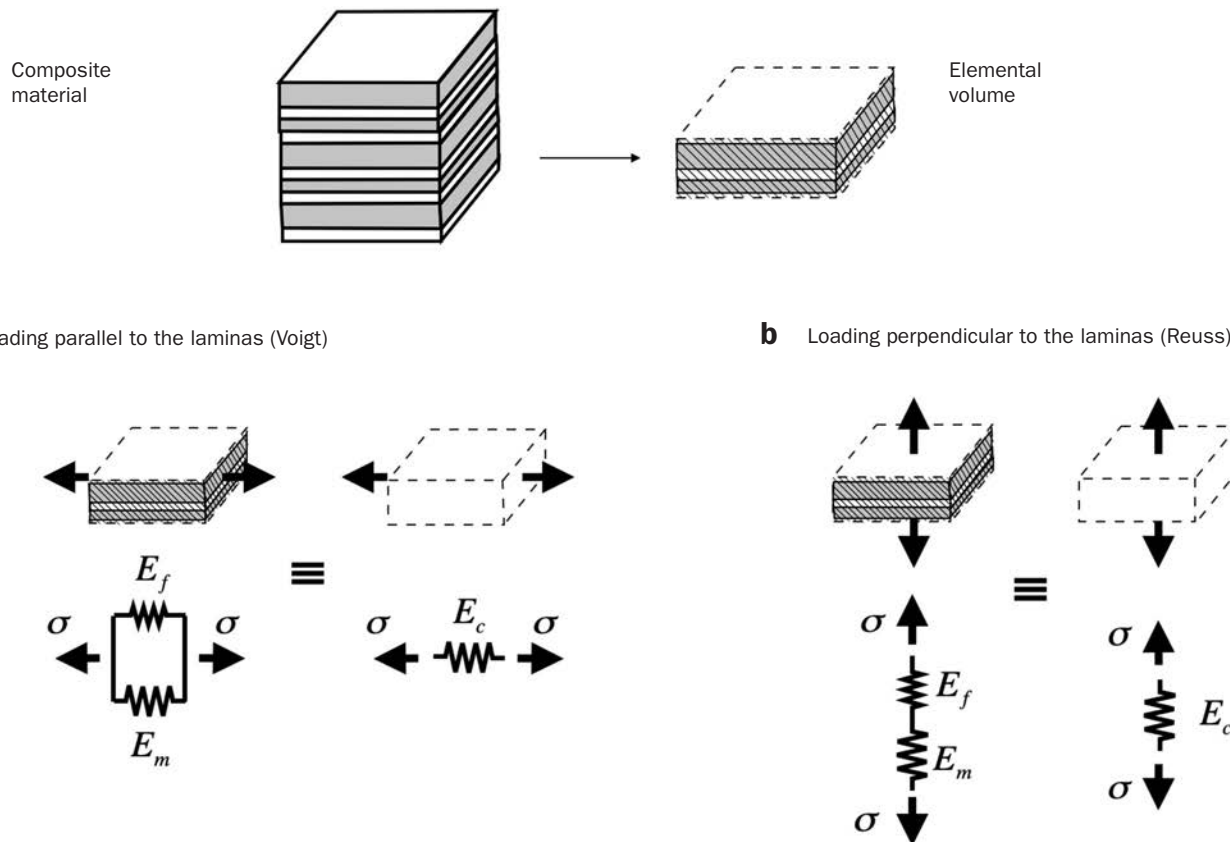


Fig. 2.24 a. Ideal composite material in which the loading is parallel to the laminas (Voigt or parallel model).
b. Ideal composite material in which the loading is perpendicular to the laminas (Reuss or series model).

EXERCISE 21

Derive Equations (2.3.3-1) and (2.3.3-2).

SOLUTION:

Consider, in the first instance, the configuration shown in Figure 2.24a, in which **loading is parallel** to the laminas, and let E_m and E_f be the elastic moduli of the matrix and reinforcement.

The strain in each lamina will be the same, while they are perfectly bonded, having the same length and subjected to the same elongation. Thus we can write $\varepsilon_m = \varepsilon_f$ where ε_m is the strain in any of the matrix laminas and –similarly– ε_f is the strain in the reinforcement laminas.

Treating it as a uniaxial tensile test with linear-elastic behaviour we have that $\varepsilon_m = \frac{\sigma_m}{E_m}$ and $\varepsilon_f = \frac{\sigma_f}{E_f}$ where σ_m and σ_f are the stresses to which the laminas of each component are subjected.

If ε_c , E_c and σ are, respectively, the strain, elastic modulus of the composite material and the stress, it can be shown that $\sigma = E_c \varepsilon_c$

Consequently $\sigma A = \sigma_m A_m + \sigma_f A_f$, where A is the area of the transverse section and A_m and A_f are the total area of those sections corresponding to each phase. Clearly, $A = A_m + A_f$. If we substitute the values of the stresses as functions of the strains in the above equation, observing that for compatibility all of them must be equal, we obtain

$$\varepsilon_c E_c A = \varepsilon_m E_m A_m + \varepsilon_f E_f A_f \quad \rightarrow \quad E_c = E_m \frac{A_m}{A} + E_f \frac{A_f}{A}$$

and then with the configuration in Figure 2.23, the volume fractions of each material can be calculated directly from the ratio of the areas of the transverse sections

$$v_m = \frac{A_m}{A} \quad \text{and} \quad v_f = \frac{A_f}{A}$$

we obtain Equation (2.3.3-1).

In the case of **loading in series**, Figure 2.24b, we must observe that now *the stress in each phase is the same* $\sigma = \sigma_m = \sigma_f$ and, therefore, the strain in each phase and also the combined material will be

$$\varepsilon_m = \frac{\sigma}{E_m} \quad , \quad \varepsilon_f = \frac{\sigma}{E_f} \quad \text{and} \quad \varepsilon_c = \frac{\sigma}{E_c}$$

If each lamina has a thickness L_i and it stretches ΔL_i , its strain ε_i will be $\varepsilon_i = \frac{\Delta L_i}{L_i}$ and the strain in the whole element in the load direction

$$\varepsilon_c = \frac{\Delta L}{L} = \frac{\sigma}{E_c} = \sum \frac{\Delta L_i}{L} = \sum \frac{\Delta L_i}{L_i} \frac{L_i}{L} = \sum \varepsilon_i \frac{L_i}{L} = \sum \frac{\sigma_i}{E_i} \frac{L_i}{L} = \sigma \sum \frac{1}{E_i} \frac{L_i}{L}$$

since the all the stresses are equal to σ .

If we group the terms corresponding to each phase in the above equation, we obtain

$$\varepsilon_c = \frac{\sigma}{E_c} = \sigma \left(\frac{1}{E_m} \frac{L_m}{L} + \frac{1}{E_f} \frac{L_f}{L} \right) \quad \rightarrow \quad \frac{1}{E_c} = \frac{1}{E_m} \frac{L_m}{L} + \frac{1}{E_f} \frac{L_f}{L}$$

in which we have called L_m and L_f the thicknesses of each phase.

From this expression, observing that the volume fraction of each phase can be written as $v_m = \frac{L_m}{L}$ and $v_f = \frac{L_f}{L}$

we recover Equation (2.3.3-2).

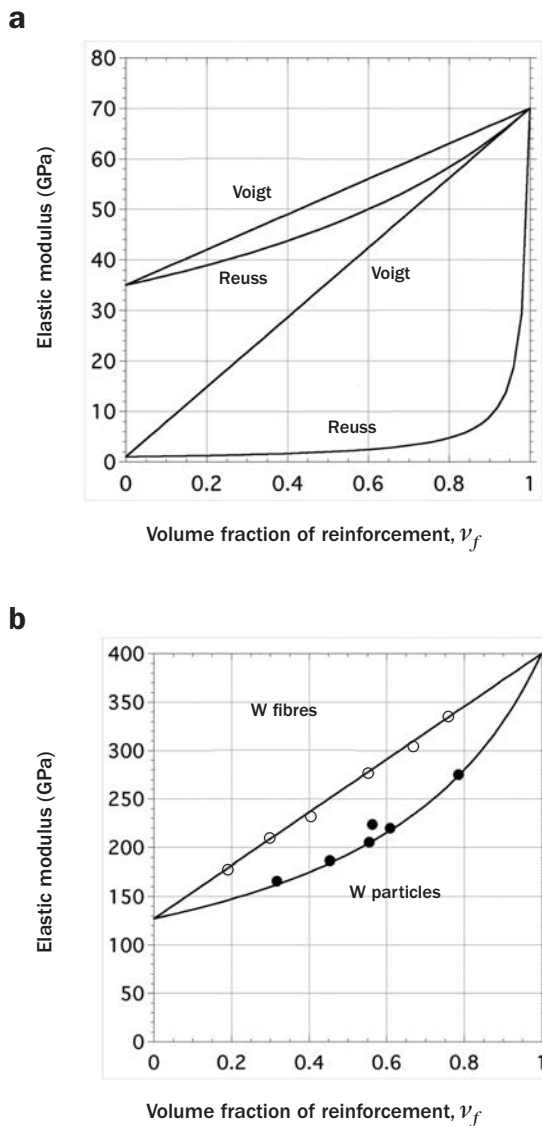


Fig. 2.25 a. Predictions of the elastic modulus of a composite material according to the Voigt and Reuss models for two materials whose moduli (in GPa) are $E_m = 1$, $E_f = 70$ and $E_m = 35$, $E_f = 70$. b. Moduli for two composite materials (W-Cu) ($E_m = 127$ GPa, $E_f = 400$ GPa). In one case the reinforcement is W fibres and in the other W particles (after Weidmann, 1990).

Figure 2.25a contains values of the elastic modulus of a composite material as a function of the volume fraction of reinforcement, according to the Voigt and Reuss models. Two situations have been illustrated; one in which the modulus of the matrix is 35 GPa and the other in which it is 1 GPa, in both cases the modulus of the reinforcement is the same and equal to 70 GPa.

It may be observed that the Voigt model always predicts values greater than those of Reuss and that this difference

is more apparent the greater the difference between the moduli of the two phases. The hypothesis of the Voigt, or homogeneous strain, model appears appropriate for a material reinforced with fibres aligned with the loading direction, while that of Reuss, or homogeneous stress, is better suited to particle reinforced materials. Figure 2.25b illustrates these observations. The results relate to a material composed of a copper matrix reinforced with tungsten fibres, in one case, and tungsten particles in the other. It can be seen that the Voigt model gives very good results for fibre reinforcement and that the Reuss model provides acceptable results for particle reinforcement.

It should be borne in mind that both models are extremely simple, that they are based on a minimum information on both phases (their moduli and volume fractions), and that they make no distinction between the phases. Among other things, they ignore the effects of geometry of the phases, how they are distributed, their Poisson's ratios, the bonding between the reinforcement and the matrix and, particularly for polymer matrices, viscoelastic effects.

The influence of the **orientation of the reinforcement**, whether it be fibres or particles (if they are not spherical), can be accounted for if an assumption is made about the orientation distribution function. One practical way of tackling this problem is by means of the so-called efficiency factor, B , in the rule of mixtures expression, that is

$$E_c = E_m v_m + B E_f v_f \quad (2.3.3-3)$$

where B can take the following values:

$B = 1$ When the fibres are completely aligned and the loading is parallel to them.

$B = 1/2$ When the fibres are arranged in two orthogonal direction and the loading is in one of these directions.

$B = 3/8$ When the fibres are arranged randomly in a plane and the loading lies in this plane.

$B = 1/5$ When the fibres are arranged randomly in three dimensions.

Models of reinforced composite materials are widely used for biological materials since, without loss of generality, it can be said that, at the super-cellular scale, practically any biological material can be considered as a material of this type. So that, for example, wood can be analysed as an amorphous matrix of hemicellulose and lignin reinforced with cellulose fibres, bone as an inorganic hydroxyapatite matrix reinforced with collagen fibres, or soft tissue – blood vessels, cartilage or skin – as glycosaminoglycans matrix reinforced with elastin and collagen fibres.

Unfortunately, except in a few cases such as shells and bones, biomechanical models of fibre reinforced materials are extremely complex, since it is necessary to take into account the large deformations produced, and this is without including the effect of temperature, time or biological variables which modify the composition and the geometry of the tissue.

In section 3.3.3 of the book on Biological Membranes comment is made on some models for blood vessels which take account of the effect of the collagen reinforcing fibres present in tissues. As a simplified example of the modelling of material with long fibres, we present below an application of Lanir's (1979) model to tensile tests on ligaments and tendons, which shows –for the case of long fibre reinforcement– the importance of considering the progressive loading of the reinforcing fibres during the deformation process.

Figure 2.26 shows a very simplified model of tendons and ligaments, in which they are analysed as a mass of collagen fibres subjected to uniaxial tension. The model assumes that all of the fibres are long and not rolled over each other (as in the case of ropes) and reach from one end of the mass to the other. Furthermore, it is assumed that not all of the fibres are orientated and parallel at the start of the deformation, but some possess a degree of laxity, which is progressively lost during the elongation. In the analysis the mechanical contribution of the matrix which bonds the fibres is neglected, considering that its resistance is far lower than these, as well as the interaction between the fibres themselves during deformation.

As can be seen in Figure 2.26, the force required to stretch the mass of fibres depends at any one time upon the number under load. Under these conditions, in order to extend a fibre of relaxed length $L_{i,0}$ (Figure 2.26a) no force is needed until it reaches a length $L_{i,0}$. From this moment the fibre exerts an increasing resistance with the elongation. When, in a similar mass, there are fibres of different relaxed lengths (Figure 2.26b) the effects accumulate, producing a J-shaped force-extension curve, typical of those obtained from tensile tests on soft materials, whose curvature is associated with the process of orientation and regrouping and progressive failure of the fibres which reinforce these materials.

In a more quantitative form, we shall consider the bunch of fibres whose initial relaxed length (without load) is L_0 . When the bunch is deformed under tensile loading its elongation is given by the ratio of the lengths

$$\Lambda = \frac{L}{L_0} \quad (2.3.3-4)$$

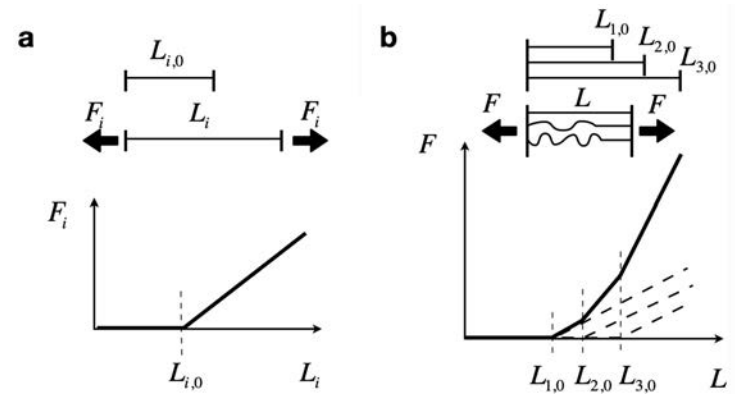


Fig. 2.26 Lanir's (1979) simplified model.

a. Behaviour of one fibre

b. Behaviour of a group of three fibres with different initial relaxed lengths.

The elongation of the bunch of fibres Λ should not be confused with the individual fibre elongation λ . However, these two quantities are related by the expression

$$\lambda = \frac{L}{L_{0f}} = \frac{L}{L_0} \frac{L_0}{L_{0f}} = \frac{\Lambda}{\theta} \quad (2.3.3-5)$$

In which the laxity θ , of the fibre, defined as the ratio between the straight relaxed length (without load on the fibre) L_{0f} and the relaxed length of the mass of fibres L_0 , that is

$$\theta = \frac{L_{0f}}{L_0} \quad (2.3.3-6)$$

By definition, the smallest value of the laxity is $\theta = 1$, corresponding to those fibres whose relaxed length coincides with the relaxed length of the mass of fibres.

Even though the fibres in the bunch have the same composition and properties, they may have different relaxed lengths and cross-sections. In order to account for these circumstances, a fibre distribution function $\Phi(\theta)$, is introduced, characteristic of the bunch, defined such that $\Phi(\theta)d\theta = dA$ is the total (relaxed) transverse area of those fibres whose laxity lies between θ and $\theta + d\theta$. The total cross-sectional area of all of the fibres in the bunch will be given by the integral

$$A = \int_1^{\theta_m} \Phi(\theta) d\theta \quad (2.3.3-7)$$

where θ_m is the maximum laxity of the fibres. Note that during the test, beyond an elongation $\Lambda = \theta_m$ all the fibres in the bunch will be stretched.

The function $\Phi(\theta)$ is shown in Figure 2.27 and can take on different shapes depending upon the initial degree of alignment of the fibres. When all of them are initially orientated and parallel, without laxity, the distribution function is a δ -Dirac: $\Phi(\theta) = A \delta(\theta - 1)$.

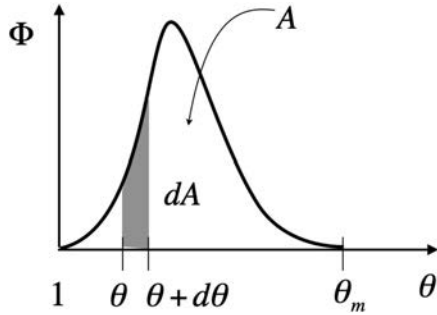


Fig. 2.27 Distribution function of the fibre cross-sections. A is the total cross-sectional area.

If we assume that all of the fibres have the same mechanical behaviour, we can establish a relationship between their engineering stress s and elongation λ given by

$$s = \begin{cases} 0 & \text{if } \lambda < 1 \\ s(\lambda) & \text{if } 1 \leq \lambda < \lambda_R \\ 0 & \text{if } \lambda \geq \lambda_R \end{cases} \quad (2.3.3-8)$$

in which we have assumed that there is no resistance to compression ($\lambda < 1$), since the fibres would buckle, and also when the elongation to failure λ_R is exceeded.

With these ingredients, we can write the force exerted by the fibres with laxity between θ and $\theta + d\theta$, when the bunch has an elongation Λ , which will be equal to

$$dF = s(\lambda)dA = s\left(\frac{\Lambda}{\theta}\right)\Phi(\theta)d\theta \quad (2.3.3-9)$$

and the total force on the bunch of fibres corresponding to the elongation Λ is obtained by integrating the above expression

$$F(\Lambda) = \int_{\max\{1, \Lambda/\lambda_R\}}^{\min\{\theta_m, \Lambda\}} s(\Lambda/\theta)\Phi(\theta)d\theta \quad (2.3.3-10)$$

since the function $\Phi(\theta)$ is defined between $1 \leq \theta \leq \theta_m$ and also $s \geq 0$ only if $1 \leq \lambda = \Lambda/\theta < \lambda_R$, from which $\Lambda \geq \theta \geq \Lambda/\lambda_R$.

The application of Lanir's model to a uniaxial tensile test to rupture of a human tendon (*extensor digitorum longus*; Schechtman et al., 2002) is shown in Figure 2.28. In order to simplify the situation it has been assumed that the collagen fibres have a linear-elastic behaviour followed

by a section of yielding before rupture (Figure 2.28a). The distribution function has been taken to be a constant value.

In Figure 2.28b we see that, despite the simplicity of a model with only four parameters ($E, \lambda_y, \lambda_R, \theta_m$), it is possible to reproduce the complete tensile test quite well over the whole range; in the initial region of progressively increasing stiffness, in the middle linear zone, in the region of maximum load, and also in the zone in which the load falls due to the progressive failure of the fibres. Furthermore, the fitting parameters lie well within the expected range for collagen fibres which we know constitute tendons, whose elastic modulus is about 1GPa (see section 3.4.2 of the "Biological Fibres" book).

The results above illustrate the usefulness of models which take into account the length and alignment of the fibres when modelling soft biological materials.

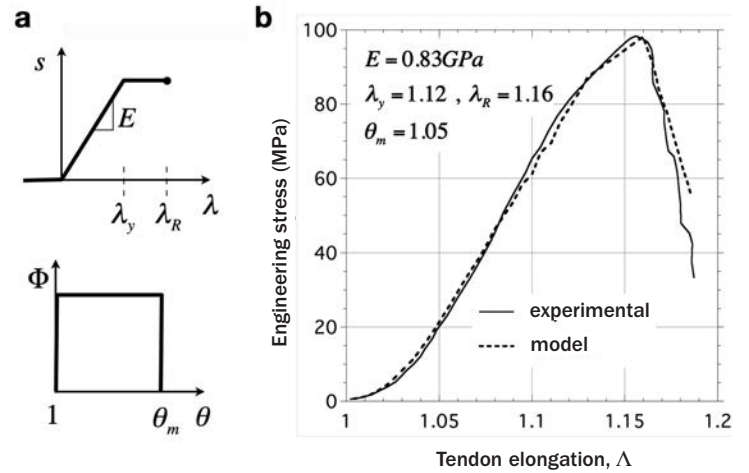


Fig. 2.28 Modelling the tensile test on the tendon of the extensor muscle of the finger (Schechtman et al. 2002).

a. Parameters of the model.

b. Experimental curve fit.

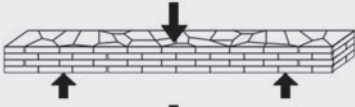

Modelling the strength or toughness of a composite material is not a simple task because, unlike homogeneous materials, fracture in composite materials may be due to various mechanisms which depend upon the type of loading and the microstructure of the composite material, geometry and orientation of the reinforcement, the bonding between the reinforcement and the matrix, and changes in the matrix as the fracture progresses. These diverse failure mechanisms, in each case, lead to numerous failure criteria. In the third part of this chapter detailed comment is provided on the modelling of some failure mechanisms and the means of estimating the strength of these biological materials - for wood, shells or bones.

EXERCISE 22

The Figure shows three-point bending tests performed by Wang and co-workers (2001) on prismatic abalone and mother-of-pearl shells. As will be noted later, these materials are formed of micrometric ceramic laminas (calcium carbonate in an aragonite structure) of thickness and average diameter of 0.3 and 7 μm , respectively, combined in a polymeric cement which constitutes approximately 5% of the total volume.

The experiments were conducted in seawater, in two different directions, with the aim of determining the anisotropy of the material. The specimens had dimensions (depth x width x length) of 0.5 x 2.5 x 12 mm. The values shown correspond the mean value and standard error.

Discuss the applicability of the Voigt and Reuss models to these materials.

$E(\text{GPa})$	Abalone	Mother-of-pearl
	69 ± 7	77 ± 12
	66 ± 2	81 ± 4

SOLUTION:

For the purpose of the analysis we shall assume that we are dealing with a composite material formed of a polymeric matrix ($v_m=0.05$) reinforced with ceramic laminas ($v_f=0.95$). Observing the experimental set up, we might suppose initially that the Voigt model is more appropriate, since in neither arrangement is the interface with largest contact surface between the ceramic laminas subjected to tension/compression. In both cases the same types of interface are subjected to tension/compression and this is reflected in the results, which show no statistically significant differences.

However, the macroscopic dimensions of the specimens invalidate the hypothesis that the reinforcing laminas are essentially continuous, required for a good fit to the Voigt model. In this case, the problem can be approached by observing that there are a large number of interfaces along the tension/compression directions, which we can estimate at $12 \text{ mm} / 7 \mu\text{m} \approx 1700$. When the loading direction is essentially perpendicular to the interfaces the Reuss model would seem to be more relevant.

In order to evaluate both models, let us take elastic modulus values for the polymeric matrix (m) and the ceramic reinforcement (f) proposed by Jackson (1988), $E_m=4 \text{ GPa}$ and $E_f=100 \text{ GPa}$.

With these values, Equations (2.3.3-1) and (2.3.3-2) lead to

$$E_{\text{Voigt}} = v_m E_m + v_f E_f = 0.05 \cdot 4 + 0.95 \cdot 100 = 95.2 \text{ GPa}$$

$$E_{\text{Reuss}} = (v_m/E_m + v_f/E_f)^{-1} = (0.05/4 + 0.95/100)^{-1} = 45.4 \text{ GPa}$$

The values obtained are far removed from the experimental measurements and, therefore, we conclude that it is necessary to employ more sophisticated models which take into account the geometry of the reinforcing laminas. In any case, it is interesting to point out that the Voigt and Reuss models provide upper and lower bounds to the stiffness of the material.

2.3.4. Cellular materials

1. Introduction

Cellular structures are present in many biological materials. Honeycomb, a classical paradigm of these structures, has caught the attention of mathematicians, physicists and biologists since antiquity; Euclid admired them for their regularity and Pliny cited the case of a man who dedicated his life to the study of these structures. Wood also shows us its cellular structure. One of the first materials examined by Robert Hooke in his new microscope (around 1660) was cork, which allowed him to see and identify the basic unit of biological structures; it was Hooke who baptised the structures he saw in cork cells.

Cellular materials can be **classified** into two major groups; two-dimensional cellular solids, –commonly called *honeycomb* structure– formed of prismatic cells, such as bee honeycomb, and *three-dimensional cellular solids* –commonly called *foams* or *sponges*– formed of polyhedral cells, such as spongy bone or actual sponges. Biological materials with a foam structure come in many different forms; woods, for example, exhibit highly elongated regular cells very similar to bee honeycomb. Spongy bone looks more like a three-dimensional framework. In other materials, such as corals or cuttlefish shells, the cells are orientated and this confers a marked mechanical anisotropy.

The **characteristic parameters** of cellular materials are; the *relative density*, the shape of the cells, and the material properties of the walls or of the framework.

The *relative density* is the ratio of between the density of the cellular material, taken together (apparent density) and the density of the solid that forms the cell walls or trabeculae. Its value is equal to the proportion, by volume, of solid material.

In terms of the *shape of the cells*, it is convenient to distinguish between open cells –connected– in which the solid material is only distributed along the edges of the polyhedral which they form, and closed cells, in which the faces are formed of solid walls.

The *basic material properties*, are obtained from the solid that forms the edges or faces of the cellular material polyhedral. Some of these basic materials are, in turn, composite materials, such as in the case of the trabeculae of spongy bone.

The **mechanical response** of cellular materials loaded in compression or tension is illustrated in Figure 2.29, in which some differences are apparent depending upon whether the cellular materials are elastomers (Fig. 2.29a and 2.29c) or elastoplastics (Fig. 2.29b and 2.29d).

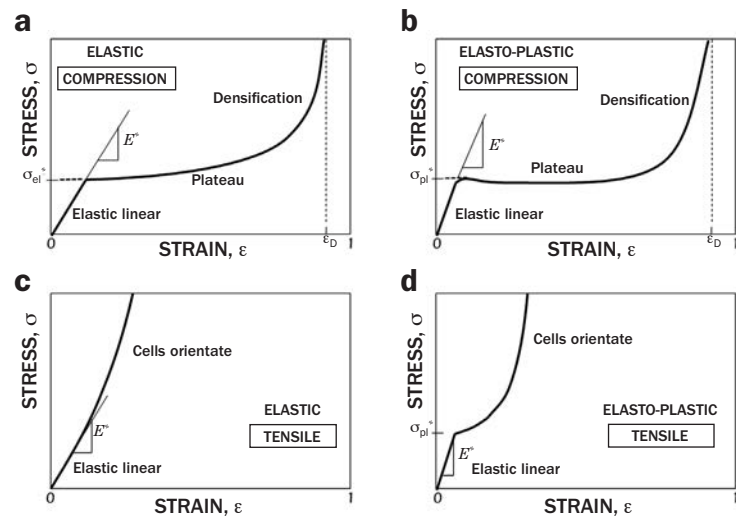


Fig. 2.29 Schematic stress-strain curves in uniaxial tests performed on cellular materials.

The stress-strain curves obtained in **compression** tests (Figs. 2.29a and 2.29b) have three characteristic stages; the first stage, an elastic linear region, corresponds to bending of the beams and columns which form the edges, or to the deformation of the walls which form the faces, of the polyhedra. In the second stage, in which the stress increases slowly or remains constant, the cells deteriorate through elastic buckling, or by rupture, depending upon the nature of the solid from which they are made. And, finally, there is a stage of densification, due to collapse and direct contact of the solid material. Cellular materials which have low relative densities –between 0.10 and 0.20– allow large strains to be achieved –between 70 and 80%– before densification, as shown in Figures 2.29a and 2.29b.

The stress-strain curves obtained in **tensile** tests are shown in Figures 2.29c and 2.29d. For small strains the response is elastic and linear, as was the case in compression tests. As the strain increases, the cells orientate themselves in the direction of the applied force and the stiffness of the cellular material increases until rupture occurs.

The mechanical behaviour of cellular materials can be **modelled** in several ways; analytically, numerically or, by simpler means, using dimensional analysis.

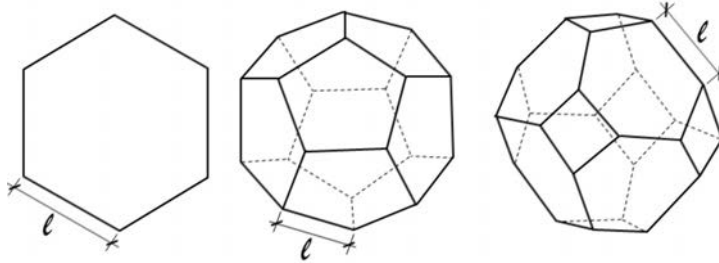


Fig. 2.30. Regular unit cells
a. Hexagon
b. Dodecahedron
c. Tetradekahedron

Initially, the models used deduced the mechanical response analytically from the unit cell deformation (see Fig. 2.30); in two dimensions, a hexagon and in three dimensions a dodecahedron, a twelve faced polyhedron, or the tetradekahedron, a polyhedron with 14 faces (Zhu et al., 1997, Warren and Kraynik, 1997). The nature of these unit cells is related to the need for a polyhedron that fills the space and whose area per unit volume is a minimum. Until 1992 it was thought that the tetradekahedron (proposed by Kelvin in 1887) was the optimum polyhedron, but it has been determined, using numerical methods, the other forms are better, although only by 0.3% (Weaire and Phelan 1994). These models are not very realistic if the material is formed of cells of different shapes and sizes, as happens in many biological materials.

Currently it is common to tackle the problem using numerical methods based on finite elements (Silva et al., 1995, van der Burg et al., 1997). These techniques allow the modelling of structures with cells of different shapes and arranged randomly, rather than periodically. Furthermore, they admit the introduction of defects which, in some cases, are essential for capturing, for example, rupture of the material. Numerical procedures can be used in conjunction with imaging techniques, such as computerised tomography, which make the study of more realistic cellular structures possible (Chen et al., 2001).

Far simpler methods, based on dimensional analysis, permit the modelling of deformation and failure mechanisms which are observed in cellular structures without the need to specify the exact geometry of the cell (Gibson and Ashby, 1982a, b, 1997). This technique assumes that the geometry of the cells is similar for foams with different relative densities. It provides results in terms of the relative density and the properties of the solid which forms the cell, but it needs some experiments, as will be seen later, in order to obtain the constants related to the cell geometry.

2. Two-dimensional cellular structures. Honeycomb structures

M. Ashby and L. Gibson (Gibson and Ashby, 1997) studied the response of a bee-honeycomb subjected to mechanical loading, particularly structures with equal, ordered, hexagonal cells. With the advent of powerful computers the problem has been generalised to structures with cells of different sizes and shapes, arranged randomly, and allowing, moreover, the introduction of defects.

The aim of this Section is to emphasise the most pertinent results of Ashby and Gibson's studies. Strictly speaking, only those results applicable to structures with regularly repeating the unit cells are considered, since, as already indicated, they are able to reproduce some cellular biological material parameters, as will be seen later when wood and spongy bone are discussed (Sections 3.2 and 3.3).

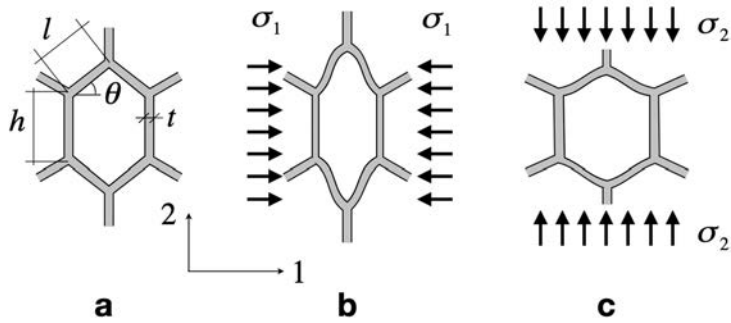


Fig. 2.31. Deformations of a two-dimensional unit cell.
a. Initial, undeformed cell.
b and c. Flexural deformations of the cell walls.

Figure 2.31a illustrates the geometrical characteristics of the unit cell, an irregular hexagon in which the sides l and h do not have to be equal. The wall thickness is constant and equal to t , which is taken to be much smaller than l or h . The cell wall material is assumed to be linear-elastic and isotropic, characterised by an elastic modulus E_s and Poisson's ratio.

The relative density of the honeycomb, d^*/d_s , is given by

$$\frac{d^*}{d_s} = \frac{h/l + 2}{2 \cos \theta (h/l + \sin \theta)} \frac{t}{l} \quad (2.3.3-11)$$

d^* is the density of the honeycomb, d_s the density of the solid material and the angle, θ , is defined in Figure 2.31a. (Note that this is also the quotient of the area of the cell and the corresponding area of its walls).

The above result indicates that the relative density is proportional to t/l and that the constant of proportionality is a function of the unit cell geometry. For example, for a regular hexagon ($h=l$, $\theta=30^\circ$) the constant is $2/\sqrt{3}$, or approximately 1.15.

In the following treatment it will be assumed that the wall thickness t , is much less than the length of the walls, l or h .

Response to loading parallel to the plane of the honeycomb

Compression of the cells

When the honeycomb is subjected to compressive forces located in the plane of the hexagons, the response in the form of the stress-strain diagram is of the type shown in Figures 2.29a and 2.29b, in which it is possible to identify three stages.

In the **initial stage**, under small strains, the behaviour is linear-elastic and the walls of the cell are deformed as indicated in Figures 2.31b and 2.31c (depending upon whether the stress acts in the 1- or 2-direction). Applying Strength of Materials concepts it is possible to deduce (see EXERCISE 23) that the ratio of the honeycomb elastic modulus, E^* , and that of the solid material E_s is given by

$$\frac{E_1^*}{E_s} = \frac{\cos \theta}{(h/l + \sin \theta) \sin^2 \theta} \left(\frac{t}{l} \right)^3 \quad (2.3.3-12)$$

when the compressive forces act in the 1-direction, and

$$\frac{E_2^*}{E_s} = \frac{h/l + \sin \theta}{\cos^3 \theta} \left(\frac{t}{l} \right)^3 \quad (2.3.3-13)$$

when they act in the 2-direction.

For regular hexagons ($h=l$, $\theta=30^\circ$) both results coincide, and

$$\frac{E_1^*}{E_s} = \frac{E_2^*}{E_s} = \frac{4}{\sqrt{3}} \left(\frac{t}{l} \right)^3 \approx 2.31 \left(\frac{t}{l} \right)^3 \quad (2.3.3-14)$$

These results indicate that the relative elastic moduli of the honeycomb are proportional to $(t/l)^3$ and that the constant of proportionality depends upon the geometry of the cell, that is to say upon h/l and θ . With this information it is possible to draw the initial slope in Figures 2.29a and 2.29b.

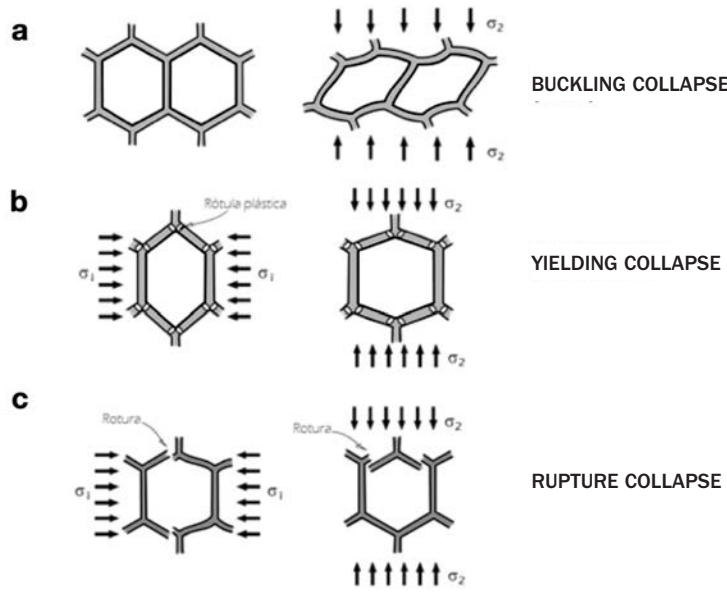


Fig. 2.32. Collapse modes in a two-dimensional unit cell.
a. By elastic buckling.
b. By formation of plastic hinges.
c. By rupture of the walls.

As the load increases, cells begin to collapse and the **second stage** (in Figures 2.29a and 2.29b) begins. Collapse may be due to several causes depending upon the cell wall material; by *buckling*, if elastic, by *yielding* (the formation of plastic hinges) if it is elasto-plastic, or by *rupture*, if fragile. These three modes are shown schematically in Figure 2.32. Ashby and Gibson have calculated the respective stresses which determine the end of the first stage and the beginning of the plateau.

- When the cells are subjected to compression in the 2-direction, the *elastic buckling* stress is calculated from the force required to cause buckling of the columns aligned with the loading direction (see Figure 2.32a), and is given by

$$\frac{\sigma_{el,2}^*}{E_s} = \frac{n^2 \pi^2}{24 \cos \theta} \frac{t^3}{lh^2} \quad (2.3.3-15)$$

where n is a factor which depends upon the rotational restraint imposed at nodes (whether very flexible or otherwise) and also upon h/l , typically varying between 0.686 ($h=l$) and 0.806 ($h=2l$). Only the collapse stress in the 2-direction is quoted, since it is the most unfavourable. In the case of regular hexagons the 1- and 2-directions are the same. The result for this situation is:

$$\frac{\sigma_{el}^*}{E_s} = 0.22 \left(\frac{t}{l} \right)^3 \quad (2.3.3-16)$$

- The stress for collapse by *plastic deformation* is calculated from the stresses that create plastic hinges in the cell walls (as illustrated in Figure 2.32b), and is given, depending upon the loading direction, by:

$$\frac{\sigma_{pl,1}^*}{\sigma_{ys}} = \frac{1}{2(h/l + \sin \theta) \sin \theta} \left(\frac{t}{l} \right)^2 \quad (2.3.3-17)$$

for compression in the 1-direction, where σ_{ys} is the yield stress of the cell wall material. For compression in the 2-direction,

$$\frac{\sigma_{pl,2}^*}{\sigma_{ys}} = \frac{1}{2 \cos^2 \theta} \left(\frac{t}{l} \right)^2 \quad (2.3.3-18)$$

In regular hexagons, once again, both values coincide and

$$\frac{\sigma_{pl}^*}{\sigma_{ys}} = \frac{2}{3} \left(\frac{t}{l} \right)^2 \quad (2.3.3-19)$$

- The stress for collapse by *cell wall rupture* (Figure 2.32c) is calculated from the moment required to break the walls, obtained from the flexural strength of the material σ_f and is given by:

$$\frac{\sigma_{r,1}^*}{\sigma_f} = \frac{1}{3(h/l + \sin \theta) \sin \theta} \left(\frac{t}{l} \right)^2 \quad (2.3.3-20)$$

for compression in the 1-direction, and also

$$\frac{\sigma_{r,2}^*}{\sigma_f} = \frac{1}{3 \cos^2 \theta} \left(\frac{t}{l} \right)^2 \quad (2.3.3-21)$$

in the 2-direction. For regular hexagons both values coincide, giving

$$\frac{\sigma_r^*}{\sigma_f} = \frac{4}{9} \left(\frac{t}{l} \right)^2 \quad (2.3.3-22)$$

In the **final stage**, the stress increases rapidly with the strain due to the *densification* of the cells. The densification strain ε_D (Figure 2.29) for the ideal case must be equal to the porosity of the material, that is to say; $1-d^*/d_s$. In practice, the cells are actually kinked, with small deformations, before exhausting all of the available pore space. Gibson and Ashby then propose the following expression for ε_D (see Figures 2.13a and 2.13b)

$$\varepsilon_D = 1 - 1.4 d^*/d_s \quad (2.3.3-23)$$

EXERCISE 23

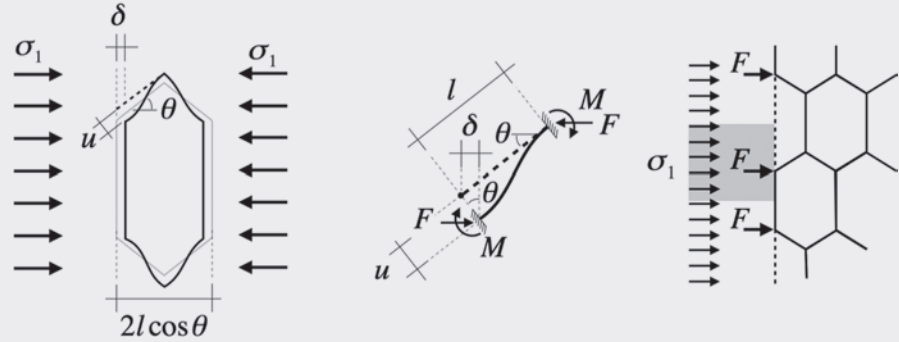
Derive Equation (2.3.3-12).

SOLUTION:

The figure shows the deformation of the cell when compressed along the 1-axis. We shall assume that all of the displacements are small.

Due to the bending of the upper and lower sides the cell shortens in the 1-direction by an amount 2δ . The strain in this direction will be

$$\varepsilon_{11} = \frac{2\delta}{2l \cos \theta} = \frac{\delta}{l \cos \theta}$$



The value of δ is related to the relative displacement of the ends of the sides, u , through the expression

$$\delta = u \sin \theta$$

In order to quantify the strain we model the sides as beams, built-in at the ends, as indicated in the figure. At each end of the beam there is a bending moment M , and a force F acts in the 1-direction, as shown, since there are no applied forces in the 2-direction. Then, for moment equilibrium,

$$F = \frac{2M}{l \sin \theta}$$

In order to obtain F , we consider equilibrium of the forces on the cell along the 1-axis. The force acting at each node, F , due to the stress σ_1 will be that corresponding to its area of influence

$$F = \sigma_1 (h + l \sin \theta) b$$

and, therefore

$$M = \frac{\sigma_1}{2} (h + l \sin \theta) b l \sin \theta$$

Strength of Materials theory provides the value of u , for a beam of length l , second moment of area I and elastic modulus E_s , subjected to equal moments M

$$u = \frac{M l^2}{6 E_s I}$$

since, in our case, $I = b t^3 / 12$, where b is the depth of the cell, we arrive at

$$\delta = \frac{2 M l^2}{E_s b t^3} \sin \theta = \frac{\sigma_1 (h + l \sin \theta) l^3 \sin^2 \theta}{E_s t^3}$$

and the strain ε_{11} will be

$$\varepsilon_{11} = \frac{\sigma_1 (h/l + \sin \theta) l^3 \sin^2 \theta}{E_s t^3 \cos \theta}$$

Finally, we can calculate the apparent elastic modulus E^* of the honeycomb as

$$E_1^* = \frac{\sigma_1}{\varepsilon_{11}} = \frac{E_s t^3 \cos \theta}{(h/l + \sin \theta) l^3 \sin^2 \theta}$$

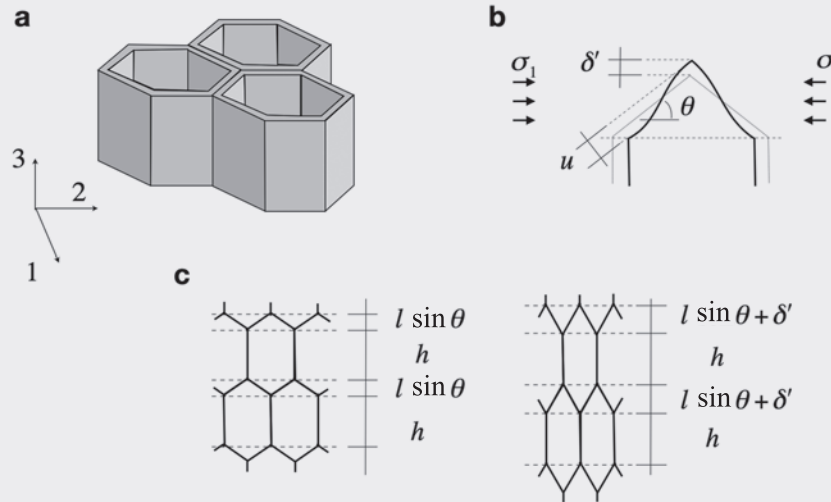
from which we obtain Equation (2.3.3-12).

EXERCISE 24

Investigate the type of anisotropy is shown by two-dimensional cellular materials with the honeycomb structure shown in Figure 2.31.

SOLUTION:

Figure (a) depicts the arrangement of the cells and their dimensions. In the direction of the 3-axis, perpendicular to the 1-2 plane, it is assumed that the cell walls do not have openings. The wall material is considered to be homogeneous and isotropic.



The equivalent homogeneous material must have the symmetry of the cell material, which, as we have seen, has a symmetry with respect to the planar coordinates $x_1=0$, $x_2=0$ and $x_3=0$. It will, therefore, be an **orthotropic** material which can be represented by a linear-elastic model with nine independent parameters, as was seen in Section 2.3.2.

Two of these parameters are the moduli of elasticity E_1^* and E_2^* given by Equations (2.3.3-12) and (2.3.3-1).

Furthermore, from the results of EXERCISE 23 it is easy to determine the Poisson's ratio ν_{12}^* , (following the nomenclature of EXERCISE 20). In order to calculate it, we observe that when a compressive load σ_1 is applied in the 1-direction each vertex of the cell is displaced in the 2-direction by an amount $\delta' = u \cos \theta$ (Figure b). Therefore, the strain (elongation) in that direction (Figure c) is

$$\varepsilon_{22} = \frac{\delta'}{h + l \sin \theta} = \frac{u \cos \theta}{h + l \sin \theta}$$

Since the strain in the 1-direction was a shortening, of value

$$\varepsilon_{11} = \frac{u \sin \theta}{l \cos \theta}$$

the final result is

$$\nu_{12}^* = -\frac{\varepsilon_{22}}{\varepsilon_{11}} = \frac{\cos^2 \theta}{(h/l + \sin \theta) \sin \theta}$$

The Poisson's ratio ν_{21}^* , can be calculated directly from the strain produced in the 1-direction when we apply a load in the 2-direction, or by making use of the symmetry relationship

$$\frac{\nu_{21}^*}{E_2^*} = \frac{\nu_{12}^*}{E_1^*}$$

which we saw in EXERCISE 20, together with the values of the elastic moduli. In both cases the result obtained is

$$\nu_{21}^* = \frac{(h/l + \sin\theta)\sin\theta}{\cos^2\theta}$$

It is worth noting that the two Poisson's ratios can have very different values. For a regular hexagonal network, it is found that $\nu_{12}^* = \nu_{21}^* = 1$. If $\theta < 0$ negative values are obtained, which implies that under a compressive (or tensile) load, the network contracts (or expands) as much in the direction of the load as perpendicular to it.

The other six independent parameters of the orthotropic model are: the elastic modulus E_3^* , Poisson's ratios ν_{31}^* and ν_{32}^* , and shear moduli G_{12}^* , G_{23}^* and G_{31}^* .

The value of E_3^* is obtained directly from proportion of solid material, which will be equal to the ratio of the cross sectional area of the cell walls to their total area

$$\frac{E_3^*}{E_s} = \frac{h/l + 2}{2(h/l + \sin\theta)\cos\theta} \frac{t}{l}$$

The Poisson's ratios ν_{31}^* and ν_{32}^* are, directly, $\nu_{31}^* = \nu_{32}^* = \nu_s$, where ν_s is the Poisson's ratio of the solid material, since a compression (or traction) in the 3-direction does not induce bending in the cell walls, and a uniform expansion (or contraction) will result in the 1-2 plane. The complementary Poisson's ratios $\nu_{13}^* = \nu_{23}^*$ are readily obtained from the symmetry relationships (EXERCISE 20)

$$\frac{\nu_{31}^*}{E_3^*} = \frac{\nu_{13}^*}{E_1^*} \quad \text{and} \quad \frac{\nu_{32}^*}{E_3^*} = \frac{\nu_{23}^*}{E_2^*}$$

which yields

$$\nu_{13}^* = \frac{2\cos^2\theta}{(h/l + 2)\sin^2\theta} \left(\frac{t}{l}\right)^2 \nu_s \quad \text{and} \quad \nu_{23}^* = \frac{2(h/l + \sin\theta)^2}{(h/l + 2)\cos^2\theta} \left(\frac{t}{l}\right)^2 \nu_s$$

which are practically zero, since t/l is small.

Calculation of the **shear modulus** is a somewhat more complicated, and Gibson and Ashby's book may be consulted.

Let us finally observe that when the honeycomb has regular hexagonal cells, symmetry makes the cell material **transversely isotropic**.

Traction of the cells

When the cells are subjected to **tensile** forces lying in the plane of the hexagon the associated stress-strain diagram is shown in Figures 2.29c and 2.29d.

The initial elastic modulus, E^* , can be calculated using the approach outlined above. In the second stage, in which the curve increases more rapidly compared to that compression tests, an alignment of the cells is produced. Rupture occurs, almost always, by propagation of a crack originating from a defect in the honeycomb.

If the honeycomb material is brittle, Gibson and Ashby suggest that the fracture toughness, K_{IC}^* , of the honeycomb can be estimated from the following expression

$$\frac{K_{IC}^*}{\sigma_f \sqrt{\pi l}} = 0.3 \left(\frac{t}{l} \right)^2 \quad (2.3.3-24)$$

where σ_f is –as before– the flexural strength (or rupture modulus) of the solid material. The assumptions and limitations of this expression are discussed in the cited reference, (Gibson and Ashby, 1997).

So far, only uniaxial compressive and tensile loadings have been considered. When honeycombs are subjected to biaxial loading their mechanical response in the elastic regime is different because the deformation mechanisms are different; under uniaxial loading the dominant mechanism is flexure of the cell walls, a mechanism that may be almost completely eliminated by the judicious choice of biaxial loads. In these circumstances the cell walls may end up failing by plastic yielding, creep or rupture, and all of these will result in a greater honeycomb strength.

Response to loading normal to the plane of the honeycomb

In some biological materials cells are found in the middle of sandwich type structures, with the aim of optimising their mechanical behaviour, for example; in the leaves of some plants, in the skull of birds, or in cuttlefish shells.

In these circumstances, if the loading is normal to the plane of the honeycomb, the mechanical function is to transmit the forces through the cell walls parallel to the axis of the hexagonal prisms. Now the walls are stretched or compressed, but not subjected to bending as before, and for this reason, the elastic modulus is greater and the loads which initiate collapse are also greater.

Gibson and Ashby (1997) have provided expressions for the initial elastic modulus and values of the initial collapse loads when the cells are compressed in the direction normal to the plane of the honeycomb (3-axis). For structures with regular hexagonal cells ($l = h$) the following results are obtained:

– for the elastic modulus E_3^* ,

$$\frac{E_3^*}{E_s} = \frac{d^*}{d_s} = 1.15 \frac{t}{l} \quad (2.3.3-25)$$

– for collapse by elastic buckling

$$\frac{\sigma_{el,3}^*}{E_s} = 5.2 \left(\frac{t}{l} \right)^3 \quad (2.3.3-26)$$

in which it has been assumed the Poisson's ratio of the wall material is 0.3.

– for collapse by plastic buckling

$$\frac{\sigma_{pl,3}^*}{\sigma_{ys}} = 5.6 \left(\frac{t}{l} \right)^{5/3} \quad (2.3.3-27)$$

where σ_{ys} is the yield stress of the cell wall material.

If buckling is avoided, whether elastic or plastic, the yield stress and the rupture strength of the honeycomb can be calculated by multiplying the relative density d^*/d_s by the corresponding properties (yield stress or failure load) of the cell wall material.

Final remarks

The brief analysis performed above (based on Gibson and Ashley book) indicates the following:

The mechanical properties of honeycombs (if the Poisson's ratio is ignored) depend upon three parameters: the ratio t/l , the cell geometry (through h/l and θ) and the properties of the cell walls (E_s , σ_{ys} , σ_f).

The ratio t/l is proportional to the relative density d^*/d_s and the percentage by volume of solid material.

For loading in the **plane of the honeycomb**, where the dominant mechanisms are bending or buckling of the walls, the elastic modulus varies with the cube of the relative density, while the collapse stresses (elastic buckling, yielding or rupture) vary with the square or cube of the relative density.

For loading normal to the **plane of the honeycomb**, where the dominant mechanism is stretching or compressing the cell walls, the elastic modulus and the strength (if buckling is eliminated) are proportional to the relative density.

3. Three-dimensional cellular structures: foams and sponges

Numerous biological materials have a sponge structure. The reason, in many cases, is mechanical; for example, in spongy bone this is to produce a lighter stronger structure. In other cases the aim is to try to optimise fluid transport or thermal insulation, such as in the stems of plants or in sponges.

The geometry of spongy materials is more complicated than that of honeycombs. In some materials the cells are open and, in reality, their structure is a framework of beams and columns (called trabeculae). In others, the cells are closed and often filled with fluids.

As already observed, the analysis of these structures may follow one of several approaches. The simplest is based on dimensional analysis, in a manner analogous to that described when dealing with honeycombs. Since the geometry of the cells is more complicated, what is obtained are proportionality relationships between the required parameters and the relative density of the material. The constant of proportionality is obtained from empirical data, as will be seen below. This process is based upon the assumption that the material cells, with different relative densities, are geometrically similar. Furthermore, the results obtained from an analysis of cubic cells can be generalised to other geometries, provided that the deformation and fracture mechanisms are the same. This conclusion has been validated in several experimental studies.

When testing these spongy materials in compression, or in tension, curves similar to those in Figure 2.29 are obtained, in which, in the compression tests, it is possible to identify three stages, as will be discussed below.

Compression of foams and sponges

In **compression** tests, in a first stage, with small strains, the behaviour is linear-elastic. The elastic modulus for open cells can be estimated using a cubic model, as shown in Figure 2.33a, in which it is assumed that the principal contribution to the strain is due to beam bending, shown in Figure 2.33b). The model yields the following result (see EXERCISE 25) for the elastic modulus of the cellular material, E^* .

$$\frac{E^*}{E_s} = A \left(\frac{t}{l} \right)^4 = C_1 \left(\frac{d^*}{d_s} \right)^2 \quad (2.3.3-28)$$

in which A and C_1 are constants, and it has been noted that the relative density is proportional to $(t/l)^2$, t being the average diameter of the trabeculae. The subindices s

indicate, as before, reference to the solid material. This analysis provides the elastic modulus of the cellular material in terms of the relative density and the modulus of the solid material. The constant C_1 encompasses the geometric characteristics of the unit cell.

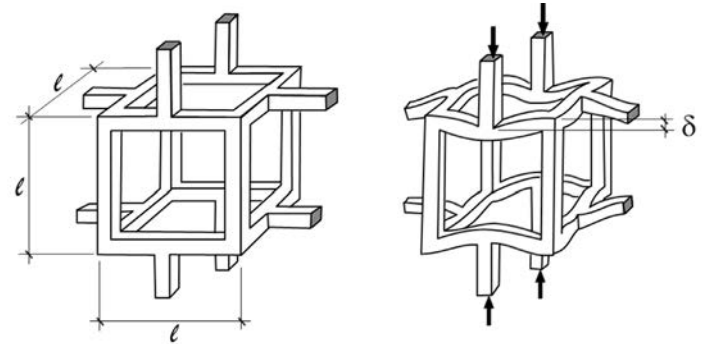


Fig. 2.33. Deformation of a three-dimensional unit cell.
a. Initial cell configuration, before deformation.
b. Bending deformation of the spans perpendicular to the loading direction.

Fitting Equation (2.3.3-28) to numerous experimental results, Ashby and Gibson obtained a value of C_1 close to unity. Warren and Kraynik, 1997, performed an analysis of a tetradechedron, rather than a cube, and yielding a value of $C_1 = 0.98$. Another estimation of C_1 was derived from a three-dimensional numerical analysis with Voronoi unit cells (randomly arranged and of different sizes). The calculation produced a value of $C_1 = 0.8$ (Vajjhala et al., 2000).

In an analogous treatment, Ashby and Gibson, proposed the following expression for the shear modulus G^* of the cellular material for the special case of isotropic open cells with a Poisson's ratio equal to $1/3$:

$$\frac{G^*}{E_s} = \frac{3}{8} \left(\frac{d^*}{d_s} \right)^2 \quad (2.3.3-29)$$

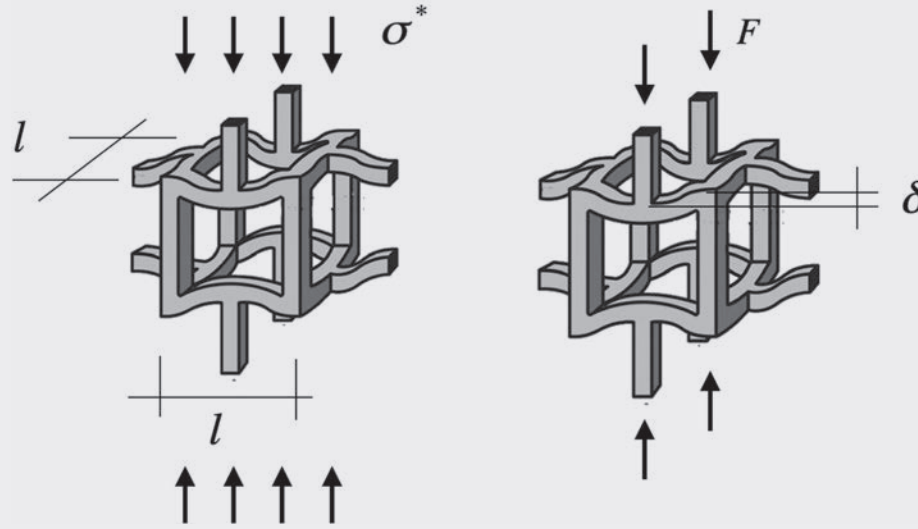
When closed liquid-filled cells were tested in compression, the fluid opposed the bending of the walls, and this affects the elastic modulus. Gibson and Ashby proposed the following expression for the new elastic modulus, E^* :

$$\frac{E^*}{E_s} = B_1 \left(\frac{d^*}{d_s} \right)^2 + B_2 \frac{d^*}{d_s} \quad (2.3.3-30)$$

in which the second term accounts for the increase in stiffness due to the fluid. The coefficients B_i are usually obtained experimentally.

EXERCISE 25

Using a Strength of Materials beam theory analysis, prove Equation (2.3.3-28).

SOLUTION:

If we consider the cubic cell in Figure 2.33, and model its trabeculae as elastic beams, Strength of Materials shows us that the displacement δ under an applied load F must be proportional to the cube of its length l , according to

$$\delta \sim \frac{Fl^3}{E_s I}$$

where I is the second moment of area of the beam section and E_s the elastic modulus of the solid material from which it is made.

The strains in the cell are proportional to δ/l so we will have

$$\varepsilon \sim \frac{\delta}{l} \sim \frac{\sigma^* l^4}{E_s t^4}$$

since the force acting must be $F \sim \sigma^* l^2$, proportional to the applied stress. We have also taken $I \sim t^4$, t being the diameter of the trabeculae.

On the other hand, the ratio of the densities will be equal to that of the cell volumes. The volume of solid material will be proportional to $t^2 l$ therefore

$$\frac{d^*}{d_s} \sim \frac{t^2 l}{l^3} \sim \left(\frac{t}{l}\right)^2$$

Finally, the elastic modulus of the cellular material will be proportional to the ratio of the stresses and strains which, with the previous expressions, results in

$$E^* \sim \frac{\sigma^*}{\varepsilon} \sim E_s \left(\frac{t}{l}\right)^4 \sim E_s \left(\frac{d^*}{d_s}\right)^2$$

which is the required expression.

The influence of **defects** on the elastic modulus of cellular materials with open cells has been investigated by several authors, particularly the effect of removing trabeculae in the cells. Gibson and Ashby summarised results in Figure 2.34, in which the elastic modulus of the damaged material, normalised with respect to the intact modulus (E^*/E_0) is plotted as a function of the percentage reduction in the relative density. These results were determined numerically; for three-dimensional cellular materials ordered tetradecahedra and random cells (Voronoi polygons) were used, for honeycombs these were ordered hexagons and random polygons (Voronoi polygons). The reduction in density was produced by eliminating bars in the models. The results indicate that the influence of the loss in density is less acute in three-dimensional structures than in two-dimensional ones. These findings may be important in the process of osteoporosis of spongy bone where a gradual loss of bone density occurs.

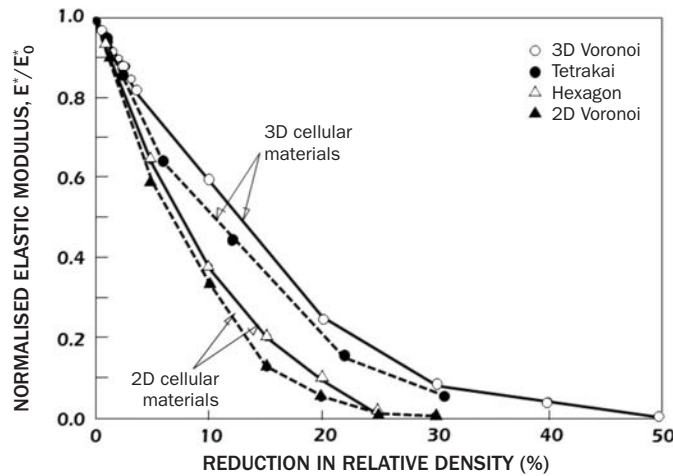


Fig. 2.34. Influence on the elastic modulus of the (random) reduction of trabeculae for two- and three-dimensional cellular materials.

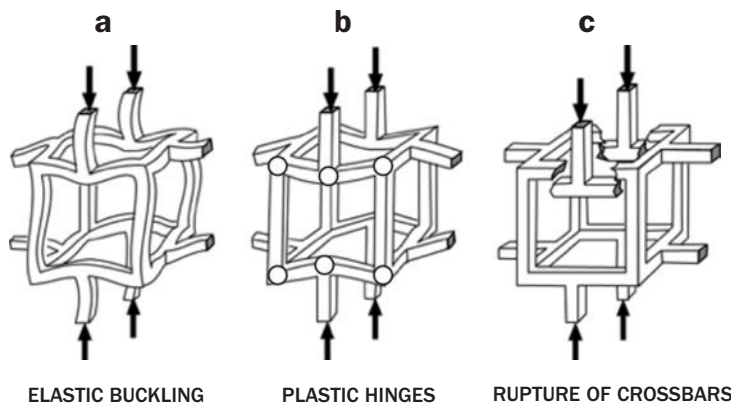


Fig. 2.35. Collapse modes in open cells.

- By elastic buckling.
- By the formation of plastic hinges in the corners of the trabeculae.
- By rupture of crossbars.

The final linear-elastic stage occurs when, for various reasons, the stress reaches a critical value in one of the cell components; by elastic buckling of the elements which work in compression, through the formation of plastic hinges at the corners, or by the rupture of a crossbar.

These collapse mechanisms in open cells are shown, in simplified forms, in Figure 2.35 for a cubic cell.

Gibson and Ashby (1997) proposed the following expressions for **open cells**:

- for collapse due to elastic buckling:

$$\frac{\sigma_{el}^*}{E_s} = C_2 \left(\frac{d^*}{d_s} \right)^2 \quad (2.3.3-31)$$

the value of C_2 obtained empirically is $C_2 \approx 0.05$.

An analysis with tetradecahedral cells gives values between 0.10 and 0.18.

- for plastic collapse resulting from plastic hinges at the corners

$$\frac{\sigma_{pl}^*}{\sigma_{ys}} = C_3 \left(\frac{d^*}{d_s} \right)^{3/2} \quad (2.3.3-32)$$

where σ_{ys} is the yield stress of the solid material and $C_3 \approx 0.3$, also obtained empirically.

- for collapse by rupture

$$\frac{\sigma_r^*}{\sigma_f} = C_4 \left(\frac{d^*}{d_s} \right)^{3/2} \quad (2.3.3-33)$$

where σ_f rupture modulus of the solid material. The value of C_4 , also obtained empirically, is approximately 0.2.

When the cells are **closed**, the walls also contribute to the mechanical response of the cellular material. If the cells are formed from liquids –as is often the case– surface tension pulls the material to the edges and leaves a very thin membrane on the faces. In these cases, even though the cells are closed, the membranes contribute little to the stiffness of the material when loaded, and usually break soon. The values found in open cells may be a good approximation in these cases.

If the cell walls are thick, as in the leaves of many plants, the values presented above are not valid, and the dependency on relative density is not so simple. The interested reader can find expressions for the stiffness of these cellular materials in Gibson and Ashby (1997).

As the compressive forces increase a point is reached when the cells collapse and the stress-strain curve increases rapidly, as indicated in Figure 2.29, its slope, as it reaches the maximum strain, ε_D , approaches the value the elastic modulus of the cell material, E_s . The value of ε_D would be expected to be that of the porosity, since, at that instant, it has been eliminated, that is to say $\varepsilon_D = 1 - d^*/d_s$. In reality, as already noted in the discussion of honeycombs, the cells stack up on top of one another and this ideal value is not achieved. Gibson and Ashby proposed the following expression for the maximum strain

$$\varepsilon_D = 1 - 1.4 \frac{d^*}{d_s} \quad (2.3.3-34)$$

Traction of foams and sponges

When the loading is **tensile** the material breaks due to the initiation and unstable propagation of a crack. For brittle cellular materials the principles of Linear-Elastic Fracture Mechanics can be applied. In these cases, for open cells, the fracture toughness of the cellular material K_{IC}^* , can be expressed in the following form:

$$\frac{K_{IC}^*}{\sigma_f \sqrt{\pi l}} = C_s \left(\frac{d^*}{d_s} \right)^{3/2} \quad (2.3.3-35)$$

where σ_f is the rupture modulus of the cell material, l the average length of a trabecula and C_s , is an experimentally-determined constant, approximately equal to 0.65.

With the availability of powerful computers it is becoming easier to perform realistic studies of cellular materials; it is no longer necessary to start with equal periodic structures, it is possible to introduce defects, more elaborate constitutive equations, and to simulate complex loadings, more in keeping with reality.

This short Section ends with two observations upon the influence of variable loads and the presence of fluids in the cells.

Fatigue of cellular materials, under repeated compressive loading, is of interest in the study of spongy bones, since it is thought that half of the fractures in patients with osteoporosis are caused as a result of this loading. Fatigue test on materials usually consists of obtaining classical $S-N$ curves, in which the stress amplitude is plotted as a against the number of fatigue cycles to failure. In general these curves have a great deal of scatter. In cellular materials it is observed that when fatigued in compression the strain decreases slowly initially but to increase more rapidly later. The number of cycles in which this sudden transition occurs is usually taken to be the corresponding fatigue value for the load being used.

We must note that, generally, a cellular material always contains **fluid** in its interior, so its effect on the macroscopic mechanical behaviour will depend upon whether it is gaseous or liquid, and also if the cells are open or closed.

If the cellular material is **closed**, the fluid (liquid or gas) always increases the rigidity and the value of the yield stress, the more, the lower its compressibility. Furthermore, in the case of gases, there will be a significant dependence upon temperature, as their compressibility is very temperature-dependent.

When it comes to **open** cellular materials, a very important stiffening effect may occur, and both the elastic modulus and the yield stress will usually depend upon the fluid viscosity, the size of the openings between cells and the strain rate.

In the case of *gaseous fluids* the effect is usually negligible, since due to their low viscosity the gases can circulate without difficulty through the interior of the material when deformed, offering little or no resistance. For the opposite to happen, the size of the cell (or better, the size of the openings between cells) must be very small, below ten microns, and –at the same time– the strain rate very high, above $10s^{-1}$.

In the case of a *liquids*, the situation changes because the viscosity is much higher. This is often the case in biological materials, in which the fluid is similar to water in its mechanical properties. However, when the openings are large, millimetre-sized, such as, for example, in trabecular bone, the effect is negligible since the liquid, moves without difficulty even at impact velocities ($> 1s^{-1}$). Nonetheless, with small pores, such as are found in the interior of cortical bone ($\sim 40\mu m$), there is a strong dependency of the mechanical properties upon the strain rate, as will be shown in Section 3.3.2.

EJERCICIO 26

Determine how the value of the yield strain ε_{ys}^* varies with the apparent density d^* in open isotropic cellular materials such as those represented in Figure 2.33, when they are loaded in a compression test.

Apply the results to the analysis of the compression tests on the human subchondral trabecular bone of different apparent densities, performed by Hayes and Carter (1976) and shown in the Figure.

SOLUCIÓN:

Equations (2.3.3-31) and (2.3.3-32) provide the stresses corresponding to the initial collapse of cells, corresponding to the two damage mechanisms operating in compression tests. Their value marks the end of the linear-elastic behaviour of the material and the beginning of the densification phase. To locate the boundary between the two behaviours, linear and nonlinear, we will estimate the values of the strains at this point by dividing the stresses by the apparent elastic modulus E^* .

Using the cited equations and Equation (2.3.3-28) which establishes the relationship between E^* and the apparent density we obtain:

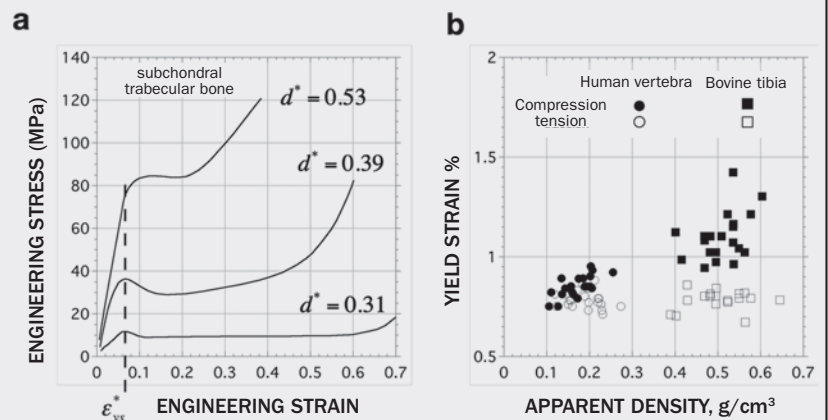
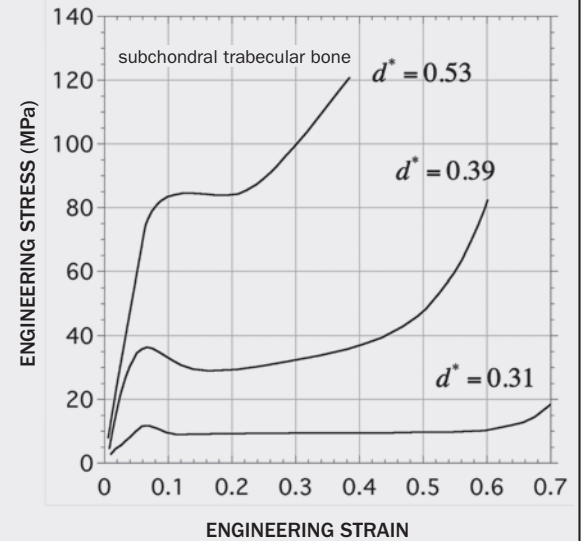
$$\text{– for the elastic buckling collapse mechanism } \varepsilon_{ys} = \frac{\sigma_{el}^*}{E^*} = \frac{C_2 E_s (d^*/d_s)^2}{C_1 E_s (d^*/d_s)^2} = \text{constant}$$

$$\text{– for the plastic hinges formation collapse mechanism } \varepsilon_{ys} = \frac{\sigma_{pl}^*}{E^*} = \frac{C_3 E_s (d^*/d_s)^{3/2}}{C_1 E_s (d^*/d_s)^2} = \frac{\text{constant}}{\sqrt{d^*}}$$

We observe that in the first case, the dependency of the collapse stress and the elastic modulus upon $(d^*)^2$ cancel, giving rise to a value of the strain ε_{ys}^* which is independent of the apparent density. This phenomenon has been observed by several authors and will be discussed later in more detail. In the second mechanism, a hyperbolic dependency is obtained and the value of ε_{ys}^* decreases with the apparent density. These relationships are valid as long as the values for the solid material are identical, which, in practice, and in relation to biological materials, requires comparison of materials from the same source, which can be difficult to achieve.

Hayes and Carter's curves confirm that the compressive yield stress has little dependence upon the apparent density, and we can see (Figure a) that yield is initiated, in the three cases tested, at a value of ε_{ys}^* close to 0.065.

The lack of correlation between the yield strain and the apparent density has also been observed in tensile tests. The results of Kopperdahl and Keaveny (1998) are summarised in Figure (b), indicating a lack of correlation between ε_{ys}^* and d^* in tension and, if anything, a very weak correlation in compression. Note that the yield strain in tension is always less than that in compression, probably because the damage and rupture mechanisms occur much sooner.



3

Examples

CHAPTER

3.1. Mollusc shells

3.2. Wood

3.3. Bone

3.4. Cartilage

The aim of this chapter is to illustrate the application of some concepts, developed in the previous chapter, related to the mechanical properties of several biological materials of interest; mollusc shells, wood, bone and cartilage.

The format of each example is the same: The structure of the material is described –at the macro, meso or microscopic level– as appropriate, and taking into account the, more or less, hierarchical nature of these materials. The next step, consists of reviewing their *mechanical properties* and attempting to model their behaviour –with the tools discussed in Chapter 2– with the aim of understanding their properties and to make predictions. The examples investigated relate to, more or less, rigid materials, which hardly deform, and in which it is possible to use the linear elastic approximation, which simplifies the modelling. Finally, some comments are made on possible applications; as **biological material**, as **biomaterial** (to correct or replace tissue, organs or functions in the human body) and in the field of **biomimetics**.

In the first example, **mollusc shells** are examined. These are composite materials, in which a weak organic matrix (between 1 and 5%) is reinforced with calcium carbonate particles.

The structure of this composite is complex and organised in such a way that its strength and toughness are far greater than the ceramic material from which it is formed. In this example only two simple structures are analysed; the parallel lamellar and crossed lamellar.

Modelling is usually based on a representative volume formed of ceramic tablets embedded in a cohesive matrix. With much simpler models, based on the rule of mixtures, it is possible to estimate maximum values of the initial elastic modulus and the tensile strength.

As a *biological material*, shells have little or no practical use, but great value as decorative items or jewellery. As a *biomaterial*, it has been used since ancient times for dental implants and currently, on occasion, to regenerate bone. The impact strength and large toughness of shells serve as an inspiration, in the field of *biomimetics*, for the design of armours.

The second example is dedicated to **wood**. This is also a composite material, at the microstructural level, of cellulose fibres in a hemicellulose or lignin matrix.

The structure of wood, at the macroscopic level, and in certain circumstances, can be considered as if it were a continuous homogeneous orthotropic material. At the mesoscopic level, it may be thought of as an aggregate of two types of cell walls. The study of cell walls belongs in the microscopic domain. However, it is possible to go even deeper by examining the structure at the nanoscopic level, if the cellulose microfibrils are considered.

The mechanical properties depend significantly upon temperature and humidity –the behaviour is viscoelastic– but, even so, it is possible to make reliable predictions of the mechanical behaviour. The material microstructure can

be modelled as a composition of cellulose fibres embedded in a hemicellulose or lignin matrix and the mesostructure modelled as a cellular honeycomb material (see Section 2.3.4), with properties calculated at the microstructural level. With this information it is possible to obtain satisfactory results for the elastic modulus, rupture load and the fracture toughness, at the macroscopic level.

As a *biological material*, wood has always played an important role in construction since its specific mechanical properties are very competitive. As a *biomaterial*, it has long been of interest –there are examples of wooden prostheses from about 2,600 years ago– and tibia prostheses survive to this day. In the field of *biomimetics* so-called biomorph ceramics are being investigated, in which the cellular structure of wood is replicated using ceramic materials.

The third example concerns **bones**, once again, a composite material. The matrix of the bone tissue is formed of collagen fibres and the reinforcement is calcium phosphate crystals. Bone does not fulfil the same functions throughout its life, and it is remodelled according to the loading it receives, it is a living material.

The structure is complex, although it may be idealised at distinct levels; at the microscopic level, the mineralised collagen fibres play the leading role. At the mesoscopic level these fibres are arranged in different ways giving rise to different types of bone. At the macroscopic level two types of structure can be identified, spongy (cancellous) bone and compact bone.

The mechanical properties depend, to a large extent, upon the relative density (quotient of the density of the bone and that of the walls). Various strategies have been applied to modelling; the analysis of a representative volume, using the techniques developed for cellular materials or modelling the bone numerically using finite elements.

Bone as a *biological material* has no relevance. As a *biomaterial*, it has. It is used for transplants and serves as a model for the fabrication of artificial prostheses, since it is essential to simulate, as closely as possible, the properties of the bone that it is to replace. The distribution of bone tissue in some bones –when the spongy bone is surrounded by compact bone– has provided inspiration in the area of *biomimetics*, since this bone architecture optimises the strength with a minimum weight possible.

Cartilage is investigated in the fourth example, in particular articular or hyaline cartilage. This is also a composite material, although between 70% and 80% of its weight is water. The cells that create and maintain it –called chondrocytes– are surrounded by a matrix formed of collagen and proteoglycans (hyaluronic acid and aggrecans).

The structure is hierarchical, but it may be considered, somewhat arbitrarily, as having two levels: At the microscopic level can be regarded as the composite material just mentioned, the collagen of the extracellular matrix forms a fine strong mesh which traps the proteoglycan molecules and carries the stresses due to the internal pressure. At the mesoscopic level an anisotropic heterogeneous structure is apparent, since the collagen fibres are distributed in different positions according to their distance from the contact surface.

As far as their mechanical properties are concerned, there is a strong time-dependency, and the pressure and internal fluid movement are also very important. For this reason emphasis is placed upon the role played by the osmotic pressure due to the difference in ionic concentration between the cartilage and the external fluid; cartilage covers the articulating ends of the bones and allows pressure transmission at the lowest possible values –the osmotic pressure reduces the external pressure– and with minimum friction. Two viscoelastic models for the study of the behaviour of cartilage have been proposed; the linear viscoelastic model and poroelastic models.

Cartilage as a *biological material* has no relevance. As a *biomaterial*, it has been of interest in eastern pharmacopoeia, as a remedy for a multitude of diseases. In the field of *biomimetics* it may be very interesting to reproduce and improve the mechanisms responsible for ultra-low friction.

3.1. MOLLUSC SHELLS

3.1.1. Introduction

Mollusc shells have piqued the interest of mankind since the earliest times; pierced shells –which were possibly parts of necklaces– have been found in Neolithic sites. It is known that shells –cowry shells– were also used as bargaining “money”, and pearls –a byproduct of shells– have always been coveted gems. The iridescent light reflected by pearls and the nacre of some mollusc shells form part of the attraction of these biological materials. However, it is the extraordinary mechanical properties of these materials which make them worthy of the special attention granted to them in this book.

Shells are organic matrix *composite materials*; between 95 and 99 per cent is calcium carbonate (in the form of aragonite or calcite) and the rest, between 1 and 5 per cent, is a protein matrix. Surprisingly, it is this tiny proportion of organic cement and a complex microstructure which confer on nacre, or mother-of-pearl, a resistance to fracture of a magnitude two or three times greater than that of aragonite or calcite.

The excellent mechanical properties of shells invite a study of their composition and microstructure in order to understand their strength and toughness. Moreover, mollusc shells can suggest means whereby brittle materials, such as aragonite, might be transformed into tough materials, if we know how to intelligently introduce the right matrices and to give them structure.

The word *mollusc* was introduced in the XVII century from the Latin *molluscus*, which means soft, and borrowed because of its similarity to the name of a thin-shelled nut called *mollusca*. However, its inventor also applied the name to barnacles, which are crustaceans, suggesting that it has never been easy to decide what is and what is not a mollusc, since they are extraordinarily varied; at the most humble extreme there are molluscs similar to worms and at the other we find fascinating creatures like octopuses. Currently, the mollusc phylum is divided into eight living classes, of which the three most important are *bivalves*, *gastropods* and *cephalopods*.

In *bivalves* the shell is composed of two parts; the valves, which are joined dorsally by an elastic ligament and articulated through a hinge. The valves are closed by means of powerful adductor muscles.

The most prominent characteristic of *gastropods* is torsion: at some point in their development, the part of the body containing internal organs rotates relative to the foot. (Some groups have reversed what appeared to be a strong evolutionary trend and undone the process). The shell of these molluscs also grows in a spiral, but through a different process, to gain more space for the visceral mass in a basically tubular shell. (Some groups have also reduced the shell or even lost it altogether).

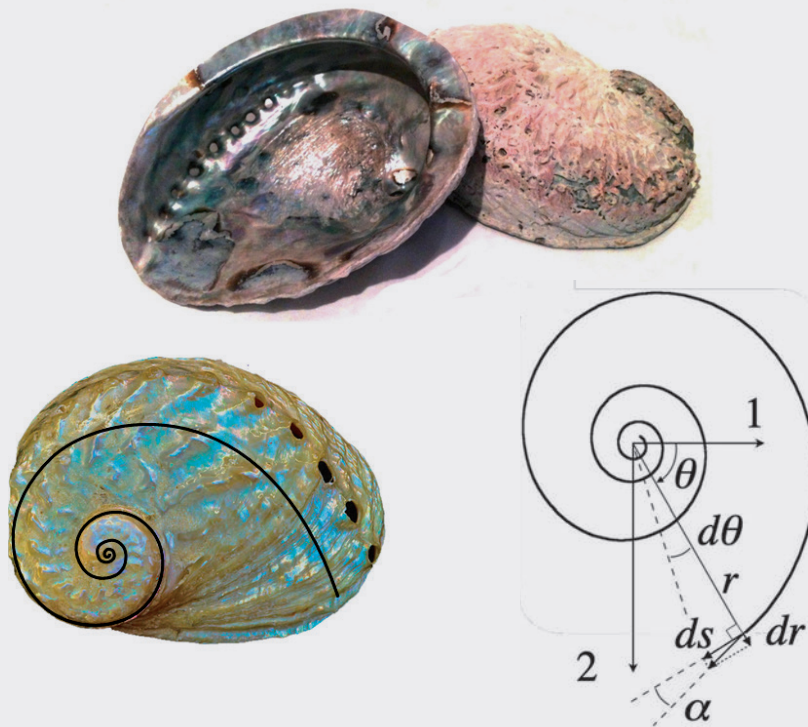
In present day *cephalopods* the shell is wound in the form of a spiral –like *nautiloids*– however, in the majority of cephalopods the shell is reduced or absent.

The architecture of the humble mollusc shell or the precious nacre of pearls has inspired new tough high-performance ceramic materials, but the information contained in mother-of-pearl does not end here. Mollusc shells have to perform as authentic protective barriers for the invertebrates; they must resist attacks from predators, withstand enormous pressures in the deep hydrothermal vents in which molluscs proliferate, or have the toughness required to stand the onslaught of waves in intertidal zones. Furthermore, they must combine their resistance with other functions; to facilitate the access of nutrients, eliminate waste, and allow growth and reproduction. To any engineer, the design of a material with all of these characteristics would create huge problems. Molluscs achieve it with common materials and water, at ambient temperature and under normal pressures (if we exclude those that live in the depths of the ocean, in hydrothermal vents), using the fundamental techniques of biomolecular engineering.

EXERCISE 27

In many snail shells and other gastropods it has been observed that the growth lines can be approximated to logarithmic spirals of the type $r = A \exp(B\theta)$, where A and B are constants and the variables r and θ are defined in the figure (Thompson, 1961).

Justify this assertion by assuming that, during the growth of the shell, in a time interval dt , the ratio of the supply of material in the radial direction and perpendicular directions, remains constant.

**SOLUTION:**

From the assumption, $dr/ds = \text{constant} = \tan \alpha$, where α is the angle between ds and the spiral.

Since $ds = r d\theta$, then:

$$\frac{dr}{r} = \tan \alpha d\theta$$

from which, by integration, we obtain

$$\ln r = \theta \tan \alpha + \text{constant}$$

or

$$r = \text{constant} e^{(\tan \alpha) \theta}$$

which is the expression given in the problem statement

A reader interested in the shapes of shells is encouraged to read, in addition to Thompson's classic book, the monograph by H. Meinhardt (2003).

3.1.2. Structure

Mollusc shells are formed of densely packed microscopic ceramic bricks, bonded with a fine biopolymer cement. The hierarchical structure of this biological material is the result of millions of years of evolution, and they are so well arranged that their strength and toughness are far superior to those of the ceramic from which they are made.

J.D. Curry (1974) has described the various types of microstructure from which the structure of many bivalve, gastropod and cephalopod shells may be fashioned. The casuistry is large and complex, and for that reason this chapter will focus only on the most representative structures which have been extensively studied; *parallel-lamellar structures*, typical pearly shells, and *crossed-lamellar structures*, very complex but common among molluscs with shells.

Parallel-lamellar structure

The two shells with this structure which have attracted the most attention are (Figure 3.1); mother-of-pearl (*Pinctada máxima*), of the bivalve class, and abalone (*Haliotis rufescens*), of the gastropod class.

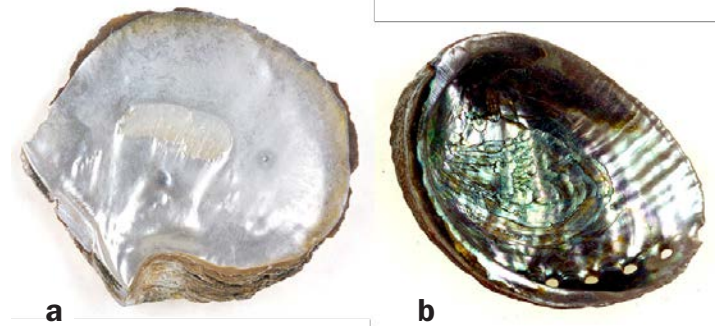


Fig. 3.1.1. a. Mother-of-pearl (*Pinctada máxima*).
b. Abalone (*Haliotis rufescens*).

The hierarchical structure of these shells, shown in a simplified form in Figure 3.1.2, spans six orders of magnitude; from millimetres to nanometres.

Figure 3.1.2a is a macroscopic section (note the millimetre scale) of a shell in which the following layers can be seen: A superficial layer, or periostrack. An intermediate layer formed of hard and brittle prismatic calcite grains. And an internal layer –mother-of-pearl or nacre– formed of a lamellar aragonite structure, not as hard but tougher than the calcite layer.

Figure 3.1.2b is a close-up, at the mesoscopic level (note the micron scale), of the previous figure. Growth bands

(possibly annual) of about 200 μm width, separated by denser zones of 20 μm , can be seen in the Figure.

A further enlargement, at the microscopic level (note the nanometric scale), of the previous figure is presented in Figure 3.1.2c, in which 200 nm thick aragonite ceramic laminae can be seen, (in other samples the thickness may be greater, up to 900 nm, and the average diameter oscillates between 5 and 8 μm) separated by 20 or 30 nm thick cement.

This structure is similar in the two cited shells. The principal difference lies in the stacking of the aragonite crystals: In the *Haliotis* shell the structure is laminar-columnar, as shown in the sketch in Figure 3.1.2c, in which the plates are almost superimposed (the common area is about 2/3 of the total area of the plate; Barthelat et al. 2007). In the *Pinctada* shells, the structure is laminar-irregular, in which the plates are stacked randomly, as has been attempted to indicate in Figure 3.1.2c.

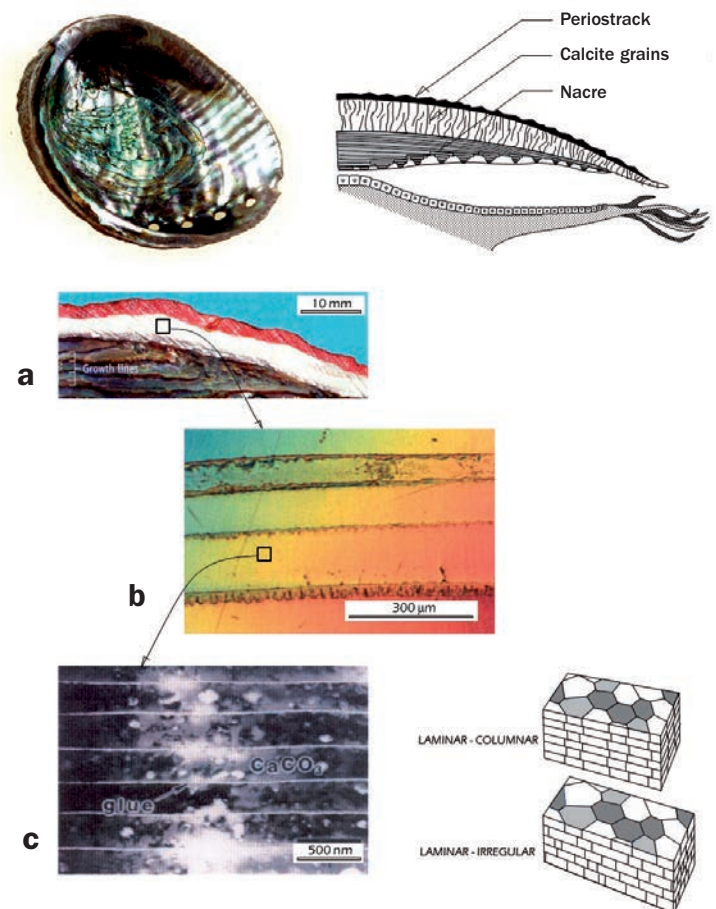


Fig. 3.1.2. Hierarchical structure of the shell of the *Haliotis rufescens*.
a. Macroscopic level (mm). Three layers.
b. Mesoscopic level (μm). Growth bands.
c. Microscopic level (nm). Aragonite cemented with an organic polymer.

Crossed-lamellar structure

Shells with a crossed-lamellar structure and which have been studied in most detail belong to the class of gastropods, specifically from the *Strombus* and *Conus* families, both represented in Figure 3.1.3.

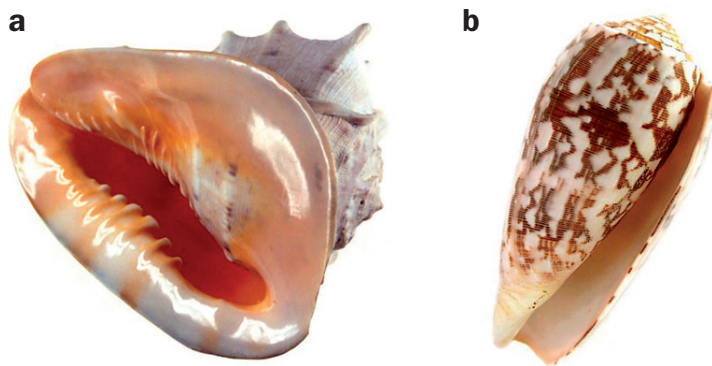


Fig. 3.1.3. a. Conch (*Strombus gigas*).
b. Cone (*Conus striatus*).

The shell which has attracted most attention, due to its size and beauty, is the Caribbean conch, *Strombus gigas*. Heuer and Li, among others, (Su et al. 2004, Ji et al. 2020), have performed a detailed study of its structure, whose most prominent features are described below.

The hierarchical structure of this shell is presented, in a simplified form, in Figure 3.1.4, spanning six orders of magnitude; from millimetres to nanometres.

The external layer is the *periostrack*, an organic membrane which protects the shell and provides a base upon which calcium carbonate is formed in a thin columnar sheet, some 2 μm thick, on which the crossed-lamellar structure will be built.

At the macroscopic level it is possible to distinguish three layers, indicated schematically in Figures 3.1.4a and 3.1.4b, known as internal, middle and external, and whose width can vary between 0.5 and 2 mm.

Within each layer, at the meso and microscopic levels, it is possible to observe three types of *lamellae*: those of the first order are shown in Figure 3.1.4b and are arranged in parallel in each sheet and perpendicularly between adjacent layers. Inside each first order lamella a second family can be found, whose transverse dimensions range from 5 to 60 μm width and 5 to 30 μm thickness. Between the adjacent first order lamellae, the directions of the second order lamellae are perpendicular to each other, (see Figure 3.1.4c). Next, second order lamellae are composed of another smaller

family, those of the third order, which are tiny aragonite crystals, whose cross sections oscillate between 140 and 300 nm wide by 130 nm thick (Figure 3.1.4d) and their length can reach several microns. Finally, small twins have been observed in the crystals.

The microstructure of the *Conus* family is similar to that described above; the shell wall is formed of three layers and in each one of them the distribution of the lamellae is also crossed-lamellar (Currey and Kohn, 1976).

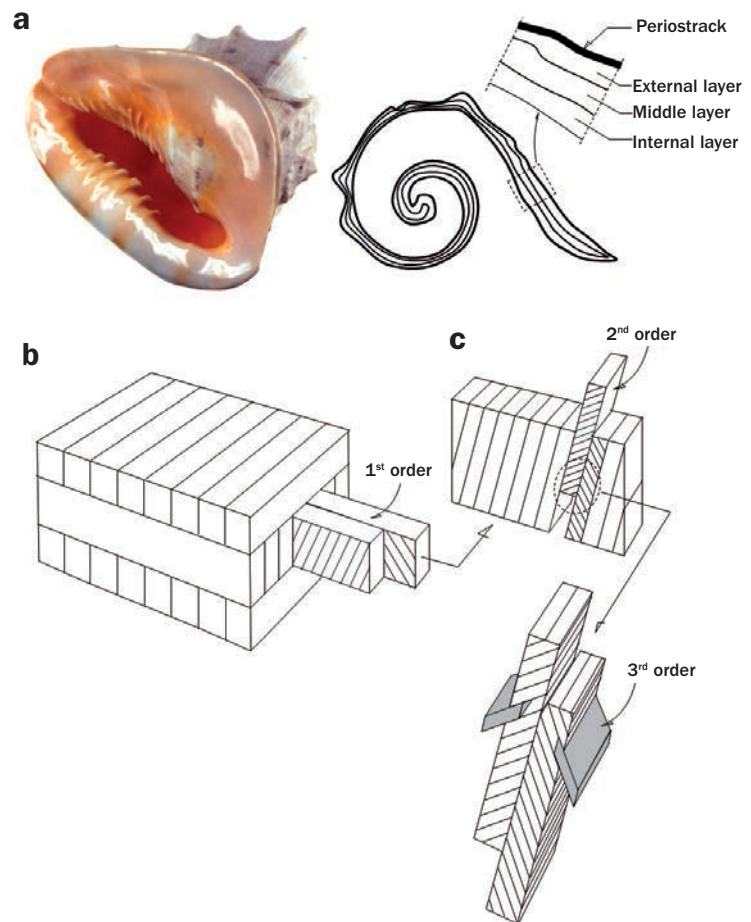


Fig. 3.1.4. Hierarchical structure of *Strombus gigas*.
a and b. Macroscopic level (mm). Three layers.
c. Second order lamellae (μm).
d. Third order lamellae (nm).

Bonding cement

The architecture of shells is a complex lattice of ceramic bricks bonded with a small amount of protein "mortar"; ranging from 0.1% to 5% of the total.

Studies performed on shell of the *Haliotis* family (parallel-lamellar structure) indicate that the organic mortar is not a homogeneous material, but one which possesses a sandwich structure (Sarıkaya et al. 1994, Meyers et al. 2008). The stiffer, middle part, is a polymer sheet rich in chitin. The lamina is covered in proteins, whose secondary structure are β leaves, and these are covered, in turn, with other proteins which are in contact with the ceramic bricks (the proteins contain aspartate which preferentially binds the calcium atoms of the aragonite).

In the case of shells of the *Strombus* family (crossed-lamellar structure) no such detailed study of the protein mortar that bonds the ceramic bricks has been made. The analysis performed by Osuna-Mascaró (Osuna et al. 2014) shows that the amount of protein material is less than that found in pearly structures (0.05% against 1% by dry weight). Another difference encountered is the near absence of chitin (at least in the part soluble in acids). The novelty was the discovery of mannose, the principal monosaccharide which occurs in the acid-soluble part.

The crossed-lamellar structure of shells is often considered to be the most successful from an evolutionary point of view and is characteristic of the biggest and heaviest shells. Nonetheless, as will be seen later, the resistance to fracture in bending tests is lower than that in shell with a parallel-lamellar structure, but its toughness is greater. One possible reason for this fact may be based upon the cost of shell calcification which is due, mainly, to the synthesis of the protein matrix rather than to the deposition of calcium carbonate. That is to say, molluscs which synthesise greater quantities of matrix use up more energy in producing and repairing their shells. From this perspective, it may be deduced that the inferior mechanical properties of crossed-lamellar structures when compared to shells with parallel-lamellar structures is offset by the energetic savings in the fabrication and repair of their shells.

Another issue associated with the protein matrix is related to biomimetics. If materials which imitate structures offered by nature are to be fabricated, it is essential to understand how the protein matrix manages to control the nucleation of inorganic crystals, their shape, size, and growth. Only in this way, when we have a better understanding of the role of the protein matrix, will it be possible to design materials which can effectively self-assemble the building blocks of materials of the future.

The types of specimens most commonly used to measure the quoted properties are shown in Figure 3.1.5. The tensile strength is usually measured directly on specimens with a reduced central section (“dog bone” type specimen) in order to avoid breaking at the grips. The shear strength is measured using special fixtures. Both types of specimen are shown in Figure 3.1.5a.

Measurement of the flexural strength involves specimens in the form a beam subjected, almost always, to three-point loading. The *parallel-lamellar* structure of shells suggested that the orientation of the laminas must be taken into consideration, as indicated in Figure 3.1.5b.

Measurement of the fracture toughness is usually made on specimens in the form of a beam with a central crack, attempting to imitate the type of specimen recommended in the Standards (ASTM, for example). It is also useful, in these cases, to consider the orientation of the laminas, as shown in Figure 3.1.5c.

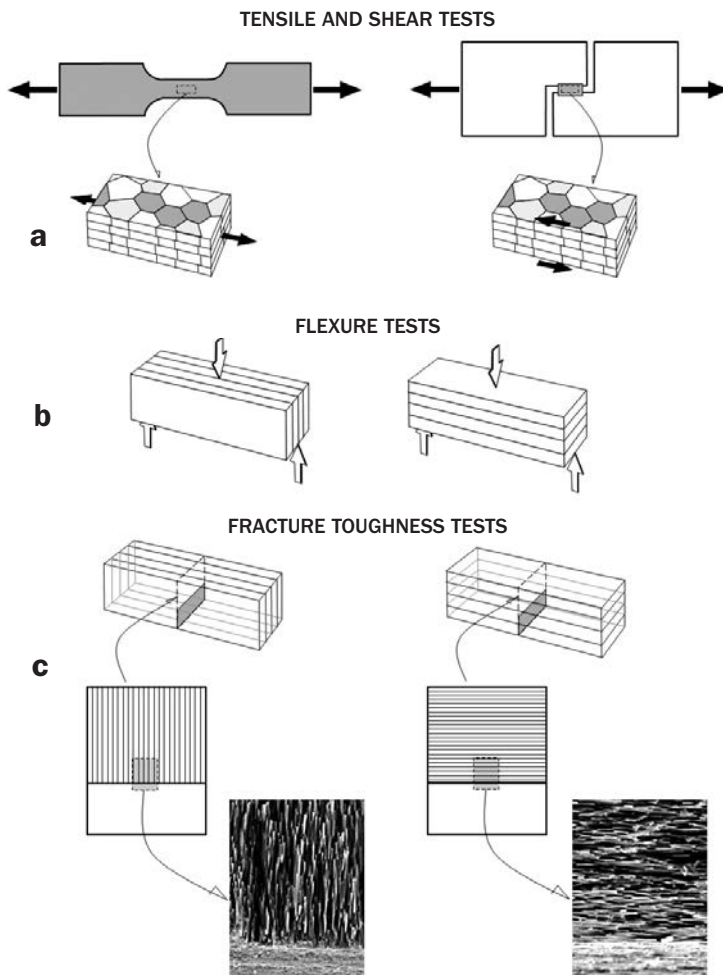


Fig. 3.1.5. a. Specimens for tensile and shear tests.
b. Specimens for flexural tests.
c. Specimens for fracture tests.

Several engineering stress-strain and load-deflection curves, representative of the tests mentioned above, are presented in Figure 3.1.6. Comparison between curves obtained by different authors is not straight forward for reasons already mentioned; the dispersion of the results due to specimen machining difficulties and different test conditions.

The **tensile** tests on *Haliotis* shells presented in Figure 3.1.6a (Barthelat et al. 2007) indicate a clear difference in the behaviour of dry and hydrated specimens. The tests were performed in the direction of the laminas (see Figure 3.1.5a) and represented two dry and two hydrated specimens. In the latter cases it can be seen that after unloading there is a permanent deformation. Also, corresponding curves of pairs of **shear strength** tests are shown in Figure 3.1.6a. Once again, the difference between dry and hydrated specimens is notable. Also, a significant residual deformation is apparent after unloading.

The effect of anisotropy in the **flexure** tests on *Haliotis* and *Pinctada* specimens (data from Wang et al. 2001) is apparent in Figure 3.1.6b. In both materials the behaviour is similar, both in the parallel and perpendicular directions. Tests were carried out with hydrated specimens.

A curve obtained from a **fracture** test on a wet *Haliotis* specimen (Barthelat and Espinosa, 2007) is shown in Figure 3.1.6c, in which it may be observed that there is some degree of linear-elastic behaviour before the initiation of failure. However, the increasing amounts of energy consumed during crack propagation—which has to proceed in a zigzag manner between the ceramic lamellae—makes the behaviour of the material deviate quickly from the linear-elastic fracture model (in which the energy consumed is constant during crack propagation). The results of numerous experiments on (dry and hydrated) *Pinctada* specimens performed by Jackson, Vincent and Turner (1988) are also included in the Figure. The Figure is illustrative because it supports the hypothesis mentioned above: experimental values of the specific fracture energy G_C (J/m²) are shown in the vertical axis and on the horizontal axis the values of G_C deduced from the expression $K_C^2 = E G_C$, which is valid only for the model of linear-elastic fracture behaviour. We see that, for the most part, the experimental data are far greater than those from the linear-elastic model. It must be borne in mind at both the values of G_C , as well as K_C , for hydrated specimens have been corrected, as if they were specimens with some degree of plasticity (see the quoted reference for more details).

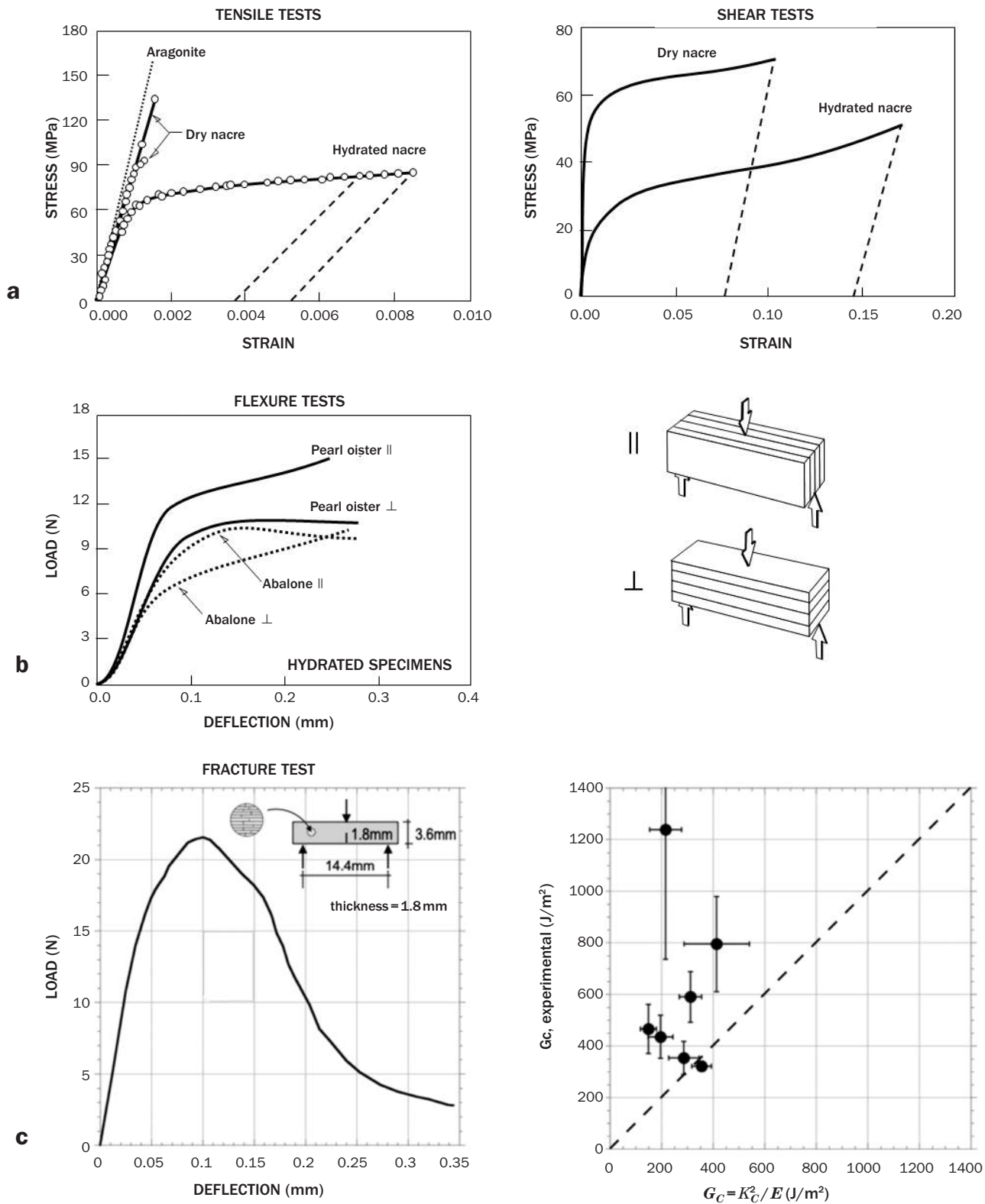


Fig. 3.1.6. a. Stress-strain curves obtained in tensile and shear tests; note the influence of the hydration of the specimen.
 b. Load-deflection curves, for nacre, obtained in flexure tests; note the influence of anisotropy.
 c. Load-deflection curves obtained in a stable fracture test. Correlation between the experimental and theoretical values of G_C .

In the quoted article, Jackson et al. (1988), an attempt was made to estimate the values of the elastic modulus, tensile strength and fracture toughness using highly simplified calculations based upon composite materials models developed in the 1970s. In contrast, more sophisticated models are also mentioned. These were more like structural calculations with finite elements, which allowed investigation of other aspects of the complex structure of mother-of-pearl, like those used by Barthelat et al. (2007).

Very simple models such as those of Voigt and Reuss, previously introduced in Section 2.3.3, may be used to predict the elastic modulus. For this, it is assumed that mother-of-pearl is a two-phase composite material: *particles* (aragonite plates) with an elastic modulus E_p and *matrix* (organic polymer) with an elastic modulus E_m . The relative proportions of both phases are V_p and $(1 - V_p)$. The Voigt model, which implies that both phases are in parallel and, therefore, undergo the same strain, yields an expression for the elastic modulus of the composite material E_c .

$$E_c = V_p E_p + (1 - V_p) E_m \quad (3.1.1)$$

The Reuss model, which implies that both phases are in series and, therefore, carry the same stress, produces the following expression for E_c

$$1/E_c = V_p/E_p + (1 - V_p)/E_m \quad (3.1.2)$$

Jackson et al., used the following values to calculate E_c : $E_p = 100$ GPa, $E_m = 4$ GPa and $V_p = 0.95$, values which are quite different from those measured experimentally; 62 GPa (dry conch) or 72 GPa (hydrated conch). These discrepancies are due to a number of causes, among these that neither model accounts for the distribution of stresses along the length of the plates (which are assumed to be infinitely long), nor the transverse shear modulus, G , of the matrix. For plates of finite length Padawer and Beecher (1970) proposed the following corrections to the Voigt model

$$E_c = V_p E_p [1 - (tg h(u)/u)] + (1 - V_p) E_m \quad (3.1.3)$$

where $u = s \{G V_p / [E_p (1 - V_p)]\}^{0.5}$, in which s is the ratio of the length to width of the ceramic plates. As can be seen, when the values of s and G are very large, Equation (3.1.3) tends to Equation (3.1.1). Even so, the model can be further refined if account is taken of the interactions between adjacent plates, according to Riley's model (Lusis et al. 1973). This new correction provides the following result

$$E_c = V_p E_p \{[1 - \ln(u + 1)]/u\} + (1 - V_p) E_m \quad (3.1.4)$$

Values of the elastic modulus of mother-of-pearl E_c according to Equations (3.1.1), (3.1.2), (3.1.3) and (3.1.4) are shown in Figure 3.1.7, as functions of the transverse shear modulus G of the matrix, together with the average experimental values for dry ($G = 4.6$ GPa) and hydrated specimens ($G = 1.4$ GPa), according to Jackson et al. In the curves it was assumed that $s = 8$ and the contribution of the second adding $(1 - V_p) E_m$ in front of the first has been neglected. It may be observed that the experimental values for hydrated specimens, 62 GPa (see Table 3.1.1) fall within the interval 58-72 GPa produced by the Riley and Padawar models. The same is true of the dry specimens, 72 GPa against 68-82 GPa.

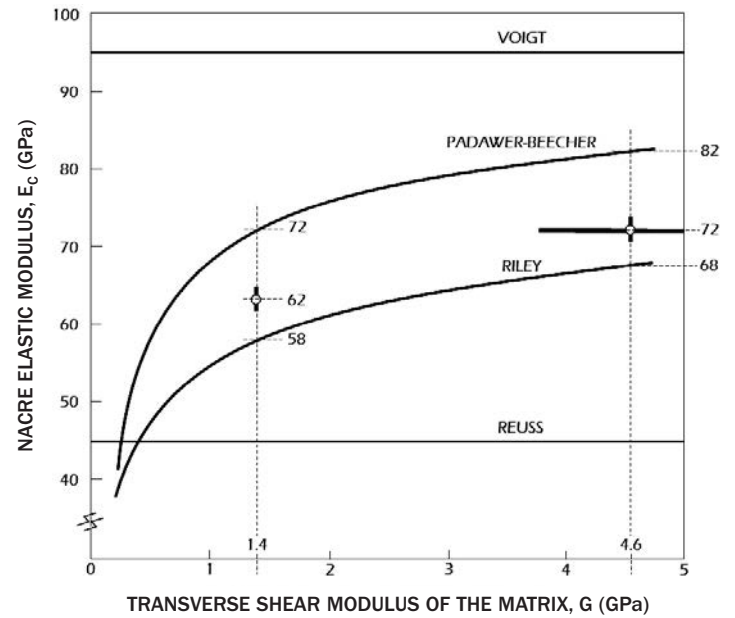


Fig. 3.1.7. Elastic modulus of mother-of-pearl as a function of the transverse shear modulus of the organic matrix, for various models.

EXERCISE 28

From the three-point bending test data presented in Figure 3.1.6c, determine if the assumption of liner-elastic behaviour is justified during specimen cracking, and estimate the values of the toughness and fracture energy of the material. Assume that, according to the authors, the elastic limit of the material is equal to its flexural strength, estimated at 70MPa, and that the generalised elastic modulus is $E' = E/(1 - \nu^2) = 50 \text{ GPa}$.

SOLUTION:

Standard test methods for measuring fracture parameters, and their validity conditions were discussed in Section 2.2.2. The specimen illustrated in Figure 3.1.6c is beam type, one of the standard geometries used in the ASTM Standard E1820. Equation (2.2.2-3) is used to calculate the value of the fracture toughness K_{I1} :

$$K_Q = \frac{6P_Q}{BW^{3/2}} \sqrt{\alpha} \frac{1.99 - \alpha(1 - \alpha)(2.15 - 3.93\alpha + 2.7\alpha^2)}{(1 + 2\alpha)(1 - \alpha)^{3/2}}$$

where P_Q is the crack initiation load, B the thickness, W the depth and $\alpha = a/W$ the relative depth of the crack (see Figure 2.14a).

To obtain the load P_Q at fracture initiation, the procedure shown in Figure 2.14c, and previously used in EXERCISE 9, is followed. With which the values $P_{max} = 21.6 \text{ N}$ and $P_Q = 15 \text{ N}$ are obtained. The value corresponding to the toughness (for $\alpha = 0.5$, $B = 1.8 \text{ mm}$ and $W = 3.6 \text{ mm}$) is $K_Q = 1.48 \text{ MPa m}^{1/2}$.

To verify that K_Q can be taken to be a proper value of K_{IC} we perform the checks set out in the standard:

- first, we see that $P_{max} / P_Q = 1.4 > 1.1$, does not satisfy the linearity requirement before the peak load
- on the other hand

$$B = b = W - a = 1.8 \text{ mm} > 2.5 \left(\frac{K_Q}{\sigma_{ys}} \right)^2 = 1.1 \text{ mm}$$

which does meet the requirements of the standard.

Since we do not have a valid value of K_{IC} , we calculate the fracture energy G_C using Equation (2.2.2-7). The value of J_{pl} is obtained using Equation (2.2.2-8) from the area A_{pl} of the force-deflection curve up to the maximum load (see the Figure)

$$J_{pl} = \frac{1.9A_{pl}}{B(W-a)} = 545 \text{ J/m}^2$$

with which we obtain, from Equation (2.2.2-7)

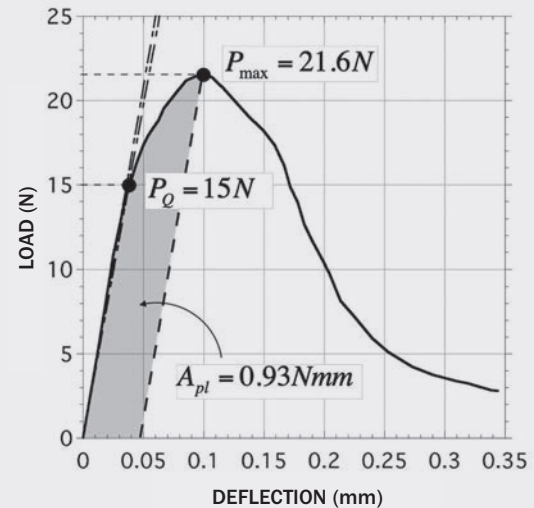
$$G_C = \frac{K_Q^2}{E'} + J_{pl} = 44 + 545 = 589 \text{ J/m}^2$$

Finally, the checks of Equation (2.2.2-13) give

$$B = b = 1.8 \text{ mm} > \frac{25G_C}{\sigma_{ys}} = 0.2 \text{ mm}$$

which indicates that the calculated value of G_C is valid, according to the Standard.

The calculated value of the fracture energy for this material (*Halotis* shell in the hydrated state, Table 3.1.1) is in good agreement with data from other authors and is almost two orders of magnitude greater than that of the ceramic base material (aragonite). We also see that the most important contribution to the value of the fracture energy is that due to the plastic part, in line with Figure 3.1.6c.



Currently, thanks to increased computing power, better detailed models are available for simulating the microstructure more accurately, allowing reproduction of the stress strain curves rather than just maximum, or rupture values, such as in the quoted article by Jackson et al. (1988). The curves, obtained from the tensile and shear tests, and shown in Figure 3.1.6a, were reasonably reproduced with the finite element model proposed by Barthelat et al. (2007).

Various studies of the behaviour of nacre in **tensile** test indicate that the principal mode of deformation is sliding of the ceramic bricks, which can be considered linear-elastic, and that there is an inelastic component which is due to the mortar which bonds them. The tensile stresses are transmitted between the bricks through shear stresses in the regions of overlap between the bricks. When these reach a maximum stress the bricks stop sliding over each other and gaps are created (Barthelat et al. 2007). The hardening, which is observed when the strain in the hydrated specimen is increased, has been attributed to several causes; the nature of the interface, the presence of nanometric asperities on the faces of the bricks (Evans et al. 2001) and waviness, at the micron scale, of the bricks (Barthelat et al. 2007). Judging from numerical simulations, the last mechanism seems to be the dominant one.

The model proposed by Barthelat et al., consisted of studying a representative volume element of the material, formed by ceramic tablets embedded in a cohesive matrix. The size, shape and distribution of the tablets was obtained from optical images (an example of which is shown in Figure 3.1.8a). A three-dimensional finite element model of two adjacent layers, which reproduced an area of nacre of 72 x 78 mm, was based up on these contours. Two types of boundary between the tablets were considered; horizontal *interfaces* and vertical *joints* (Figure 3.1.8b). The bricks (tablets) were modelled as transversely isotropic linear-elastic solids, with property data corresponding to aragonite crystals (with 5 elastic constants). The cohesive elements were located in both the interfaces and the joints. The chosen parameters were based on the mechanisms associated with the behaviour of biopolymers, the nano-asperities and the small mineral bridges between the tablets. A representation of the cohesive function used is provided in Figure 3.1.8b.

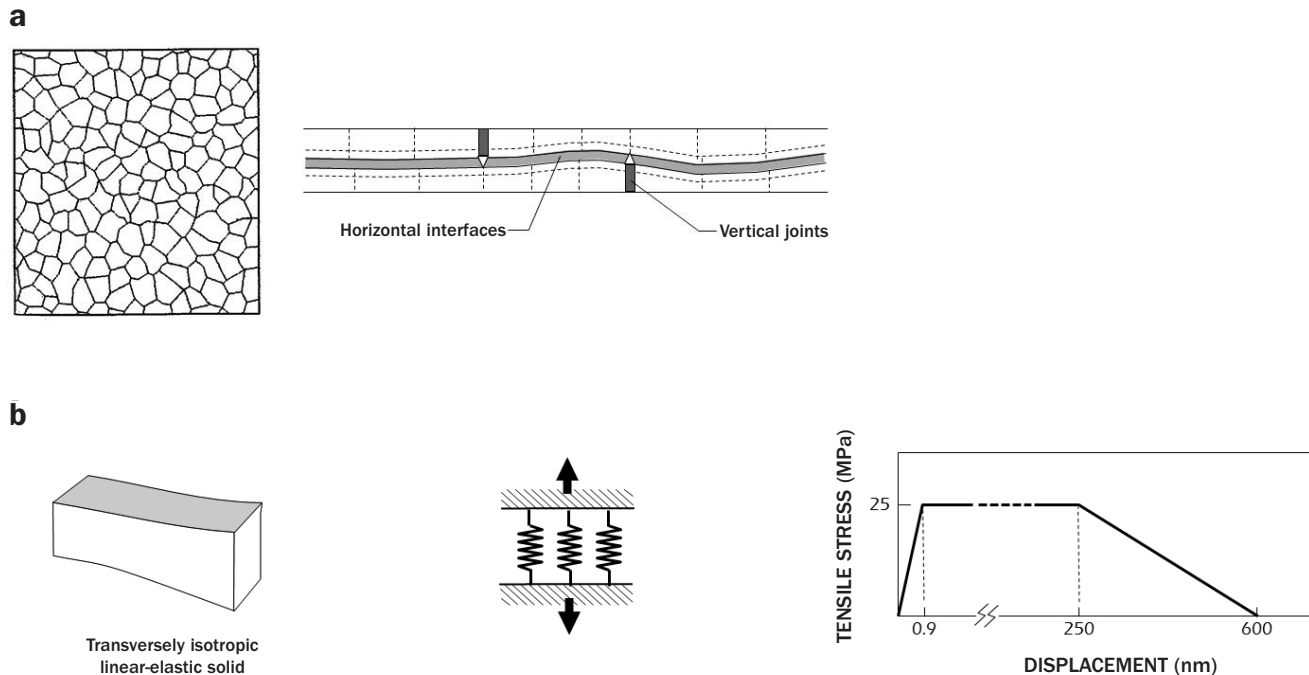


Fig. 3.1.8. Model of mother-of-pearl (Barthelat et al. 2007).
a. Plant and transverse section of the model.
b. Details of the cohesive model for the joint material.

The most significant results obtained with this model are illustrated in Figure 3.1.9a; the presence of waviness provides good agreement with the experimental results. However, when the tablets are flat the calculated strain is much lower. The influence of the *joints* (see Figure 3.1.8b) is reflected in Figure 3.1.9b. In the initial part of the curve it is observed that the joints increase the stiffness of the mother-of-pearl (when removing them the initial modulus falls from 70 GPa to 40 GPa) and the strength is also reduced when they are not considered. Note that, even though the joints add stiffness and strength, they do not appear to influence the strain hardening (since both curves are practically parallel). Another interesting aspect is that this model allows investigation of the *distribution* of the platelets; whether regular or random. To this end an ordered distribution of hexagonal platelets of the same area was studied. The results are shown in Figure 3.1.9c for hexagonal platelets with, and without, surface undulations. In both cases the results are significantly different from those of the experiments, and demonstrate the importance of incorporating randomly distributed platelets in the microstructural design of materials aimed at imitating shells.

Perhaps, the most interesting result of this study is the importance of surface undulations in the platelets. Previously, various explanations were given to justify the strain hardening in hydrated mother-of-pearl; nanometric asperities (Evans et al. 2001, Wang et al. 2001) and the interfacial strength. The asperities can account for hardening by sliding up to 15 or 20 nm, but not for the 100 or 200 nm observed. The strength provided by the biopolymer interfaces, certainly, contributes to strain hardening, but it alone is not sufficient (Barthelat et al. 2007). The undulations in the platelets appear to be able to explain this effect.

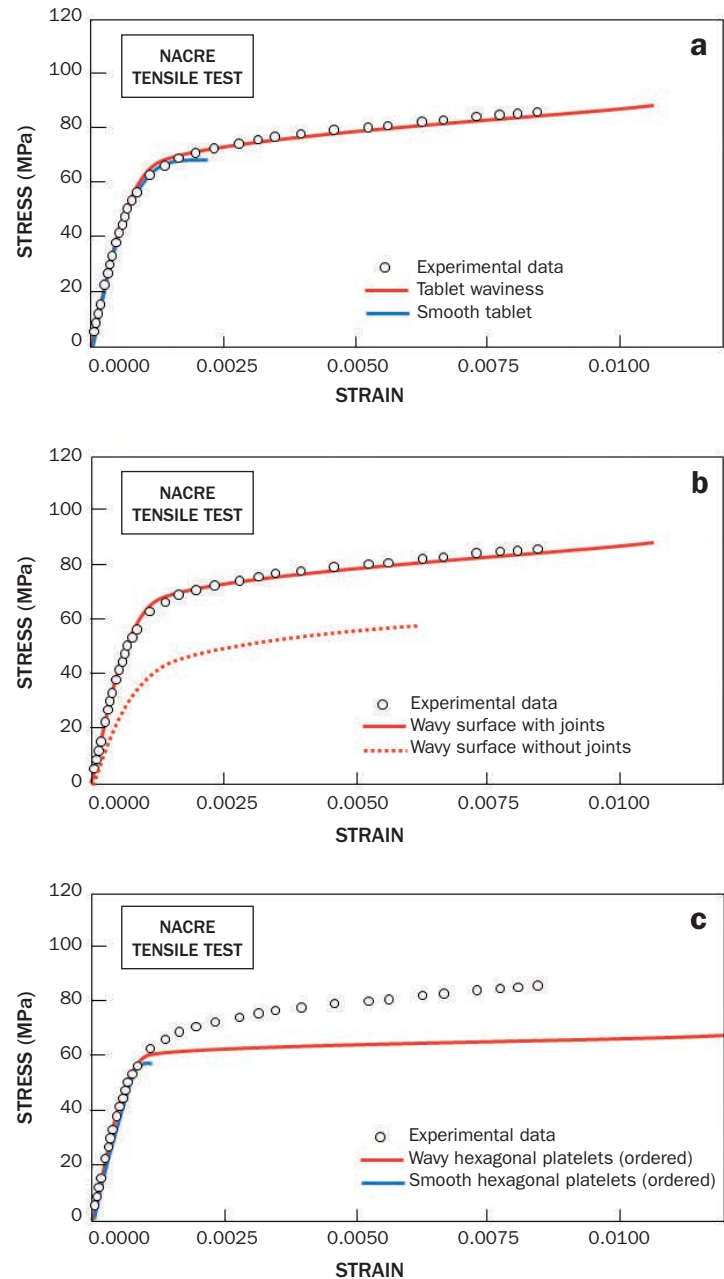


Fig. 3.1.9. Stress-strain curves. Circles; experimental data. Curves; numerical data from the model of Barthelat et al.
a. Influence of waviness of the tablets.
b. Influences of the vertical joints.
c. Influence of the distribution of the ordered tablets.

Values of the mechanical properties of gastropod shells, specifically of *Conus striatus* and *Strombus gigas*, are presented in Table 3.1.2. If the values are compared to those in Table 3.1.1, corresponding to bivalves (*Haliotis* and *Pinctada*), it may be observed that the specific fracture energies are much greater, while the flexural strengths are less; approximately half. All of this seems to suggest that the *crossed-lamellar* structure provides greater toughness than the *parallel-lamellar*, but with lower flexural strength.

The data in Table 3.1.2 also illustrate the influence of humidity and loading rate upon the values obtained. These aspects will be discussed briefly, below, using experimental data obtained from *Strombus gigas* shells.

TABLE 3.1.2 MECHANICAL PROPERTIES OF THE CROSSED-LAMELLAR STRUCTURE

SHELL	INITIAL MODULUS E (GPa)	FLEXURAL STRENGTH σ_{FT} (MPa)	COMPRESSIVE STRENGTH σ_C (MPa)	FRACTURE ENERGY G_C (J/m ²)	REFERENCE
Conus		70 – 200 (3P)			Currey, Kohn (1976)
Strombus		100 (4P)			Laraia, Heuer (1989)
Strombus	60	56 ± 22 (4P) (84 ± 49)*		4000 ± 2000 (13000 ± 7000)*	Kuhn et al. (1996)
Strombus		29 – 74	166 – 218 (249 – 361)**		Menig et al. (2001)

3P, 4P Tests on beams under three- or four-point loading.

* Tests on dry specimens.

** Dynamic tests (10 – 25) · 10³ GPa/s.

Figure 3.1.10a contains stress-strain curves from compression tests on specimens loaded in different directions; with the outer face of the shell (shaded in the Figure) perpendicular and parallel to the loading direction (Mening et al. 2001). The results indicate that the strength is greater when the load is parallel to the external surface. In all of the tests there was quite a lot of scatter, but the average values obtained (shown in Table 3.1.2) were 166 MPa in the perpendicular and 218 MPa in the parallel directions. These tests were performed slowly; between 3 and 300 MPa per second. When they were repeated at higher velocities, between 10,000 and 25,000 GPa per second, the values obtained were 50% greater; 249 MPa in the perpendicular and 361 MPa in the parallel directions. All of these results are for dry specimens.

Force-deflection curves for dry and hydrated specimens in four-point bending tests (Kuhn-Spearing et al. 1996) are shown in Figure 3.1.10b. The relative position of the external load is shown in the adjoining Figure. It can be seen from the curves that the hydrated specimens are more flexible. The average values of the maximum stress (calculated assuming linear-elastic behaviour) were 56 ± 22 MPa (from 13 dry

specimens) and 84 ± 49 MPa (from 9 hydrated specimens). These curves were used to estimate the specific fracture energy from the procedure indicated in Section 2.2.2; measuring the area under the curve and dividing it by the specimen cross-sectional area (a fairly approximate process because of the difficulty in determining the fracture area bearing in mind the profusion of cracks created in the test). The values obtained were about 4 ± 2 kJ/m² (from 11 dry specimens) and 13 ± 7 kJ/m² (from 8 hydrated specimens). A schematic representation of the appearance of cracks in the inner layer is provided in the adjoining figure, together with subsequent bifurcations as they penetrate the middle lamellae which have a different orientation. The large toughness of shells with a crossed-lamellar structure seems to be due to several factors, among these are; crack bifurcation, formation of bridges between the cracks and sliding between the lamellae. All of the elements mentioned when describing the microstructure come into play in these processes; the three layers and the first and second order lamellae, at least. This analysis may serve as the inspiration for the design of high-performance ceramics if the advantages of structuring the material at different scales can be included. For example, overlapping alternating laminas (stacking sequence 0/90/0 degrees) and within each lamina, incorporating sub-laminas with a stacking sequence of ± 45 degrees.

Finally, Figure 3.1.10c contains force-deflection curves from a four-point bending test (Kuhn-Spearing et al. 1996). It may be observed that the behaviour is far from being linear-elastic and that, moreover, it exhibits hysteresis, even when the loads are not high (compared with those of Figure 3.1.10b). All of this must be borne in mind when interpreting data from tests with these types of biological materials in which certain simplifying assumptions must be made when attempting to interpret the results.

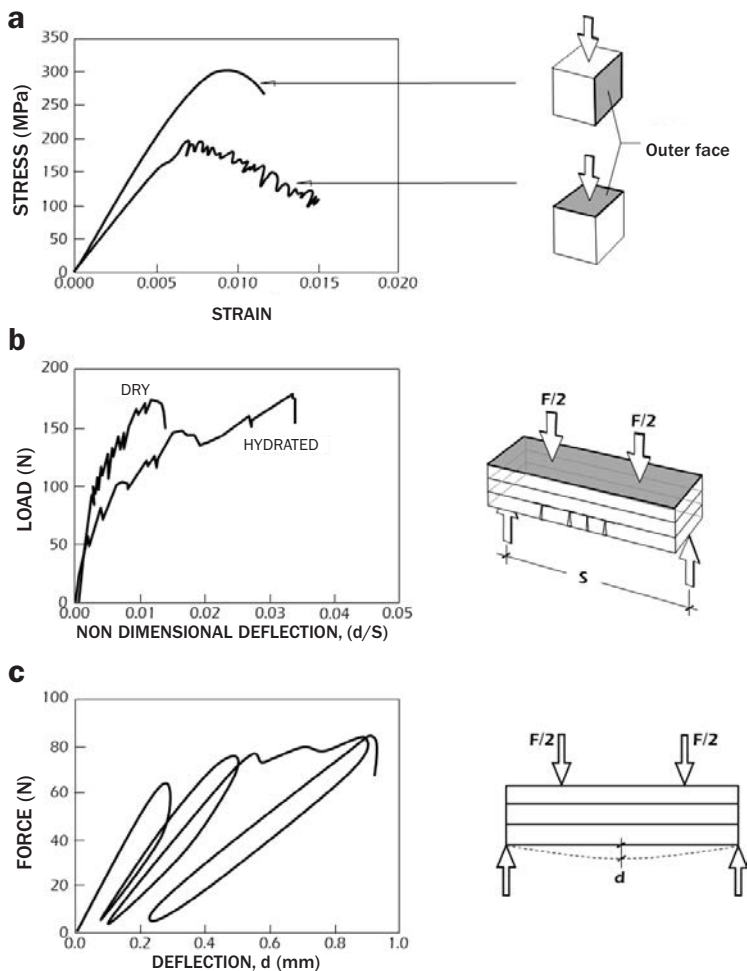


Fig. 3.1.10. *Strophomena gigas* shells.

a. Stress-strain curves obtained in compression tests. Note the orientation information.

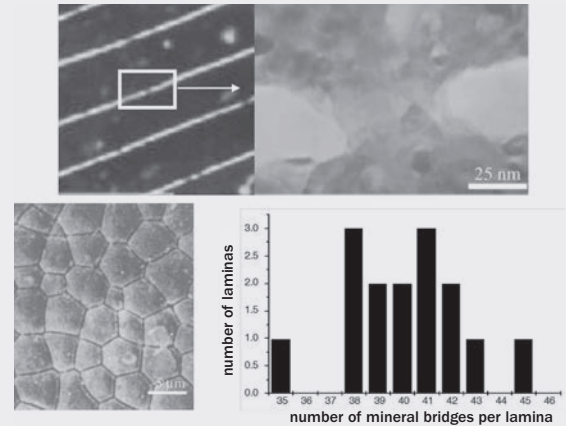
b. Force-deflection curves obtained in four-point bending tests. Note the influence of hydration.

c. Force-deflection curves obtained in four-point bending tests. Note the hysteresis.

EXERCISE 29

For a parallel-laminal structure, it has been proposed that the tensile strength in a direction perpendicular to the laminae is due, to a large extent, to the presence of mineral bridges between the laminae. An acceptable value for this strength is 3 MPa (Meyers et al. 2008). Song et al. (2003) have measured the size and number of these bridges, whose image is shown in the Figure.

Assuming, that the bridges are approximately cylindrical, calculate their fracture stress and discuss the possible presence of defects within them.

**SOLUTION:**

From the Figure in the problem statement we see that the average number of bridges per lamina is $n = 40$, and that the laminae have an average diameter of approximately $l = 4.5 \mu\text{m}$. With these values we can estimate that the average force required to break the bridges will be

$$F = \frac{\sigma_c}{n} \frac{\pi l^2}{4} = 1.19 \mu\text{N}$$

where $\sigma_c = 3 \text{ MPa}$ is fracture stress of the interface as measured by Meyers and co-workers.

Estimating, also from the Figure in the problem statement, an approximate bridge diameter of $D = 50 \text{ nm}$, the breaking stress of these will be

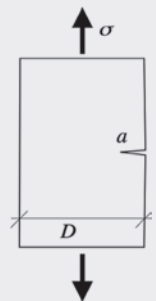
$$\sigma_R = \frac{F}{\pi D^2/4} = 0.5 \text{ GPa} \text{ which is the required fracture stress.}$$

In order to consider the presence of defects which might have been the cause of failure of the mineral bridges, we compare the value obtained in the calculation with the theoretical strength of the crystal, whose value is estimated at $\sigma_{teor} \approx E/30$, where E is the elastic modulus of the material (Hertzberg, 1996).

From Table 3.1 we see that $E_{\text{aragonite}} = 50 \text{ to } 100 \text{ GPa}$, which yields a theoretical strength lying between 1.7 and 3.3 GPa, values vary far beyond the strength.

We conclude, therefore, that the rupture stress of the mineral bridges must be affected by the presence of defects which reduce their strength.

If the rupture of the mineral bridges occurs due to brittle fracture, it is possible to estimate the size of the defects present, with the aid of the fracture mechanics model shown in the Figure below. In it, the defect has been idealised as a small crack in the surface of the bridge since, if the crack were deep, it would have probably been detected in the electron microscope images.



For this configuration the value of the stress intensity factor is $K(\sigma, a) = 1.12\sigma\sqrt{\pi a}$

Using the linear-elastic fracture criterion $K = K_C$ (Equation 2.2.2-1) and a value of $K_C \approx 1 \text{ MPa}^{1/2}$ we find that the size of the crack which produces failure at a stress σ_R

$$a = \frac{1}{\pi} \left(\frac{K_C}{1.12\sigma_R} \right)^2 = 1015 \text{ nm} \text{ which we see is several orders of magnitude greater than the size of the mineral bridge mineral itself.}$$

Even if we were to refine the model it would be difficult to justify a mechanism of failure by brittle fracture, so that it seems reasonable to assume that, either there will be some other damage mechanism, or perhaps that the material properties of the mineral bridges do not correspond exactly to those of crystalline aragonite.

3.1.4. Final remarks

Mollusc shells offer us the possibility of considering their wider application from three points of view; as *biological materials*, as *biomaterials* and as models for *biomimetics*.

As **biological materials**, shells have enjoyed little practical application but are highly valued as decorative items and jewellery. One of the few references to the practical use of shells is that of B.G. Moir (1990), in which he comments on the inhabitants of the Takuu atoll, in New Guinea, using the giant shells of the *Tridacna gigas* (which can measure up to 1 metre and weigh 300 kilos) to fabricate knives and hoes, due to a lack of suitable minerals in the atoll. With this exception, the mother-of-pearl of shells, for decorative uses, and the pearls, in jewellery, are the most known applications of some shells.

Pearl has been recognised as a gem since the earliest times because, as well as its rarity and mysterious origins, it has been attributed with healing powers; virtues symbols and mystical properties. It appears that the custom of adorning oneself with pearls has its origin in India, from which the Phoenicians introduced it to Europe. The Greeks called pearls *margarites*, and there are those who think that this comes from the Persian *murwari*, which means daughter of light. The harsh reality is that the pearl is the response of the mollusc to the irritation produced when a material enters from outside its shell. To protect its delicate tissue the mollusc coats the foreign body with fine layers of calcium carbonate. Currently, pearls do not have as much value as in the past because the majority of them are now cultivated and produced in large quantities. The most prized are those cultivated in seawater. Those cultivated in freshwater are smaller (between 3,5 and 7 mm), often asymmetrical, and less brilliant and their production is widespread (more than 1500 tonnes per year). The iridescent colours of the light reflected by the mother-of-pearl is another of the attractions of the shells used for decorative purposes. This special glow –also called *oriente*– is due to the process of optical interference when light rays pass through and are reflected in the fine layers, whose thickness is of the order of the wavelength of visible light.

Shells, as a **biomaterial**, have also been used since ancient times. In 1931 a fragment of jaw, from the Mayan civilisation, was found with dental implants made of mother-of-pearl. X-rays showed that the roots of the implant were well integrated into the bone. The discovery was made by the archaeologist couple, Dorothy and Wilson Popenoe, during an excavation at the *Playa de los Muertos*, in the Ulua valley in Honduras. The jaw, dated to around 600 AD, belonged to a young woman who was about 20 years old. She had three implanted mother-of-pearl incisors, which were initially believed to have been inserted after death, but a detailed X-ray analysis showed that compacted bone had formed around the implants (Bobbio, 1972).

Recently, Evelyn López and co-workers (Atlan et al. 1997) used the *mother-of-pearl* of the mollusc *Pinctada maxima* as a biomaterial; they ground it finely and mixed it with the blood of eight patients, women between 45 and 55 years old, who had suffered bone loss in the upper jaw. This solution was injected into the tissue affected by the bone loss and these were biopsied after six months. The results showed that there was no inflammation, and that the mother-of-pearl had been accepted by the tissue, as if it were the bone of the patients themselves. Furthermore, the osteoblasts (specialised cells which secrete the bone matrix) were activated and formed healthy bone tissue in the implant. The new bone tissue remained welded to the mother-of-pearl particles without any intermediate soft or fibrous tissue. The osteoclasts (cells which participate in the process of bone tissue absorption) remained active around the bone, but did not interact with the mother-of-pearl.

As **models for biomimetics**, mollusc shells suggest procedures by which brittle materials, such as aragonite, can be transformed into tough materials, if they can be suitably structured and bonded. Nature has done this, improving and refining these structures over millions of years. The Science and Engineering of Materials attempts to take advantage of these findings through a new branch, the interdisciplinary area of *Biomimetics* (Crossman et al. 2019).

The first attempts at the biomimetics of shells date to the 1980s and 1990s (see, for example, Meyers et al. 2008). Imitating the structure of mother-of-pearl, they fabricated pieces of silicon carbide (SiC) which were much tougher than conventional forms. Working on SiC small plates coated in graphite, they managed to increase the fracture toughness from 4 up to 18 MPa m^{1/2}, and the fracture energy went from 30 to 6000 Jm⁻². In this new material the SiC took on the role of the aragonite and the graphite that of the protein glue.

Monolithic fibrous ceramics are a second generation of tough ceramics, developed at the beginning of this century. The excellent properties of these materials result from their design (at the micron scale), their structure (small strong hexagonal bricks), and the fine but weak adhesive which bonds the bricks. Silicon nitride Si₃N₄ cells –in the form of 250 µm diameter fibres– are cemented in a 10 to 20 µm thick boron nitride BN mortar. The rupture modulus of this material is about 510 MPa at ambient temperature and about 290 MPa at 1300°C. The laminates formed of Si₃N₄ bonded with BN, also exhibit excellent fracture behaviour, almost two orders of magnitude greater than monolithic Si₃N₄.

A third, even more promising generation, developed by Deville et al. (2007), is based upon *freeze casting*. On freezing an aqueous solution of ceramic material, the ice crystals expel the ceramic particles and form ice columns and laminae several microns thick. By sublimating the ice a ceramic lattice is left, which can be infiltrated with a polymer or metal. Using this technique, Ritchie and co-workers (Munch et al. 2008) fabricated materials which imitate the structure of mother-of-pearl; manufacturing an alumina scaffold (by freeze casting), sintering it and then infiltrating it with an alloy of aluminium and silicon. The mechanical properties achieved are impressive; flexural strength between 120 and 210 MPa, fracture toughness values of 5 MPa m^{1/2} (for crack initiation) and G_C values between 5 and 8 kJ/m² (obtained from the area under the force-deflection curve). These properties have been improved upon by increasing the contact between the aluminium alloys and the alumina, and adding small amounts of titanium to the alloy they managed to reduce the surface tension and improve impregnation. With 0.5% of titanium the fracture toughness was increased 10 MPa m^{1/2} and the strength approached 600 MPa. Possibly, by reducing the surface tension the aluminium alloy infiltrated more effectively. In the article by W. Gao et al. (2020) there is a summary of this *freeze casting* technique.

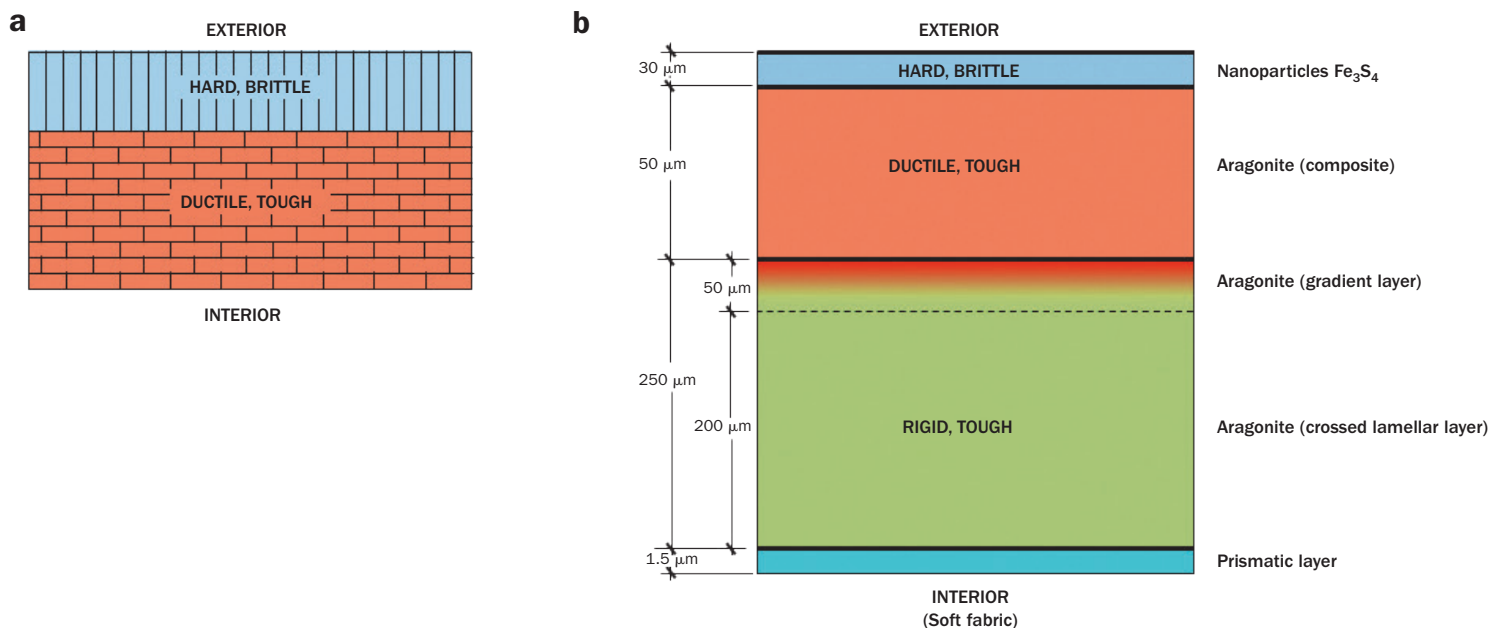


Fig. 3.1.11. a. Cross-section of an armour.
b. Cross-section of the *Chrysomallon squamiferum* shell

It is worth noting that, although the microstructure of these artificial materials is similar to that of the shell biological materials, the fracture mechanisms are different. It has been observed that one of the most effective mechanisms in the fracture of mother-of-pearl is *pull-out* of the rather rigid, wavy, bricks, a mechanism which is more effective when the shell is hydrated because the mortar is more ductile and facilitates this process. However, in the artificial materials it is believed that the dominant mechanism is the plastic deformation of the aluminium bricks.

Molluscs have developed a shell structure which is highly effective in resisting the impact of predators, very similar to military armour. A simplified form of the cross-section of armour (Sánchez-Gálvez, 2012) is shown in Figure 3.1.11a; the external layer is a hard, brittle material (almost always a ceramic) in order to splinter the projectile and the internal layer is a tough, deformable, ductile material (steel or aluminium) to absorb the excess kinetic energy of the projectile. Note the similarity of Figure 3.1.11a to the cross-sections of the shells shown in Figures 3.1.2a and 3.1.4a, in which the external layer is formed of calcite (a brittle material) columns and the interior is a lamellar structure composed of bonded aragonite (a more ductile tough material) plates.

The external layer does not have to be monolithic, it may also imitate the structure of mother-of-pearl, such as in the LAST® armour, manufactured by Foster-Miller, and which consists of hexagonal SiC or B₄C tiles wrapped in Kevlar® and joined tightly with a Velcro® type adhesive, which facilitates the repair of the armour when a plate is broken.

Mollusc shells which survive at great depths in the presence of hot springs may possess special structures to withstand such aggressive conditions, structures that are worth investigating. With this in mind, C. Ortiz and co-workers studied the shell of the gastropod *Chrysomallon squamiferum*, which lives in hydrothermal chimneys more than 3000 m deep (Yao et al. 2010). The cross-section of a representative fragment of the shell is shown in Figure 3.1.11b, where three layers unlike other known shells can be distinguished: An intermediate layer of organic material, relatively thick and flexible, is paired with two rigid, highly-mineralised layers; the exterior rich in iron sulphide and the interior formed of aragonite.

The authors of the quoted article modelled the structure using finite elements, considering an elasto-plastic behaviour in each layer, and obtaining values of the elastic modulus and elastic limit for each layer from nano-indentation tests. They simulated the response of the shell subjected to an external indenter and demonstrated that cracks may initiate in the internal aragonite layer. When these cracks progress towards the exterior they may be blocked by the, more ductile, intermediate layer. The thin external layer –a material composed of iron sulphide nanoparticles (about 20 nm in diameter) embedded in an organic matrix– it seems that they take on a role as the first line of defence against impacts.

Mollusc shells provide a good example of how Nature designs both a material and a structure. Materials engineers should keep this in mind when designing new materials; thinking not only of the material in isolation, but rather as in integral element of the structure.

3.2. WOOD

3.2.1. Introduction

Wood is one of the oldest biological materials. Ancient uses, as a *biological material*, were in structural applications and also as *biomaterial* as evidenced by the wooden prosthesis for the big toe of an Egyptian woman who lived more than 2,600 years ago.

It should be noted that the word *material*, derived from the Latin *materia*, was used to designate the wood from a tree; specifically, the trunk of trees that were used in construction.

Wood possesses very interesting mechanical properties, as will be seen later, especially when specific properties (that is, per unit mass) are considered, because under this criterion they can approach values comparable to steel. The mechanical properties exhibited by wood are due to the hierarchical structure of its components. Optimised by Nature over millions of years, trees have had to withstand adverse loads (wind, weather, predators, ...).

Currently the annual production of wood is more than 1,500 million tonnes, a similar quantity to that of steel. About 20% of this production is for structural purposes; beams, posts and panels. Other uses range from paper to furniture, boats, and musical instruments (L García Esteban et al. 2002).

Trees are the tallest and longest-living lifeforms populating our planet.

Among the oldest trees are the sequoias (*Sequoia sempervirens*), which have survived in the natural state only in North America. One of them (the Founder's tree) is 112m high (in October 1996) and a little over 500 years old, another (the General Sherman) is 85 m high with a base circumference of 24 m.

A Rocky Mountain pine (*Pinus aristata*, called Methuselah) is one of the oldest trees; it has lived for 4,700 years, at an altitude of 3,050 m, but is only 12m tall. A dragon tree (*Dracaena draco*), in the Canary Islands, could be more than 6,000 years old. The baobab tree (*Adansonia digitata*), in Kenya, could be 5,000 years old, with a 40m base circumference. The oldest giant sequoias could be over 4,000 years old. In Tasmania, there is a royal holly (*Lomatia tasmania*) whose shoots come from a mother stock which is still alive after 40,000 years. This tree was a contemporary of Upper Paleolithic humans (B. Fischesser, 2009). In Europe, it is possible that the oldest tree is a pine, in Bosnia (*Pinus heldreichii*), which could be 1,075 years old (New Scientist 27.08.2016).

The structure of wood, its mechanical properties and principal applications are briefly described below.

3.2.2. Structure

Trees are classified into two families; *coniferous* plants (gymnosperms, or softwoods,) and *leafy* plants (angiosperms, or hardwoods).

Coniferous wood contains cells, called *tracheids*, which serve three functions: transport of sap, provision of strength and water storage in the sapwood. Hardwood contains vessels, tracheid, various types of sclerenchyma fibres and parenchyma cells: the vessels which are responsible for the conduction of sap and the *fibres*, which underpin the strength.

Another tree classification is based upon whether the leaf is perennial or falls. Most conifers have perennial leaves while most hardwoods have leaves that fall.

In general, the average density (specific gravity) of coniferous wood (0.41) is less than that of hardwoods (0.50), but there is some degree of overlap between the two families; the density of conifers can vary between 0.29 and 0.60, while that of hardwood ranges from 0.32 to 0.81.

The wood of conifers, being a very ancient species (they appeared during the Triassic period, between 248 and 206 million years ago), is quite homogeneous due to the limited diversity of its woody cells. Cells in hardwoods are more heterogeneous due to their great specialisation, characteristic of species that originated later (during the Cretaceous period, between 144 and 65 million years ago). For more details see L. Gil (2013) or B. Fischesser (2000).

The structure of wood can be studied at various levels; macroscopic, mesoscopic and microscopic.

Figure 3.2.1 shows the most characteristic details at the **macroscopic** level. Three distinct regions can be identified in the cross-section of a tree trunk: the *xylem*, the *cambium* and the *bark*. In the xylem, which takes up practically the entire section, two regions can be identified; the central, darker one, also called the *heartwood*, is formed of dead cells and the outer, lighter zone, known as the *sapwood*, is formed of living cells. All cells in the wood are produced by the *cambium*, a thin ring which surrounds the xylem. The *bark* is situated on the exterior of the cambium.

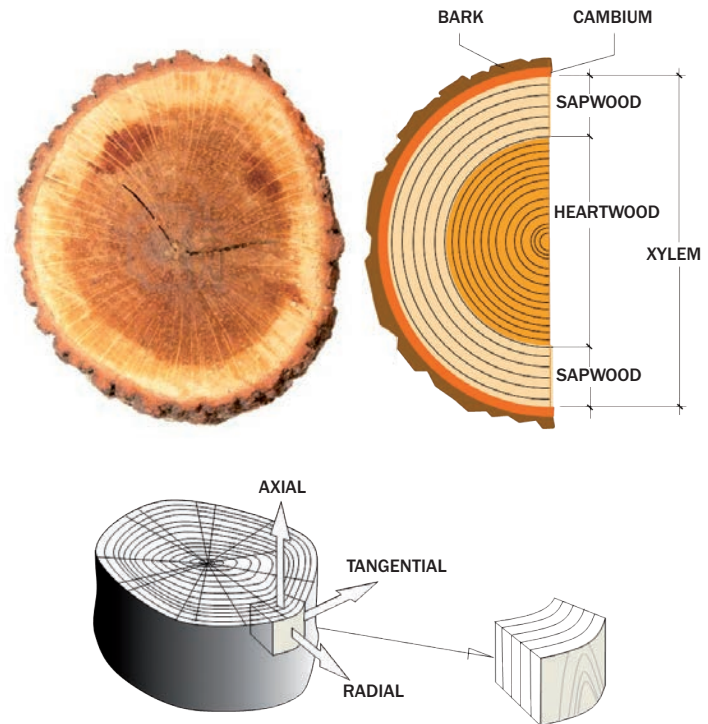


Fig. 3.2.1. Macrostructure of the section of a trunk, and the notation used.

A series of concentric rings can also be observed in the cross-section of the trunk. In each ring there is a lighter zone which is formed at the start of the growing season and another, narrower and darker, produced at the end of the season. With the exception of trees in tropical regions, the *cambium* produces only one ring each year and, for this reason, these are known as annual growth rings, and are a great help in dating past events. The science on which this is based is dendrochronology (from the Greek δένδρον, tree).

Generically, wood can be considered as a homogeneous, orthotropic continuous material with three planes of symmetry; radial, tangential and axial (Figure 3.2.1). The stiffness and strength are greatest in the axial direction, parallel to the trunk. In the radial and tangential directions these values are less and go from 1/2 to 1/20 of the axial properties, depending upon the tree under consideration.

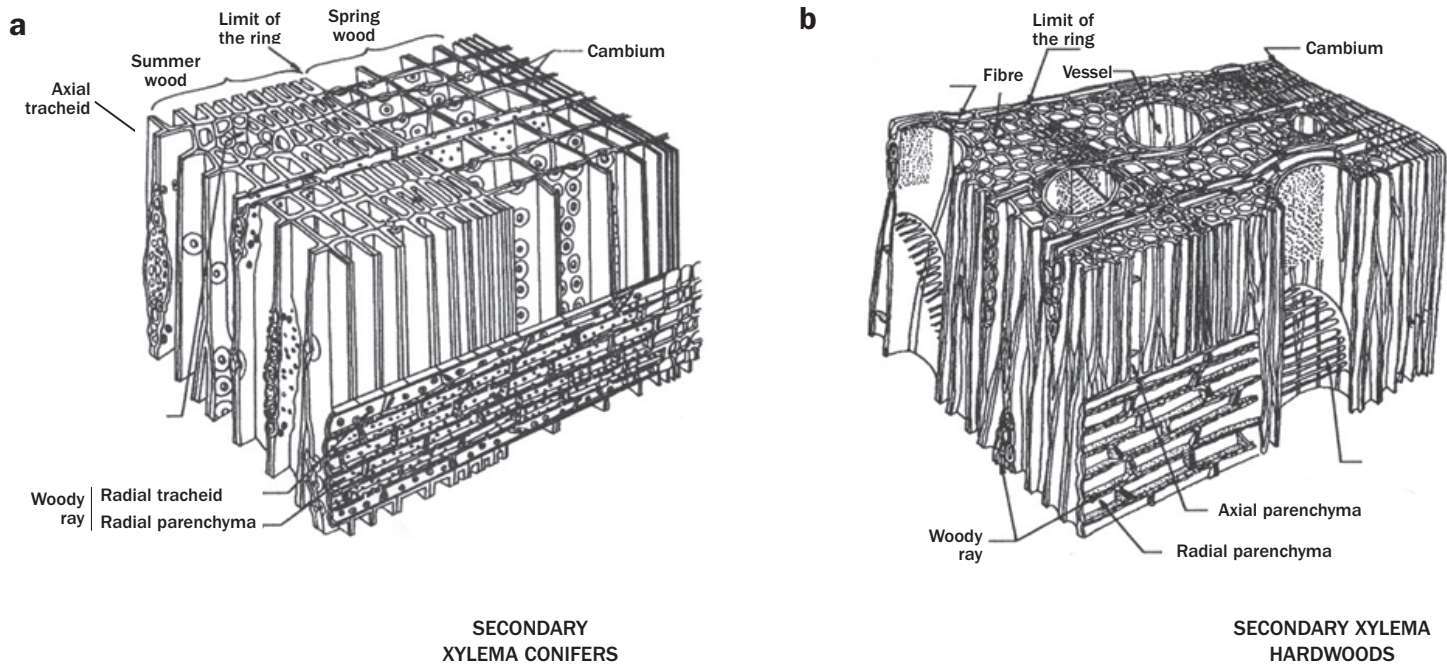


Fig. 3.2.2. Mesoscopic structure of wood (L. Gil, 2003)

At the **mesoscopic** scale (as shown in Figure 3.2.2) the structure of wood can be considered as an aggregate of cellular walls, of two types; some in the form of fibres and others more parallelepipedic, as shown in Figure 3.2.2.

The **fibrous cells**, which are aligned with the longitudinal (or axial) direction of the trunk, have relatively thick walls and are quite wide (the ratio of the length and diameter may be about 20). Their principal function is mechanical, that of support. In conifers these cells are the *tracheids* (Figure 3.2.2a) and, in hardwoods, the *fibres* (Figure 3.2.2b). In conifers the tracheids also perform a transport function and water storage.

The **non-fibrous cells** are grouped in tissues, oriented in the axial and radial directions, and performing transport and storage functions (starch, sugars, lipids, proteins, ...). They form vessels in hardwoods and *radial* and *axial parenchyma* in both conifers and hardwoods.

The different types of cells and their principal functions are summarised in Table 3.2.1, for both conifers and hardwoods.

TABLE 3.2.1. FUNCTION OF CELLS IN WOOD

FUNCTION	CONIFERS	HARDWOODS
Mechanical	Tracheids	Fibres
Transport	Radial Parenchyma Tracheids	Radial Parenchyma Vessels
Storage	Axial Parenchyma	Axial Parenchyma

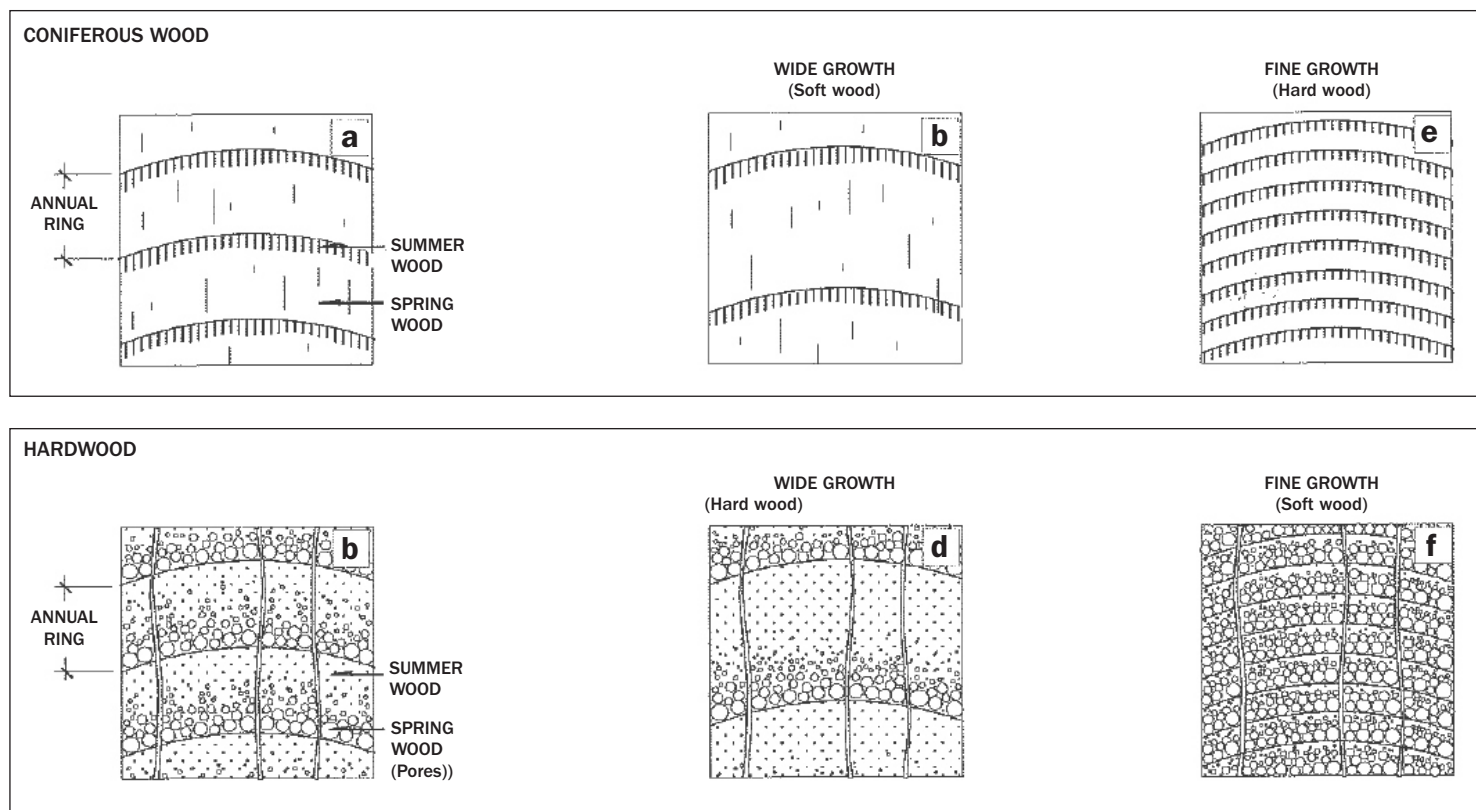


Fig. 3.2.3. Structure of the growth rings in conifers and hardwoods.

The **mesostructure** of conifers is quite uniform. The tracheids which take up 90 to 95% of the volume, have lengths between 3 and 5 mm and diameters typically ranging from 25 to 45 μm . The mechanical properties of this wood are principally determined by the tracheids.

A detailed representation of the cross-section of a conifer is provided in Figure 3.2.3a, in which the growth rings are highlighted. The spring wood is lighter than the summer wood, which is denser and more coloured. In spring wood, cell width is large and wall thickness thin. In summer wood, width is small and thickness thick. When the rings are wide, the texture is weak and the wood soft. On the contrary, if the growth rings are thin, the texture is strong and the wood hard (see Figure 3.2.3a).

The mesostructure of hardwood is more complex because there are, at least, four types of cell involved. The *fibres* occupy a minimum of 50% of the volume and have a great influence on the mechanical properties of these woods.

The *vessels* may occupy about 20% of the volume and have the role of transporting water and nutrients. *Pores* may be observed on the cross-section of the vessels in Figure 3.2.3b. The mechanical properties depend, to a large extent, upon number of pores per unit volume. The *radial parenchyma* may represent 17%, or more, of the volume, while the *longitudinal (axial) parenchyma* can range between 1 and 24% of the volume.

A detail of the cross-section of a hardwood is shown in Figure 3.2.3b, in which the appearance of the growth rings and pores present in them are highlighted; the spring wood is very porous and the summer wood has the finest pores. When the rings are very thin the density of the pores is large and the wood is soft, when the rings are wide the density of the pores is less and the wood is harder (see Figure 3.2.3b). The presence of pores allows classification of the woods, if vessels are not visible the wood is a conifer.

A study of the cell wall rests the **microscopic** domain. The cell wall structure is shown schematically in Figure 3.2.4. This is formed of a series of layers and all of these contain cellulose microfibrils –except the intermediate lamina– with different orientation with respect to the wall axis.

The *primary wall* (*P*) is very thin and associated with the *intermediate lamina* (*M*) which has the role of bonding the walls of adjacent cells. The microfibrils of the primary wall have no preferential orientation. In the *secondary wall* (*S*) the microfibrils are aligned and densely packed. This wall is subdivided into three layers; the exterior (*S*₁), intermediate (*S*₂) and interior (*S*₃). Intermediate layer *S*₂, the thickest, is the one with the greatest influence on the mechanical properties. Table 3.2.2 contains data on the relative thicknesses of the layers, the angle of the microfibrils with respect to the vertical axis, and the number of laminae which constitute each layer.

TABLE 3.2.2. CELL WALL STRUCTURE OF SPRUCE

LAYER TYPE	RELATIVE THICKNESS (%)	MICROFIBRIL ANGLE*	NUMBER OF LAMINAE
M + P	5	Random	–
<i>S</i> ₁	10	50° - 70°	4 – 6
<i>S</i> ₂	75	10° - 30°	30 – 150
<i>S</i> ₃	10	60° - 90°	0 – 6

* The angle is measured relative to the vertical axis

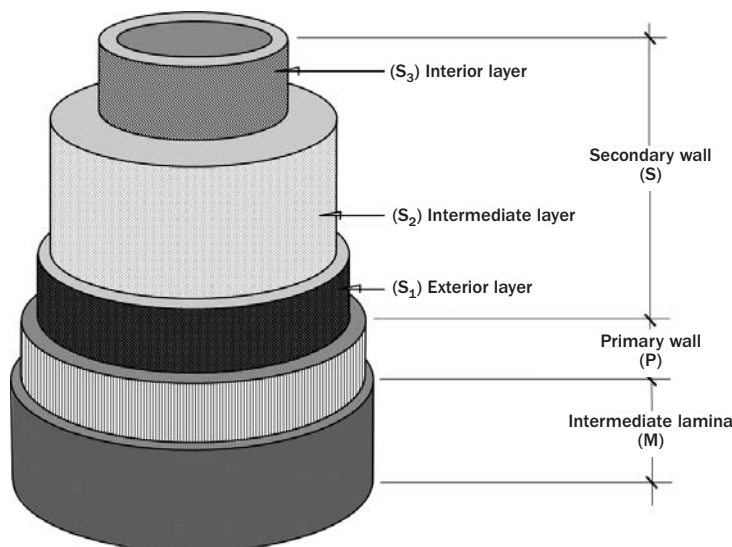


Fig. 3.2.4. Microscopic structure of the cell wall.

It is possible to go to an even deeper level in the mesostructure if the details of the *cellulose microfibrils* are considered. In this the approach is **nanoscopic**, since the cross-section of these fibres is 3.5 x 10 nm.

Cellulose is a polymer formed of long glucose chains (between 5000 and 10000 units) without branches (see Section 1.2.1). These chains are arranged to form microfibrils in which there are highly-ordered (crystalline) and less-ordered regions (amorphous zones). The (more compact) crystalline regions hardly absorb water, while the amorphous regions may absorb more water, changing the mechanical properties of the microfibrils. This may explain the variation in the properties of wood with changes in humidity and temperature, since between 40 and 50% of the composition of wood is cellulose, whose density is about 1550 kg/m³.

Other components of the cell wall, at the nanoscopic level, are *hemicellulose* and *lignin* which have the function of binding the cellulose fibres; to some extent the cell walls may be modelled as a composite material constituted of cellulose fibres embedded in a matrix of hemicellulose and lignin.

Hemicellulose is a polysaccharide but, unlike cellulose, its chains are short (between 500 and 3000 monomer units), they are branched and, largely, amorphous. Due to its structure, it is easily hydrolysed by acids and enzymes. In conifers it represents 25% by weight and in hardwoods 35%. Its density is about 1500 kg/m³. Lignin is a complex phenolic (a diverse group of aromatic compounds) and its structure is amorphous.

Lignin is the main adhesive which bonds both the components of the cell wall and other cells. In hardwoods it represents between 20 and 30% by weight. In conifers it is somewhat less. Its density is about 1400 kg/m³. It begins to soften at about 170 °C, a characteristic which is exploited in the fabrication of wood products.

3.2.3. Mechanical properties

Modelling the mechanical properties of wood is a complex task, as might be imagined from its intrinsic structure. In addition, the microstructure varies, not only between different species but also within species, because it changes during different growth stages. Wood is an orthotropic material and its properties depend upon humidity and temperature. Time also comes into play since it exhibits viscoelastic behaviour. Even so it is possible to make reliable predictions of wood's mechanical behaviour.

Ideally, starting from the *microstructure*, it should be possible to estimate the mechanical properties of the cell walls, modelling them as a material composed of cellulose fibres embedded in a hemicellulose or lignin matrix. And, in a second stage, starting from the *mesostructure*, wood may be modelled as a cellular material with a honeycomb structure whose walls have the previously calculated properties. Despite these simplifications the results obtained are quite satisfactory, in particular if they are limited to the linear elastic modulus, the compressive strength, and the fracture toughness.

Easterling et al. (1982) studied the structure and mechanical properties of balsa wood by means of experiments performed in a scanning electron microscope and observing how the cell walls behaved. Initially, they examined how the cell walls deformed elastically and,

then, how they underwent plastic collapse or rupture. The results showed that the elastic modulus, rupture load and anisotropy of the wood were controlled, in part, by the mechanical properties of the cell walls and, also, by their dimensions and shape. All of this indicated that the mechanical properties of the wood depended strongly upon its density. Data from other woods suggest that these findings can be generalised.

The model used by Easterling et al. for deducing the mechanical behaviour is illustrated in Figure 3.2.5a. It consists of a cellular honeycomb structure and is intended to be a simplification of the mesoscopic structure shown in Figure 3.2.2. The structure is composed of elongated cell blocks, separated by partitions (spokes or radii) formed of smaller cells and of other shapes. The model was inspired by photos of balsa wood, Figure 3.2.5b.

The *growth rings* form cylindrical surfaces normal to the radii and are visible to the naked eye, but they become diffuse when viewed in the electron microscope. For this reason, these differences have not been included in the model, which only considers the two materials mentioned; the elongated cell bundles and the spoke cell panels. (This may create some confusion when simplified models are developed, in which the role of the growth rings is ignored, as in Easterling's model).

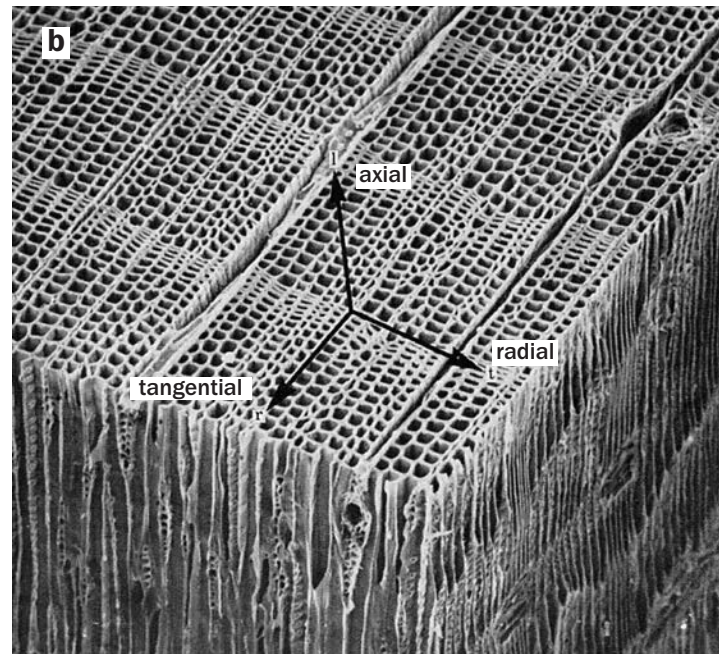
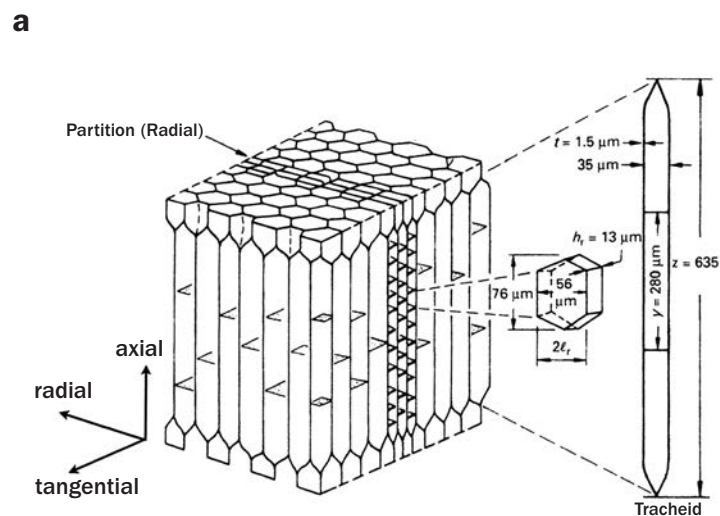


Fig. 3.2.5. a. Easterling's model.
b. Balsa wood (Easterling et al. 1982).

3.1. Elastic modulus

Figure 3.2.6 shows average values of the stress-strain curves for various woods of a range of densities (beech, 750 kg/m³; willow, 400 kg/m³; balsa, 110 kg/m³), obtained from axial (in the direction parallel to the fibres) and radial (in the direction perpendicular to the fibres) compression tests. Results from tests in the tangential direction are very similar to those in the radial direction.

For small strains (less than 0.02%) the behaviour is linear elastic in both directions. The elastic modulus in the axial direction is always greater than that in the radial (this effect cannot be observed in the Figure). Beyond the linear elastic region the curves exhibit a plateau, which can extend to strains of the order of 0.2% (for beech wood) and 0.8% (for balsa). Then the stress increases rapidly.

The deformation mechanisms in the cell walls during the compression test are shown in Figure 3.2.7. These can be, more or less, confirmed by the scanning electron microscope studies performed by Easterling et al. (1982).

In the *axial compression* tests the cell walls are initially compressed; after, with increasing strain, the approximately prismatic cells collapse by folding and breaking of the cell bases (Figure 3.2.7a). This mechanism is more apparent in low density woods, such as balsa; the cells are coupled together, like the teeth of two opposing combs, until the bases collapse and, a load drop is detected. The process is repeated in the next row of cells and the resulting curve has a sawtooth profile with multiple breaks until the wood is practically dense at which point the load increases.

In compression tests in the *tangential direction* (and also in the *radial*) the cells bend and the walls end up collapsing (Figures 3.2.7b and c); in some woods a small load drop is detected after the elastic limit, which is usually associated with this process.

As mentioned in Section 2.3.4, these tests can be modelled with a cell or honeycomb structure.

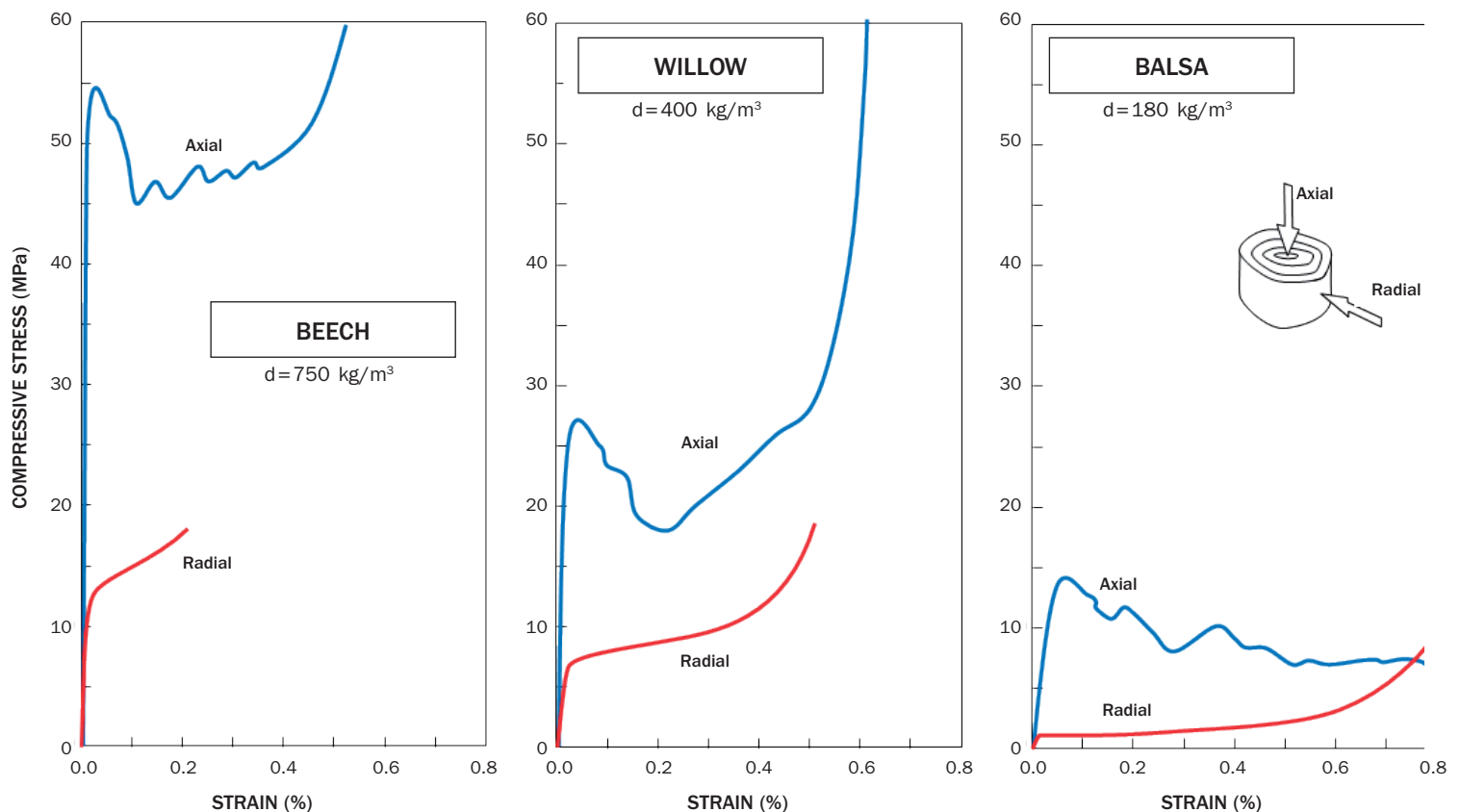


Fig. 3.2.6. Engineering stress-strain curves obtained from compression tests in the axial and radial directions, for woods of very different densities.

A model for balsa wood, according to Easterling et al. (1982), is shown in Figure 3.2.5. The tracheids and fibres can be idealised as hexagonal prisms in which, occasionally, there are some transverse membranes. The radii are transverse bundles with rectangular sections, as shown in the Figure. The model could be refined, if necessary, by adding growth rings and channels.

Assuming an approximately hexagonal cellular structure which deforms by bending of the walls (Figure 3.2.7b) we can estimate the elastic modulus in the tangential direction, E_T , by means of Equations (2.3.3-11) and (2.3.3-12):

$$\frac{E_T}{E_c} = C_1 \left(\frac{d}{d_c} \right)^3 \quad (3.2-1)$$

where E_c and d_c are the modulus and density of the cell wall material, respectively. C_1 is a constant which depends upon the geometry of the honeycomb. To avoid confusion due to the anisotropy of the cell wall E_c it is usual to take it as equal to the wall modulus in the axial direction (~ 35 GPa). The value of d_c is—as we have seen—about 1500 kg/m^3 . d is density of the wood.

The elastic modulus in the radial direction, E_R , might be expected to be similar to E_T , but the presence of the radii, which have a greater density and modulus, make the structure appear stiffer in this direction.

$$E_R \approx 1.5 E_T \quad (3.2-2)$$

The elastic modulus of the wood in the axial direction, E_A , is greater than E_T because, in this case, the cell walls are loaded in compression, rather than bending. The result is the same as loading the honeycomb in the perpendicular direction to the plane. The result which was obtained in Section 2.3.4, Equation (2.3.3-25), is simply

$$\frac{E_A}{E_c} = \frac{d}{d_c} \quad (3.2-3)$$

The theoretical values of E_A and E_T have been represented in Figure 3.2.8 as a function of the relative densities, d/d_c , together with numerous experimental results for E_A , E_T and E_R , following Gibson and Ashby (1997). The predictions for the axial modulus, E_A , are quite good. The predictions for E_T and E_R are also acceptable for high densities. For relatively low densities—of the order of 0.1—the values of E_R are somewhat greater, perhaps for the reasons mentioned previously.

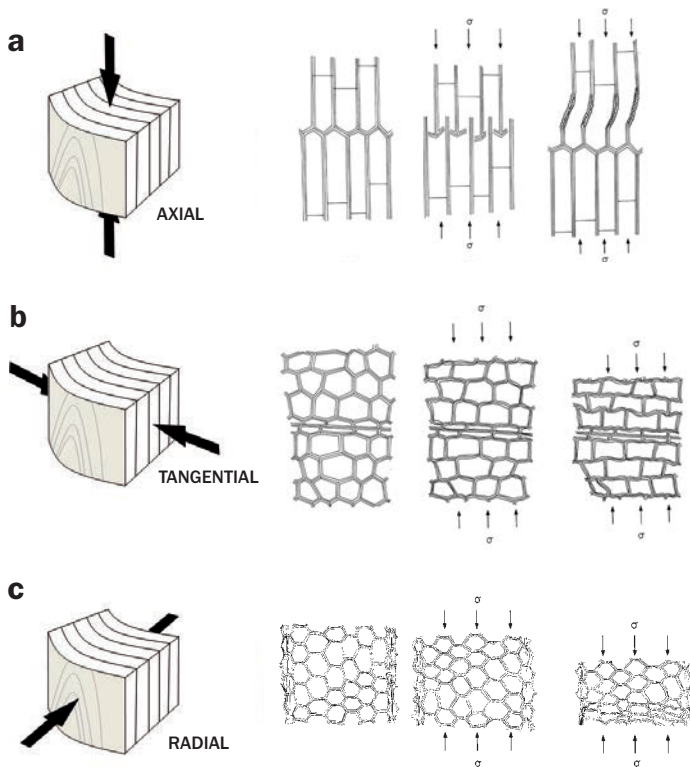


Fig. 3.2.7. Deformation mechanisms in cell walls subjected to compression. a. Axial direction, b. Tangential direction, c. Radial direction.

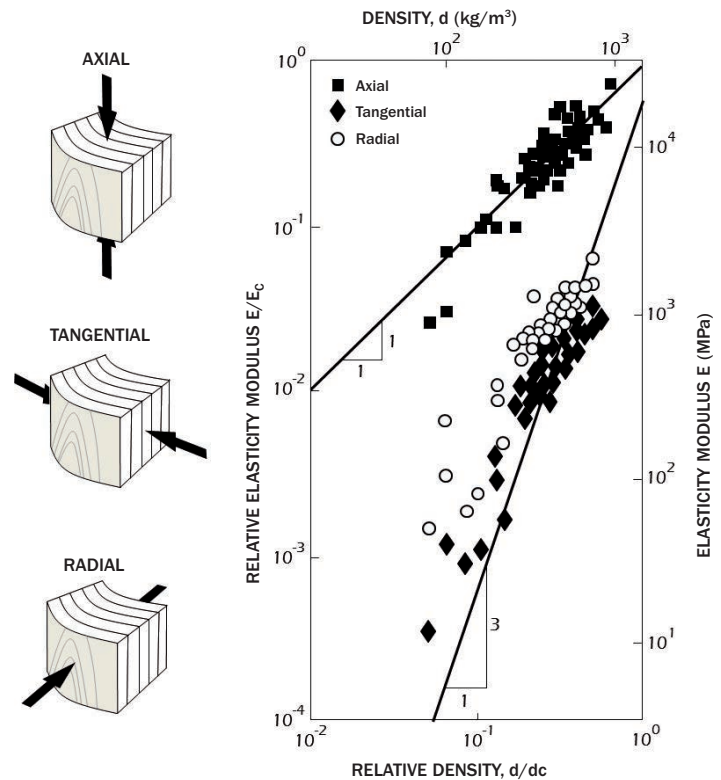
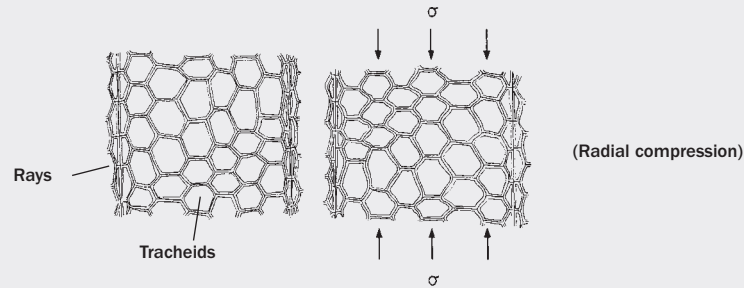


Fig. 3.2.8. Values of the elastic moduli (axial, tangential and radial) relative to those of the cell walls, as a function of the relative density.

EXERCISE 30

Justify Equation (3.2-2) $-E_R \approx 1.5 E_T$. gives **elastic modulus** in the **radial** direction as a function of the elastic modulus in the **tangential** direction.

**SOLUTION:**

To evaluate E_R we assume that the wood is a material composed of two components: the **tracheid cells** zone as one part, and the **ray** zone for the other (Figure 3.2.5).

On applying a radial compression (Figure 3.2.7c) both components act in parallel, according to the Voigt model shown Figure 2.24. As a result, the radial modulus E_R is given by Equation (2.3.3-1) and it will be a combination of the modulus of the region formed by the tracheid cells, which we can approximate by E_T , and the modulus E_{CR} of the zone occupied by the rays:

$$E_R = V_R E_{CR} + (1 - V_R) E_T$$

where V_R is **volume fraction of the rays**; about 10% in hardwoods and 20% in conifers.

On the other hand, if d_R is the density of the wood in the ray zone, the modulus E_{CR} will be

$$\frac{E_{CR}}{E_c} = C_1 \left(\frac{d_R}{d_c} \right)^3$$

since the deformation of the ray cells is also due to bending of their walls, which we assume is similar to that of the tracheid cells.

Combining the previous expression with Equation (3.2-1) we obtain

$$\frac{E_{CR}}{E_T} = \left(\frac{d_R}{d} \right)^3 = R^3$$

where R is the ratio of the ray and wood densities. R usually lies between 1.1 and 2.

With this result we can calculate the value of E_R

$$E_R = V_R R^3 E_T + (1 - V_R) E_T = [1 + V_R (R^3 - 1)] E_T$$

For **balsa** $V_R = 0.14$ and $R = 2$, which leads to $E_R \approx 2 E_T$.

For **woods of greater densities** R is practically 1 so that $E_R \approx E_T$.

Generally, Gibson and Ashby (1997) propose an intermediate value of $E_R \approx 1.5 E_T$

3.2. Compressive strength

The compressive strength can also be modelled using the results obtained in Chapter 2, employing cellular honeycomb models.

For loading in the *tangential* direction when the structures, subjected to bending, yield or buckle. The collapse stress due to plastic deformation, $\sigma_{R,T}$, is given by (Section 2.3.4, Equations 2.3.3-17 and 2.3.3-18):

$$\frac{\sigma_{R,T}}{\sigma_{y,c}} = C_3 \left(\frac{d}{d_c} \right)^2 \quad (3.2-4)$$

where $\sigma_{y,c}$ is the value of the yield stress of the cell wall material (~ 350 MPa) and d_c is its density.

For loading in the *radial* direction, the rays act as reinforcement and, once again, (according to Gibson and Ashby 1997) applying the rule of mixtures the strength in the radial direction, $\sigma_{R,R}$, for balsa wood can be estimated as

$$\sigma_{R,R} = 1,4 \sigma_{R,T} \quad (3.2-5)$$

This result is more approximate for low density woods (Easterling, 1982), but the difference between $\sigma_{R,R}$ and $\sigma_{R,T}$ decreases as the density increases.

Finally, for loading in the *axial* direction, failure is due to the plastic collapse of the bases of the prisms in low density woods (such as balsa) or yielding and buckling of the prisms in higher density woods (such as spruce). In any case, the failure is initiated by axial plastic strain, but the mechanism is not quite as simple as that described in Section 2.3.4. Easterling et al. (1982) have proposed the following expression:

$$\frac{\sigma_{R,A}}{\sigma_{y,c}} = C_4 \left(\frac{d}{d_c} \right) \quad (3.2-6)$$

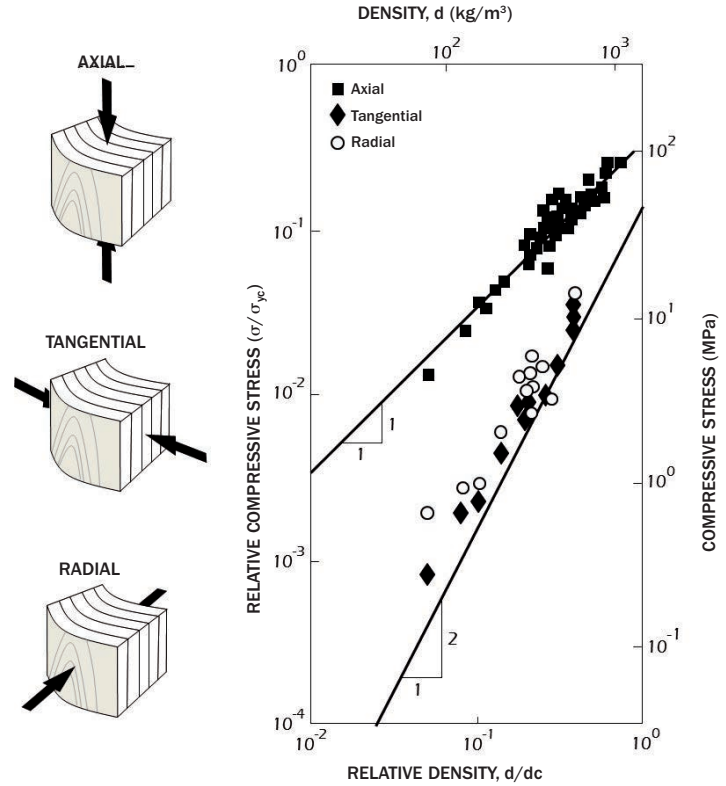


Fig. 3.2.9. Values of compressive strength (axial, tangential and radial) relative to the compressive strength of the cell walls, as a function of the relative density.

Theoretical values of $\sigma_{R,T}$ and $\sigma_{R,A}$ are shown in Figure 3.2.9 as a function of the relative density, together with numerous experimental results for $\sigma_{R,A}$, $\sigma_{R,T}$ and $\sigma_{R,R}$, according to Gibson and Ashby (1997). As may be observed, the predictions are quite good and illustrate a marked anisotropy which, moreover, is a function of the density; the ratio of the axial to transverse strength is about 2 for dense woods but may reach 10 for woods such as balsa.

3.3. Fracture and toughness

The study of the fracture of wood is tackled using the tools of Fracture Mechanics for linear elastic homogeneous isotropic materials, even though it is well known that wood is orthotropic. Nor is its behaviour linear elastic for large deformations.

However, despite wood having a variable and heterogeneous microstructure, the proposed approximation yields reproducible results and data which, in most cases, are useful for design purposes. In what follows, account has been taken of the works of Ashby (Ashby et al., 1985, and Gibson and Ashby 1997). A more refined study of the fracture of wood can be found in Stanzl-Tschegg (2006) or in Reiterer et al. (2002).

Values of the fracture toughness of ten woods are shown in Figure 3.2.10, as a function of their relative densities. The toughness was measured using standard procedures. Their values are referred to as K_{IC}^{*n} , when the initial crack is normal to the fibre direction and K_{IC}^{*p} when parallel to the fibre direction (Figure 3.2.10). Since, strictly, these are not true toughnesses –because of the simplifications discussed above– an asterisk is added to reflect this approximation. Note that the values of K_{IC}^{*n} are, in general, ten times than those of K_{IC}^{*p} . The experiments were performed at ambient temperature, with a relative humidity of about 10% and with a loading rate of 0.01 mm/s, since it has been demonstrated that the fracture toughness values –

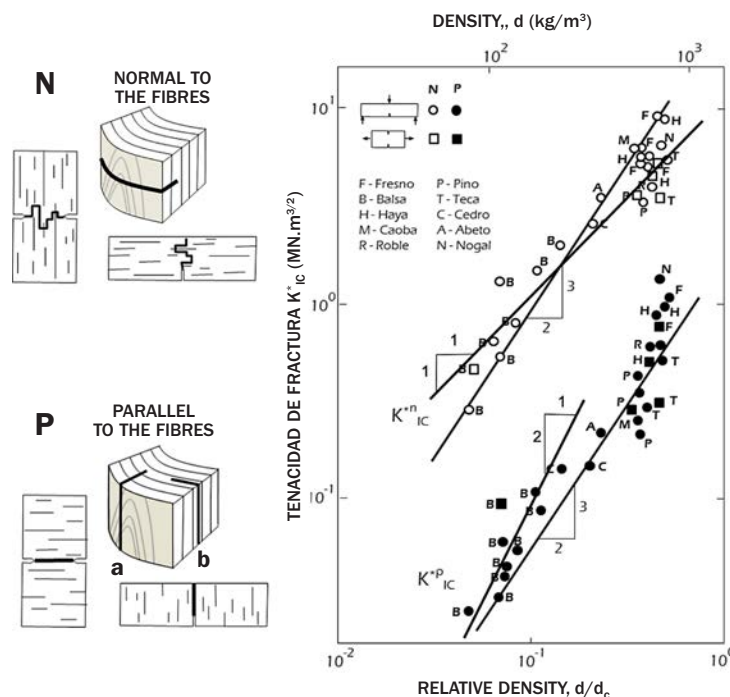


Fig. 3.2.10. Values of the fracture toughness depending upon the crack location (normal or parallel to the fibres) for ten types of wood as a function of their relative densities.

like the elastic modulus and strength– depend upon the temperature, humidity and loading rate (Jeronimidis, 1980). A notable aspect of Figure 3.2.10 is that, under normal circumstances, the fracture toughness depends primarily upon the relative density of the wood.

Microscopic observation of the crack propagation in mode I allows identification of some failure mechanisms at the cell level. The most characteristic are shown schematically in Figure 3.2.11 (Ashby et al. 1985). For tests in the *direction parallel* to the fibres, in general, it was observed that in low density woods ($d/d_c < 0.2$) the cracks advance breaking the cell walls (Figure 3.2.11a). In dense woods ($d/d_c > 0.2$) two mechanisms occur; failure of the cell walls (Figure 3.2.11a) and debonding of the cell walls (Figure 3.2.11b). For tests in the *direction perpendicular* to the fibres this second mechanism dominates (Figure 3.2.11b); the crack progresses seeking out the easiest route and when energetically favourable the walls disbond rather than break. This phenomenon produces a tortuous path such as that represented in Figure 3.2.10. It is also observed that when the crack encounters a large pore, or a channel, it often stops because the stress concentration at the crack tip is reduced (Figure 3.2.11c).

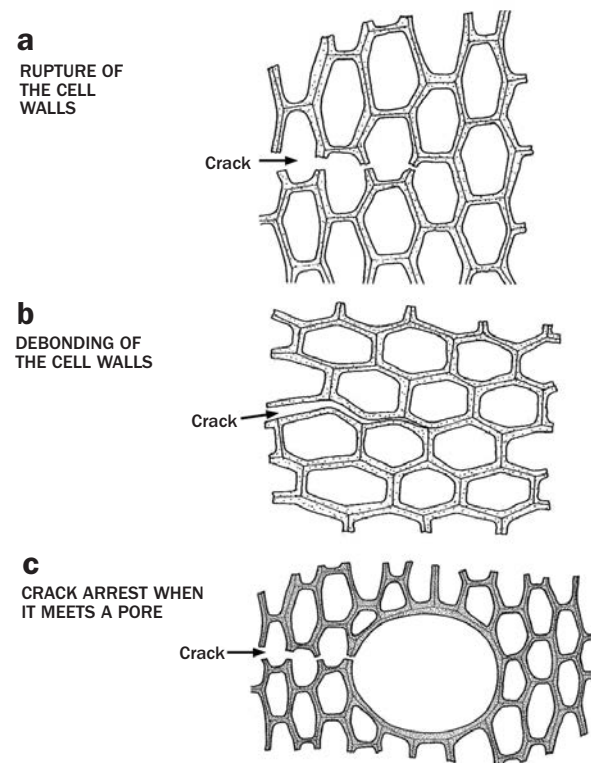


Fig. 3.2.11. Schematic representation of various rupture mechanisms at the cell level.

A macroscopic view of the cracks is shown in simplified form in Figure 3.2.10; when the initial notch is *parallel to the fibre direction* the crack grows in the same plane, when the notch is *normal* to the fibre direction the trajectory is more complex. In this case, the crack tends to propagate a certain distance in the direction perpendicular to the plane of the notch. Moving away from the plane of the notch the stress is increased and the cell walls rupture following propagation in a plane parallel to the initial notch. Then, the above process is repeated. This is known as the Cook and Gordon (1964) fracture mechanism.

The trend of the results depicted in Figure 3.2.10 can be justified, following the reasoning of Ashby (1985), from the basic concepts of linear elastic Fracture Mechanics, and from the simplifications introduced above to model the structure as a honeycomb. Following Ashby, we introduce the values of the specific fracture energy of the wood for rupture of the cell wall G_r , and for disbonding between the walls G_d . We can assume that the values G_r and G_d are essentially constant (although they depend upon the ambient temperature and humidity) for diverse woods, since the composition and structure of the cell wall vary little between species.

When crack propagation **parallel to the fibres** is produced, the primary mechanism is –as we have seen– rupture in the case of low densities and rupture combined with cell wall debonding in the case of high densities.

Consider the propagation of a crack whose plane is perpendicular to the tangential direction and which grows in the radial direction. (Figure 3.2.10-P a). The following approximate relationship may be established for the value of the stress intensity factor at the crack tip K_I and the energy available for crack propagation G given by Equation 2.2.2.2

$$K_I^2 = E_T G \quad (3.2-7)$$

In the previous equation we have taken the elastic modulus in the tangential direction to be representative of the elastic modulus of the material, that is to say in the direction perpendicular to the plane of the crack since, when it propagates, it produces a release of elastic energy principally due to strains perpendicular to the plane of the crack.

When propagation is associated with **debonding** of the walls, we have

$$\left(K_{IC}^{*p}\right)^2 = E_T G_d \quad (3.2-8)$$

Taking into account the result previously obtained for E_T , (Equation 3.2-1) we see that:

$$K_{IC}^{*p} = \sqrt{E_T G_d} = \sqrt{C_1 E_c G_d} \left(\frac{d}{d_c}\right)^{3/2} = C_5 \left(\frac{d}{d_c}\right)^{3/2} \quad (3.2-9)$$

A similar dependency of K_{IC}^{*p} with density is obtained if we consider a crack *perpendicular* to the radial direction (Figure 3.2.10-P b) which grows in the tangential direction (in this case the modulus E_R is used). The result, represented in Figure 3.2.10, shows good agreement –on average– with recorded experimental data.

When the propagation is produced by rupture of the cell wall the energy consumed will be G_r . In this case, the fraction of area occupied by the cell walls in the plane of the break is, for regular panels, approximately $t/(2l \cos \theta) = t/(l\sqrt{3})$ (Figure 2.31a). Using Equation (2.3.3-11) we see that $t/(l\sqrt{3}) = (1/2)(d/d_c)$ and, for unit crack area, a fracture energy of $0.5 (d/d_c) G_r$ is consumed.

For propagation *parallel* to the fibres which go through the cell walls we can write

$$K_{IC}^{*p} = \sqrt{0.5 E_T G_r \left(\frac{d}{d_c}\right)} = \sqrt{0.5 C_1 E_c G_r} \left(\frac{d}{d_c}\right)^4 = C_6 \left(\frac{d}{d_c}\right)^2 \quad (3.2-10)$$

When the crack propagates in a direction **normal to the wood fibres**, progressing through the rupture of the cell walls, the energy consumed per unit area of crack propagation will be equal to $(d/d_c) G_r$, since the proportion of ruptured surface is d/d_c .

Repeating the reasoning of the previous paragraphs, but now using the axial elastic modulus E_A whose dependency on density is given by Equation (3.2-3) it is found that:

$$K_{IC}^{*n} = \sqrt{E_A G_r \left(\frac{d}{d_c}\right)} = \sqrt{E_c G_r} \left(\frac{d}{d_c}\right)^2 = C_7 \left(\frac{d}{d_c}\right) \quad (3.2-11)$$

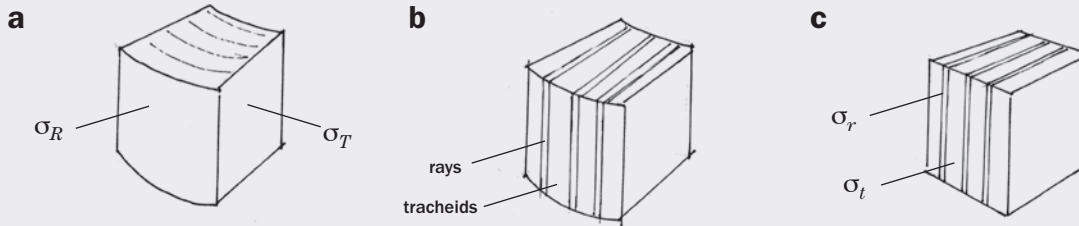
Representations of Equations (3.2-9), (3.2-10) and (3.2-11) are shown in Figure 3.2.10. It may be observed that the experimental results indicate that the behaviour lies approximately between the two extreme cases studied. Equation (3.2-10) has been adjusted only to the experimental density values of less than 0.2.

EXERCISE 31

Justify Equation (3.2-5) $-\sigma_{R,R} \approx 1.4 \sigma_{T,R}$ which expresses **the compressive strength** in the **radial** direction in terms of the compressive strength in the **tangential** direction for balsa wood.

SOLUTION:

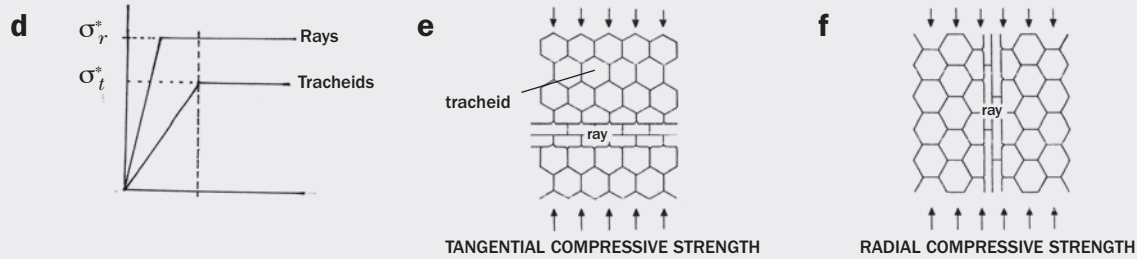
The hypothesis that was made to simplify the problem –for balsa wood– is outlined in the following sketch (Easterling et al. 1982).



The notation employed is shown in Figure *a*, the essential elements that need to be considered are highlighted in Figure *b*: rays and tracheids (note that the effect of the growth rings is ignored), and Figure *c* illustrates the most appropriate material model (Voigt), along with the notation.

The radial stress σ_R , according to this model, is given by $\sigma_R = V_r \sigma_r + (1 - V_r) \sigma_t$ where, V_r is the volume fraction of the radial component and σ_r and σ_t are shown in Figure *c*.

To calculate the strength, it is assumed that the two materials considered (rays and tracheids) are elastic- perfectly-plastic, as indicated in Figure *d*. Structural collapse at $\sigma_{R,R}$ will occur when the yield strain of the most flexible material (tracheids) is reached. Therefore: $\sigma_{R,R} = V_r \sigma_r^* + (1 - V_r) \sigma_t^*$ where σ_r^* and σ_t^* are indicated in Figure *d*.



Figures *e* and *f* contain sketches of the structures of the elements of the rays and tracheids which suggest the hypothesis that the compressive strength of the **wood** in the tangential direction $\sigma_{T,R}$ must be similar to that of the **tracheids** in the radial direction σ_t^* , a hypothesis which leads to $\sigma_{R,R} = V_r \sigma_r^* + (1 - V_r) \sigma_{T,R}$

To calculate σ_r^* the honeycomb cell model may be used, from which $\sigma_r^* / \sigma_{yc} = C_3 (d_r / d_s)^2$ where d_r is the density of the radial cells and σ_{yc} and d_s the values for balsawood, and account has been taken of the fact that t/l is proportional to d_r / d_s .

On the other hand, according to Equation (3.2.4), $\sigma_{T,R} / \sigma_{yc} = C_3 (d_t / d_s)^2$ where d_t is, now, the density of the trabecular region.

The ratio between σ_r^* y $\sigma_{T,R}$ will be $\sigma_r^* / \sigma_{T,R} = (d_r / d_t)^2 = R^2$

For balsawood, the following approximate values may be taken (Easterling et al. 1982), d_r is twice d_t , so that $R=2$ and the volume fraction of the radial component, $V_r = 0,4$

Finally, from these data, $\sigma_{R,R} = V_r \sigma_r^* + (1 - V_r) \sigma_{T,R} = [1 - (R^2 - 1) V_r] \sigma_{T,R} = (1 + 3 V_r) \sigma_{T,R} \approx 1,4 \sigma_{T,R}$

3.2.4. Final remarks

Wood, as a **biological material**, has recently generated an interest in studying the relationship between structure and mechanical properties. One reason for this is the growth in the use of wood as a construction material, contrary to the trend of the last few years when it was thought that new materials were going to replace it, but its low density (which facilitates transport and makes its specific properties competitive), low thermal conductivity and very low electrical conductivity, together with low production costs, have made this material so attractive in both Civil Engineering and in Architecture. Another reason which has given impetus to the study of the relationship between the microstructure and properties is the growing interest in biomimetics. Many biological materials exhibit mechanical properties –such as strength, stiffness, or toughness– far superior to the those of their basic constituents, as is the case in wood. These properties are not accounted for using only composite materials models, something more is needed, it is necessary to take into account the hierarchical structure and other peculiarities. The aim is to unravel these aspects in order to design more competitive materials.

To design wooden structural elements account has to be taken of the orthotropic nature of wood whose axes are longitudinal (in the direction of the trunk), radial, and tangential (as indicated in Figure 3.2.1). Furthermore, wood is a heterogeneous and hygroscopic material. Nonetheless, it is possible to design wooden structural components, assuming that the material is homogeneous and that its characteristics remain constant within a range of relative humidity, temperature and loading rate. The interested reader can refer to the book by Smith, Laudis and Gong (2003).

Wood, a biological material par excellence, enjoyed a certain role –years ago– as as **biomaterial**, in the sense of “material to treat, correct or *replace* tissues, organs or functions in the human body” (Soc Eur de Biomateriales, 1991), since it was used to fabricate prosthetic devices.

A wooden prosthetic toe was discovered in an Egyptian mummy of a 50-year old woman who lived 2,600 years ago. The prosthesis was articulated and must have been functional, as was demonstrated by replicas made at Salford University. Herodotus tells that in the year 550 B.C., the soldier Hegesistratus underwent amputation of a foot and was given a wooden implant to allow him to walk. There are numerous references to wooden prostheses in more recent times, with the best-known being those involving pirates and, amongst these, the famous Cornelius Jol (1597-1641), nicknamed *Peg Leg* (*Houtebeen*, in Dutch). He was an admiral in the Dutch East India Company during the Eighty Years War that the Low Countries waged against Imperial Spain. Jol, more than a soldier was a privateer who plundered Spanish and Portuguese vessels in the Atlantic Ocean. His nickname came from the use of a wooden prosthesis which replaced a leg lost in battle.

In the field of **biomimetics** attempts have been made to replicate the cell structure of wood with ceramic materials. These are called biomorphic ceramics. Honeycomb structures have been fabricated with ceramic cells of the order of 50 μm much less than conventional ceramic cells, (see for example Zollfranc and Sieber, 2005). These materials can be competitive for use at high temperatures, heat exchangers, filters or catalyst supports.

Another strategy based on densifying the wood by chemical treatment plus compression and high temperature (Song et al. 2018), produces a high-performance material for structural uses –increasing the failure load, toughness and impact resistance by an order of magnitude– and making it competitive with many metals on cost, weight and mechanical properties.

EXERCISE 32

A construction will employ single-piece pine beams whose dimensions are; length $L = 5\text{ m}$, depth $D = 20\text{ cm}$, width $B = 10\text{ cm}$. These beams are supported at their ends and carry a working load of $F = 1,000\text{ N}$ acting at the middle.

It is required to calculate:

- The central deflection of the beams
- By how much the load may be increased before rupture.
What will be the safety factor, defined as the ratio rupture load/working load?
- If one beam has a defect located in the centre of the beam—in the form of a through-the-thickness crack, such as that in Figure 2.14a—whose size is $a = 1\text{ cm}$, what is the new safety factor?
- The longest defect, such as that in the previous paragraph, that can be tolerated by the beam under the working load.

NOTE. Assume linear-elastic behaviour. The value of the Stress Intensity Factor for this example may be found in any manual or in the Fracture book of M Elices and G V Guinea (2021).

SOLUTION:

- The geometry of the problem is illustrated in Figure 2.9a. Equation 2.2.1-23 gives the central deflection of *an uncracked beam* subjected to three-point bending

$$\delta_{3P} = \frac{FL^3}{48EI} = \frac{4FL^3}{EBD^3}$$

in which we have substituted the second moment of area of the rectangular section $B \times D$

$$I = \frac{1}{12}BD^3$$

The elastic modulus, E , is taken to be the modulus in the axial direction E_A , (Section 3.2.3) bearing in mind that—from the dimensions of the beam— the wood fibres will be parallel to the length of the beam, and the bending strains will occur in the axial direction. Equation 3.2-3 gives the value

$$E_A = E_c \frac{d}{d_c} = 13\text{ GPa}$$

in which we have taken the ratio $d/d_c = 0.37$, from Figure 3.2.10 and $E_c \approx 35\text{ GPa}$, the modulus of the cell wall in the axial direction. The value obtained is slightly higher than the usual range for Scots pine for structural use (8 to 11 GPa). With E_A and the beam dimensions, the resulting deflection is

$$\delta = 0.048\text{ m}$$

- b) To estimate the failure load for the *uncracked beam*, we calculate the maximum compressive stress that can be supported in the direction parallel to the fibres, from Figure 3.2.9. For $d/dc=0.37$ we obtain $\sigma_{R,A} \approx 40$ MPa. This value is quite close to the experimental results obtained in compression tests in the fibre direction.

In EXERCISE 8 the maximum stress in a rectangular beam was calculated as

$$\sigma_{\max} = \frac{3FL}{2BD^2}$$

This value is equal to the *maximum compressive stress* on the upper face of the beam and, also, the *maximum tensile stress* on the lower face. If we specify that the maximum compression in the fibre must not exceed $\sigma_{R,A}$ then

$$F_R = \frac{2BD^2}{3L} \sigma_{R,A} = 21.3 \text{ kN}$$

the maximum load that the beam can support without collapse.

In practice, the value of F_R is greater, since collapse usually occurs by tensile rupture, which in the case of pine is at a stress of about 100 MPa. In this case, the linear elastic model that we are using ceases to be a good approximation. It induces, –among other phenomena– a compressive yielding in the upper fibres, and a stress distribution which is no longer symmetrical about the central fibre of the beam. Nonetheless, supposing that the above formula can be extrapolated to the point of tensile rupture a value $F_R=53.3$ kN is obtained.

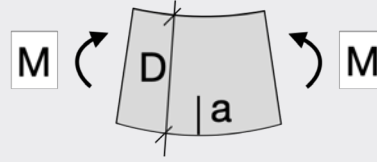
The safety factor of the structure will then be $21.3/5 = 4.3$, or $53.3/5 = 10.7$, for one failure load or another.

- c) In this case we consider a beam with a central crack. The equations used in the previous paragraph are no longer valid.

Specifically, calculation of the deflection produced in the presence of the crack is complex and beyond the scope of this text. Suffice it to say that the deflection of a cracked beam –in the linear-elastic regime– is the sum of the beam deflection without the crack (calculated previously) plus a contribution which depends upon the ratio of the crack length to the depth of the beam a/D , which diverges when a tends to D .

To calculate the rupture load *when there are cracks*, we must resort to fracture mechanics. For a linear-elastic material, as we saw in Section 2.2.2, structural failure occurs when $K_I=K_{IC}$ (the local approach to fracture). The value of K_{IC} for our pine wood can be estimated from the data in Figure 3.2.10, from which we obtain $K_{IC} \approx 3.3 \text{ MPam}^{1/2}$.

Equation 2.2.2-3 provides the value of K_I for a rectangular cross-section beam in bending with a length to depth ratio $(L/D)=4$. In our case $L/D=25$ so the formula is not strictly applicable, and we must refer to manuals which tabulate the value of K_I (for example Elices and Guinea, 2021). To simplify the calculation we take the problem to be equivalent to that of a cracked beam of rectangular cross-section, subjected to a bending moment $M=FL/4$, whose solution is



$$K_I = \frac{6M}{BD^2} \sqrt{\pi a} \left[1.122 - 1.40(a/D) + 7.33(a/D)^2 - 13.08(a/D)^3 + 14(a/D)^4 \right]$$

$$= \frac{3FL}{2BD^2} \sqrt{\pi a} \left[1.122 - 1.40(a/D) + 7.33(a/D)^2 - 13.08(a/D)^3 + 14(a/D)^4 \right]$$

For $a=1\text{ cm}$, the fracture load that causes $K_I=K_{IC}$ is $F_R=0.845\text{ kN}$. which is below the working load $F_T = 5\text{ kN}$. The safety factor is then about 0.16.

d) To calculate the maximum crack size compatible with the working load it is necessary to solve the equation $K_I(F_T, a_c) = K_{IC}$ taking the value of a_c as an unknown, that is

$$K_{IC} = \frac{3F_T L}{2BD^2} \sqrt{\pi a_c} \left[1.122 - 1.40(a_c/D) + 7.33(a_c/D)^2 - 13.08(a_c/D)^3 + 14(a_c/D)^4 \right]$$

whose solution gives $a_c = 0.26\text{ mm}$

We see that the beams are extremely sensitive to the presence of cracks. This fact is true for any cracked structure –within the hypothesis of linear-elastic behaviour– the presence of these defects drastically reduces the maximum loads that may be supported.

3.3. BONE

3.3.1. Introduction

Bone tissue contains an abundant extracellular matrix, the osteoid matrix, which surrounds widely spaced cells, together this is called **bone**, and in humans it is composed of approximately 30% collagen fibres, 55% crystal salt minerals, and 15% water.

Bone is formed in embryos from collagen. It has already been observed that collagen has good properties when it is subjected to tension but since it is very flexible it cannot support compression or bending which are the loads that bones have to resist. For this reason, during birth, animals add small amounts of hydroxyapatite to the collagen fibres, which provide the bone with rigidity. In adult animals, some bone may contain as much as 67% hydroxyapatite.

Bones, like other biological materials, possess enviable properties for an engineer since they are capable of self-repair and, also remodel themselves in response to mechanical loading. When the stresses carried by the bone decrease, the mass of the bones also decrease; a phenomenon recognised by astronauts after long periods in space. On the other hand, osteocytes (mature bone cells) detect the deformations induced when the stresses increase, and release chemical substances which stimulate the osteoblasts (boneforming cells) in order to fabricate new bone tissue.

The bones of mammals and birds can be considered, at the microscopic level, as a **material composed** of a collagen fibre matrix reinforced with calcium phosphate (hydroxyapatite) crystals. The structure of bone is not simple, it is heirarchical, as will be seen later. Bone tissue, furthermore, contains water (which plays an important role in the mechanical properties), living cells –osteocytes, osteoblasts (previously mentioned), and osteoclasts (cells which reabsorb the bone)– and blood vessels. Bone is covered with a compact conjunctive tissue called the *periosteum*. Tendons and ligaments are inserted into bones, and their extremes present a uniform transition from pure collagen fibres through to a *fibrocartilage* zone which is progressively calcified until it fuses with the bone.

Other tissues, such as antlers and dentin, may also be considered as bone tissue; the antlers present in the deer family are totally bone when fully developed. On the other hand, the *horns* of bovids are not bones, but are hollow sheaths of the keratinised epidermis which are arranged around a bone core which emerges from the skull.

Bone is also a **multifunctional material**. Bones have evolved to be able to fulfil many functions, both within the same animal species and between different species. Three examples, taken from Currey (2002) and Cotterell (2010), serve to illustrate this point: The femur of mammals perform two classic functions; to support and facilitate movement. They must, therefore, be strong and stiff. Antlers, which have to withstand the blows of the confrontations of the male deers in the mating season, must be tough (more resistant to fracture) than normal bone, and they need not be so stiff. The third example is provided by the middle ear bone of whales which need not be so stiff and strong as those already cited but which must be very dense in order to transmit and pick up sound. All of these properties are summarised in Table 3.3.1, in which density, stiffness (in terms of the elastic modulus) and the toughness (specific farcture energy) are shown.

TABLE 3.3.1. PROPERTIES OF VARIOUS TYPES OF BONE			
PROPERTY	DEER ANTLER	HUMAN FEMUR	WHALE TYMPANUM
Density (kg/m ³)	1860	2060	2470
Stiffness Elastic modulus (GPa)	7.4	13.5	33.0
Toughness Fracture energy (J/m ²)	6190	1710	200

Bone is a **living material**, dynamic tissue, in which growth and restructuring are complex processes which implies *destruction* –achieved by cells which reabsord the bone (osteoclasts)– and *construction* –due to bone-forming cells (osteoblasts). For example, in a long bone such as the femur, the internal medulary cavity becomes larger as a result of reabsorption of the internal surface of the surrounding bone and at the same time it adds new bone by deposition. The growth of the bone is regulated by various hormones. These, together with a derivative of vitamin D, are responsible for keeping the level of calcium in the blood constant. After the menopause women lose about 5% of their bone mass annually, which may lead to a condition known as osteoporosis and an increased risk of bone fractures.

Bone density is an important parameter which allows characterisation of several mechanical properties, as will be seen later. **Trabecular, cancellous or spongy** bone, consists of a framework of bone tissue with a structure of interconnected voids. The direction of the tiny beams or trabeculae is orientated so as to optimise the resistance to the stresses that the bone must withstand under normal conditions. All bone is initially formed as spongy bone, but some become compact as a result of later remodelling.

Compact bone (also known as **cortical** bone) is dense and apparently solid to the naked eye. In many bones the external part is formed of compact bone and the internal, spongy bone. In some cases, such as the extremities of long bones and in vertebrae, this configuration minimises the weight of the bones and improves the distribution of load between them. In other cases, such as in the cranial vault or in the iliac crest, the bone structure adopts the form of a sandwich –with compact bone on the outside and spongy bone on the inside–. This arrangement is much more mechanically efficient than homogeneous bone with the same mass.

The greater part of this chapter is dedicated to the knowledge of the mechanical behaviour of spongy bone, which is very important in biomedicine. In patients with *osteoporosis*, bone mass reduces until eventually bones may fracture under loads which might be regarded as normal in healthy individuals. These breaks are common in the femoral head, in vertebrae, and in the wrist, and are due, in part, to a reduction of spongy bone. Spongy bone is also involved in *osteoarthritis*, a degenerative disease of the joints in which the lubricating cartilage is eroded and may even disappear; in this condition the distribution of forces which act on the joints depends upon the mechanical properties of the underlying spongy bone. Consequently, if the bone structure is altered, and with it its properties, changes in the distribution of forces on the joint may damage its lubrication system.

In order to quantify the mechanical behaviour of bone it is necessary to know, in some detail, its microstructure (which is addressed in Section 3.3.2) and, from that information, to model it. To this end, previously described models for composite and cellular materials are used (which are applied in Section 3.3.3).

3.3.2. Structure

The structure of bone is complex and in order to model the mechanical behaviour it is necessary to consider it at three distinct levels and to try to simplify it –idealising it– in each one of these levels. Going from bottom to top, the first level is that of the mineralised collagen fibres (microscopic level). These fibres can be arranged in various ways giving rise to different types of bone (mesoscopic level). The third level, which can be seen with the naked eye, (macroscopic level), consists of structures formed by combinations of the different types of bone mentioned above.

Microscopic level

The basic component of bone is collagen fibre mineralised with calcium phosphate crystals as shown schematically in Figure 3.3.1a. The crystalline structure of the mineral phase is not easy to identify, due to the nanometric size of its crystals, but it is known to belong to the apatite group, specifically hydroxyapatite. The presence of small amounts of carbonate suggests that there could also be dahllite.

The mineralised collagen fibres can be arranged in two ways; ordered, giving rise to *lamellar* bone, or random, creating a tissue called *amorphous* (or *woven*) bone. Both types are shown, in simplified form, in Figures 3.3.1b and 3.3.1c, respectively. The fibres of amorphous bone are between 0.1 and 0.3 microns in diameter. The fibres in lamellar bone are thicker, between 2 and 3 microns, and arranged regularly to form plates whose thickness varies from 2 to 6 microns

Mesoscopic level

The different combinations adopted by lamellar and amorphous bone are shown in Figures 3.3.1d-g.

Amorphous bone regions are found in young animals, and in the foetus, and in the callouses which are produced when bone is repaired after fracture. This is a fast-growing bone. Some blood channels which traverse the bone are included in Figure 3.3.1d.

Figure 3.3.1e is similar to Figure 3.3.1d, with orientated fibres. This type of bone is usually called *primary lamellar* or *laminar*. It is common in reptiles, and also in birds and mammals in the form of circular layers; particularly in the periosteum. Its growth is slower than that of amorphous bone.

Figure 3.3.1f, shows a mixture of the two previous types of bone; lamellar and amorphous. This type of bone is usually called *fibrolamellar*.

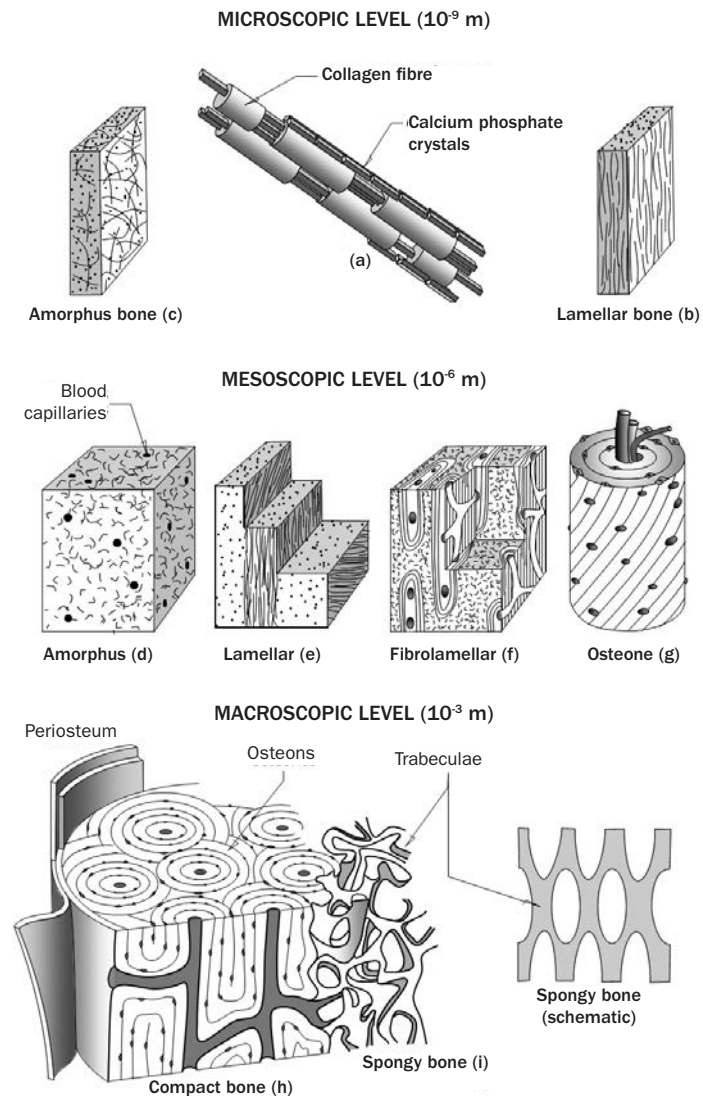


Fig. 3.3.1 Bone structures that can be discerned at different levels of observation.

Figure 3.3.1g contains a representation of an osteone, the basic histological unit of bones. These are essentially lamellar bone cylinders, whose diameter measures about 200 μm , with a central canal (also called the Havers or Haversian canal) through which arteries, veins and nerves may pass. This type of bone is also called Haversian. As indicated in the figure, there are also osteocytes connected through canals in the osteones.

Bone tissue is formed, in essence, by osteones cemented together and interconnected by blood vessels and nerves, where the cellular matrix dominates.

Macroscopic level

To the naked eye bone appears to be a solid homogeneous material, but when sectioned it is far from homogeneous and exhibits a complicated structure; the outer part is dense compact bone while on the inside a spongy structure is observed. Both structures are shown in Figures 3.3.1h and 3.3.1i. The four previously described mesoscopic structures are involved in the formation of **compact bone**. On the other hand, **spongy** or **trabecular bone**, is formed principally of laminar bone and osteone fragments. The structure of spongy bone is cellular; when the density is low the structure resembles that of sponge while when it is high it is more like a foam with perforated bubble walls.

Compact bone is dense, with a **porosity** –percentage of the total volume not occupied by bone– almost always less than 15%. When the porosity is greater than 50% bone is then considered *spongy*. The transition between compact and spongy bone is usually clear and occurs within a narrow range; it is rare to find porosities between 15% and 50% (Currey 2002, p. 23). The **relative density** –the ratio between the total or *apparent* density of the bone and the density of the wall material (1800 kg/m^3)– is also used for classification; in practice the relative density of spongy bone ranges from 0.05 to 0.5 (technically any bone with a relative density less than 0.7 is classified as spongy).

Bone grows in response to mechanical loads, as already mentioned, everything seems to indicate that the trabeculas tend to orient themselves in the direction of the principal stresses following the isostatics shown in Figure 3.3.2. It is understood that the density of spongy bone depends upon the magnitude of the stresses that it supports while the mesostructural anisotropy is a function of the direction and values of the principal stresses.

For a more detailed explanation of the different structures cited the reader is directed to Currey (2002), Chapter. 1.

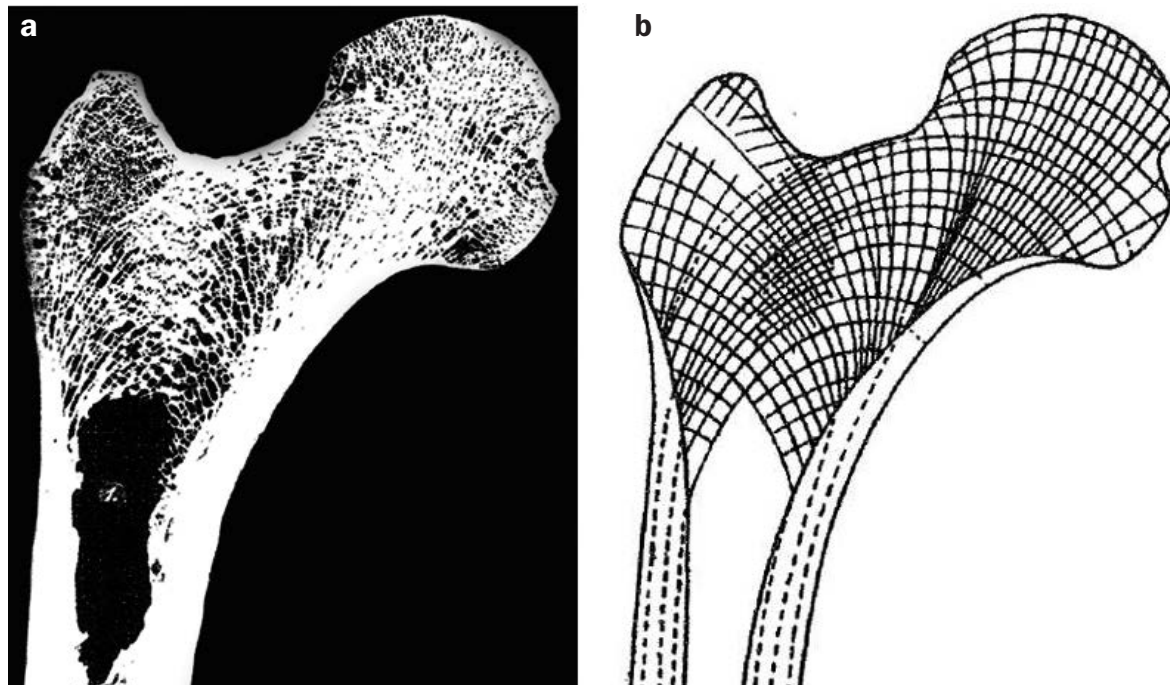


Fig. 3.3.2. a) Longitudinal section of the femoral head.
b) Isostatics (zones of pure compression or tension) obtained for an elastic model when the head is subjected to physiological loads.

3.3.3. Mechanical properties

A knowledge of the mechanical properties of bone is required for an understanding their behaviour and function, whether they are healthy or damaged; consider, for example, the risk of fractures in osteoporosis or the advantage of knowing the stress distribution in the design of implants. For these purposes models are needed for the prediction of the mechanical behaviour of bones.

The simplest models are based upon homogenising the mechanical analysis, considering the average properties of a representative volume of the material for compact bone, or a representative cell, or set of cells, in the case of spongy bone. In all of them it is essential to have information about the basic components; data which are obtained experimentally for each case.

Another, even simpler, way of tackling the global problem, consists of using dimensional analysis to model the deformation and failure mechanisms observed in cellular materials without specifying exactly the geometry of the cells. This is the approach adopted by Gibson and Ashby (1997, 2010). For spongy bone these models assume that the cell geometries are similar, independent of their density. The mechanical properties are obtained as functions of the relative density and of the values of compact bone. Even so, experimental data are needed to provide the constants related to the the cell geometry, as will be seen later.

A third approach is based upon detailed modelling of the bone using finite element analysis, a procedure that is gaining increased favour as computing capacity increases and, with it, the possibility of observing and recording, in each case, the mesoscopic and microscopic bone structure, such as with computer ised tomog raphy . This method allows consideration of local geometrical effects, such as notches, or imperfections.

From now on, and in order to make the section more succinct, the treatment is basically restricted to dimensional models.

Stiffness and strength

Figure 3.3.3 and 3.3.4 contain the stress-strain curves obtained from compression (Figure 3.3.3) and tensile (Figure 3.3.4) tests on various types of bone. One of the purposes of these figures is to show the diversity which is obtained depending upon the type of bone, the anisotropy and the type of test.

The relative density of the bone has a great effect in compression tests (Figure 3.3.3); compact bone is very stiff and not very flexible, while spongy bone suffers reduced stiffness and increased flexibility as its porosity increases.

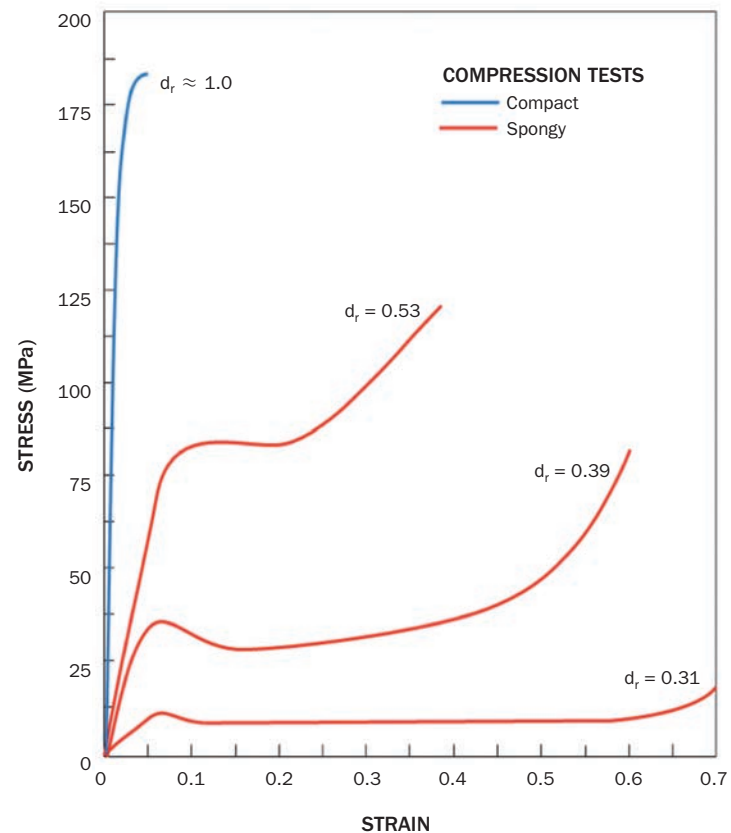


Fig. 3.3.3 Influence of the relative density (d_r) in compression tests on compact and spongy bones (data from Hayes and Carter (1976) and Hayes and Gerhart (1985)).

The form of loading, depending upon whether it is in the longitudinal or transverse direction, is clear in tensile tests (Figure 3.3.4) performed on compact bone. Other tensile test results for spongy bone have been included in the figure to illustrate the different values of strength and strain to failure.

Bone, as has been mentioned several times already, is a complex material in which, as well as the density and anisotropy, time also influences the mechanical properties, as will be discussed later. For these reasons, modelling the mechanical behaviour of bone is difficult. Figure 3.3.5 shows, in schematic form, the mechanism responsible for the deformation of spongy bone subjected to compression (Figure 3.3.5a) and tension (Figure 3.3.5b).

A great deal of data (strength, strain to failure and initial elastic modulus) can be found in Currey (2002) for compact human and bovine bones, tested in the longitudinal, radial and circumferential directions.

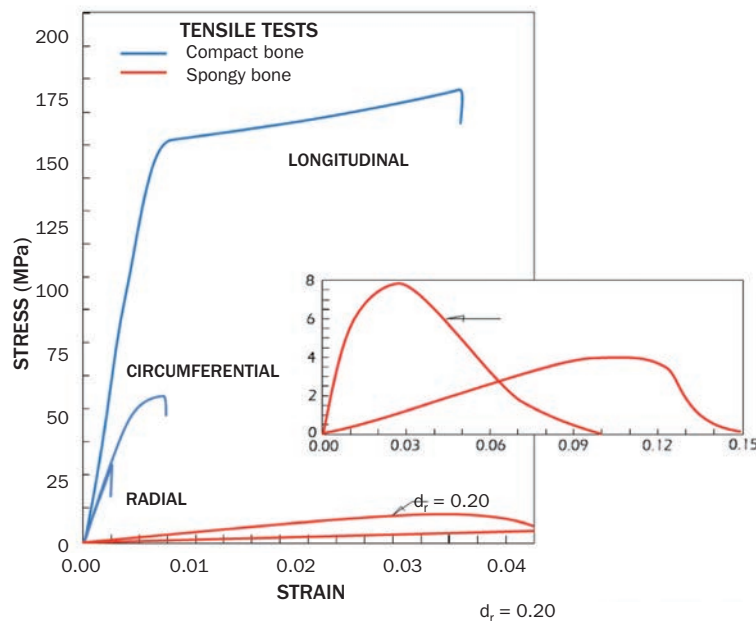


Fig. 3.3.4 Influence of anisotropy and relative density (d_r) in **tensile** tests on compact and spongy bones (data from Carter et al. (1980) and Kefalas and Eftaviopoulos, 2012).

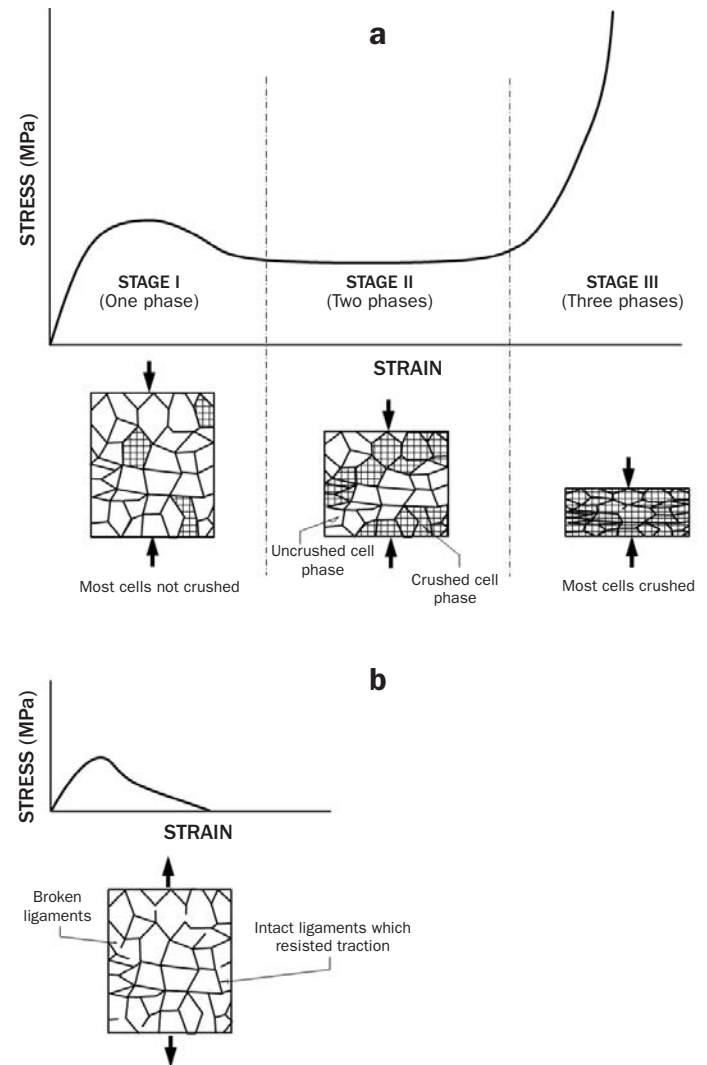


Fig. 3.3.5 Mechanisms responsible for the deformation of spongy bone when tested in compression (a) and tension (b).

Next, two essential aspects are analysed in some detail in order to understand the mechanical behaviour of bone; the *stiffness* and *strength*.

The **stiffness** of bone, measured in terms of the *elastic modulus*, may vary from 7 GPa (for example, for the compact femoral bone of a young, 3 month old, polar bear) to 30 GPa (for the femur of a deer). The value for femoral compact bone in a human adult is around 17 GPa. These values are much lower than the, approximately, 120 GPa of hydroxyapatite. The average modulus of collagen –the other component of bone– is of the order of 1 GPa.

Several attempts have been made to model bone. The first, and simplest, for compact bone were based on **composite material** models. Katz (1971) considered two extreme cases: When the load is in the direction of the reinforcement (Voigt model) and when it is perpendicular (Reuss model). The corresponding elastic moduli are given by (see Section 2.3.3).

$$E (Voigt) = V_m E_m + V_c E_c \quad (3.3.1)$$

and

$$1/E (Reuss) = V_m/E_m + V_c/E_c \quad (3.3.2)$$

where the subindices *m* and *c* refer to the mineral and collagen, respectively and *V* is the volume fraction of each constituent. Both extreme cases are represented in Figure 3.3.6, together with the experimental values taken from Currey (2002). This model has little predictive capability and was later refined by (Katz 1981, Wagner and Weiner 1992, Pidaparti *et al.* 1996, and Jager and Fratzl 2000, among others). Upper and lower bounds of a more refined model, that of Hashin-Shtrikman, are also shown in Figure 3.3.6, also considered by Katz. The dentine region has been included because in that type of bone the fibres are highly orientated in the loading direction and for that reason the Reuss model gives a reasonable prediction.

The elastic modulus in bone –which, as has already been noted, is essentially a material composed of hydroxyapatite, collagen and water– is basically a function of two variables; the percentage of mineral content and the porosity. The relationship between the elastic modulus and mineral content can be seen in Figure 3.3.6. The trend is clear, but if the contribution of porosity is added, as will be seen later, the correspondence of these two variables improves markedly.

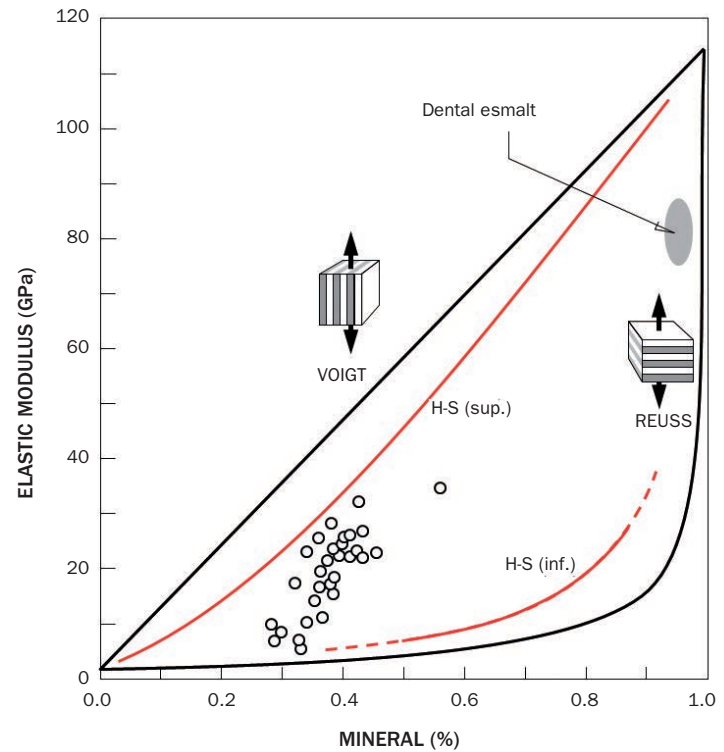


Fig. 3.3.6 Values of the elastic modulus (for different compact bones) as a function of their mineral content. The predictions of various models (see text) are also shown in the Figure. The experimental data are from Currey (2002).

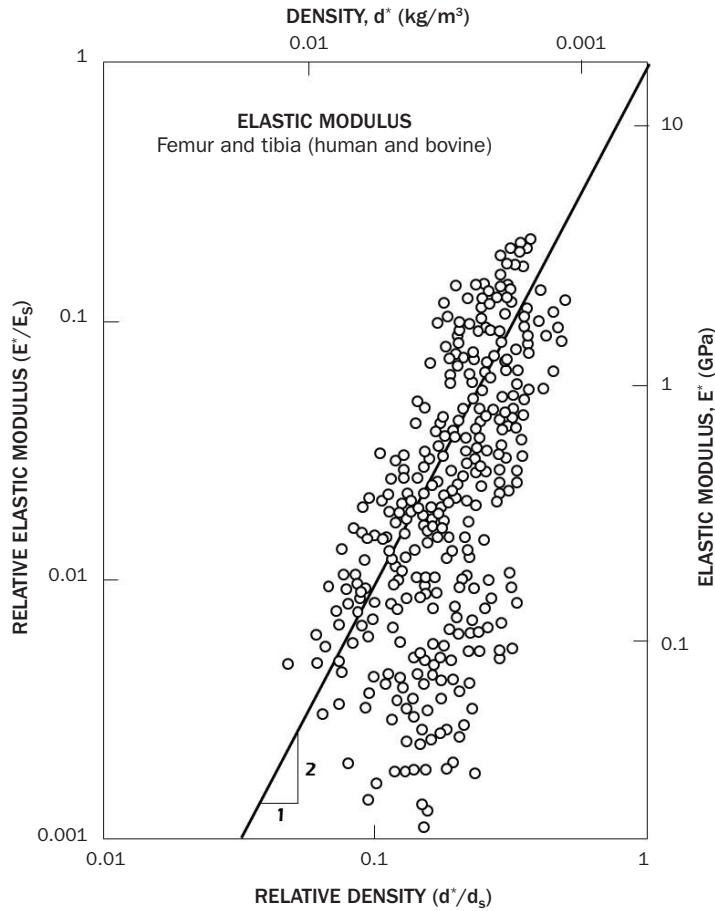


Fig. 3.3.7. Values of the elastic modulus (for different bones) as a function of their relative density (based on Gibson et al., 2010).

The contribution of porosity, more specifically for spongy bone, has been analysed in detail by Ashby and Gibson using the **cellular model** described in Section 2.3.4.

In order to estimate the initial elastic modulus, E^* , it may be assumed that the cellular structure deforms linear elastically and that the trabeculae are tiny beams which deform in bending. In these circumstances it is found – Section 2.3.4, Equation (2.3.3-28) – that the relative elastic modulus (E^*/E_s) varies as the square of the relative density (d^*/d_s), that is to say:

$$\frac{E^*}{E_s} = C_1 \left(\frac{d^*}{d_s} \right)^2 \quad (3.3.3)$$

The experimental results from numerous measurements on human and bovine bones (principally on tibias and femurs) are presented in Figure 3.3.7, and reasonable agreement with Equation (3.3-3) is apparent. The elastic modulus E^* and the density d^* of the spongy bones have been normalised with respect to the trabecular wall values of the bone (indicated in Table 3.3.2); 18 GPa and

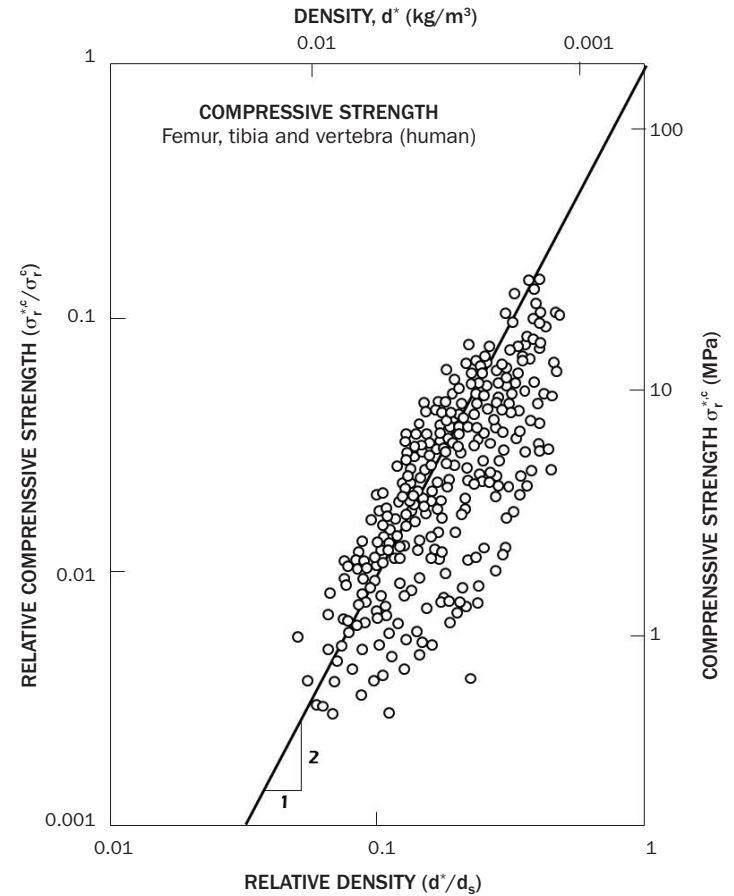


Fig. 3.3.8. Values of the compressive strength (for human bone) as a function of their relative density (based on Gibson et al., 2010).

1800 kg/m³, respectively. The value of C_1 is, approximately, unity (Gibson et al. 2010).

TABLE 3.3.2. AVERAGE VALUES OF THE TRABECULAE OF HUMAN SPONGY BONE

DENSITY KG/M ³	ELASTIC MODULUS (GPa)	σ_r^c (COMPRESSION) (MPa)	σ_r^t (TENSION) (MPa)
1800	18	182	115

The dispersion in the experimental results is due to several causes: the marked *anisotropy* of the spongy bone and the fact that measured values depend upon the direction in which the load is applied (see, for example, the data obtained by Williams and Lewis 1982). The *duration of the tests* also influences the results, as will be seen later; the strain rate may vary by five orders of magnitude. Finally, the *water content*, or the relative humidity during the test, can also affect the values obtained.

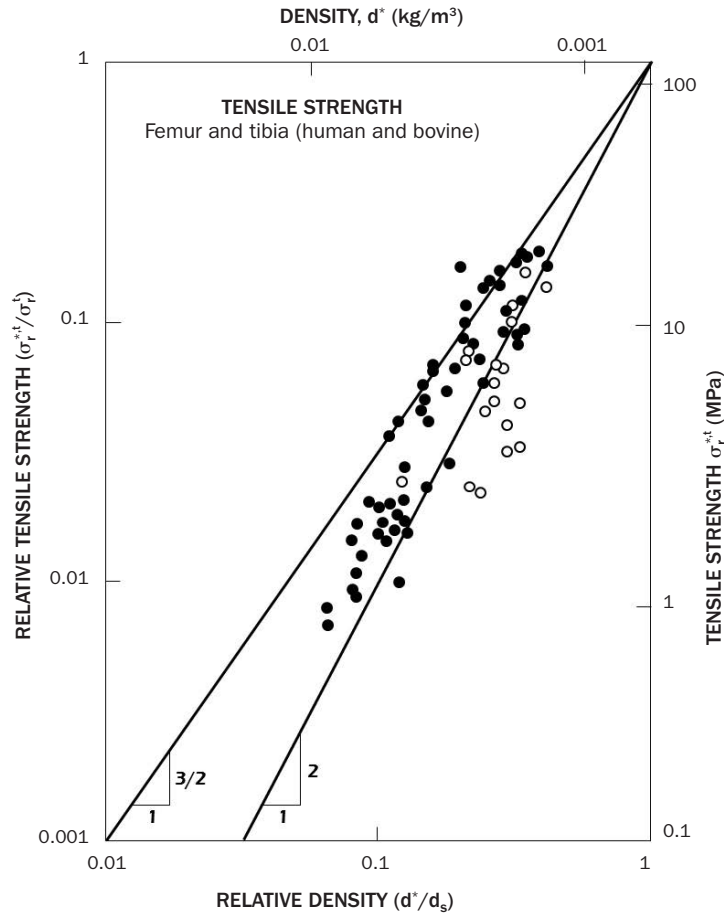


Fig. 3.3.9. Tensile strength (for human and bovine bones) as a function of the relative density. The filled symbols correspond to specimens in which longitudinal direction coincides with the bone axis (based on Gibson et al., 2010).

The values of the **strength**, in tension as well as compression, do not show such a clear dependence upon the mineral phase content as the elastic modulus and the classical models for composite materials yield poor predictions. The cellular models provide more acceptable results for *spongy bone*.

In order to estimate the *compressive strength* of spongy bone it may be assumed that the structure collapses by buckling of the trabeculae, according to the analysis in Section (2.3.3- 31), in which it was found that:

$$\frac{\sigma_{rot}^{*,c}}{E_s} = C_2 \left(\frac{d^*}{d_s} \right)^2 \quad (3.3.4)$$

The experimental measurements on human bone are presented in Figure 3.3.8, in which good agreement with Equation (3.3-4) is apparent. The rupture load $\sigma_{rot}^{*,c}$ must be normalised by the corresponding elastic modulus, since this datum is difficult to obtain the rupture stress in compression

in compact bone has been used ($\sigma_r^c = 182$ MPa). The density is normalised, as before, with that of the cell wall of the bone (1800 kg/m^3). The dispersion in the results is due to the same causes as mentioned before.

The *tensile strength* of spongy bone may also be estimated with the cellular model assuming that rupture is produced by the formation of plastic hinges in the trabeculae as was analysed in Section 2.3.4., Equation (2.3.3- 32), from which:

$$\frac{\sigma_{rot}^{*,t}}{\sigma_r^t} = C_3 \left(\frac{d^*}{d_s} \right)^{3/2} \quad (3.3.5)$$

Figure 3.3.9 contains Equation (3.3- 5) together with experimental results obtained with human and bovine bones. The rupture stress has been normalised by the tensile strength of compact bone ($\sigma_r^t = 115$ MPa) instead of σ_{ys} and the density by that of the bone wall (1800 kg/m^3). The tests in which the longitudinal direction of the specimen coincide with the bone axis (femur or tibia) are represented by filled symbols and fall within lines of slopes 3/2 and 2. The tests represented by open symbols correspond to specimens tested transversely.

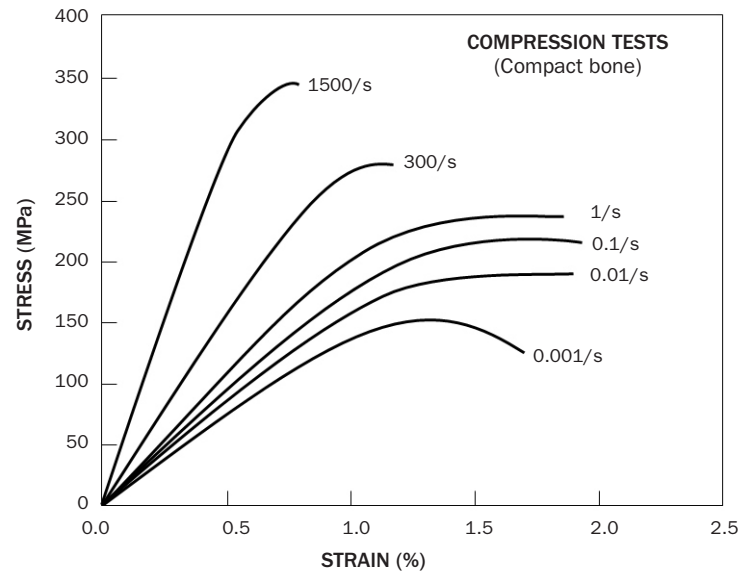
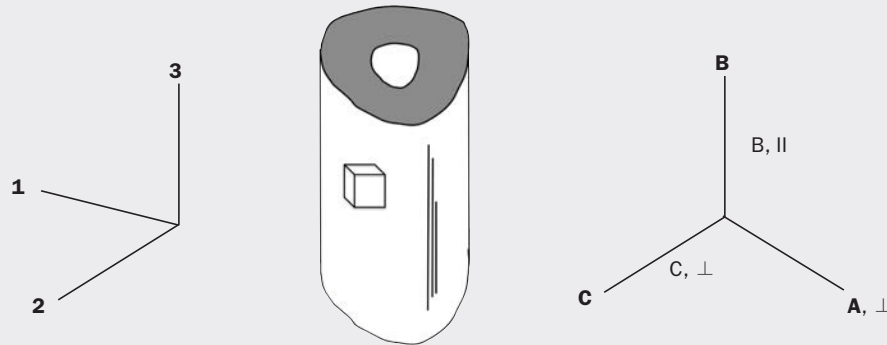


Fig. 3.3.10. Compression tests on compact bone (human and bovine) performed at different strain rates (McElhaney and Byars 1966).

EXERCISE 33

Compression tests have been carried out in the three directions of the edges of a cube removed from cortical bone, as shown in the figure.

In all of the tests the bone was compressed uniaxially up to the same value of strain, and the strain produced in the other directions measured. The table presents the values obtained.



COMPRESSION SENSE	ϵ_{AA} (%)	ϵ_{BB} (%)	ϵ_{CC} (%)	$\epsilon_{AB}, \epsilon_{AC}, \epsilon_{BC}$
axis A	-0.067	0.022	0.036	0
axis B	0.022	-0.067	0.022	0
axis C	0.037	0.023	-0.067	0

Using the results of Section 2.3.2 and EXERCISE 20 give reasoned responses to the following questions:

- Which mechanical behaviour –orthotropic or transversely isotropic– better fits the results obtained .
- What is the direction of the osteons? We will call this the parallel axis (||) and the axes at 90°, perpendicular axis (⊥).
- What is the value of the Poisson's ratio $\nu_{\perp\perp}$?
- What is the value of the Poisson's ratio $\nu_{\perp||}$?

SOLUTION:

a) and b) As has been seen, cortical bone is an anisotropic material which responds in different ways according to the direction of the loading. In the experiments performed we observe that the shear stresses ε_{ij} are zero, since the A, B, C directions coincide with the axes of orthotropy, as deduced from the structure of the flexibility tensor presented in EXERCISE 20:

$$\begin{bmatrix} \varepsilon_{11} \\ \varepsilon_{22} \\ \varepsilon_{33} \\ \varepsilon_{23} \\ \varepsilon_{31} \\ \varepsilon_{12} \end{bmatrix} = \begin{bmatrix} 1/E_1 & -\nu_{21}/E_2 & -\nu_{31}/E_3 \\ -\nu_{12}/E_1 & 1/E_2 & -\nu_{32}/E_3 \\ -\nu_{13}/E_1 & -\nu_{23}/E_2 & 1/E_3 \\ & & & 1/(2G_{23}) \\ & & & & 1/(2G_{31}) \\ & & & & & 1/(2G_{12}) \end{bmatrix} \begin{bmatrix} \sigma_{11} \\ \sigma_{22} \\ \sigma_{33} \\ \sigma_{23} \\ \sigma_{31} \\ \sigma_{12} \end{bmatrix}$$

in which 1,2, 3 are the directions of orthotropy. This tensor is symmetrical so that

$$-\frac{\nu_{21}}{E_2} = -\frac{\nu_{12}}{E_1} \quad -\frac{\nu_{31}}{E_3} = -\frac{\nu_{13}}{E_1} \quad \text{and} \quad -\frac{\nu_{32}}{E_3} = -\frac{\nu_{23}}{E_2}$$

In the case of a transversely isotropic material, where the 3-axis is that of isotropy, then

$$\frac{1}{E_2} = \frac{1}{E_1} \quad \frac{\nu_{31}}{E_3} = \frac{\nu_{13}}{E_1} = \frac{\nu_{32}}{E_3} = \frac{\nu_{23}}{E_2} \quad \text{and} \quad \frac{1}{2G_{23}} = \frac{1}{2G_{31}} \quad \frac{1}{2G_{12}} = \frac{1+\nu_{12}}{E_1}$$

When a load is applied along the axis of transverse isotropy the strain along the other two axes is the same, a situation that does not occur if the material is orthotropic. We see that this is our case when the compression is applied along the B axis, which we will identify as the axis of transverse isotropy, axis 3. This axis will also be the axis of the osteons, the parallel axis (\parallel).

For small numerical differences (0.037 vs 0.036 and 0.022 vs 0.023), we see that the strains fit the **transversely isotropic** model, axes A and C being axes 1 and 2, or perpendicular axes (\perp).

c) In order to obtain the Poisson's ratio $\nu_{\perp\perp}$ which we identify with ν_{12} , we consider the load along the axis A (or axis 1) and the strain along C (or axis 2). In this case it will be

$$\varepsilon_{AA} = -0.067\% \quad \varepsilon_{CC} = +0.036\% \quad \text{and} \quad \nu_{12} = -\frac{\varepsilon_{CC}}{\varepsilon_{AA}} = 0.54$$

If we consider compression along the other perpendicular axis, C (or axis 2), and the strain produced in the axis A (or axis 1) we will have

$$\varepsilon_{AA} = +0.037\% \quad \varepsilon_{CC} = -0.067\% \quad \text{and} \quad \nu_{21} = -\frac{\varepsilon_{AA}}{\varepsilon_{CC}} = 0.55$$

then, approximately, $\nu_{12} \approx \nu_{21}$.

d) The Poisson's ratio $\nu_{\perp\parallel}$, which we identify with ν_{13} , is obtained in a similar manner, considering now the compressive load along the axis A and the strain produced along B:

$$\varepsilon_{AA} = -0.067\% \quad \varepsilon_{BB} = +0.022\% \quad \text{and} \quad \nu_{13} = -\frac{\varepsilon_{BB}}{\varepsilon_{AA}} = 0.33$$

or also, loading along C and considering the strain along B

$$\varepsilon_{BB} = 0.023\% \quad \varepsilon_{CC} = -0.067\% \quad \text{and} \quad \nu_{23} = -\frac{\varepsilon_{BB}}{\varepsilon_{CC}} = 0.34$$

leading again to $\nu_{13} \approx \nu_{23}$.

Creep and relaxation

The experimental results of mechanical tests indicate that the values obtained may depend upon time, since they are a function of the loading rate and the duration of the test. Figure 3.3.10 shows several results from compression tests on small compact bone, human and bovine, performed at various strain rates –from very slow, $d\varepsilon/dt = 0,001/s$, to very rapid, $d\varepsilon/dt = 1500/s$ – (McElhaney 1966). The rupture

stress ranges from 150 MPa, for slow tests, to 350 MPa for very fast ones. The elastic modulus increases and the elongation under maximum load decreases with increasing test speed. In another type of experiment it is observed that the residual deformation after unloading depends upon the maximum load and the duration of the cycle. All of this indicates that bone is a visco-elastoplastic material.

These aspects are important for an understanding of the mechanical behaviour of bone. For example; during vigorous activity, long bones may sustain strain rates of 0.03/s in the human body, and 0.08/s in galloping horses. Impact fractures could be produced with higher strain rates, between 0.3/s and 1/s (Currey 2002). Note that for a race horse the values are even higher, and this may be why frequent fractures are found. If the strain in a bone is maintained for a while it is observed that the stress relaxes. On the other hand, if the stress is held constant, the strain increases and the bone creeps.

Figures 3.3.11a and b show the results of two creep tests, in which it is observed that the strain increase with time when the bone specimen supports a constant stress σ_0 . The data in Figure 3.3.11a is for spongy bone from the tibia of a bovine under a constant stress of $\sigma_0 = 19$ MPa. Figure 3.3.11b is for compact bone from the femur of a cow, subjected to a constant stress of $\sigma_0 = 86$ MPa.

It may be observed that in both Figures from the start of the test the strain rate (tangent to the curve) decreases rapidly with time until it reaches a practically stable value. This first stage is known as primary creep. The stage when the strain rate is constant is called secondary or stationary creep. Finally, a later stage, when the strain rate increases rapidly, is called tertiary creep, and rupture of the specimen quickly follows. Currey (2002) has suggested that it is possible to find a threshold stress below which the strain rate in the stationary phase is negligible; for human bones this threshold is about 65MPa. Data from Rimnac and coworkers (1993) for bovine compact bone (Figure 3.3.11b) suggest that the threshold –if it exists in this case– must be below 86MPa.

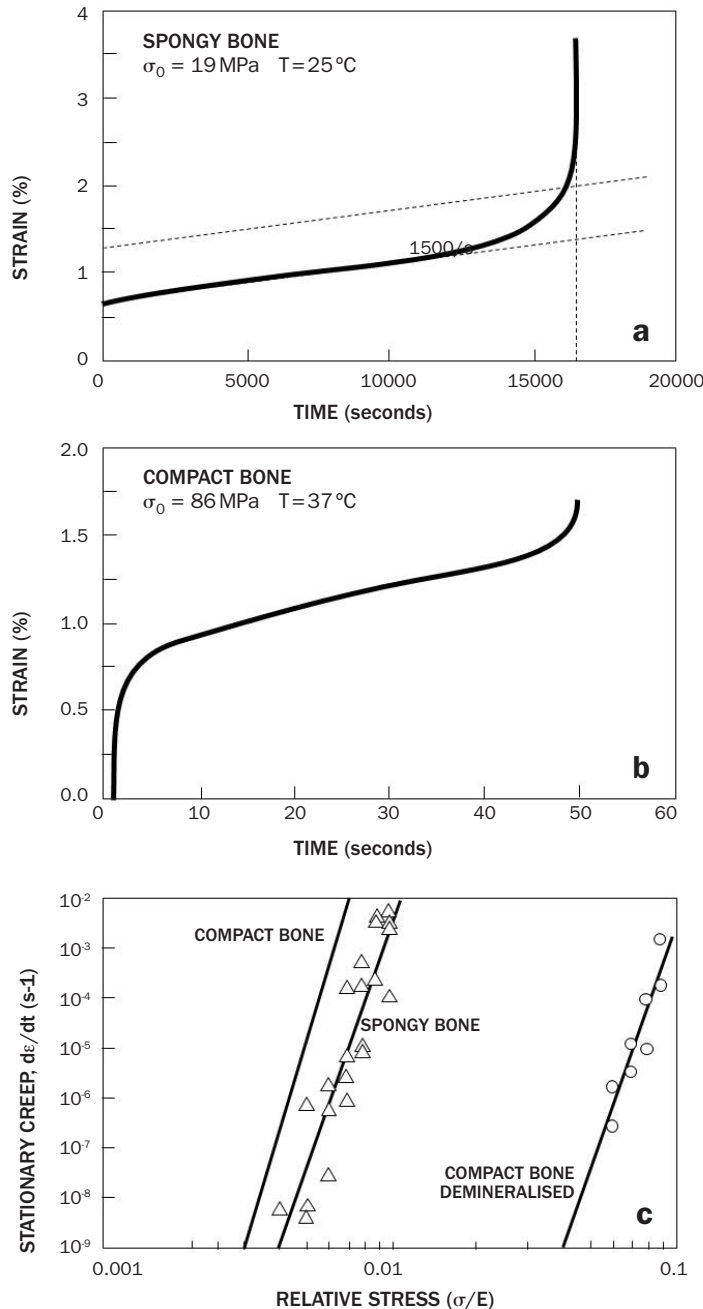


Fig. 3.3.11. Creep tests.

- a. Spongy bone. Bovine tibia (Bowman et al., 1998).
- b. Compact bone. Cow femur (Rimnac et al., 1993).
- c. Compact, spongy and demineralised bone (Bowman et al., 1999).

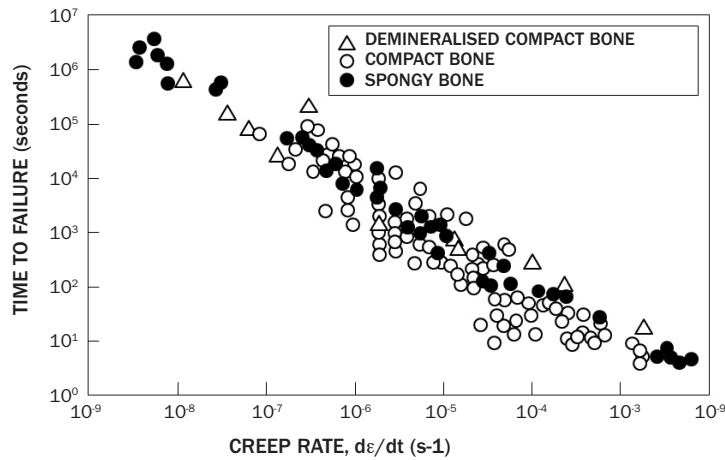


Fig. 3.3.12. Time to failure as a function of the stationary creep rate for different types of bone; compact, spongy, demineralised (after Bowman et al., 1999).

If the values of the strain rate in the stationary regime (secondary creep) are plotted as a function of the stress normalised with respect to the elastic modulus (σ_0/E), on a logarithmic scale, the results are quite well aligned, as shown in Figure 3.3.11c, in which data for spongy, demineralised compact bones are presented (taken from Bowman et al. 1999), together with a line corresponding to compact bone (according to Fondrk et al. 1992. The individual data have not been drawn). Two fairly obvious conclusions emerge from this Figure:

The first is that the experimental results can be represented as a power function of (σ/E), that is to say:

$$\text{Compact bone} \quad d\epsilon/dt = 3.38 \cdot 10^{38} \cdot (\sigma/E)^{18.9}$$

$$\text{Spongy bone} \quad d\epsilon/dt = 1.18 \cdot 10^{28} \cdot (\sigma/E)^{15.6}$$

$$\text{Demineralised compact bone} \quad d\epsilon/dt = 6.74 \cdot 10^{12} \cdot (\sigma/E)^{15.5}$$

where the constants which multiply (σ/E) have dimensions of s^{-1} . Gibson et al. (2010) have suggested that an exponential fit is more realistic than the power law indicated above.

The second conclusion lies in the exponents of (σ/E); the similarity of the exponents for compact, spongy, and demineralised bones suggest that the demineralised component of the bone (which reflects the role of collagen) is what is responsible for the creep, as much as for compact bone as for spongy. In both, the mineral component plays the part of a hard elastic inclusion.

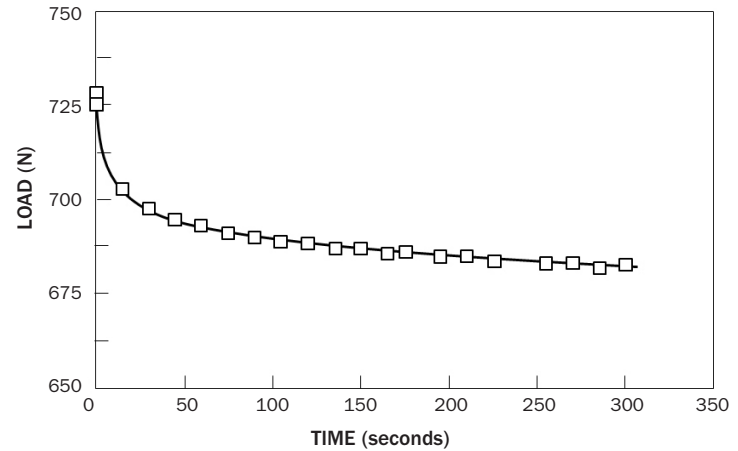


Fig. 3.3.13. Relaxation test on spongy bone. Bovine femur (Quaglini et al., 2009).

Figure 3.3.12 shows the time taken to break a bone specimen in a creep test as a function of the strain rate in the stationary region (both logarithmic scales). The data come from Bowman et al. (1999). The results for the previous three types of bone are a close fit to a straight line given by:

$$t(\text{failure}) = 0.03 (d\epsilon/dt)^{-0.91}$$

where t is given in seconds and ($d\epsilon/dt$) in $(\text{seconds})^{-1}$. The result obtained is characteristic of creep phenomena and known as the Monkman-Grant formula.

Figure 3.3.13 contains results of a *relaxation* test in which it is apparent that the stress decreases with time when the bone specimen supports a constant strain. The tests on spongy bone indicate that the behaviour does not conform to a linear viscoelastic model (Quaglini et al. 2009).

Anisotropy is an other issue which complicates the analysys of these tests (Iyo et al. 2004). In general, the procedure used to understand this phenomenon is based on separately considering the contribution of the collagen matrix (an integral part of the isotropic component) and the contribution of the bone structure (responsible for the anisotropy). It is unusual to observe rupture with time in relaxation tests (as opposed to creep tests) what is observed –when the initial strain is above that corresponding to the yield stress– is the generation of damage in the bone, a process which is reflected in rupture tests (Nagaraja et al. 2007).

Visco-elastoplasticity also manifests itself in bone subjected to *cyclic loading*. In the first part of this book –under the heading linear viscoelasticity Section 2.5.3– the storage (G_1) and loss moduli (G_2), as well as the loss tangent $tg \delta = G_2/G_1$ were defined. Both G_2 and $tg \delta$ are indicators of the energy dissipated in each cycle, while G_1 is a measure of the elastic modulus.

Lakes et al. (1979), studied the viscoelastic response of human and bovine compact bone as a function of temperature, using cyclic torsion tests and came to the conclusion that temperature was important and that experiments must be performed at body temperature if tests are to be relevant to in vivo situations. More recently, Yamashita et al. (2001), studied the behaviour of human femur compact bone by means of cyclic flexure tests at a frequency of 1 Hz and at 37°C; they measured the loss tangent, $tg \delta$, and the storage modulus G_1 . A typical results from these tests is represented in Figure 3.3.14. The intention of this study was to keep the loads low to use the formalism of linear viscoelasticity, but they found that for very low loads the dispersion in the results was large. It was necessary to find a threshold load that resulted in little scatter and which was sufficiently low to stay within the bounds of the linear hypothesis, (these values depend upon the size and type of specimen). The moisture content in the specimens has a strong effect on the value of $tg \delta$; dry specimens produce lower values than wet ones.

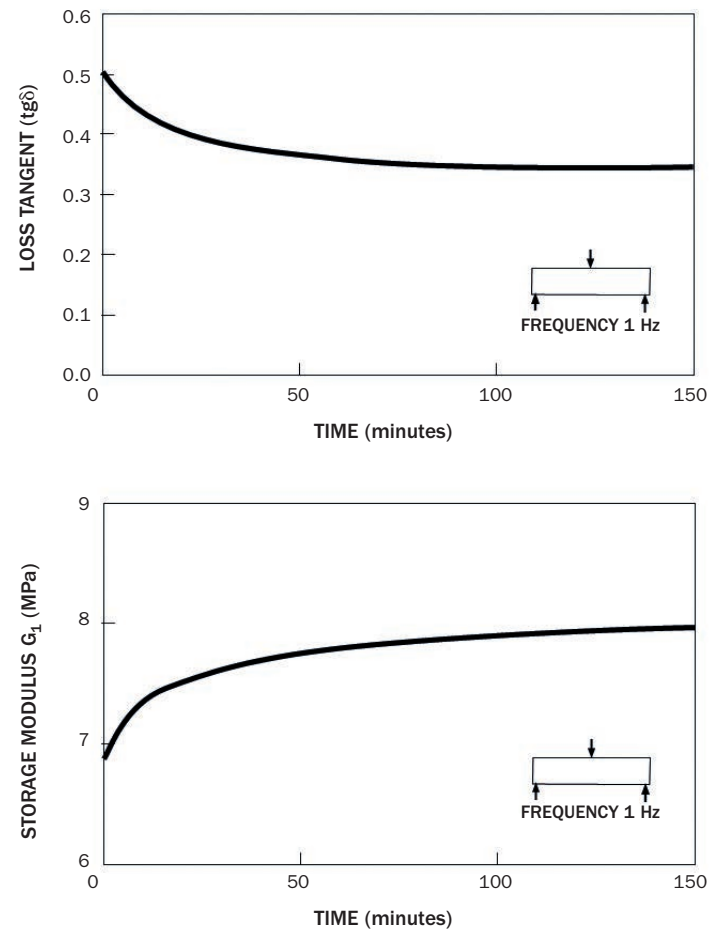
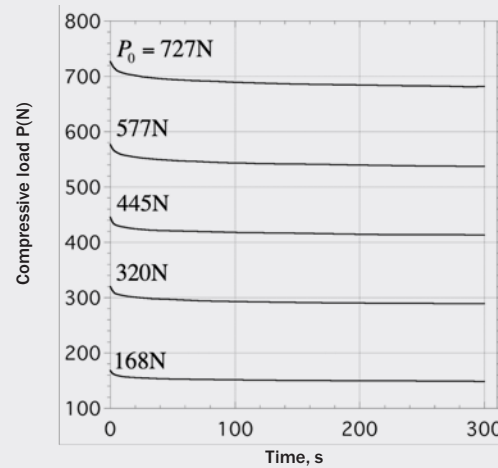


Fig. 3.3.14. Cyclic load tests. Application of the linear viscoelastic model to human femur compact bone. (Yamashita et al., 2001).
a. Loss tangent.
b. Storage modulus.

EXERCISE 34

The Figure shows the compressive relaxation experiments of Quaglini et al. (2009), on 10mm diameter cylindrical trabecular bone specimens. Using the results of Section 2.5.3 of the "Biological Fibres" volume, show that the linear viscoelastic model is inapplicable to this material.

**SOLUTION:**

In the cited Section, for linear viscoelasticity, we see that in a relaxation experiment the stress σ on the specimen must satisfy Equation (40)

$$\sigma(t) = \varepsilon_0 G(t)$$

where ε_0 is the initial applied strain, which is held constant throughout the test, and $G(t)$ is the relaxation modulus, a function of time which depends only upon the material. If we divide the above expression by the values at time $t = 0$ we obtain

$$\sigma / \sigma_0 = P / P_0 = G(t) / G(0)$$

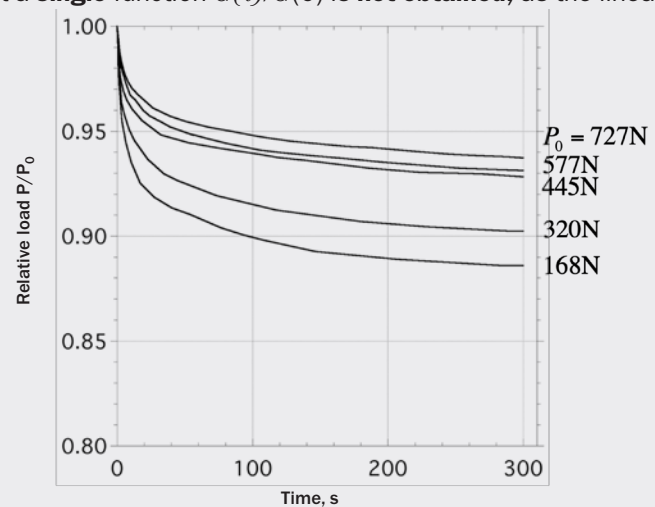
so that the stress will be proportional to the applied load P .

Plotting the values of the relative load P/P_0 against time, we see that a **single** function $G(t)/G(0)$ is **not obtained**, as the linear viscoelastic model demands.

As discussed in Section 2.5.3 of the "Biological Fibres" volume, strict applicability of the linear viscoelastic model is quite limited and no biological material –bone included– satisfies the requirements for its application.

Even so, the linear viscoelastic model can be used to model trabecular bone –and other materials– provided the load and time intervals considered are limited.

As an example, in our case we see that the curves corresponding to P in the range 445 to 727 N, and upto 300 seconds are reasonably concurrent. So that, a linear viscoelastic model with an average function $G(t)$ obtained from these relaxation can be sufficiently accurate for loads and times within the specified ranges.



Fracture

Fractures in healthy bone are due to overloading (loads higher than normal) or suddenly applied loads. In both cases the crack responsible for the fracture is initiated in a place in which a stress concentration or excessive strain is produced; a notch, or a cavity. Other types of fracture are due to the bone being weakened and fracturing under normal loads. The weakening, or damage, originates from various causes; *osteoporosis* is the most frequent, but repeated loads, *fatigue*, can also weaken bone tissue, *creep*, as already noted, can be another cause but it is rare under normal circumstances. Below, both processes; overloading and fatigue, are briefly analysed.

Fractures due to static loading are initiated by the generation and unstable propagation of cracks, and for their study it is possible, in principle, to apply the fracture criteria described in Section 2.2.2. To this end, fracture tests have been performed on cracked specimens, in the form of beams (SEN) or compact tension specimens (C), and values of the fracture toughness (K_{Ic}) and the specific fracture energy (G_c) measured. These results must be treated with caution since bone does not always behave as a linear elastic material (and therefore the concept of K may lose its validity), is anisotropic and the results depend upon how the specimen was machined. Humidity, temperature and time, also affect the results. Therefore, when values are taken from the literature, note must be taken as to how they were obtained.

In Figure 3.3.15 the common geometries used to measure fracture toughness are shown. The specimens are machined so that the crack propagates in the direction of the osteons (longitudinal, *L*) or transverse to them (*T*). The results depend upon the orientation of the specimens as illustrated in the adjoining graphic, the values of K_{Ic} double when the crack propagates transversely to the direction of the osteons. (The data correspond to human compact humerus bone; Ritchie et al. 2005).

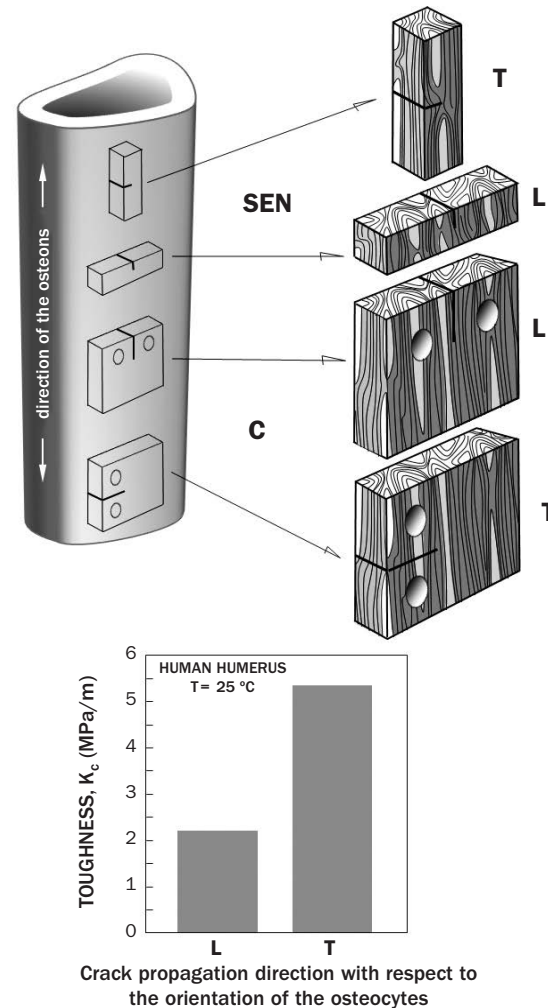


Fig. 3.3.15. Common geometries and specimen arrangement for fracture toughness measurement. The data correspond to human humerus compact bone. (Ritchie et al., 2005).

In Table 3.3.3 values of K_{Ic} and G_c are included for different species, bone types and specimens machined in different orientations (Ritchie et al. 2005).

TABLE 3.3.3. FRACTURE TOUGHNESS OF COMPACT BONE (RITCHIE ET AL. 2005)

SPECIES	BONE	ORIENTATION	K_{Ic} (MPa m ^{1/2})	WHALE TYMPANUM	SPECIMEN GEOMETRY
Human	Femur	L	6.4 ± 0.3	—	SEN
Human	Humerus	T	2.2 ± 0.2	—	SEN
Human	Humerus	L	5.3 ± 0.4	—	SEN
Bovine	Femur	L	2.4 – 5.2 ^a	920 – 2780	C
Bovine	Tibia	L	4.5 – 5.4 ^a	760 – 2130	C
Bovine	Tibia	L	2.8 – 6.3 ^a	630 – 2880	C
Baboon	Femur	T	1.8 ± 0.5	—	C
Baboon	Femur	L	6.2 ± 0.7	—	SEN

a. Specimens performed at different loading rates. SEN: cracked beam specimens. C: compact tension specimens. L and T: Orientations shown in Figure 3.3.15.

It is shown in Figure 3.3.16 that the values of the toughness can be a function of the crack propagation before reaching an unstable size; the R-curve behaviour discussed when studying fracture in Section 2.2.2. These experimental results illustrate the existence of intrinsic hardening mechanisms which hinder crack propagation, a topic which will be discussed next. Figure 3.3.16a shows, once more, that bone is an anisotropic material and that it is more difficult to cross the osteons than to propagate parallel to them (data from An et al. 2011). In Figure 3.3.16b the cracks propagate parallel to the direction of the osteons but it indicates that the mechanisms which impede their propagation decrease with age, not only the resistance to propagation (slope of the line) but also the initial toughness (ordinate at the origin) (data from Koester et al. 2011). Therefore, once a crack is induced it is more likely to be arrested in a young person than in an old individual.

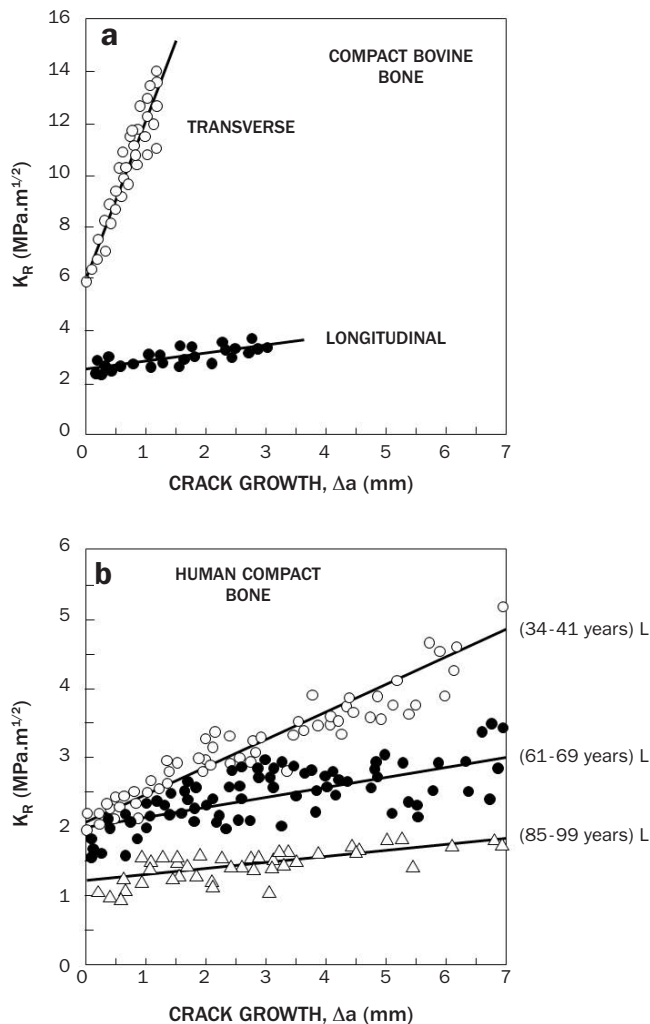


Fig. 3.3.16. Values of the fracture toughness, K_{Rv} , as a function of the crack growth.
a. Effect of anisotropy (An et al., 2011).
b. Effect of age (Koester et al., 2011).

In order to explain the increase in toughness with crack progression several mechanisms have been proposed, the most accepted are illustrated in Figure 3.3.17. The most important is due to ligaments, or *bridges*, between the two crack faces, Figure 3.3.17a. If the number of bridges increases as the crack grows so will the toughness. In some cases, when the number of ligaments created is equal to the number destroyed when the crack advances, the Rcurve (indicated in Figure 3.3.16) stops increasing and remains horizontal until unstable fracture. Another mechanism which impedes crack advance, because the stress intensity factor decreases, its deviation in the vicinity of osteons (Figure 3.3.17b), when the crack plane is transverse (see Figure 3.3.15, direction T). The interfaces between the osteons are highly mineralised (usually called *cement lines*) and are microstructurally weak and, therefore, preferred paths for cracking. Finally, crazing around the crack (Figure 3.3.17c) can also increase the toughness if the microcracking is accompanied by dilatation. All of these mechanisms are analysed in detail in Nalla et al. (2005) and in Ritchie et al. (2005).

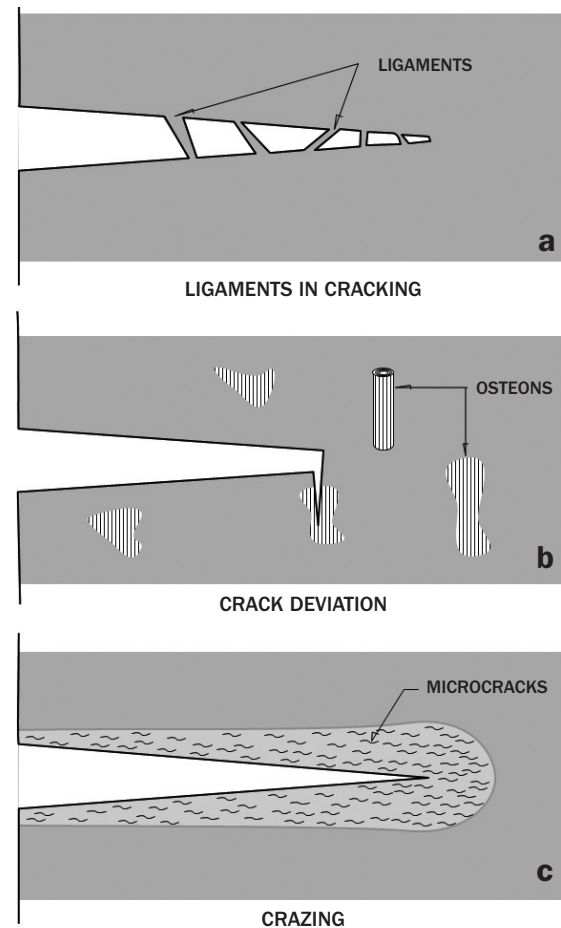


Fig. 3.3.17. Mechanisms explaining the increase in toughness with crack growth
a. Formation of bridges between crack faces b. Promotion of crack deviation c. Crazing (diffuse cracking) accompanied by dilatation.

Fracture due to variable loads, *fatigue fracture*, is due to the generation of stable cracks over time until a critical crack size, when unstable fracture is produced. It is estimated that in humans half of vertebra fractures and 10% of hip fractures, are due to the variable loads which we support in our daily lives and not due to a traumatic event (Meyers and Wilson 1997). In both cases, most of the loads are borne by spongy bone working in compression and for this reason almost all of the investigations into the fatigue fracture of bones have been carried out with cyclic compression tests on spongy bone.

The simplest tests consist of subjecting bone specimens to cyclic compressive loads and recording the number of cycles to failure. S-N curves, previously discussed in Section 2.2.2, are produced by this procedure. Various authors have suggested highly simplified models to explain these results.

Figure 3.3.18a shows the results from a compressive fatigue test on bovine spongy bone. The values obtained conform quite well with the following expression (Bowman et al. 1998):

$$N_f = 1,77 \cdot 10^{-23} (\Delta\sigma/E_0)^{-11.19}$$

in which N_f is the number of cycles to failure, $\Delta\sigma$ is the stress range and E_0 is the initial elastic modulus; 2690 MPa.

The previous results lie on a straight line when the scales of the axes are logarithmic. However, in Figure 3.3.18b, we see that the data from the fatigue tests of five authors (according to Gibson et al. 2010) do not provide such a satisfactory fit. This may be due to the inclusion of different species of bone (human and bovine), different types of specimen tested in different orientations, to the contribution of creep and to the specific damage produced by the cyclic loads. In any case, a similar trend is observed in all of the results, the line which represents them has a slope of about -12.

Attempts at modelling the fatigue behaviour of spongy bone have used the finite element method with various architectures; two-dimensional hexagonal honeycombs, or three-dimensional Voronoi polyhedra. Cracks were introduced into these low density idealised spongy bone structures and Paris' formula was used to calculate their propagation (Guo et al. 1994, Schaffner et al. 2000 or Makiyama et al. 2002). The results provided a potential relationship between N_f and $(\Delta\sigma/E_0)$, but with a somewhat different exponent; 4,5 rather than 12. It is possible that these differences are due to the fact that the models ignore the crack initiation phase and the damage produced by microcracking. In any case, the exponent 12 is more appropriate for dense spongy bone, while the models discussed refer to low density spongy bone.

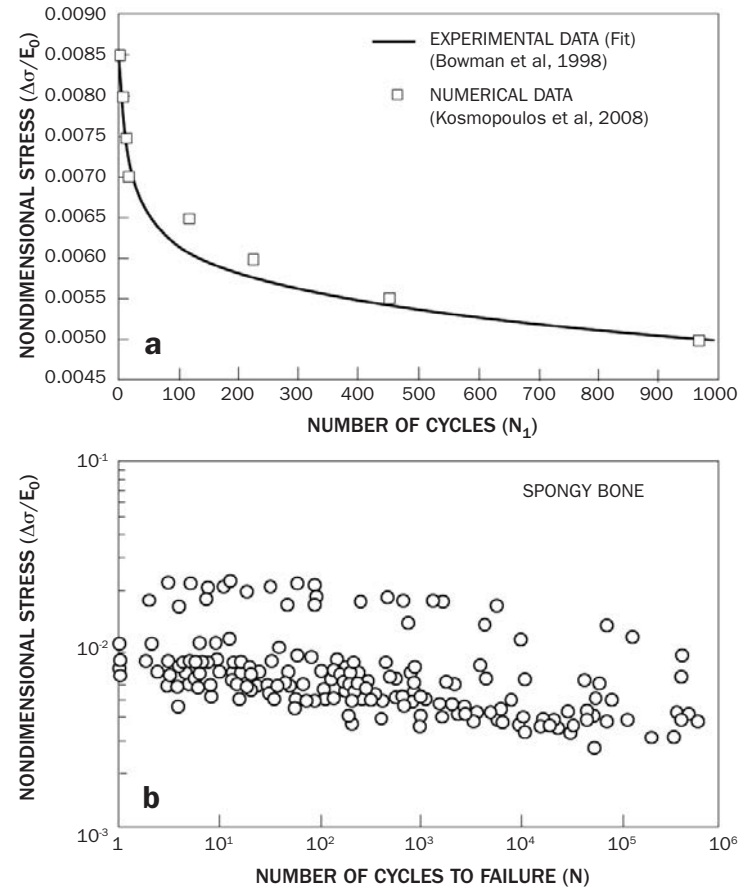


Fig. 3.3.18. Compressive fatigue tests. a. Bovine spongy bone. Curve fitted to experimental data (Bowman et al., 1998) and data from a numerical model (Kosmopoulos et al. 2008). b. Log-log plot of $(\Delta\sigma/E)$ against number of cycles to failure N_f . Various experiments (Gibson et al., 2010).

Kosmopoulos et al. (2008) have proposed a model for dense spongy bone which gives an exponent of 12.2, very close to the experimental results. The model assumes that the repeating loads which are produced during everyday life produce microdamage in the bone, which initiates a gradual reduction in the elastic modulus and its strength before the appearance of microcracks. The numerical results agree well with those of the experiments, as may be seen in Figure 3.3.18a.

For a more detailed account of the different methods of testing bone the reader is advised to consult the book of An and Draughn (2000). More information on the mechanical properties can be found in the previously cited book by Currey (2002).

3.3.4. Final remarks

Bone as a **biological material**.

The material of bone, as previously mentioned, is a network of collagen intermixed with calcium phosphate, and water. Collagen is widespread throughout the animal kingdom and it is perhaps surprising that other realms have not used the combination of collagen and minerals to create strong tough structures. Combinations of organic material and minerals are rarely found; in mollusc shells in which calcium carbonate is associated with an organic material, the constitution of the latter is hardly 5%. As for silica, another material used by living organisms, it does not form composites with organic materials, even though it is the skeletal material of various protozoas and the spicules of some sponges.

Stiffness in the plant kingdom is achieved through the formation of highly hierarchical structures with organic materials, as discussed in the analysis of wood. In invertebrates stiffness is produced by means of minerals in the form of small crystals, also with a very hierarchical structure, bonded by a low protein matrix (between 1 and 5 per cent) or with highly structured organic materials, as happens in arthropods, whose cuticles are formed of chitin fibres held together with protein cross-links. The drawback of these cuticles is that they are not reabsorbed as the animal grows and must be shed periodically. Animal with bones do not have this inconvenience, the bone is remodelled.

Bone does not perform the same functions during its lifetime and changes as the individual develops and in response to the loadings it receives. Currey has investigated the mechanical properties of dry human femur from the age of 3.5 to 40 years (Currey 2002). The elastic modulus and strength (in flexural tests), increase rapidly up to 10 years of age and then grow more slowly or stabilise. The impact strength, on the other hand, decreases rapidly up to 10 years and then decreases more slowly. It is possible to correlate these results with human behaviour if it is borne in mind that children are subjected to different selective pressures than adults; children are quite curious and have a tendency to fall, but don't have to run long distances in search of prey. For the young it is very useful not to have bones break easily, while in grown ups strength is more advantageous than toughness. As has been mentioned repeatedly, it is very difficult to simultaneously achieve high strength and toughness.

The changes produced in bone after 40 years of age, to take an approximate date, are not usually of the adaptive type but rather of the senile nature. The structure of spongy bone changes with age because its mass is reduced; the already thin trabeculae go on reducing their thickness and many are reabsorbed, which results in a marked reduction in the elastic modulus and strength of the bone. Guo and Kim (2002) have developed a microstructural model of spongy bone which allows simulation of the trabecular thinning, including their progressive disappearance. The results indicate that the loss of trabeculae is more damaging than the thinning, as much for the elastic modulus as the strength. For example; a random reduction by *disappearance* of 10% in the number of trabeculae induces a reduction of 40% in the elastic modulus and the strength, while the same reduction in the *thickness* of the trabeculae only produces a loss of 20%. These results indicate that the usual medical treatments for osteoporosis –which, basically, provoke an increase in the thickness of the trabeculae, but not their number– are incapable of totally recovering the initial properties of the bone.

Bone, as a structural material, had a pivotal role during the earliest human settlements. In region where caves or sufficient wood were not available for construction, dwellings were made with mammoth bones. Archeologists have discovered the remains of homes in Siberia, up to eight metres in diameter, whose structure –now collapsed– was made of mammoth bones. Of course, these structures would have been covered with skins.

It should not surprise us, taking into account the above, that bone has played an important role in the arts; particularly in music. In 2006, a flute, made from a griffon vulture bone, was discovered in a cave in Germany. The instrument was 34 cm long and 8 mm in diameter with five finger holes and a mouthpiece adequate for its function, it appears to have been made 35,000 years ago (national geographic.com2009). Also, in a nearby cave, two flutes made from swan bones were found, dated between 42,000 and 43,000 years ago. Another impressive find, in a cave in Slovenia in 1995, is a piece of femur from a cave bear with four artificial holes, which could well have been a flute. Interestingly, it has been dated at about 60,000 years ago and fabricated by Neandertals (Wikipedia. Babe flute).

Bone as a **biomaterial**.

Again –in the sense of a material “to treat, correct or replace tissue or organs in the human body” (Biomaterials Eur. Soc.)– bone is a *biomaterial*, because it has been used for grafts.

Bone grafts are used in surgery of the locomotor system, vertebral infusions or post-traumatic bone defects, to name but a few examples. Autologous bone graft or autograft (obtained from the patient him or herself) is the material of choice of surgeons, but it has disadvantages related to the morbidity of the donor site (usually the iliac crest) which restricts its application. Available alternatives are bone graft obtained from another patient (allograft) or other synthetic materials (biomaterials).

The first successful allograft operation appears to be by McEwen, in 1881, to repair a humerus (McEwen W. 1881). Since then, its use has spread in centers that treat complex pathologies. In the USA more than 150,000 bone allografts are performed each year. (Tomford W. et al., 1999). The advantages of these grafts over autografts are; greater availability, absence of problems in the donor zone, and shorter surgical time. Among the inconveniences are, there are the longer incorporation times and lower osteoconductive and osteoinductive capacities than autografts. Compatibility and the risk of transmission of infections improve with proper donor selection (Calvo R. et al, 2011).

A knowledge of the relationships between structure and mechanical properties of bone not only allows understanding of its behaviour but it also provides a valuable aid to the design of implants because it is essential to simulate, as well as possible, the properties of the bone which it is going to substitute. In femoral head implants, for example, the differences between the properties of the implant and the surrounding bone are believed to be one of the reasons why the prostheses decouple after ten or fifteen years. In these cases, the replacement of the prosthesis is then not so straightforward or safe as before. The design of prostheses more like bone would have considerable economic repercussions since the number of femoral implants in the world is extremely high; in the USA alone, more than 200,000 were performed in 2010.

To conclude this short chapter it is worth pointing out, as has been done in the previous examples, some ideas which this extraordinary biological material may offer to **biomimetics**. It has been observed that spongy bone is surrounded by compact bone, and this bone architecture has the effect of optimising the strength for the minimum possible mass.

Long bones can be considered as if they were thick-walled cylinders of compact bone with enlarged ends and in whose interior is spongy bone. The wall thickness is optimised so that the stiffness of the bone be maximised for the function it performs (Alexander et al. 1990).

Flat bones have a sandwich structure; two compact bone laminas with spongy bone between. In this type of bone the transition between the compact and spongy bone is quite abrupt, opposite to what happens in long bones where the transition is gradual. This structure is also optimised, for the functions it has to perform, so that the mass is minimal (Gibson et al. 2002).

In some circumstances engineers also design structures to optimise the weight according to purely mechanical criteria and at other times they are inspired by Nature. The design of the structure of the fuselage and wings of aircraft are based on maximum strength with minimum weight. During the Second World War, the wings of the English multirole “Mosquito” aircraft were fabricated with a sandwich structure using birch for the surfaces with a balsa core. This was made possible, among other things, by the development of suitable adhesives. Nature already used these principles millions of years ago to design the skeletons of birds.

3.4. CARTILAGE

3.4.1 Introduction

There are three types of cartilage tissue in human beings, *hyaline* or *articular cartilage*, –the one that will concern us most in this section– *fibrous cartilage*, a special case of articular cartilage with a higher degree of collagen fibre reinforcement and which is situated primarily in the intervertebral discs and menisci and the *elastic cartilage*, which is yellowish and more elastic than articular cartilage due to the presence of elastin fibres. Elastic cartilage is present in the epiglottis, the larynx, external auditory canal and the Eustachian tube.

Articular cartilage, also called hyaline because of its whitish/bluish appearance, is more abundant in human organisms and contains type II collagen fibres. Its presence strengthens the nasal skeleton, the larynx, trachea and the bronchi and forms the costal arches of the ribs (Figure 3.4.1). Its principal function is, however, to cover the articular extremes of bones so that mechanical loads are transmitted with minimum friction (Figure 3.4.2). Like other cartilage, it is avascular, alymphatic and aneural.

Articular cartilage is composed of 70-80% by weight of water. The rest is made up of cells that create and sustain it, called chondrocytes, and an extracellular matrix formed fundamentally of type II collagen (~80% of dry weight) and proteoglycans (~20% dry weight) (Mow *et al.* 1990).

The cellular volume is about 10%, its contribution as dry weight being insignificant. Cartilage is one of the tissues with the least cell density in the body, possessing an average of a million cells per cm³ compared to 100 million for most other tissues. This fact makes tissue regeneration difficult, once damaged. The low cellular density is related a low capacity to receive nutrients which can only reach the cells through diffusion, since they lack a vascular network.

The extracellular matrix is formed of collagen and complex molecules called proteoglycans, whose structure is shown in Figure 3.4.3. This is a combination of proteins and mucopolysaccharides (also known as glycosaminoglycans, or GAGs for short) which produce a fabric capable of retaining large quantities of water.

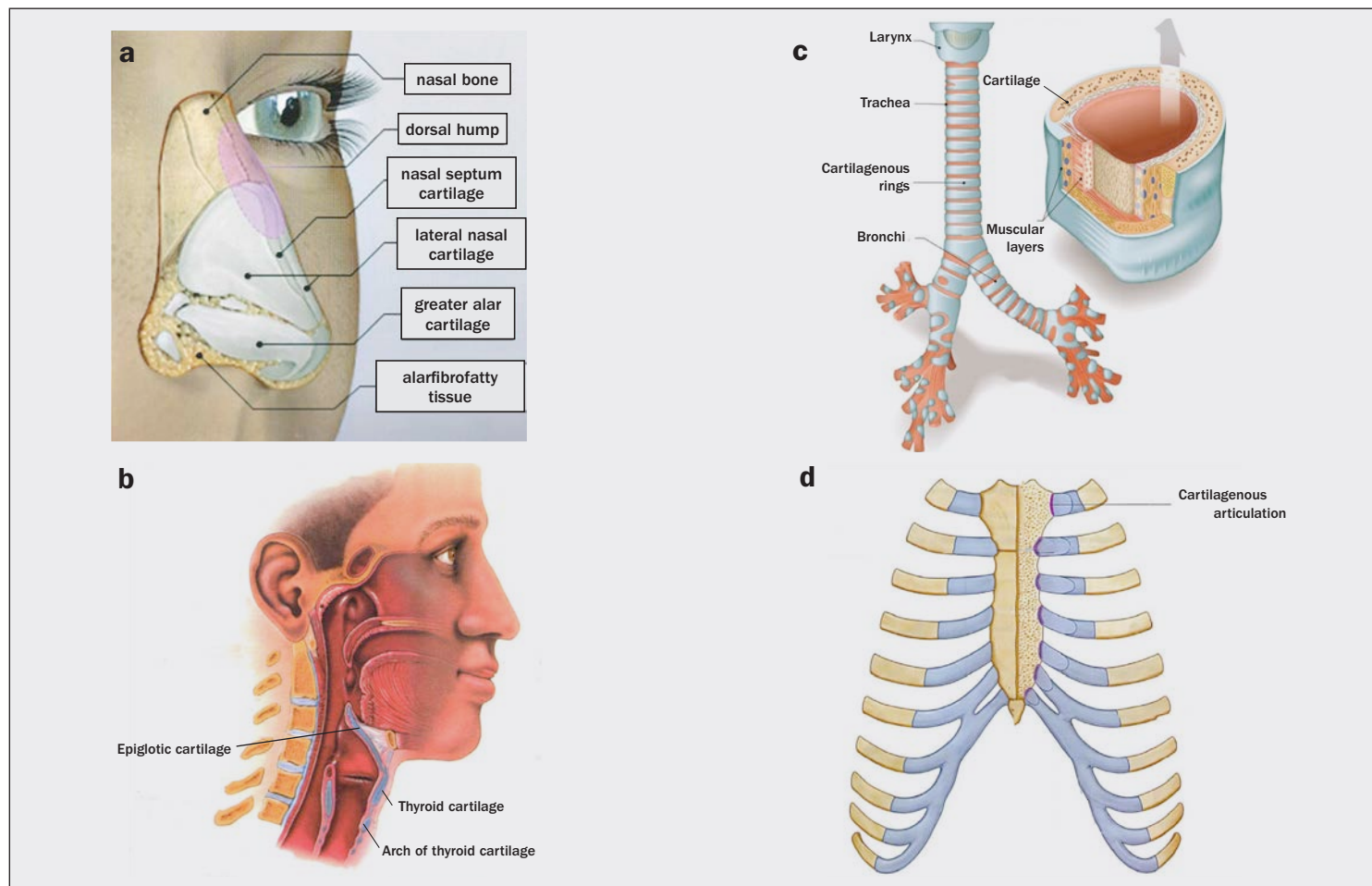


Fig. 3.4.1. Articular cartilage: a) nasal structure; b) larynx; c) trachea; d) costal arches

Articular cartilage covers joints in thicknesses less than a few millimetres and it is capable of supporting large loads with the lowest coefficients of friction, as shown in Table 3.4.1. To this end the joints are encapsulated in approximately 1ml of lubricating fluid called synovium (from the Latin *syn* –with– and *ovum* –egg) since its colour and consistency are reminiscent of egg white (Figure 3.4.2). Synovial liquid is a thixotropic fluid which reduces its viscosity with motion, in a way that further reduces the friction. Its composition includes hyaluronic acid secreted by the cells of the synovial membrane which surrounds the joint, a proteoglycan called lubricin which is produced by the chondrocytes of the cartilage, and interstitial fluid from blood plasma.

Due to the effects of movement, articular cartilage is almost perpetually subjected to alternating loads which, in the case of the hip or knee, may reach ten times the body weight, acting on surface areas of the order of cm². These loads induce motion of the internal fluid of the cartilage and facilitate transport of nutrients and waste products. The structure of cartilage is capable of supporting these loads without loss of hydration, maintaining its low coefficient of friction.

TABLE 3.4.1. COEFFICIENT OF FRICTION OF ARTICULAR CARTILAGE AND OTHER MATERIALS

MATERIAL	COEFFICIENT OF FRICTION
Articular cartilage**	
Human knee	0.005 - 0.02
Porcine shoulder	0.02 - 0.35
Canine ankle	0.005 - 0.01
Other materials	
Rubber on concrete*	1.0
Brake material on iron*	0.1 - 0.4
Graphite on steel*	0.1
Hickory on dry snow**	0.08 - 0.18
Ice on ice**	0.02

* Static
** Dynamic

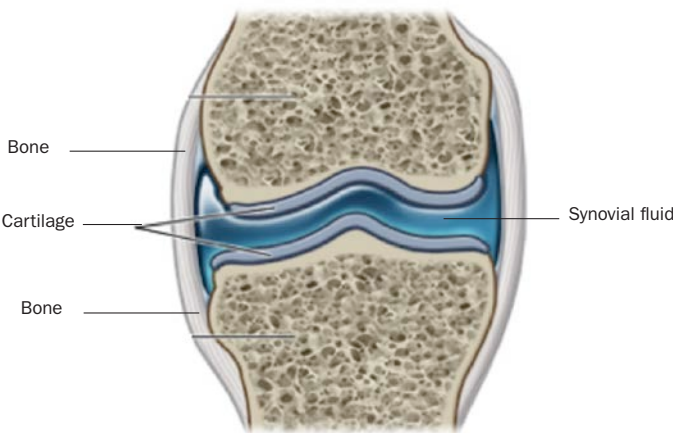


Fig. 3.4.2. Articular end.

3.4.2. Structure

Articular cartilage, like any other biological materials has a highly hierarchical structure from the molecular to the anatomical level. However, to facilitate description and analysis, we will distinguish—with some arbitrariness—the microscopic (molecular) and mesoscopic levels in its structure.

Microscopic level

At this level, cartilage can be considered as a material composed of water, cells (chondrocytes) and an extracellular matrix formed of collagen and proteoglycans (hyaluronic acid and aggrecans).

Hyaluronic acid is a fundamental component of cartilage and its presence is essential for it to correctly fulfil its biological purpose.

Hyaluronic acid is a glycosaminoglycan formed by the repetition of disaccharide glucuronic acid/N-acetylglucosamine, which constitutes the backbone of the large molecules of the cartilage. In an average weight man (70kg) there are about 15 grammes of hyaluronic acid, and about a third of this is degraded and synthesised every day (Stern 2004). Its name comes from *hyalos*—in Greek “transparent glass”—since it was first observed in the vitrius humor, and from the uronic acid which forms it. Hyaluronic acid is used widely in the treatment diseases of the cartilage such as arthritis or osteoarthritis and is obtained principally from natural sources such as the crests of roosters and the umbilical cord (Boeriu *et al.* 2013).

Protein chains are covalently bonded to the hyaluronic acid chains which, in turn, have cross-links to other GAG chains, called **aggrecans**, as shown in Figure 3.4.3. The principal aggrecans present in cartilage are chondroitin sulphate and keratan sulphate, both—like the rest of the GAGs—constructed of a repeated disaccharide unit. In the case of chondroitin sulphate it is glucuronic acid and N-acetyl-galactosamine and in keratan sulphate it is galactose and N-acetyl-glucosamine. The average molecular weight of the long proteoglycan chains is about 200–300MDa.

The fact that the sugars in the chondroitin sulphate and keratan sulphate chains are heavily sulphated is the key for the correct functioning of the cartilage, since the sulphate groups ($-\text{SO}_3\text{H}$), as well as the acid groups ($-\text{COOH}$) tend to easily lose their proton (H^+) and are active osmotically in attracting cations such as Na^+ , Ca^{2+} or K^+ . On average, there are about 50g of GAG saccharides per litre of cartilage and each disaccharide, again on average, is ionised with a charge $-2e$. The average molecular weight is about 502 Da from which we can estimate that in 0.2M ($M=\text{moles/litre}$) the negative electric charge associated with the cartilage. Given that this charge cannot be displaced and it is anchored to the GAGs, it is given the name *fixed charge density*, FCD, and its role is crucial in the development of the osmotic pressures which sustain the structure and functioning of the articular cartilage.

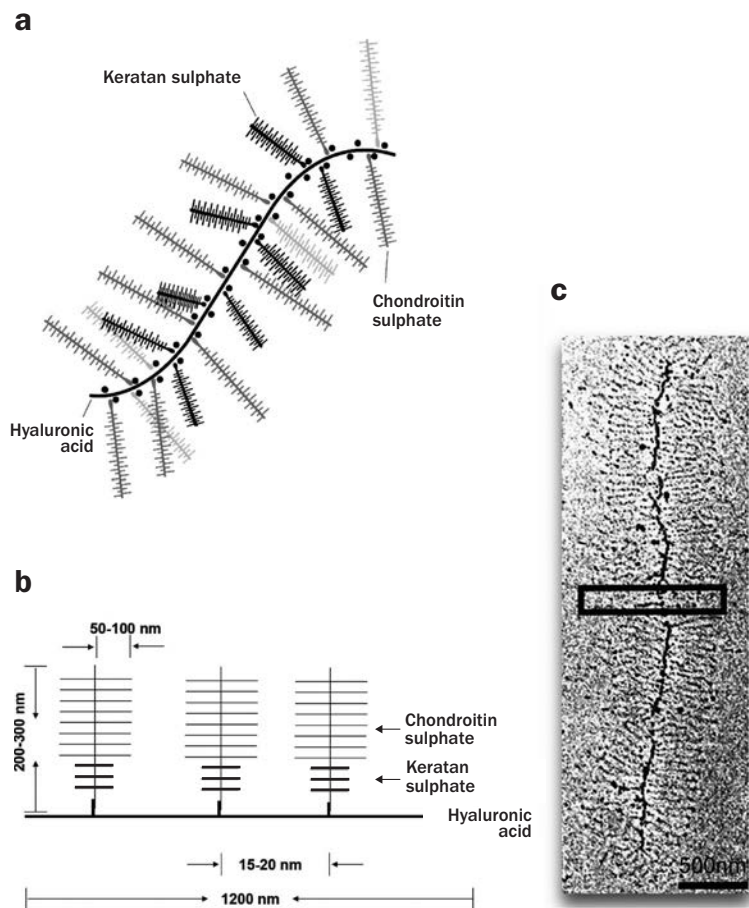


Fig. 3.4.3. Proteoglycans of articular cartilage:
a) Structure of the proteoglycans formed by hyaluronic acid.
b) Molecular distances.
c) Transmission micrograph of bovine articular cartilage showing the principal hyaluronic acid chain and side chains (inset).

The **collagen** present in the extracellular matrix forms a fine strong mesh that traps the proteoglycan molecules and supports the stresses due to the internal pressure. For the most part they are type II collagen fibrils (between 80 and 95%), finer than those of type I and with a higher degree of cross-linking. There are also even finer types IX and XI collagen fibrils interlacing the type II collagen fibres with each other and with proteoglycans, especially in immature cartilage.

Chondrocytes are the only cells present in cartilage and they produce *collagen*, proteoglycans and hyaluronic acid. Their concentration is very low since their survival is subject to the diffusion of nutrients and metabolites from the articular surface, cartilage being an avascular tissue. Small pores, called lagoons (lacunae), are commonly found isolated in the matrix.

Mesoscopic level

Collagen fibres in the articular collagen take up different positions according to their distance from the contact surface, as shown in Figure 3.4.4a, and give rise to three layers known as *superficial or tangential*, *middle* and *deep* (Glenister 1976).

The *superficial* layer, which can be as much as one fifth of the thickness, has collagen fibres arranged in leaves parallel to the surface. This layer is responsible for carrying the frictional forces produced during articulation and has the greatest concentration of collagen fibres and water content. Split lines can also be seen in the superficial layer, which are produced when the surface is punctured and they are marked with ink. The fibre distribution results in a local crack in the surface tissue which indicates the direction of the collagen (Figure 3.4.4b).

The *middle* layer contains the highest concentration of proteoglycans as well as high water content and collagen fibres. The last of these lose their orientation parallel to the surface to become, more or less, perpendicular to the contact with the underlying bone. This layer can be as much as half of the total cartilage thickness and carries the combined compression and shear forces.

The *deep* layer includes the gradual junction of the articular cartilage and the bone, since the cartilage is progressively calcified. This is the zone of lowest water content, collagen and proteoglycans and, typically, occupies one third of the thickness. A *tidemark* which separates the calcified collagen from the rest is located in this layer (Figure 3.4.4a)

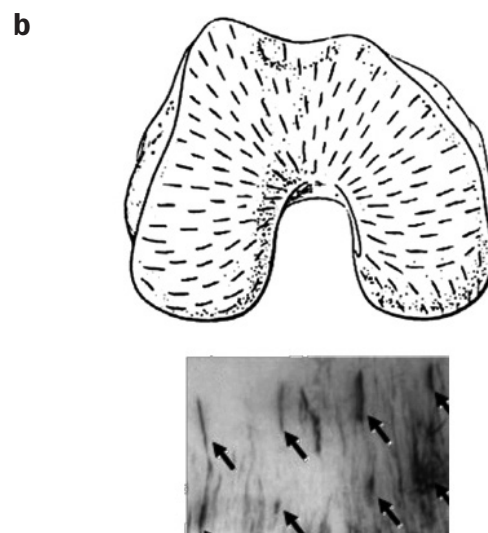
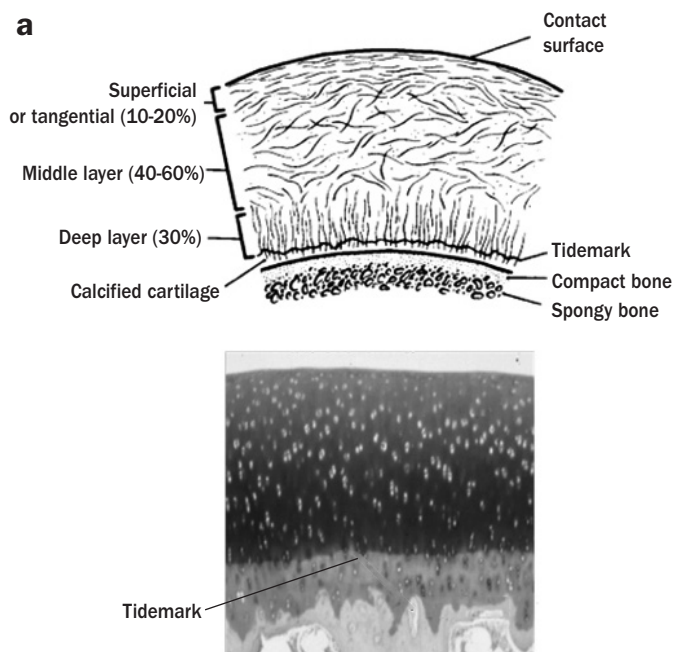


Fig. 3.4.4. Structure of articular cartilage:
a) Layers in cartilage.
b) Split lines.

3.4.3. Mechanical properties

Turgidity

Turgidity (swelling) in cartilage is due to the **osmotic pressure** caused by the ionic balance between the synovial liquid and the liquid in the interior of the cartilage, whose walls act like a semi-permeable membrane. (see Figure 3.4.5)

The presence of the negative charge associated with the collagen molecular structure—the fixed charge density or FCD mentioned in the previous section—allows cartilage to retain water molecules even in the presence of significant external pressure. Thanks to the swelling, cartilage can bear large external pressures, counteracted by the osmotic pressure.

To better understand this phenomenon it is helpful to examine in detail, first how the osmotic pressure, Π , can be quantified as a function of the ion concentration inside and outside the cartilage (Equation 3.4.7) and, secondly, how to calculate the effective pressure, $p - \Pi$, which the cartilage supports, and turns out to be much smaller than the external applied pressure p (see Figure 3.4.5c).

Figure 3.4.5 illustrates this situation in a schematic form. For greater simplicity we will only consider equilibrium of the Na^+ and Cl^- ions, which are the most abundant in the interstitial fluid.

Under equilibrium conditions, the Na^+ ions displace the H^+ protons and tend to occupy positions close to the negative charges of the GAGs ($-\text{SO}_3^-$, $-\text{COO}^-$), increasing their concentration in the interior of the cartilage. This increase is counteracted by the entrance of water molecules, which induce an increase in the osmotic pressure.

If $[\text{Na}^+]_e$ and $[\text{Cl}^-]_e$, and $[\text{Na}^+]_i$ and $[\text{Cl}^-]_i$ are the ion concentrations in the external and interior fluids, respectively, the equations governing the problem are:

$$\text{Neutrality of the exterior fluid} \quad [\text{Na}^+]_e = [\text{Cl}^-]_e \quad (3.4.1)$$

$$\text{Neutrality of the fluid in the cartilage} \quad [\text{Na}^+]_i = [\text{Cl}^-]_i + \text{FCD} \quad (3.4.2)$$

and the Gibbs-Donnan equation, obtained by equating the Gibbs functions and ignoring the coefficients of activity, which relate the concentrations of the electrically charged species on either side of the membrane.

$$\frac{[\text{Cl}^-]_e}{[\text{Cl}^-]_i} = \frac{[\text{Na}^+]_i}{[\text{Na}^+]_e} \quad (3.4.3)$$

Observe that to establish electro-neutrality of the cartilage it is necessary to consider the fixed charge density (FCD) coming from the GAGs.

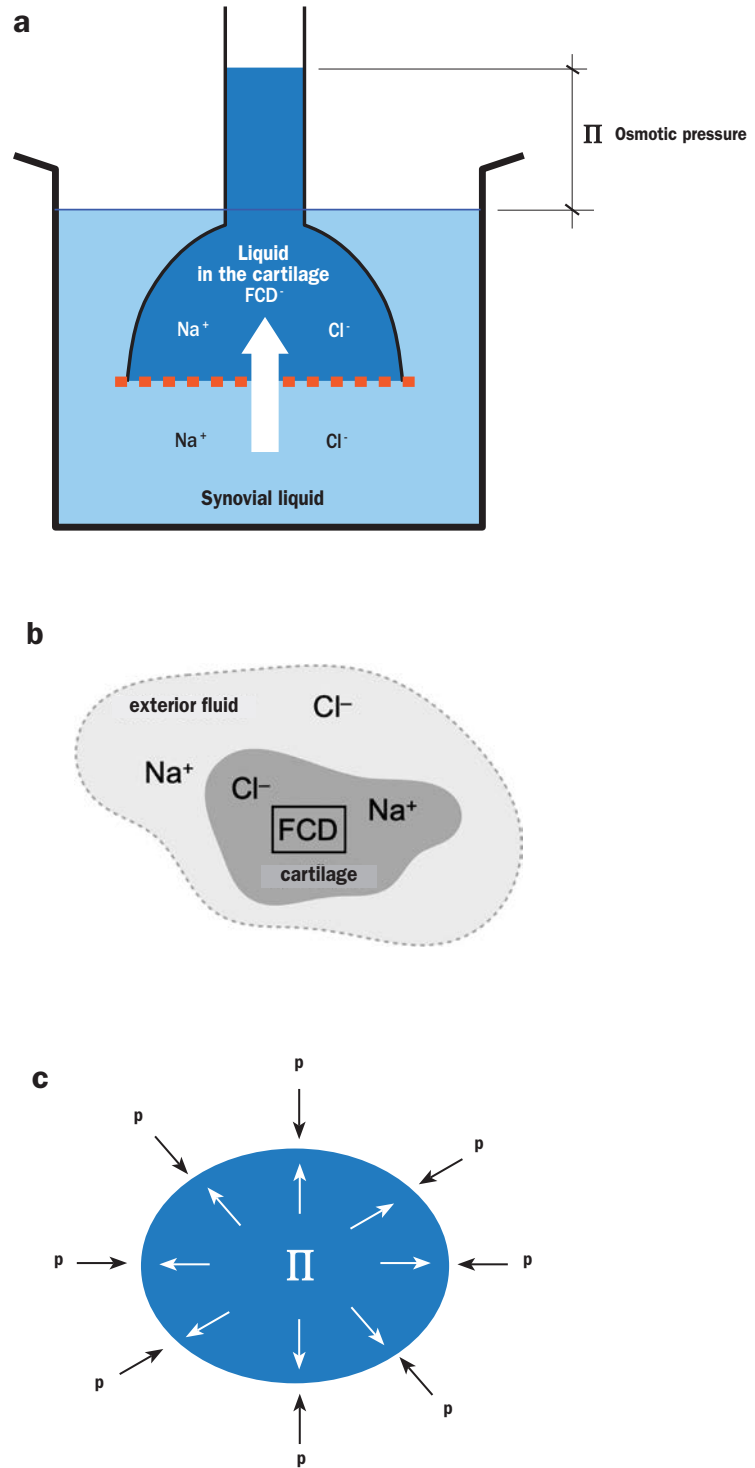


Fig. 3.4.5. Ionic equilibrium model in cartilage.
a) Osmotic pressure Π .
b) Cartilage and synovial liquid (schematic).
c) Effective pressure: $p - \Pi$

If the external equilibrium concentration of NaCl is C , it is easy to solve the three previous equations to obtain the concentrations:

$$[\text{Na}^+]_e = [\text{Cl}^-]_e = C \quad (3.4.4)$$

$$[\text{Na}^+]_i = \frac{FCD}{2} + \sqrt{\left(\frac{FCD}{2}\right)^2 + C^2} \quad (3.4.5)$$

$$[\text{Cl}^-]_i = -\frac{FCD}{2} + \sqrt{\left(\frac{FCD}{2}\right)^2 + C^2} \quad (3.4.6)$$

whose values are shown in Figure 3.4.6a as a function of FCD/C , the ratio of the fixed charge density and the external saline concentration.

The difference in ionic concentration between the cartilage and the external fluid provokes displacement of the water molecules and the appearance of an osmotic pressure which can be calculated by means of van't Hoof's equation:

$$\begin{aligned} \Pi &= RT \{ [\text{Na}^+]_i + [\text{Cl}^-]_i - [\text{Na}^+]_e - [\text{Cl}^-]_e \} = \\ &= RT(\sqrt{FCD^2 + 4C^2} - 2C) \end{aligned} \quad (3.4.7)$$

where R is the Gas Constant ($R=8.31 \text{ J/mol/K}$) and T the absolute temperature. Figure 3.4.6b depicts its variation with saline concentration.

For an isotonic external concentration ($[\text{NaCl}]=0.15\text{M}$), at physiological temperature (37°C) and with fixed charge density of 0.2M the osmotic pressure works out at 0.16MPa , a value approximately 60% higher than the atmospheric pressure of 0.1MPa (recall that the internal osmotic pressure of the cartilage is a gauge pressure, above atmospheric pressure).

If the fixed charge density is reduced by a factor of ten, $FCD=0.02\text{M}$ (through loss of *GAGs*, for example), the value of the osmotic pressure falls drastically by two orders of magnitude to 0.0017MPa . This fact highlights the importance of keeping the content of the cartilage *GAGs* as high as possible.

Since the osmotic pressure is intimately linked to the fixed charge density FCD and that to the *GAG* content, it is interesting to estimate the concentration of the latter. The *GAG* content in cartilage can be determined from a measure of the salt in the external fluid and the $[\text{Na}^+]_i$ content in the internal tissue. To obtain this last value the ^{23}Na isotope is used, which is detected by nuclear magnetic resonance. Knowing the concentrations of $[\text{Na}^+]_e$ and $[\text{Na}^+]_i$ the fixed charge density is calculated as:

$$FCD = \frac{[\text{Na}^+]_i^2}{[\text{Na}^+]_e} - [\text{Na}^+]_e \quad (3.4.8)$$

obtained directly from Equations (3.4.1), (3.4.2) and (3.4.3).

With this value of the FCD , the average electric charge of -2 electrons per disaccharide, and the average molecular weight of the *GAG* disaccharides (502.5 Da) we obtain

$$GAG_s = \frac{FCD \times (502.5 \text{ g/mol})}{2} \quad (3.4.9)$$

Typical values lie between 15 and 65 g/l depending upon the age and location of the cartilage ($\sim 50 \text{ g/l}$ for $FCD=0.2\text{M}$).

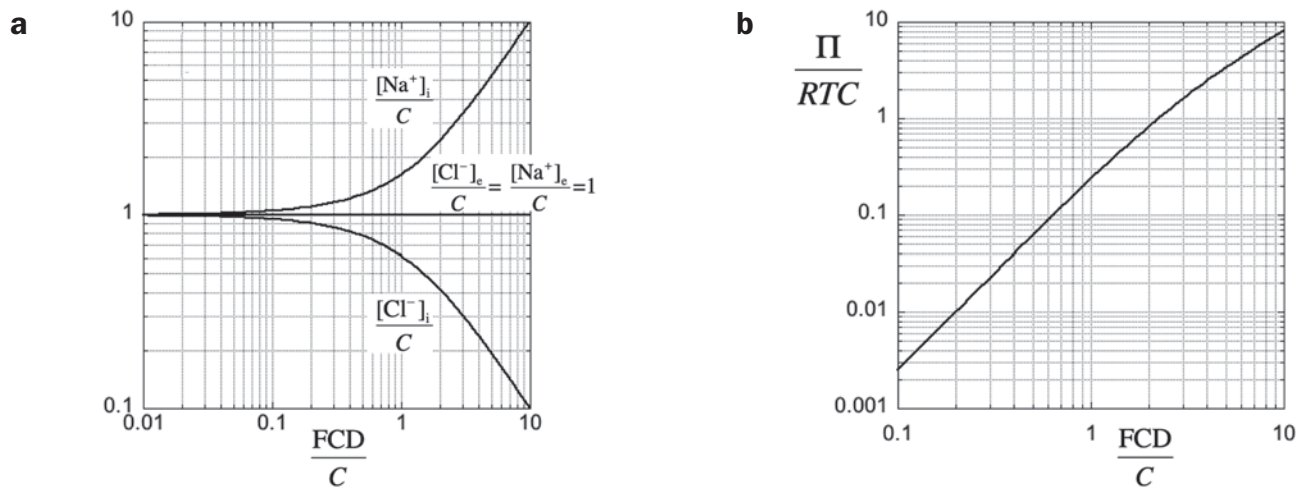


Fig. 3.4.6. Ionic equilibrium in cartilage: a) equilibrium concentrations; b) osmotic pressures.

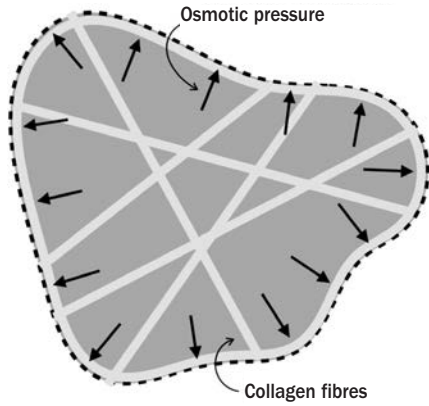


Fig. 3.4.7. Structural network of the articular cartilage.

Finally, with the data obtained, it is possible to estimate the net pressure supported by the cartilage as the difference between the external applied pressure and the osmotic pressure. The osmotic pressure in the cartilage is supported by the structure of the collagen fibres in its interior, in such a way that a network with internal pre-tensions is generated, which not only holds its shape and retains water, improving lubrication, but it is also stable under applied tensile or compressive loads (Figure 3.4.7).

It is interesting to observe that when the cartilage is compressed the concentration of the fixed charge increases, when as the GAG structures are approached. This phenomenon produces an increase in the osmotic pressure which –in turn– reduces the net pressure which supports the cartilage structure. A simple calculation reveals the importance of this mechanism.

The net pressure will be the difference between the applied pressure and the osmotic pressure,

$$p_{net} = p - \Pi = p - RT(\sqrt{FCD^2 + 4C^2} - 2C) \quad (3.4.10)$$

where FCD will be the fixed charge density in the compressed volume, which we will call V . If we consider the bulk modulus K of the cartilage, defined as the change in pressure required to cause a unit reduction in volume:

$$K = \frac{\Delta p_{net}}{-(\Delta V/V)} \quad (3.4.11)$$

we can integrate the previous expression with the initial condition $V=V_0$, $p_{net} = 0 - \Pi_0$ and obtain

$$V = V_0 \exp\left(-\frac{p_{net} + \Pi_0}{K}\right) \quad (3.4.12)$$

In which Π_0 is given by

$$\Pi_0 = RT(\sqrt{FCD_0^2 + 4C^2} - 2C) \quad (3.4.13)$$

The fixed charge density FCD in the compressed volume can be easily calculated by means of the relationship

$$FCD \cdot V = FCD_0 \cdot V_0 \quad (3.4.14)$$

since the total charge in the GAGs must be conserved.

The combination of Equations (3.4.10) (3.4.12) (3.4.13) and (3.4.14) allows calculation of p_{net} as a function of the applied external pressure p knowing C , FCD_0 , T and K .

Figure 3.4.8 shows p_{net} as a function of p for various values of the GAG content in the cartilage, within the physiological range. The following values were used in the calculation: $T=37^\circ\text{C}$, physiological saline concentration (0.15M) and the cartilage bulk modulus 0.2MPa (Rotter et al., 2002).

In Figure 3.4.8 we see that the pressure supported by the collagen structure and GAGs p_{net} is much lower than the applied external pressure p , and that the osmotic pressure supports the greater part of the load. This is a very effective mechanism in avoiding overload of the weak cartilage structure.

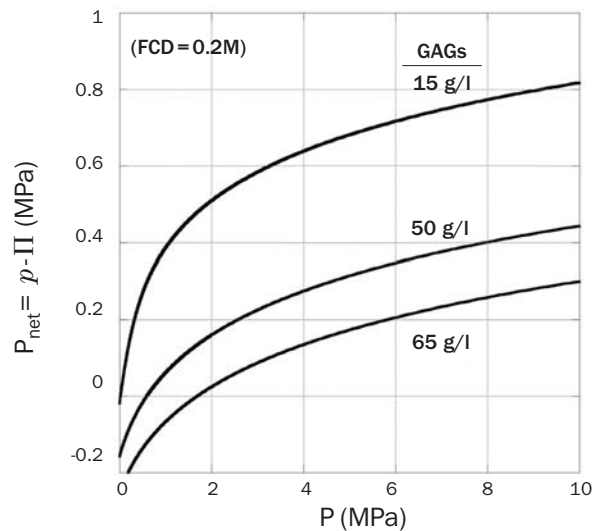
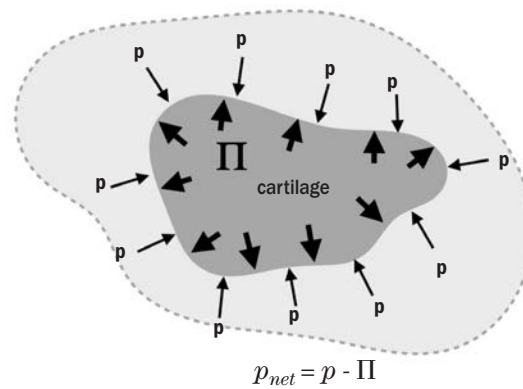


Fig. 3.4.8. Net pressure supported by the cartilage as a function of the applied external pressure [NaCl]=0.15M, $T=37^\circ\text{C}$, $K = 0.2\text{MPa}$

Stiffness and strength

Articular cartilage is a porous material with a high water content, and very sensitive to the applied loading rate. Consequently, values determined experimentally are usually equilibrium values, allowing a steady state to be achieved after application of the external load. Otherwise, the loading rate should be specified, since measurements may differ by an order of magnitude.

Figure 3.4.9. shows the results from tensile tests performed by Woo et al. (1976) on specimens taken from bovine articular cartilage. The test-pieces, standard dog bone specimens 250 μ m thick, were taken from different depths in the cartilage, as indicated in the Figure (numbered 1, 2 and 3). Tests were carried out in the directions parallel and perpendicular to the lines of collagen alignment (*split lines*).

The curves have a characteristic J-shape corresponding to tissue in which the reinforcing fibres group together and progressively align as the deformation increases. The highest stress values are obtained in the tests parallel to the collagen fibres (that is, parallel to the *split lines*). As the sample is taken from deeper inside the cartilage this effect is attenuated, since as we have noted, the orientation of the fibres changes and is no longer parallel to the surface and the *split lines*.

Table 3.4.2 summarises the data obtained by Woo et al. (1976), of the stiffness in the linear zone of the tensile curve, once the fibres are aligned. Their values are obtained from the stresses produced by letting the specimen relax between two points in the linear zone, typically those from strains of 10 and 20% ($\varepsilon_1=0.1$, $\varepsilon_2=0.2$):

$$E_{equilibrium} = \frac{\sigma(\varepsilon_2, \infty) - \sigma(\varepsilon_1, \infty)}{\varepsilon_2 - \varepsilon_1} \quad (3.4.14)$$

The values in Table 3.4.2. clearly show the anisotropy of this material. Similar values are obtained for human patellar cartilage, as illustrated in Figure 3.4.10 which is taken from (Bae et al. 2008). As we see, the values are also dependent the position and orientation of the specimen.

TABLE 3.4.2. VALUE OF THE EQUILIBRIUM MODULUS OF THE BOVINE ARTICULAR AS A FUNCTION OF POSITION AND ORIENTATION CARTILAGE (WOO ET AL., 1976)

DIRECTION WITH RESPECT TO THE SPLIT LINES	LAYER/DEPTH	TENSILE STRENGTH (MPa)
Parallel	1	23.0
	2	11.2
	3	5.0
Perpendicular	1	12.2
	2	6.6
	3	3.6

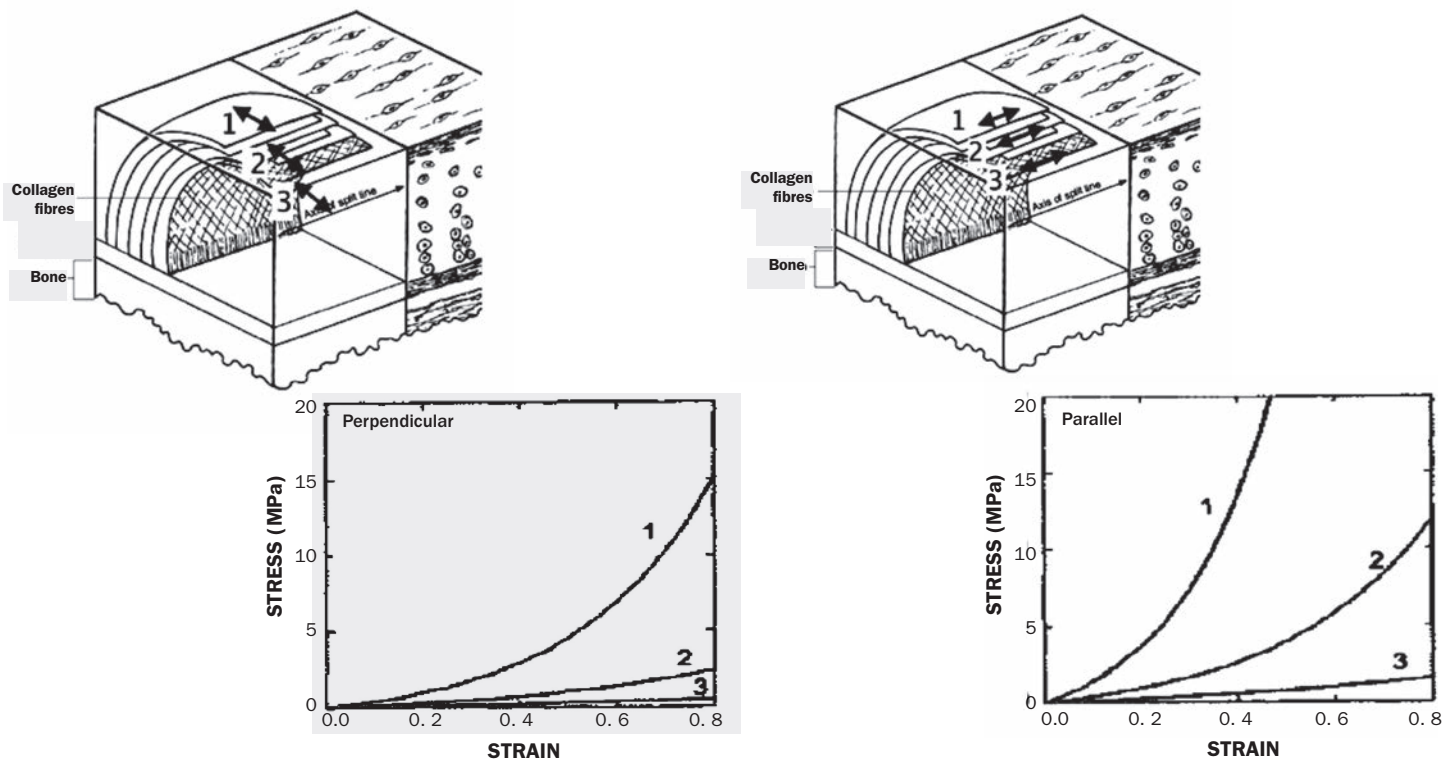


Fig. 3.4.9. Tensile tests of bovine cartilage specimens(Woo et al. 1976).

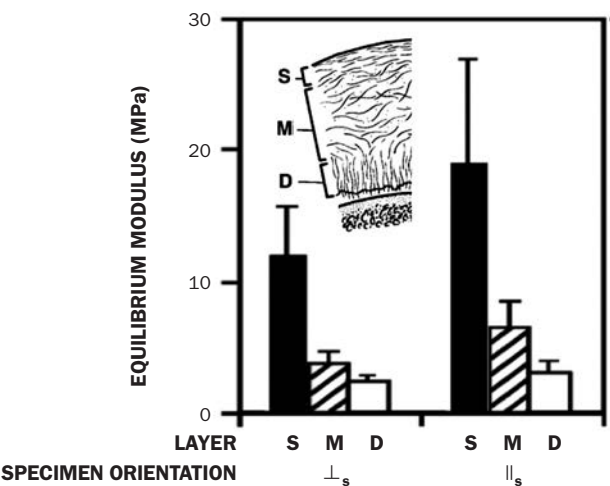


Fig. 3.4.10. Values of the for human patellar cartilage specimens (Bae et al. 2008)
S: Superficial
M: Middle
D: Deep

The stiffness dependence (measured by the equilibrium modulus) of the cartilage with the external saline concentration is shown in Figure 3.4.11. The mechanical properties of this tissue are very sensitive to the electrochemical equilibrium, as we have shown in previous paragraphs. This fact means that the variations in ion concentration (through changes in saline concentration or in the fixed charge density, for example) can bring about important biomechanical changes.

Like the elastic modulus, the tensile strength of articular cartilage is dependent upon the rate of loading in the test, the zone and orientation of the specimen, so that published data show large variations. Williamson et al. (2003) measured the tensile strength of articular bovine cartilage, obtaining values between 3 and 10MPa, with strains to failure of between 40 and 70%.

Figure 3.4.12 shows Kempson’s results for specimens from the surface layer of human femoral cartilage human, for men and women between 8 and 90 years old. The specimens were orientated in the direction of the collagen fibres. The strengths obtained were almost all over 10MPa, reaching average values of 40MPa for ages between 20 and 30 years.

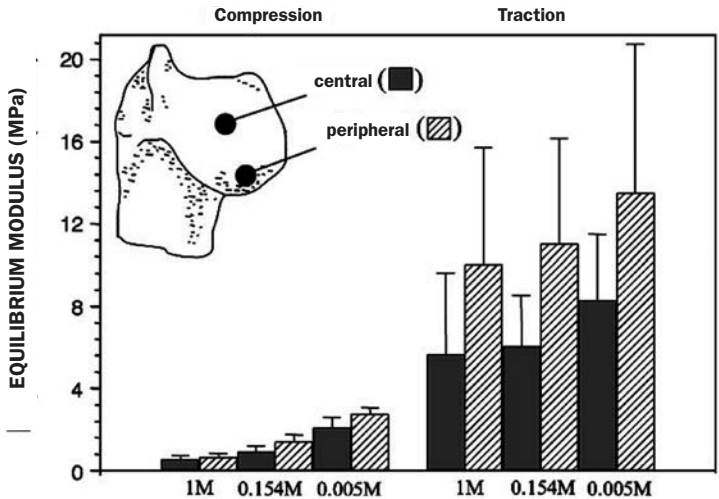


Fig. 3.4.11. Values of the equilibrium modulus for bovine articular cartilage as a function of the external saline concentration (Korhonen et al. 2010).

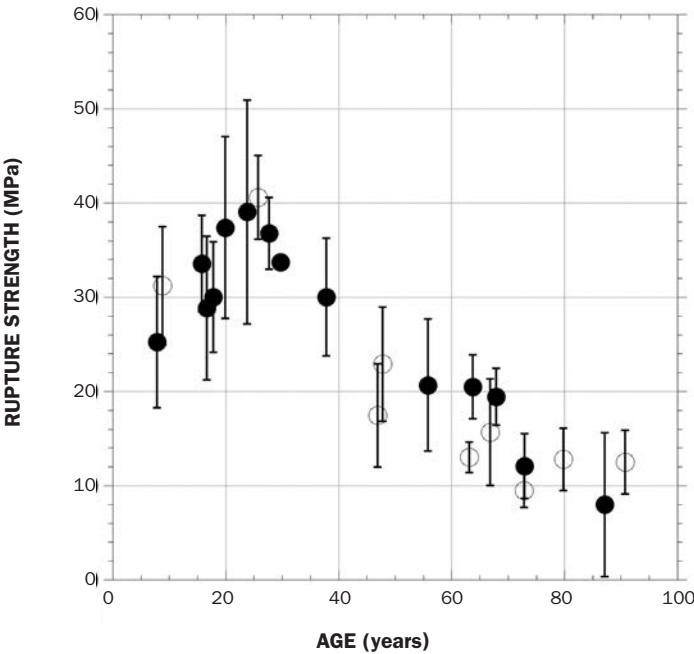


Fig. 3.4.12. Rupture strength of femoral cartilage. Filled points correspond to male and open symbols to women (Kempson 1982).

Time dependent behaviour

As has been discussed, the response of articular cartilage during the application of a load is not constant with time. Fluid motion in its interior causes a delayed response which –if the load is constant– may take some time to reach equilibrium.

Figure 3.4.13a shows the values obtained by Salak *et al.* (1987) for tensile tests at three different strain rates and

Figure 3.4.13b contains the results of Radin *et al.* (1970) for the variation in elastic modulus of bovine cartilage with strain rate. The results of Oloyede *et al.* 1992, summarised in Figure 3.4.13c, were obtained from compression test and different loading rates. Bearing in mind that in running or jumping strain rates of over 0.05/s can be encountered, it is evident that in order to analyse the biomechanical behaviour of cartilage under physiological loads it is essential to consider its dependency on time.

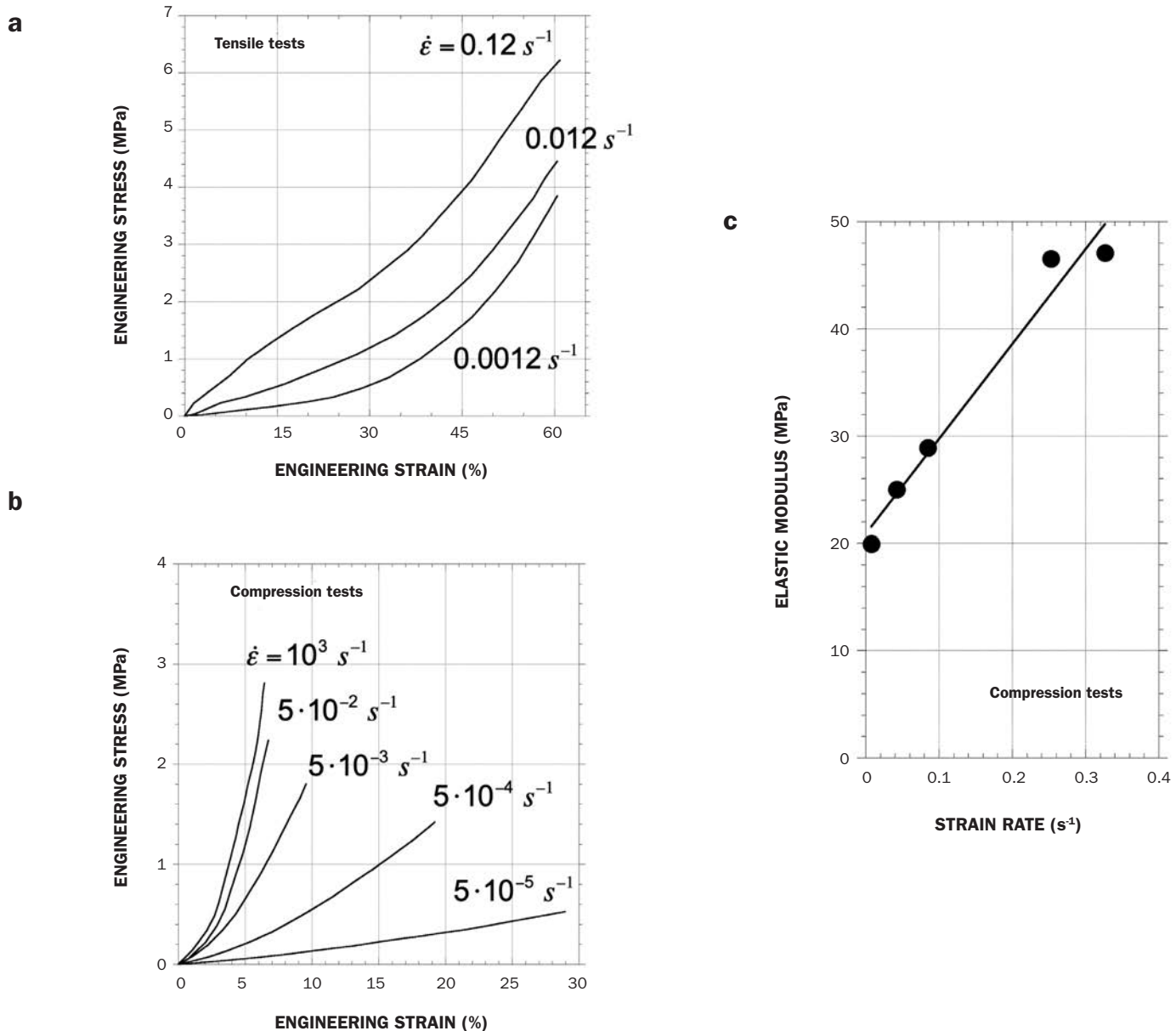


Fig. 3.4.13. Dependency of the mechanical properties of cartilage with time.

a) Tensile tests (Salak *et al.* 1987).

b) Compression tests (Oloyede *et al.* 1992).

c) Elastic modulus at a strain of 10% (Radin *et al.* 1970).

Models

Two different, but complementary, approximations have been proposed in order to model cartilage. The easiest is to consider cartilage as a linear *viscoelastic* material and, in its simplest form, to represent its behaviour as a Prony series, obtained by an empirical fit to the parameters (G_∞, G_i, τ_i). The model, depicted in Figure 3.4.14, shows the viscoelastic parameters measured in a dynamic experiment with a sinusoidal cyclic strain.

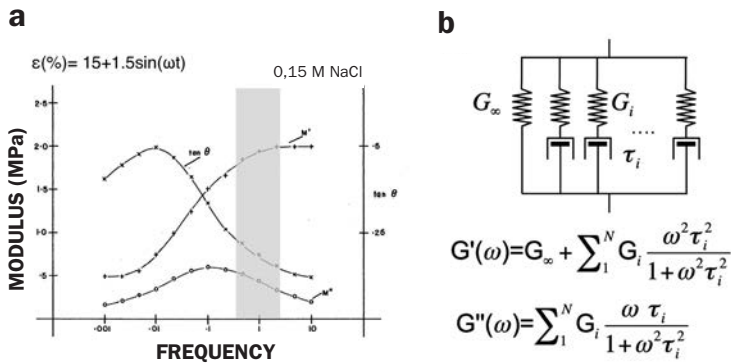


Fig. 3.4.14. a) Dynamic experiments with cyclic strains applied to bovine cartilage. Storage modulus G' , loss modulus G'' , tangent of the phase angle between strain and stress waves $\tan \theta = G''/G'$. The shaded zone corresponds to the walk-run frequencies (Frank 1980).

b) Prony series approximation with discrete relaxation time steps.

Parameters obtained from the viscoelastic model depend upon the load level or applied strain. A quasi-linear viscoelastic approach proposed by Fung provides some improvement in modelling (Fung 1993).

Poroelastic models assume that the cartilage is a connected porous material through which fluid similar to synovial liquid and various ions carrying charge can move. These models are an alternative method of representing cartilage which, due to their complexity, are not widely used since they require numerical calculation and need parameters that are difficult to estimate directly, such as the viscosity of the fluid moving inside the cartilage, its porosity or the mechanical behaviour of its collagen matrix and GAGs.

A brief description of the more important poroelastic models is provided below. The interested reader may find more detail in Fung (1993).

The biphasic model (Mow et al. 1980) assumes that cartilage is composed of a *hyperelastic* matrix and a viscous fluid, both of which are incompressible, and the effect of the electric charge is neglected. A solution to the problem is based upon conservation of mass (continuity), equilibrium (without movement) and constitutive equations of the binary composite. Figure 3.4.15 shows the application of the model in a confined compression test, in which the lateral strain of the cartilage is constrained.

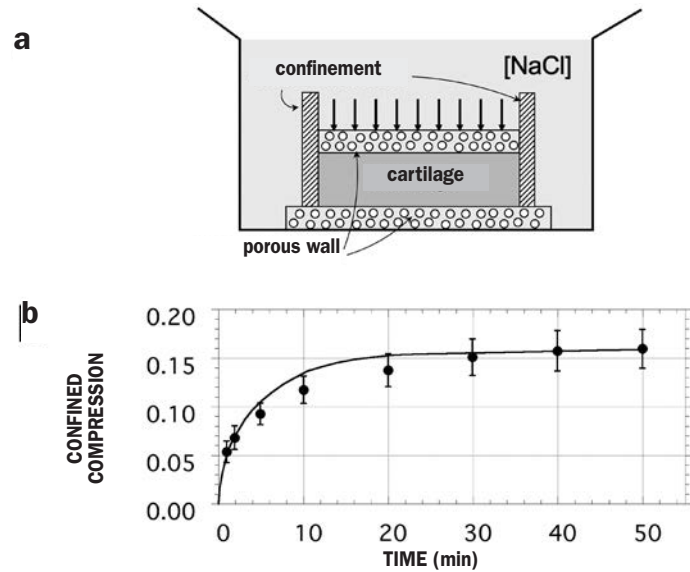


Fig. 3.4.15. Confined compression test on bovine cartilage and curve fit from the biphasic poroelastic model.

a) Experimental configuration

b) Creep curve under compression. Applied pressure 0.1 MPa (Mow et al. 1980).

A development of the biphasic poroelastic model includes the (+) y (-) ions as additional phases taking into account their electrochemical equilibrium (Lai et al. 1991). In contrast to the biphasic model (and to the viscoelastic models), the inclusion of the ionic interaction allows account to be taken of the effect of the saline concentration of the external fluid, as illustrated in Figure 3.4.16. This shows the axial contraction tests on bovine cartilage performed by Mow et al. (1984) and the fit of the previously cited triphase model of Lai et al.

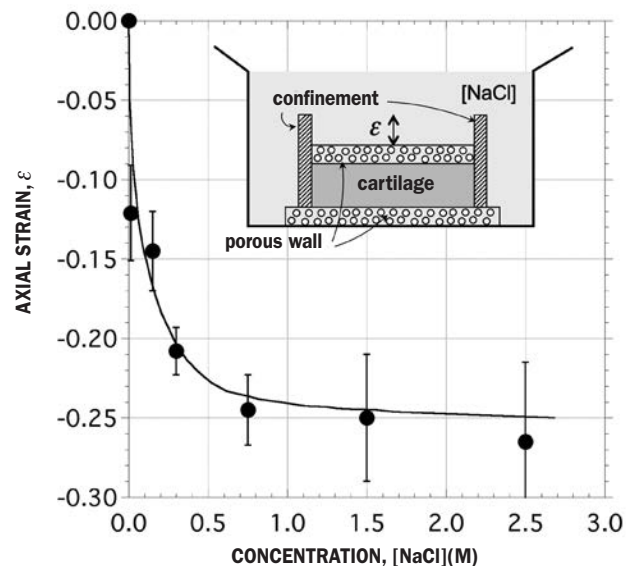


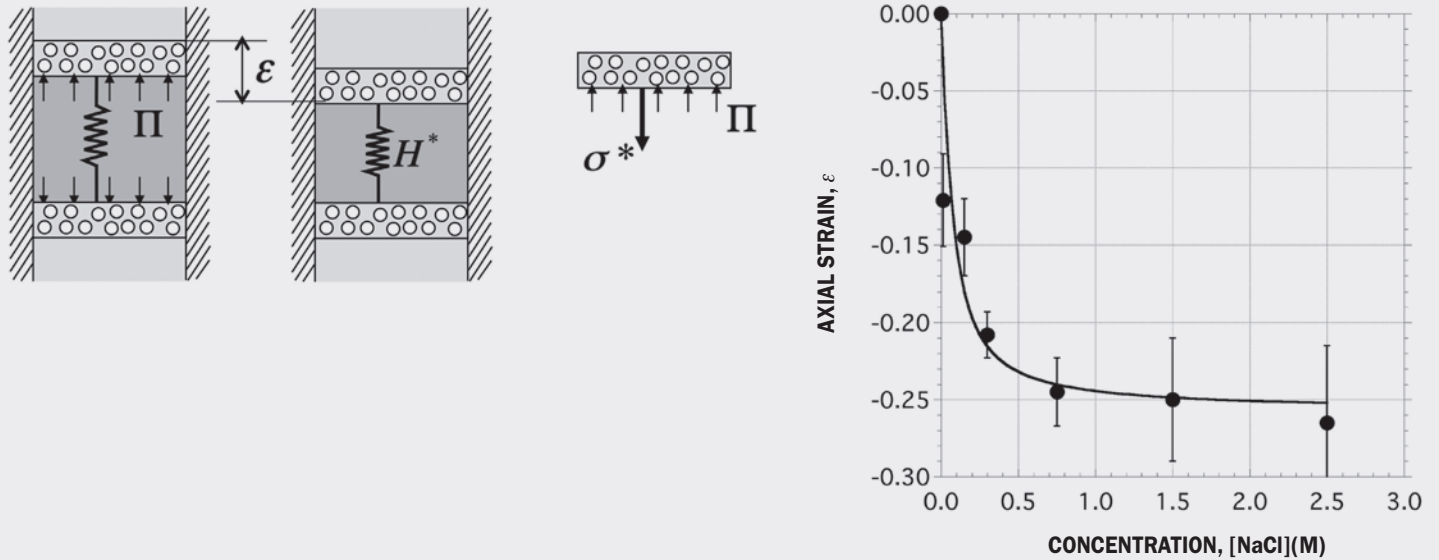
Fig. 3.4.16. Fit of the triphase poroelastic model to the experimental axial contract of bovine cartilage in NaCl (Lai et al. 1991). The cylindrically shaped specimen is confined in all directions except the axial. The value $[NaCl] = 0$ corresponds to tests in distilled water.

EXERCISE 35

Analyse the cartilage axial contraction data of Mow et al. (1984) shown in Figure 3.4.16 using the biphasic model which assumes that the collagen fibre matrix and proteoglycans of the cartilage has a constant aggregate modulus, H^* , and the interstitial fluid behaves according to the electrochemical equilibrium Equations (3.4.1) - (3.4.3).

SOLUTION:

The sketch shows a simplified analysis of the axial contraction test. The cartilage is subjected to an osmotic pressure Π and a matrix stress σ^* . Mechanical equilibrium requires that $\Pi = \sigma^*$.



The axial strain, ε , can be calculated from the aggregate modulus as

$$\varepsilon = \frac{\sigma^*}{H^*} = \frac{\Pi}{H^*} = \frac{RT}{H^*} \left[\sqrt{FCD^2 + 4C^2} - 2C \right]$$

in which Equation (3.4.7) has been used for the osmotic pressure Π .

Using the data in Figure 3.4.16, take as a reference the strain that is produced when $[\text{NaCl}] = 0$, and fit the function

$$\tilde{\varepsilon} = \varepsilon - \varepsilon(0) = \frac{RT}{H^*} \left[\sqrt{FCD^2 + 4C^2} - 2C \right] - \frac{RT}{H^*} FCD$$

taking reference values $T = 300^\circ\text{K}$ and $FCD = 0.2\text{M}$.

The resulting fit is shown in the Figure, which represents a good approximation to the experimental data. Note that the fit is very similar to that obtained with the triphase model (Figure 3.4.16)

Observe also that in this case the only adjustable parameter is the aggregate modulus which turns out to be $H^* = 1.94\text{MPa}$. This value is consistent with that of 2MPa measured by Mow et al. (1984) for this material under hypertonic conditions ($[\text{NaCl}] = 0$).

Fracture

Articular cartilage can crack due to the applied load, wear or friction on the surface, and the differences in stiffness with the subchondral bone especially when the loads are dynamic and the cartilage is very stiff, as we have seen. The causes of the appearance of cracking are not well-established and it is not well-understood how a microcrack progresses under the action of physiological loads.

The small thickness of cartilage makes it difficult to fabricate and test specimens with the desired orientation. As a first step, some authors have measured the fracture strength of cartilage by adapting procedures developed for other materials, in particular polymers. Chin-Purcell and Lewis (1996) measured the fracture strength of canine patella cartilage using mixed bone cartilage specimens with a deep crack, so as to minimise the effect of the constrained zone. Figure 3.4.17a shows the general arrangement of the test. The initial crack passes through the bone and enters the cartilage, penetrating it as it propagates. The specimens have a thickness of about 0.2 mm.

The breaking strengths measured by Chin-Purcell and Lewis were between 0.14 and 1.2 kJ/m², in line with those obtained for other tissues containing collagen such as skin.

These authors also performed tear tests on trouser-shaped specimens (Figure 3.4.17b), obtaining values consistently lower, between 0.24 and 0.8 kJ/m².

Xiao *et al* (2015), using the same configuration as Chin-Purcell and Lewis, measured the toughness of porcine articular cartilage and obtained a value of 11 MPam^{1/2}.

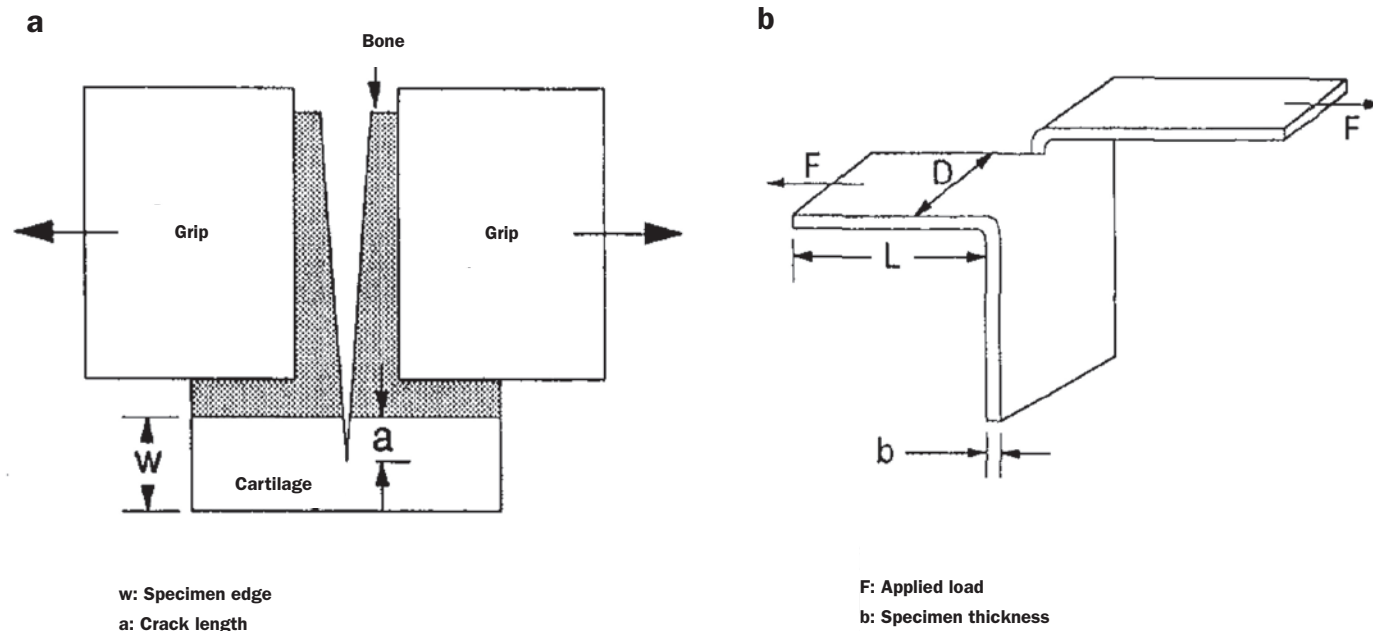


Fig. 3.4.17. Fracture tests on canine patellar cartilage (Chin-Purcell *et al.* 1996).

a) Notched specimen.

b) Tear specimen.

Friction

Thanks to the capacity of cartilage to retain large amounts of water and the presence of synovial fluid, articular contact is one with the lowest coefficients of friction (Table 3.4.1), which is vitally important in avoiding tissue wear and tear and in facilitating its regeneration.

The mechanisms thought to be involved in this phenomenon are illustrated in Stribeck's curve (Figure 3.4.18), which is widely used in the study of friction between surfaces. In this representation, the coefficient of friction is plotted as a function of the Sommerfeld Number ($\eta va/N$), the product of the fluid viscosity η , the sliding velocity v , the contact length a and the inverse of the force applied normal to the surfaces of contact N . In this figure two basic regimes are identified: *limiting friction* and *hydrodynamic lubrication*, separated by a mixed transition region.

Limiting friction occurs through direct contact of the surfaces. In the case of cartilage, this situation compresses the tissue producing an increase in the osmotic pressure, as we have seen, which in turn impedes the loss of fluid. In addition, the proteoglycan lubricin present in the synovial liquid interacts with the proteoglycan chains of the articular surface and helps maintain hydration and the viscosity of the contact.

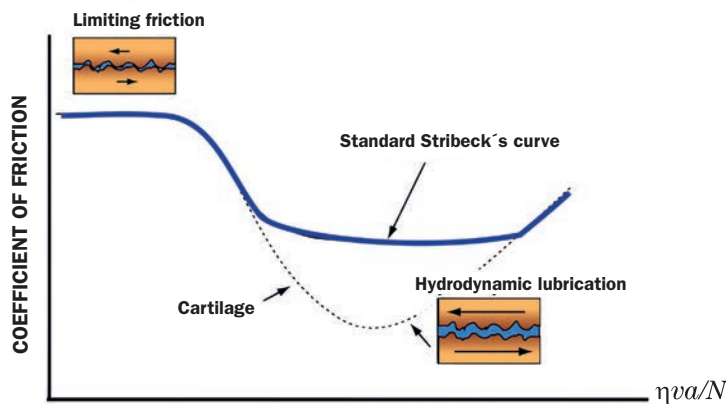


Fig. 3.4.18. Stribeck's curve.

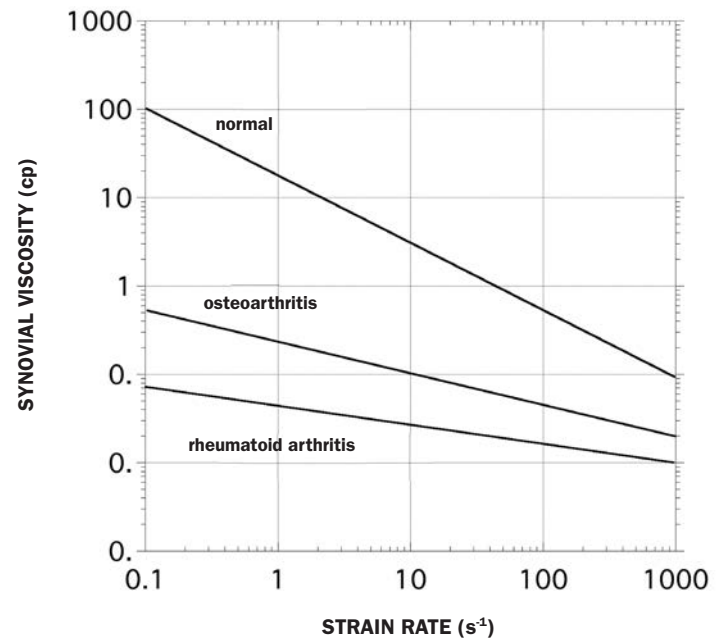


Fig. 3.4.19. Variation of the synovial viscosity with strain rate.

During *hydrodynamic lubrication* the articular surfaces do not come into direct contact and load transfer is made through a layer of synovial fluid. This mechanism is more efficient and provides a lower coefficient of friction, although in order to come into play it is necessary to exceed a certain sliding velocity or, alternatively to reduce the load on the joint.

The fact that the synovial fluid is thixotropic (Figure 3.4.19) improves both lubrication mechanisms since, at low velocities, the increase in viscosity keeps the fluid between the contact surfaces for a longer time, protecting the proteoglycan structures and impeding the loss of water. In the hydrodynamic regime, the reduction in viscosity when the sliding velocity increases reduces the shear stresses that give rise to friction. When a degenerative process occurs, as we saw in Figure 3.4.19, the synovial fluid loses viscosity and its thixotropy is also diminished.

3.4.4. Final remarks

Hyaline or articular cartilage is preferentially located in the joints and plays a fundamental role in the transmission of forces and movement, maintaining a very low coefficient of friction.

It is a highly hydrated tissue, with neither blood vessels nor nerve ends, and very low cellular density (up to one hundred times less than other body tissues) which makes recovery difficult once damaged. Its matrix is made up of a network of negatively charged collagen fibres and proteoglycans which, thanks to osmotic equilibrium, is effective in retaining water molecules.

Its mechanical behaviour is very dependent upon time and is governed by the pressure in internal fluid movement, and in turn influenced by the electrochemical equilibrium. This makes the models which have been proposed for its study very complex and difficult to implement in practice, principally due to the difficulty in reliably determining their parameters.

Articular cartilage, because of its location and physiological function, is subjected to dynamic and impact loads which in the long term may produce fatigue cracks and cause rupture. Biomechanical factors, together with others of a biological nature, are the basis of the appearance of severe degenerative conditions such as osteoarthritis. For this reason, it is important to be able to evaluate and understand the biomechanical properties of this tissue in order to act appropriately to prevent, diagnose and treat these diseases.

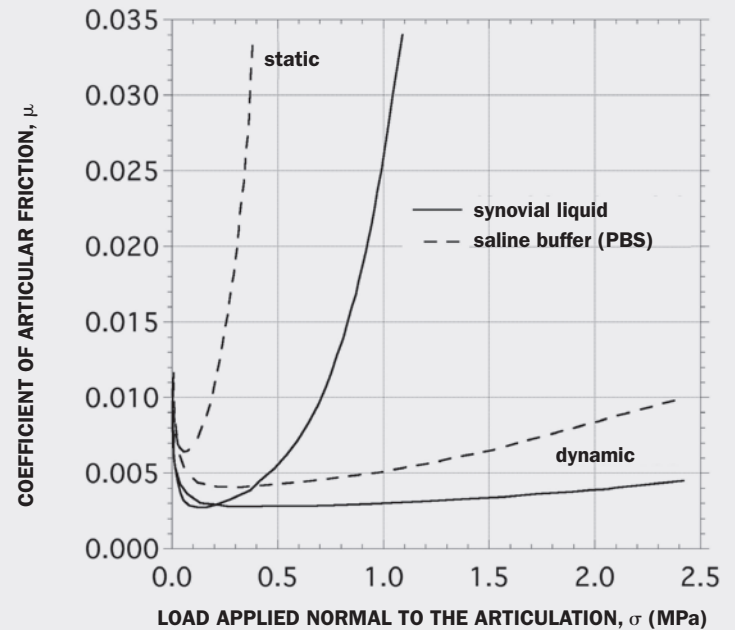
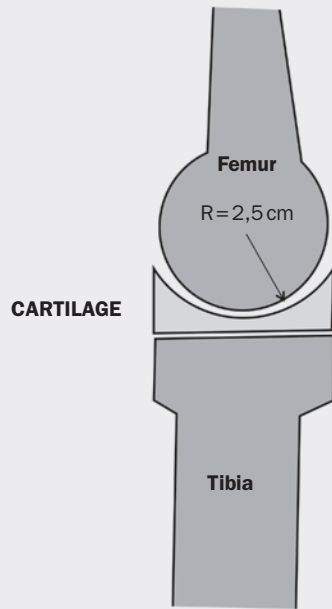
EXERCISE 36

Calculate the mechanical moment required to mobilise the articulation of the femur with the knee in the configuration of 0° flexure, indicated in the diagram.

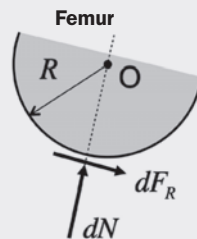
Apply the result to a person of mass: a) 50kg, b) 75kg, c) 90kg. Consider the situations that the person would encounter standing on two feet, walking and running. Comment on the results obtained.

DATA:

- Cartilage contact area: $A=10 \text{ cm}^2$. Assume a spherical contact of radius $R=2.5 \text{ cm}$.
- Maximum force on the knee: $W/2$ for standing, W when walking and $3W$ when running. W is the body weight.
- The coefficient of articular friction is shown in the Figure, obtained by LL. Malcom (An experimental investigation of the frictional and deformational responses of articular cartilage interfaces to static and dynamic loading. PhD Thesis, University of California, San Diego, 1976).

**SOLUTION:**

A sketch of the forces acting on an infinitesimal element of the contact is provided in the figure.



If dN is the normal force acting, the value of the frictional force produced in movement will be $dF_R = \mu dN$ where μ is the coefficient of friction.

The moment dM about the centre of rotation of the articulation, point O , will be $dM = R dF_R = \mu R dN$

The total value is obtained by integration $M = \int \mu R dN = \mu R \int dN = \mu R N$

In order to estimate the value of the coefficient of friction from Malcom's data we need to know both the stress normal to the to contact, σ , and the nature of the motion (static or dynamic) in each case.

The normal stress is calculated by distributing the total load N across the contact area A

$$\sigma = N/A$$

The table gives the values corresponding to each of the required situations.

SITUATION	PARAMETERS	UNITS	m (kg)		
			50	75	90
standing	$N = mg/2$	N	245	368	441
walking	mg		491	736	883
running	3 mg		1472	2207	2649
standing	$\sigma = N/A$	MPa	0.245	0.368	0.441
walking			0.491	0.736	0.883
running			1.472	2.207	2.649
standing	μ (synovia)		0.0030	0.0039	0.0048
walking			0.0028	0.0028	0.0029
running			0.0033	0.0042	0.0048
standing	μ (PBS)		0.0140	0.0290	> 0.035
walking			0.0042	0.0046	0.0049
running			0.0064	0.0092	0.0110
standing	M (sinovia)	Nm	0.0184	0.0359	0.0530
walking			0.0343	0.0515	0.0640
running			0.1214	0.2318	0.3178
standing	M (PBS)	Nm	0.0858	0.2667	> 0.3900
walking			0.0515	0.0846	0.1082
running			0.2354	0.5077	0.7284

From the data obtained we can see that the values of the dynamic coefficient of friction are always less than the static ones and, furthermore, their increment when the load applied normal to the articulation increases is much less.

Similarly, the values of the coefficient of friction for articulation lubricated with synovial liquid are significantly less than those corresponding to an articulation lubricated with a saline buffer (PBS), whose behaviour and viscosity are similar to water. Although this situation is unrealistic it is useful to put into perspective the importance, as we have seen, of synovial fluid which is thixotropic. This fact, together with the hydrodynamic lubrication mechanism, leads to a significant reduction in the value of μ in dynamic situations (mobile articulation). Hence the importance of having the synovial fluid in a healthy state.

We observe also that the values of the frictional force and the mechanical moment grow more rapidly than the weight of the individual, accentuating this phenomenon in static situations. This fact points to the danger of obesity in relation to the deterioration of articular cartilage.

4

CHAPTER

References

Alexander R.McN., Ker R.F., Bennett M.B.I (1990)
Optimum stiffness for leg bones
J Zool, London **222**, 471-478

An B., Liu Y., Arola D., Zhang D. (2011)
Fracture toughening mechanism of cortical bone: An experimental and numerical approach
J Mech Behav Biom Mater **4**, 983-992

An Y.H., Draughn R.A. (Eds.) (2000)
Mechanical Testing of bone and the Bone-implants Interface
CRC Press

Ashby M.F., Easterling K.E., Harrysson R., Maiti S.K. (1985)
The fracture and toughness of woods
Proc Roy Soc A **398**, 261-280

ASM Handbook Vol. 8 (2000)
Hardness Testing
ASM, Materials Park, Ohio

ASTM C39 (2012)
Standard Test Method for Compressive Strength of Cylindrical Concrete Specimens
Annual Book of ASTM Standards, Vol. 04.02, American Society for Testing and Materials, West Conshohocken, PA

ASTM D695 (2010)
Standard Test Method for Compressive Properties of Rigid Plastics
Annual Book of ASTM Standards, Vol. 08.01, American Society for Testing and Materials, West Conshohocken, PA

ASTM D790 (2003)
Standard Test Methods for Flexural Properties of Unreinforced and Reinforced Plastics and Electrical Insulating Materials
Annual Book of ASTM Standards, Vol. 08.01, American Society for Testing and Materials, West Conshohocken, PA

ASTM D2240 (2015)
Standard Test Method for Rubber Property—Durometer Hardness
Annual Book of ASTM Standards, Vol. 09.01, American Society for Testing and Materials, West Conshohocken, PA

ASTM D6272 (2010)
Standard Test Method for Flexural Properties of Unreinforced and Reinforced Plastics and Electrical Insulating Materials by Four-Point Bending
Annual Book of ASTM Standards, Vol. 08.03, American Society for Testing and Materials, West Conshohocken, PA

ASTM E8 (2013)
Standard Test Methods for Tension Testing of Metallic Materials
Annual Book of ASTM Standards, Vol. 03.01, American Society for Testing and Materials, West Conshohocken, PA

ASTM E9 (1995)
Standard Test Methods of Compression Testing of Metallic Materials at Room Temperature
Annual Book of ASTM Standards, Vol. 03.01, American Society for Testing and Materials, West Conshohocken, PA

ASTM E384 (2017)
Standard Test Method for Microindentation Hardness of Materials
Annual Book of ASTM Standards, Vol. 03.01, American Society for Testing and Materials, West Conshohocken, PA

ASTM E399 (2012)
Standard Test Method for Linear-Elastic Plane-Strain Fracture Toughness K_{Ic} of Metallic Materials
Annual Book of ASTM Standards, Vol. 03.01, American Society for Testing and Materials, West Conshohocken, PA

ASTM E1304 (2002)
Standard Test Method for Plane-Strain (Chevron-Notch) Fracture Toughness of Metallic Materials
Annual Book of ASTM Standards, Vol. 03.01, American Society for Testing and Materials, West Conshohocken, PA

ASTM E1820 (2013)
Standard Test Method for Measurement of Fracture Toughness
Annual Book of ASTM Standards, Vol. 03.01, American Society for Testing and Materials, West Conshohocken, PA

Atlan G., Balmain N., Berland S., Vidal B., López E. (1997)
Reconstruction of human maxillary defects with nacre powder: Histological evidence of bone regeneration
C R Acad Sci Paris / Life Sci **320**, 253-258

- Bae W.C., Wong V.W., Hwang J., Antonacci J.M., Nugent-Derfus G.E., Blewis M.E., Temple-Wong M.M., Sah R.L. (2008) Wear-lines and split-lines of human patellar cartilage: Relation to tensile biomechanical properties
Osteoarthritis Cartilage **16**(7), 841-845
- Barthelat F., Tang H., Zavattieri P.D., Li C.M., Espinosa H.D. (2007) On the mechanics of mother-of-pearl: A key feature in the material hierarchical structure
J Mech Phys Solids **55**, 306-337
- Bhattacharya, A.K., Nix W.D. (1988) Finite element simulation of indentation experiments
Int J Solids Structures **24**, 1287-1298
- Bobbio A. (1972) The first endosseous alloplastic implant in the history of man
Bull Hist Dent **20**, 1-6
- Boeriu C.G., Springer J., Kooy, F.K., Broek L.A.M. van den, Eggink G. (2013) Production methods for hyaluronan
Int J Carbohydrate Chem **2013**, 624967
- Bowman S.M., Gibson L.J., Hayes W.C., McMahon T.A. (1999) Results from demineralized bone creep tests suggest that collagen is responsible for the creep behavior of bone
J Biomech Eng **121**, 253-258
- Bowman S.M., Guo X.E., Cheng D.W., Keaveny T.M., Gibson L.J., Hayes W.C., McMahon T.A. (1998) Creep contributes to the fatigue behavior of bovine trabecular bone
J Biomech Eng **120**, 647-654
- Calvo F., Sanz-Moreno V., Agudo-Ibáñez L., Wallberg F., Sahai E., Marshall C.J., Crespo P. (2011) RasGRF suppresses Cdc42-mediated tumour cell movement, cytoskeletal dynamics and transformation
Nature Cell Biology **13**(7), 819-826
- Capaldi F.M. (2012) *Continuum Mechanics*
Cambridge Univ. Press
- Carter D.R., Schwab G.H., Spengler D.M. (1980) Tensile fracture of cancellous bone
Acta Orthopaed Scan **51**, 733-741
- Chan Y.L., Ngan A.H.W. (2010) Invariant elastic modulus of viscoelastic materials measured by rate-jump tests
Polymer Testing **29**, 558-564
- Chawla K.K. (2012) *Composite Materials* (3rd. Ed.)
Springer
- Chen C., Lu T.J., Fleck N.A. (2001) Effect of inclusions and holes on the stiffness and strength of honeycombs
Int J Mech Sci **43**, 487-504
- Chin-Purcell M.V., Lewis J.L. (1996) Fracture of articular cartilage
J Biomech Eng **118**(4), 545-556
- Christensen R.M. (1979) *Mechanics of Composite Materials*
John Wiley & Sons
- Cook R.B., Zioupos P. (2009) The fracture toughness of cancellous bone
J Biomech **42**, 2054-2060
- Cook J., Gordon J.E. (1964) A mechanism for the control of crack propagation in all-brittle systems
Proc Roy Soc A **282**, 508-520
- Cotterell B. (2010) *Fracture and Life*
Imperial College Press
- Cowin, S.C., Doty, S.B. (2007) *Tissue Mechanics*
Springer, New York
- Currey J.D. (2002) *Bones: Structure and Mechanics*
Princeton Univ Press
- Currey J.D., Kohn A.J. (1976) Fracture in the crossed-lamellar structure of *Conus* shells
J Mater Sci **11**, 1615-1623
- Currey J.D., Taylor J.D. (1974) The mechanical behaviour of some molluscan hard tissues
J Zool Lond **173**, 395-406
- Daza R., Cruces J., Arroyo-Hernández M., Marí-Buyé N., Fuente M., Plaza G.R., Elices M., Pérez-Rigueiro J., Guinea G.V. (2015) Topographical and mechanical characterization of living eukaryotic cells on opaque substrates: Development of a general procedure and its application to the study of non-adherent lymphocytes
Phys Biol **12**, 026005

Deville S., Sáiz E., Tomsia A.P. (2007)
Ice-templated porous alumina structures
Acta Mater **55**(6), 1965-1974

Doerner M.F., Nix W.D. (1986)
A method for interpreting the data from depth-sensing indentation instruments
J Mater Res **1**(4), 601-609

Easterling K.E., Harrysson R., Gibson L.J., Ashby M.F. (1982)
On the mechanics of balsa and other woods
Proc Roy Soc A **383**, 31-41

Ebenstein D.M., Coughlin D., Chapman J., Li C., Pruitt L.A. (2008)
Nanomechanical properties of calcification, fibrous tissue, and hematoma from atherosclerotic plaques
J Biomed Mater Res **91A**, 1028-1037

Ekeland A., Engesaeter L.B., Langeland N. (1982)
Influence of age on mechanical properties of healing fractures and intact bones in rats
Acta Orthop Scand **53**, 527-534

Ekeland A., Engesaeter L.B., Langeland N. (1981)
Mechanical properties of fractured and intact rat femora evaluated by bending, torsional and tensile tests
Acta Orthop Scand **52**(6), 605-613

Elices M., Guinea G.V. (2021)
Mecánica de la Fractura
En prensa

Evans A.G., Suo Z., Wang R.Z., Aksay I.A., He M.Y., Hutchinson J.W. (2001)
Model for the robust mechanical behavior of nacre
J Mater Res **16**(9), 2475-2484

Evans F G. (1973)
Mechanical properties of bone
Charles C Thomas. Springfield IL

Fernandes M.C., Aizenberg J., Weaver J.C., Bertoldi K. (2021)
Mechanically robust lattices inspired by deep-sea glass sponges
Nature Materials **20**, 237-241

Fischesser B. (2000)
El árbol
El Drac, S.L.

Fondrk M., Bahniuk E., Davy D.T., Michaels C. (1988)
Some viscoplastic characteristics of bovine and human cortical bone
J Biomech **21**, 623-630

Frank E.H. (1980)
Electromechanical Dynamics of a Charged Hydrated Polymer
Thesis (B.S.), MIT

Fung Y.C. (1993)
Biomechanics. Mechanical Properties of Living Tissues
Springer

Gao W., Wang M., Bai H. (2020)
A review of multifunctional nacre-mimetic materials based on bidirectional freeze casting
J Mech Behav Biomed Mat **109**, 103820

Gao H., Chiu C.H., Lee, J. (1992)
Elastic contact versus indentation modeling of multi-layered materials
Int J Solids Structures **29**, 2471-24

García Esteban L., et al. (2002)
La madera y su tecnología
Fundación Conde del Valle de Salazar. Madrid

Gibson L.J., Ashby M.F., Harley B.A. (2010)
Cellular Materials
Cambridge UP

Gibson L.J., Ashby M.F. (1997)
Cellular Solids: Structure and Properties, 2nd Edn
Cambridge U.P

Gibson L.J., Ashby M.F., Schajer G.S., Robertson C.L. (1982)
The mechanics of two-dimensional cellular materials
Proc Roy Soc Lond **A382**, 25-42

Gibson L.J., Ashby M.F. (1982)
The mechanics of three-dimensional cellular materials
Proc Roy Soc Lond **A382**, 43-59

Gil L. (2010)
Anatomía vegetal aplicada a las especies forestales
Fundación Conde del Valle de Salazar. Madrid

Glenister T.W. (1976)
An embryological view of cartilage
J Anat **122**, 323-330

Grossman M, Pivovarov D, Bouville F, Dransfeld C, Masania K, Studart A R. (2019)
Hierarchical toughening of nacre-like composites
Adv. Funct. Mater. **29** 1806800

Guo X.E., Kim C.H. (2002)
Mechanical consequences of trabecular bone loss and its treatment: A three dimensional model simulation
Bone **30**, 404-411

- Guo X.E., McMahon T.A., Keaveny T.M., Hayes W.C., Gibson L.J. (1994)
Finite element modeling of damage accumulation in trabecular bone under cyclic loading
J Biomech **27**, 145-155
- Hay J.L., O'Hern M.E., Oliver W.C. (1998)
The importance of contact radius for substrate-independent property measurement of thin films
Mat Res Soc Symp Proc **522**, 27-32
- Hayes W.C., Gerhart T.N. (1985)
Biomechanics of bone applications for assessment of bone strength
Bone and Mineral Research **3**, 259-294
- Hayes W.C., Carter D.R. (1976)
Post yield behavior of subchondrial trabecular bone
J Biomed Mat Res Symp **7**, 537-544
- Ikai A. (2010)
A review on: Atomic force microscopy applied to nano-mechanics of the cell
Adv Biochem Engin/Biotechnol **119**, 47-61
- ISO 6506-1 (2014)
Metallic materials –Brinell hardness test– Part 1: Test method
International Organization for Standardization
- ISO 6506-2 (2014)
Metallic materials –Brinell hardness test– Part 2: Verification and calibration of testing machines
International Organization for Standardization
- ISO 6506-3 (2014)
Metallic materials –Brinell hardness test– Part 3: Calibration of reference blocks
International Organization for Standardization
- ISO 6506-2 (2014)
Metallic materials –Brinell hardness test– Part 4: Table of hardness values
International Organization for Standardization
- ISO 14577-4 (2007)
Metallic materials –Instrumented indentation test for hardness and materials parameters– Part 4: Test method for metallic and non-metallic coatings
International Organization for Standardization
- Iyo T., Maki Y., Sasaki N., Nakata M. (2004)
Anisotropic viscoelastic properties of cortical bone
J Biomech **37**, 1433-1437
- Jackson A.P., Vincent J.F.V., Turner R.M. (1988)
The mechanical design of nacre
Proc R Soc Lond **B234**, 415-440
- Jäger L., Fratzl P. (2000)
Mineralized collagen fibrils: A mechanical model with a staggered arrangement of mineral particles
Biophysical Journal **79**, 1737-1746
- Jeronimidis G. (1980)
The fracture behaviour of wood and the relations between morphology
Proc Roy Soc B208, 447-460
- Ji H.M., Yang W., Chen D.L., Li X.W. (2020)
Natural arrangement of fiber-like aragonites and its impact on mechanical behavior of mollusk shells: A review
J Mech Behav Biom Mat **110**, 103940
- Katz J.L. (1971)
Composite material models for cortical bone
En Mechanical Properties of Bone (Cowin S.C., Ed.), 171-184
- Kefalas V., Eftaxiopoulos D.A. (2012)
Experimental study of cancellous bone under large strains and a constitutive probabilistic model
J Mech Behav Biomed Mater **6**, 41-52
- Kempson G.E. (1982)
Relationship between the tensile properties of articular cartilage from the human knee and age
Annals of the Rheumatic Diseases **41**, 508-511
- King R.B. (1987)
Elastic analysis of some punch problems for a layered medium
Int J Solids Structures **23**, 1657-1664
- Knets I. Malmeisters A. (1977)
Deformability and strength of human compact bone tissue in: *Mechanics of Biological Solids*, Proceedings Euromech. Colloquim 68, Varna, Bulgaria, 1975, Sofia, 123–141
- Koester K.J., Barth H.D., Ritchie R.O. (2011)
Effect of aging on the transverse toughness of human cortical bone: Evaluation by R-curves
J Mech Behav Biom Mater **4**, 1504-1513
- Kopperdahl D.L., Keaveny T.M. (1998)
Yield strain behavior of trabecular bone
J Biomech **31**, 601-608
- Korhonen R.K., Jurvelin J.S. (2010)
Compressive and tensile properties of articular cartilage in axial loading are modulated differently by osmotic environment
Medical Engineering & Physics **32**, 155-160

- Kosmopoulos V., Schizas C., Keller T.S. (2008)
Modeling the onset and propagation of trabecular bone microdamage during low-cycle fatigue
J Biomech **41**, 515-522
- Kruzic J.J., Kim D.K., Koester K.J., Ritchie R.O. (2009)
Indentation techniques for evaluating the fracture toughness of biomaterials and hard tissues
J Mech Behav Biomed Mater **2**, 384-395
- Kuhn-Spearing L.T., Kessler H., Chateau E., Ballarini R., Heuer A.H., Spearing S.M. (1996)
Fracture mechanisms of the *Strombus gigas* conch shell: Implications for the design of brittle laminates
J Mater Sci **31**, 6583-6594
- Lai W.M., Hou J.S., Mow V.C. (1991)
A triphasic theory for the swelling and deformation behaviors of articular cartilage
J Biomech Eng **113**, 245-258
- Lakes R.S., Katz J.L., Sternstein S. (1979)
Viscoelastic properties of wet cortical bone – I. Torsional and biaxial studies
J Biomech **12**, 657-678
- Landau L.D., Lifshitz E.H. (1986)
Theory of Elasticity (3rd. Ed.)
Pergamon Pres
- Lanir Y. (1979)
A structural theory for the homogeneous biaxial stress-strain relationships in flat collagenous tissues
J Biomechanics **12**, 423-436
- Laraia V.J., Heuer A.H. (1989)
Novel composite microstructure and mechanical behavior of mollusk shell
J Am Ceram Soc **72**, 2177-2179
- Lawn B. (1993)
Fracture of Brittle Solids (2nd Ed)
Cambridge Univ Press
- Libonati F., Vergani L. (2016)
Understanding the structure-property relationship in cortical bone to design a biomimetic composite
Composite Structures **139**, 188-198
- Linde A., Lussi A. Crenshaw M.A. (1989)
Mineral induction by immobilized polyanionic proteins.
Calcif. Tissue Int. **44**, 286–95.
- Lusis J., Woodhams R.T., Xanthos M. (1973)
The effect of flake aspect ratio on the flexural properties of mica reinforced plastics
Polym Engng Sci **13**, 139-145
- Makiyama A.M., Vajjhala S., Gibson L.J. (2002)
Analysis of crack growth in a 3D Voronoi structure: A model for fatigue in low density trabecular bone
J Biomech Eng **124**, 512-520
- Malcom L.L. (1976)
An experimental investigation of the frictional and deformational responses of articular cartilage interfaces to static and dynamic loading
Thesis, University of California, San Diego
- McElhaney J.H., Byars E.F. (1966)
Dynamic response of bone and muscle tissue
J Appl Physiol **21**, 4
- McEwen W. (1881)
Observation concerning transplantation of bone. Illustrated by a case of inter-human osseous transplantation, where by over two-thirds of the shaft of the humerus was restored.
Proc Roy Soc London **32** 232-247
- Meinhardt H. (2003)
The algorithmic beauty of sea shells
Springer
- Menig R. Meyers M.H., Meyers M.A., Vecchio K.S. (2001)
Quasi-static and dynamic mechanical response of *Strombus gigas* (conch) shells
Mater Sci Eng A **297**, 203-211
- Menig R., Meyers M.H., Meyers M.A., Vecchio K.S. (2000)
Quasi-static and dynamic mechanical response of *Haliotis rufescens* (abalone) shells
Acta Mater **48**, 2383-2398
- Meyers M.A., Chen P.Y., Lin A.Y.M., Seki, Y. (2008)
Biological materials: Structure and mechanical properties
Progress Mater Sci **53**, 1-206
- Meyers M.A., Lin A.Y.M., Chen P.Y., Muiyco J. (2008)
Mechanical strength of abalone nacre: Role of the soft organic layer
J Mech Behav Biom Mater **1**, 76-85
- Moir B.G. (1990)
Comparative studies of “fresh” and “aged” *Tridacna gigas* shell: Preliminary investigations of a reported technique for pretreatment of tool material
J Archaeol Sci **17**, 329-345

- Mow V.C., Woo S.L-Y., Ratcliffe A. (Eds.) (1990)
Biomechanics of Diarthrodial Joints, Vol. 1 & 2
Springer, New York
- Mow V.C., Schoonbeck J. (1984)
Contribution of Donnan osmotic pressure towards the biphasic modulus of articular cartilage
Trans Orthop Res Soc, 262
- Mow, V.C., Kuei, S., Lai, W.M. and Armstrong, C.G. (1980)
Biphasic creep and stress relaxation of articular cartilage in compression: Theory and experiments
Journal of Biomechanical Engineering **102**, 73-84.
- Munch E., Launey M.E., Alsem D.H., Saiz E., Tomsia A.P., Ritchie R.O. (2008)
Tough, bio-inspired hybrid materials
Science **322**, 1516-1520
- Myers E.R., Wilson S.R. (1997)
Biomechanics of osteoporosis and vertebral fracture
Spine **22**, 25S-31S
- Nagaraja S., Ball M.D., Guldberg R.E. (2007)
Time-dependent damage accumulation under stress relaxation testing of bovine trabecular bone
Int J Fatigue **29**, 1034-1038
- Nalla R.K., Kruzic J.J., Kinney J.H., Ritchie R.O. (2005)
Mechanistic aspects of fracture and R-curve behavior in human cortical bone
Biomaterials **26**, 217-231
- Oliver W.C., Pharr G.M. (1992)
An improved technique for determining hardness and elastic modulus using load and displacement sensing indentation experiments
J Mater Res **7**(6), 1564-1583
- Oloyede A., Flachsmann R., Broom N.D. (1992)
The dramatic influence of loading velocity on the compressive response of articular cartilage
Connective Tissue Res **27**(4), 211-224
- Osuna-Mascaró A., Cruz-Bustos T., Behamada S., Guichard N., Marie B., Plasseraud L., Corneillat M., Alcaraz G. Checa A., Marín F. (2014)
The Shell organic matrix of the crossed lamellar Queen conch shell (*Strombus gigas*)
Comp Biochem Physiol B **168**, 76-85
- Oyen M.L., Cook R.F. (2009)
A practical guide for analysis of nanoindentation data
J Mech Behav Biomed Mater **2**, 396-407
- Padawer G.E., Beecher N. (1970)
On the strength and stiffness of planar reinforced plastic resins
Polym Engng Sci **10**, 185-192
- Pastor J.Y., Elices M. (2001)
Comportamiento mecánico de la madreperla
Anales de Mecánica de la Fractura **18**, 237-243
- Pidaparti R.M.V., Chandran A., Takano Y., Turner C.H. (1996)
Bone mineral lies mainly outside collagen fibrils: Predictions of a composite model for osteonal bone
J Biomech **29**, 909-916
- Planas, J., Elices, M., Guinea G.V. (1994)
Cohesive cracks as a solution of a class of nonlocal models
In *Fracture and Damage in Quasibrittle Structures* (Bazant et al. Eds.) E & FN Spon, London, 131-144
- Planas, J., Guinea, G.V., Elices M. (1994)
Stiffness associate with quasi-concentrated loads
Materials and Structures **27**, 311-318
- Quaglini V., La Russa V., Corneo S. (2009)
Nonlinear stress relaxation of trabecular bone
Mechanics Research Communications **36**, 275-283
- Radin E.L., Paul I.L., Lowy M. (1970)
A comparison of the dynamic force transmitting properties of subchondral bone and articular cartilage
J Bone Joint Surg **52A**, 444-456
- Reiterer A., Sinn G., Stanzl-Tschegg S.E. (2002)
Fracture characteristics of different wood species under mode I loading perpendicular to the grain
Mat Sci Eng A **332**, 29-36
- Rico F., Roca-Cusachs P., Gavara N., Farré R., Rotger M., Navajas D. (2005)
Probing mechanical properties of living cells by atomic force microscopy with blunted pyramidal cantilever tips
Physical Review E **72**, 021914
- Rimnac C.M., Petko A.A., Santner T.J., Wright T.M. (1993)
The effect of temperature stress and microstructure on the creep of compact bovine bone
J Biomech **26**, 219-228
- Ritchie R.O., Kinney J.H., Kruzic J.J., Nalla R.K. (2005)
A fracture mechanics and mechanistic approach to the failure of cortical bone
Fatigue Fract Engng Mater Struct **28**, 345-371

Rotter N., tobias G., Lebl M., Roy A.K., Hansen M.C., Vacanti C.A., Bonassar L.J. (2002)
Age-related changes in the composition and mechanical properties of human nasal cartilage
Archives of Biochemistry and Biophysics **403**, 132-140

Sakar-Deliormanli A., Güden M. (2006)
Microhardness and fracture toughness of dental materials by indentation method
Journal of Biomedical Materials Research, Part B Applied Biomaterials **76B**(2), 257-264

Skalak R., Chien S. (1987)
Handbook of Bioengineering
McGraw Hill, New York

Sánchez-Gálvez V. (2012)
Materiales para la Defensa
ISDEFE-UPM, Cuadernos 10

Sarikaya M., Liu J., Aksay I.A. (1995)
Nacre: Properties, Crystallography, morphology, and formation
In *Biomimetics: Design and Processing of Materials* (Sarikaya, Aksay Eds.) AIP Press

Schaffner G., Guo, X.E., Silva M.J., Gibson L.J. (2000)
Modelling fatigue damage accumulation in two-dimensional Voronoi honeycombs
Int J Mech Sci **42**, 645-656

Schechtman H., Bader D.L. (2002)
Fatigue damage of human tendons
Journal of Biomechanics **35**, 347-353

Seki Y, Schneider M.S., Meyers M.A. (2005)
Structure and mechanical behavior of a toucan beak
Acta Mater **53**, 5281-5296

Silva M J, Hayes W C, Gibson LJ. (1995)
The effects of non-periodic microstructure on the elastic properties of two dimensional solids.
Int J Mech Sci **37** 1161-1177.

Smith I., Landis E., Gong M. (2003)
Fracture and Fatigue in Wood
John Wiley & Sons

Song F. Soh A.K., Bai Y.L. (2003)
Structural and mechanical properties of the organic matrix layers of nacre
Biomaterials **24**, 3623-3631

Song J., Chen C., Zhu S., Zhu M., Dai J., Ray U., Li Y., Kuang Y. Li Y., Quispe N., Yao Y. Gong A. Leiste U.H., Bruck H.A. Zhu J.Y., Vellore A., Li H., Minus M.L., Jia Z., Martini A., Li, T. Hu L. (2018)
Processing bulk natural wood into a high-performance structural material
Nature **554**, 224-228

Spatz, H.C, O'Leary, E.J., Vincent J.F.V. (1996)
Young's moduli and shear moduli in cortical bone
Proc R Soc Lond **B263**, 287-294

Stanzl-Tschegg S.E. (2006)
Microstructure and fracture mechanical response of wood
Int J Fracture **139**, 495-508

Stern R. (2004)
Hyaluronan catabolism: A new metabolic pathway
Eur J Cell Biol **83**(7), 317-325

Su X.W., Zhang D.M., Heuer A.H. (2004)
Tissue regeneration in the shell of the giant Queen conch, *Strombus gigas*
Chem Mater **16**, 581-593

Tang B., Ngan A.H.W. (2011)
Nanoindentation using an atomic force microscope
Philosophical Magazine **91**, 1329-1338

Thomson d'Arcy (1961)
On Growth and Form
Cambridge Univ. Pres

Timoshenko S. P, Goodier J. N. (1982)
Theory of Elasticity
McGraw Hill

Tomford W.W., Mankin H.J. (1999)
Bone banking update on methods and materials
Orthopedic Clinics of North America **30**(4), 565-570

UNE-EN 23878 (2001)
Metal duro. Ensayo de dureza Vickers
Asociación Española de Normalización

UNE-EN ISO 3738-1 (2011)
Metales duros. Ensayo de dureza Rockwell (escala A). Parte 1: Método de ensayo
Asociación Española de Normalización

UNE-EN ISO 3738-2 (2007)
Metal duro. Ensayo de dureza Rockwell (Escala A). Parte 2: Preparación y calibración de bloques patrón
Asociación Española de Normalización

- Vajjhala S., Kraynik A.M., Gibson L.J. (2000)
A cellular solid model for modulus reduction due to resorption of trabeculae in bone
J Biomech Eng **122**, 511-515
- Van der Burg M, Shulmeister V, van der Geissen E, Marissen R. (1997)
On the linear elastic properties of regular and random open-cell foam models.
J Cellular Plastics **33**, 31-54
- Wagner H.D., Weiner S. (1992)
On the relationship between the microstructure of bone and its mechanical stiffness
J Biomech **25**, 1311-1320
- Wang R.Z., Suo Z, Evans A.G., Yao N., Aksay I.A. (2001)
Deformation mechanisms in nacre
J Mater Res **16**(9), 2485-2493
- Warren W.E., Kraynik A.M. (1997)
Linear elastic behavior of a low-density Kelvin foam with open cells
J Appl Mech **64**, 787-794
- Weaire D., Phelan R. (1994)
A counter-example to Kelvin's conjecture on minimal surfaces
Phil Mag Lett **69**, 107-110
- Weidmann G. (1990)
Structural Materials, Cap. 7
Open Univ. Press
- Williams J.L., Lewis J.L. (1982)
Properties and an anisotropic model of cancellous bone from the proximal tibial epiphysis
J Biomech Eng **104**, 50-56
- Williamson A.K., Chen A.C., Masuda K., Thonar E.J-M.A, Sah R.L. (2003)
Tensile mechanical properties of bovine articular cartilage: Variations with growth and relationships to collagen network components
J Orthop Res **21**, 872-880
- Woo S.L-Y., Akeson W.H., Jemcott G.F. (1976)
Measurements of nonhomogeneous, directional mechanical properties of articular cartilage in tension
J Biomech **9**(12), 785-791
- Xiao Y., Rennerfeldt D.A., Friis E.A., Gehrke H., Detamore M.S. (2017)
Evaluation of apparent fracture toughness of articular cartilage and hydrogels
J Tissue Eng Regen Med **11**(1), 121-128
- Yamashita J., Furman B.R., Rawis H.R., Wang X., Agrawal C.M. (2001)
The use of dynamic mechanical analysis to assess the viscoelastic properties of human cortical bone
J Biomed Mater Res (Appl Biomater) **58**, 47-53
- Yao H., Dao M., Imholt T., Huang J., Wheeler K., Bonilla A., Suresh S., Ortiz C. (2010)
Protection mechanisms of the iron-plated armor of a deep-sea hydrothermal vent gastropod
PNAS **107**, 987-992
- Zhou Z.L., Ngan A.H.W., Tang B., Wang A.X. (2012)
Reliable measurement of elastic modulus of cells by nanoindentation in an atomic force microscope
J Mech Behav Biomed Mater **8**, 134-142
- Zhu H.X., Knott J.F., Mills N.J. (1997)
Analysis of the elastic properties of open-cell foams with tetrakaidecahedral cells
J Mech Phys Solids **45**, 319-343
- Zollfrank C., Sieber, H. (2005)
Microstructure evolution and reaction mechanism of biomorphous SiSiC ceramics
J Am Ceram Soc **88**, 51-58

SUBJECT INDEX

A

Adansonia digitate 102
 aggrecans 141
 aggregate modulus H_A 13
 amorphous silica 8
 amorphous bone
 animal tissues 6
 anisotropic materials 56
 antlers 119
 armour 101
 arthritis 141
 ASTM C39 13
 ASTM D-695 13
 ASTM D790 20
 ASTM D 2240 36
 ASTM D6272 20
 ASTM E8 10
 ASTM E-9 13
 ASTM E 384 36
 ASTM E384 36
 ASTM E399 27
 ASTM E1304 27, 28
 ASTM E1820 27, 30
 atherosclerotic plaques 33
 atomic force microscope 39
 axial parenchyma 104

B

bark 103
 Barthelat model 94
 basic modes of fracture 26
 mode I opening (tensile) mode 26
 mode II in plane (shear) mode 26
 mode III out-of plane (tear) mode 26
 bayonet crab 7
 Berkovich pyramid 38
 biological material, concept 81
 biomaterial, concept 81
 biomimetism, concept 81, 100, 115, 136
 biomineralisation 8
 biomorphic ceramics 115

bone 119-137

 anisotropy 132
 as biological material 137
 as biomaterial 138
 compression strength 127
 compression tests 123
 fatigue tests 136
 creep tests 130
 fatigue fractures 136
 fracture toughness 134

 overloading fractures 134
 porosity 122, 126
 relaxation tests 131
 specific fracture energy 134
 tensile strength 127
 tensile tests 124
 visco-elastoplastic behaviour 132
 bone grafts 138
 buckling 12

C

calcium carbonate 8
 calcium phosphate 8
 cambium 103

cartilage 139-135

 coefficient of friction 140
 deep layer 142
 effective pressure 143
 equilibrium modulus 146, 147
 fixed charge density FCD 141, 143
 fracture 151
 middle layer 142
 net pressure 145
 split lines 142, 146
 stiffness 146, 147
 superficial layer 142
 tensile strength 147
 tidemarks 142
 time dependent mechanical properties 148
 turgidity 143
 cellular materials 67-80
 compression tests 67
 shape of the cells 67
 tensile tests 67
 cellulose 106
 cellulose microfibrils 106
 chondrocytes 139, 141, 142
 collagen 137, 141, 142
 collagen fibres 119, 139
 composite materials 60
 compression test 12-13, 67, 76, 108
 buckling 12
 edge effect 13, 53
 coniferous plants or softwoods 103
 constrained compression test 13, 53
 aggregate modulus, H_A 13
Conus striatus 87, 96
 Cook and Gordon fracture mechanism 113
 cortical (compact) bone 7, 120, 122, 123
 crack blunting 30
 creep test 130
Chrysomallon squamiferum 101

D

dahlite 121
 dendrochronology 103
 dentin 119
 deviatoric stress tensor, σ' 51
Dracaena draco 102

E

Easterling model 107
 efficiency factor, B 63
 elastic cartilage 139
 elastic flexibility tensor, S_{ijkl} 56
 elastic modulus generalised, E' 27
 elastic modulus tensor, C_{ijkl} 56
 elastic modulus, E 27, 52, 92, 125
 elemental volumen 60
 EN 23878 34
Euplectella aspergillum 8

F

fatigue fracture in bones 136
 fibre laxity 64
 fibrous cartilage 139
 fixed charge density FCD 141, 143
 flexural strength or rupture modulus, σ_f 23
 flexure test 90
 foams and sponges 76-80
 compression tests 76
 defects 78
 structures 67
 tensile tests 79
 fracture toughness measurement, K_C 27
 fracture toughness, K_C 26, 74
 fracture, global approach 27
 specific fracture energy, G_C 27
 strain energy rate, G 27
 fracture, local approach 26
 fracture toughness, K_C 26, 74
 stress intensity factor, K 26
 free energy per unit volumen, F 47, 51
 freeze casting 100
 Fung quasi-linear viscoelastic model 149

G

GAGs 139, 141, 143, 144, 145
 Gibbs-Donnan equation 143
 glycosaminoglycans, GAGs 139
 growth rings 103, 105, 107

H

Halotis 88, 89, 96
Halotis rufescens 86
 hardness, Brinell HB 33, 34
 hardness, Knoop HK 36
 hardness, Rockwell HR 34
 hardness, Vickers HV 34, 36
 Hashin-Shtrikman model 125
 Haversian bone 121
 Haversian canal 121
 hearthwood 103
 hemicellulose 106
 heterogeneous materials 60-66
 elemental volume 60
 Reuss model 61
 Voigt model 61
 homogeneous deformation 51
 homogeneous materials 46-59
 honeycomb structures 67, 69
 buckling collapse 70
 cells compression 69
 cells densification 70
 cells traction 74
 rupture collapse 70
 yielding collapse 70
 Hooke's law 52
 horns of bovids 119
 horsetail stem 6, 8
 hyaline or articular cartilage 139
 hyaluronic acid 141
 hydrostatic or compressibility modulus, K 51
 hydrostatic stress tensor, σ_h 51
 hydrostatic tension (or compression) state 51
 hydroxyapatite 119, 121

I

indentation in the macroscopic domain 34
 indentation in the microscopic domain 36
 indentation in the nanoscopic domain 38
 indentation of laminas and thin films 42
 indentation techniques for measuring fracture toughness 42
 indentation tests 33-43
 indentation, yield stress 33
 internal energy per unit volume, U 47
 ISO 14577 33
 ISO 3738 34
 isotropic materials 51, 56

K

Kosmopoulos model 136

L

Lai poroelastic triphase model 149
 Lamé coefficients 51
 lamellar bone 121
 Lanir model 64, 65
 leafy plants or hardwoods 103
 lignin 106
Lomatia Tasmania 103
 longitudinal parenchyma 105

M

mineralised collagen fibres 121
 mollusc 83
 bivalves 83
 cephalopods 83
 gastropods 83, 85, 86
 periostrack 86, 87
mollusc shells 6, 83-101
 as Biological material 99
 as biomaterial 99
 biomimetics 100
 crossed-lamellar structure 87, 96
 crossed-lamellar structure, mechanical properties 96
 lamellae 87
 parallel-lamellar structure 86, 96
 parallel-lamellar structure, mechanical properties 89
 toughness 97
 Mow et al. poroelastic biphasic model 149

N

nacre or mother-of-pearl 86, 99
 Navier hypothesis 21
 necking instability 10
 neutral axis 20, 21, 22

O

osmotic pressure 143, 144
 osteoarthritis 120, 141, 152
 osteoblasts 119
 osteoclasts 119
 osteocytes 119
 osteone 121
 osteoporosis 119, 120, 134, 137
 overloading fracture in bones 134

P

Padawer-Beecher model 92
 pearl 99
 periosteum 119
Pinctada 89, 96
Pinctada máxima 86, 99
Pinus aristata 102
Pinus heldreichii 102
 plant tissues 6
 Poisson's ratio 52
 proteoglycans 139, 141
 pure shear state 51

R

radial parenchyma 104, 105
 relative density 67, 69
 Reuss model 61, 92, 125
 rheumatoid arthritis 152
 Riley model 92
 rupture modulus or flexural strength, σ_f 23
 rupture tests 26-32

S

Saint-Venant principle 10, 13
 sapwood 103
Sequoia sempervirens 102
 shear modulus, G 16, 51
 shear test 90
 Shore durometer 36
 specific fracture energy measurement, G_C 30
 specific fracture energy, G_C 27, 90
 strain energy release rate, G 27
 strain tensor, ε 46
 strength and toughness 6
 stress intensity factor, K 26
 stress tensor, σ 46, 47
Strombus 88
Strombus gigas 87, 96
 synovial fluid 140, 152

T

tensile test 10, 53, 67, 79, 90
 tensile test, slow strain rate 146
 thixotropy 152
 torsion test 16-17
 toucan beak 7
 tough ceramics 100
 trabecular (cancellous or spongy) bone 7, 120, 122, 123
 tracheids 103, 104
 transversely isotropic material 56
Tridacna gigas 99

U

uniaxial tensile test 10, 53

unit cells 68, 69

V

Voigt model 61, 92, 125

W**wood 102-117**

as biological material 115

as biomaterial 115

balsa wood 107, 109

biomimetics 115

cells 104

compressive strength 111

elastic modulus 108

Easterling model 107

fibres 104

fracture and toughness 112

X

xylem 103